Etude par Sonde Atomique Tomographique de la formation de nano-particules dans les aciers ODS et NDS

Olena Kalokhtina

Université de Rouen

U.F.R. des Sciences et Techniques

Ecole doctorale « SPMII »

THESE

Discipline : Physique

Spécialité : Sciences des Matériaux

Présentée par

Olena KALOKHTINA

Pour l'obtention du grade de

DOCTEUR DE L'UNIVERSITE DE ROUEN

Le 5 juin 2012

STUDY OF THE FORMATION OF NANO-PARTICLES IN ODS AND NDS STEELS BY ATOM PROBE TOMOGRAPHY

Directeur de thèse : Philippe PAREIGE

Encadrant : Bertrand RADIGUET

Membres du jury :

Mme. Marie-France BARTHE	Directeur de Recherches – Orléans	Présidente
M. Michel PEREZ	Professeur des Universités - Lyon	Rapporteur
Mme. Brigitte DECAMPS	Directeur de Recherches - Orsay	Rapporteur
Mme. Martine BLAT	Ingénieur Chercheur EDF - Les Renardières	
M. Yann de CARLAN	Ingénieur CEA - Saclay	
M. Philippe PAREIGE	Professeur des Universités - Rouen	
M. Bertrand RADIGUET	Maitre de Conférences - Rouen	

Study of the formation nano-particles in ODS and NDS steels by Atom Probe Tomography

Abstract: Thanks to their good mechanical properties at high temperature and their stability under irradiation and thermal ageing, Oxide Dispersion Strengthened (ODS) steels are good candidates for fuel claddings of several Generation IV nuclear reactors. Based on the same principle, ferritic/martensitic (FM) steels can also be reinforced by nitrides (Nitride Dispersion Strengthened (NDS) steels).

In both cases, elaboration processes have to be optimized to get a fine and dense dispersion of nano-reinforcements. Such optimization requires characterizing the microstructure at the nanometer scale, in order to understand the basic mechanisms of formation of the nitrides and oxides during elaboration. In this work, Atom Probe Tomography has been used to investigate the nanostructure of ODS and NDS steels at different steps of the elaboration.

- An ODS model alloy, with a high level of Y, Ti and O, as well as a ferritic ODS steel produced by mechanical alloying (MA) of Fe-18CrWTi and 0.5% Y_2O_3 (wt.%) powders in industrial attritor were investigated in as milled state. In addition, the steel was characterized after annealing at 850°C during 1 hour and after extrusion at 1100°C. It is shown that milling results in partial dissolution of Y and O in the matrix. However, Y, O and in a less extend Ti rich nanoclusters are present in as-milled state. During subsequent annealing and consolidation, these nanoclusters act as nuclei for formation of Y-Ti-O-rich nanoparticles.
- Ferritic NDS steels elaborated by two distinct ways, (i) mechanical alloying or (ii) nitriding of pre-alloyed powders, followed by annealing at different temperatures or hot-extrusion, were investigated. In the first case a high density of Ti and N rich nanoparticles is observed since as-milled state. It is shown that consolidation should be performed at 800°C to get the highest density of particles since coarsening occurs at higher temperatures. In the second case, Cr and Ti nitrides are observed after annealing. This result is encouraging. However, the process needs to be improved, in order to get a more homogeneous microstructure.

This research has been supported by the Agence Nationale de la Recherche within the aXtrem project.

Key words: ferritic-martensitic ODS steels, mechanical alloying, nitriding, 3D atom-probe, phase transformations.

Acknowledgements

It would not have been possible to write this doctoral thesis without the help and support of the kind people around me who made my stay throughout my thesis so rich and valuable.

Above all, I would like to express my deep and sincere gratitude to my supervisors, Pr. Philippe PAREIGE and Dr. Bertrand RADIGUET, who accepted me as their Ph.D. student, giving wonderful opportunity to perform this research. They offered me so much advice, good teaching and lots of good ideas, patiently supervising and allowing me to develop the understanding of the subject.

I am very thankful to Mr. Michel PEREZ, Professeur des Universités INSA Lyon and Mme Brigitte DECAMPS Directrice de Recherches CSNSM Orsay, who kindly accepted to review this manuscript in extremely short period of time. Their constructive comments and remarks improved the quality of my Ph.D. work.

My sincere thanks also go to the president of the dissertation committee Mme Marie-France BARTHE, Directrice de Recherches CEMHTI/CNRS Orléans, for her time and efforts in the understanding of this work.

I would like to express my deep gratitude to Mr Yann de CARLAN Ingénieur CEA Saclay and Mme Martine BLAT Ingénieur Chercheur EDF Les Renardières, for the organization of my work within my research project and participation in the dissertation committee of the thesis.

Appreciation also goes to Stéphanie Hollner, Ingénieur post-doc CEA Saclay, for her timely help and advices concerning MatCalc simulations.

There are all the other people who played very special role over all those years.

I am very grateful to Gerald DA COSTA and Francois VURPILLOT for their capability to quickly answer the questions and give their personal opinion on the experimental topics.

I also would like to express my appreciation to Fabien CUVILLY, who patiently introduced me to the world of SEM/FIB tip preparation. It would be no exaggeration to say that this study would not have been completed today without his motivation and help.

My thanks go to Constantinos HATZOGLOU, for his kind help with the modeling of evaporation behavior adapted to the case of materials studied in the thesis.

I am very thankful to the technical staff of GPM laboratory for providing me a wonderful working environment. My thanks go to Sylvain CHAMBRELAND, Laurence CHEVALIER,

Béatrice FOULON, Cécile GENEVOIS-MAZELIER, Jonathan HOUARD, Charly VAUDOLON, Romain VINCENT for their full-time assistance during my research work and timely help.

I owe my deepest gratitude to GPM office staff. In particular, Christine CLERGET, Agnès DALLE, Caroline JORRY, Germain MARTIGNY for their kind help in organization questions and in communication with state institutions, where their assistance was very valuable.

I would like also to acknowledge my dear friends with whom I shared my PhD years Irina, Victor, Alexander, Slava and Alla. Also, these three and a half years in Rouen would not been so good time without wonderful people Marilyne, Adeline, Manuel, Nicolas, Maria, Thomas, Julien, Hefei, Wanghua and all others my colleagues and friends. Thank you for your support, assistance and friendship!

The last but not the least, I am greatly indebted to my family, that despite the geographical distance was always nearby. These thanks are for my parents for their unlimited support and lots of wise words when it was needed. I am also very grateful to my husband for his incredible amount of patience, care and encouragements all the time.

Though it will not be enough to express my gratitude in words to all those people who support me all this time…Thank you!

Table of content

INTRODUCTION ____ **1**

CHAPTER 1. DEVELOPMENT OF NANO-REINFORCED F/M STEELS ____ **4**

I. Generation IV nuclear reactors 4

II. Materials requirements and possible candidates for SFR 8

II.1. Austenitic steels 9

II.2. Ferritic/Martensitic (F/M) steels 10

II.3. Nano-reinforced steels 10

III. Elaboration process of ODS 10

III.1. Mechanical Alloying process 11

III.2. Consolidation of powder and additional TMT 13

III.3. Microstructure and influence of elaboration parameters 14

a)Ferritic or ferritic/martenticitic (F/M) matrix 14
b)Dispersion of oxides particles 16
c)Mechanism of formation of nanoparticles 23
d)Influence of the elaboration parameters on the microstructure of ODS 25

III.4. Partial conclusion 28

IV. Nitride Dispersion Strengthened (NDS) alloys 30

IV.1. NDS elaboration by nitriding 30

a)Principle 30
b)NDS production since 80`s 32
c)Mechanism of formation of nitrides 35

IV.2. NDS elaboration by Mechanical Alloying 37

IV.3. Partial conclusions 38

V. Bibliography of Chapter 1 39

CHAPTER 2. MATERIALS, EXPERIMENTAL AND SIMULATION TECHNIQUES ____ **46**

I. Materials 46

I.1. ODS model alloy 47

I.2. ODS steel 48

I.3. Mechanically alloyed NDS steel (MA NDS) 49

I.4. Nitrided NDS 50

II. Atom Probe Tomography (APT) 52

II.1. Principle **52**

II.2. Laser assisted field evaporation 56

II.3. Experimental devices and their performances 57

II.4. Particular case of ODS and NDS materials 60

a)Determination of experimental parameters 60
b)Isotope overlaps 64
c)Methods for APT data treatment 69
d)Local magnification effect 71

III. Modelling of precipitation kinetics with MatCalc and Thermocalc 79

III.1. Theory of precipitation kinetics 79

III.2. Modelling of precipitation kinetics with MatCalc 80

a)Precipitate nucleation 80
b)Evolution of radius and composition of precipitates 81
c)Evaluation of interfacial energies 82

III.3. Used parameters for MatCalc calculations 83

III.4. ThermoCalc software 84

IV. Conclusions of the Chapter 2. 86

V. Bibliography of the Chapter 2 87

CHAPTER 3. OXIDE DISPERSION STRENGTHENED STEELS_____90

I. ODS model alloy 91

I.1. Investigation of as-milled state 91

a)Microstructure 91
b)Evaporation artifacts 94
c)Chemical composition of Y-Ti-O-rich and Fe-rich phases 99

I.2. Discussion 103

I.3.Partial conclusion 107

II. ODS industrial steel 108

II.1. Global chemical composition 108

II.2. Nanoparticles study 110

a)Distribution, number density and size 110
b)Chemical composition 112
c)Interfacial structure of nanoparticles 115

II.3. Discussion 117

a)Comparison between APT, SANS and TEM results 117
b)Composition of nanoparticles 121
c)Formation mechanism of nanoparticles in ODS steel 125

II.4.Partial conclusion 127

III. Bibliography of Chapter 3 128

CHAPTER 4. NITRIDE DISPERSION STRENGTHENED STEELS_____131

I. Study of MA NDS steel 131

I.1. Matrix chemical composition 132

I.2. Grain boundaries study 133

a)Powder annealed at 600°C/1h 133
b)Powder annealed at 700°C/1h 135
c)Hot extruded state 136
d)Segregation intensity as a function of temperature 137

I.3. Nanoparticles characterization 138

a)As-milled condition 138
b)Annealing at 600°C/1h 141
c)Annealing at 700°C/1h 144
d)Hot extruded condition (800°C) 146
e) Annealing at 850°C/1h 148
f)Annealing at 1000°C/1h 152

I.4. Discussion 153

a)Chemical composition of nanoparticles 153
b)Precipitation and kinetics 158
c)Comparison between ODS and NDS 162

I.5. Partial conclusion 165

II. Study of nitrided NDS 166

II.1. Characterization of powders 166

a)Powder in as-nitrided state 167
b)Powder annealing at 600°C/1h 168
c)Powder annealing at 700°C/1h 171

II.2. Characterization of consolidated material 175

a)Experiment 1. LATAP 175
b)Experiment 2. LAWATAP 176
c)Experiment 3. LAWATAP 178

II.3. Discussion 180

II.4 Partial conclusion 183

III. Bibliography of the Chapter 4 184

GENERAL CONCLUSIONS AND PERSPECTIVES_____186

APPENDIXES 192

Appendix 1.ANR AXTREM program 193

Appendix 2. 3DAP sample preparation methods 195
a) "Double layer" method 195
b) "Micro-loop" method 196
c) Preparation of APT tips from powders 196
d) Specimen preparation for neutron diffraction experiments 198

Appendix 3. 3DAP data treatment methods 200
a) Statistical tests 200
b) Method of "iso position" 201
c) "Erosion" method 203

Appendix 3. Field evaporation model 205

Appendix 4. MatCalc script 207

Bibliography of Appendixes 211

Introduction

Today many research programs are devoted to the improvement of existing materials and to the development of new ones that will be able to meet the different challenges for the new generations of nuclear reactors (Generation IV and fusion). The objective of Generation IV (GEN IV) reactors is to produce an abundant, reliable, proliferation resistant, safe and of course competitive energy. All these innovative systems are based on a higher running temperature associated to more severe irradiation conditions (higher irradiation dose, fast neutrons). As it is easily understandable, the combination of high temperature, high neutron dose and severe environment is a major challenge for the viability of structural materials.

Oxide-Dispersion-Strengthened (ODS) ferritic / martensitic steels are developed in order to combine the swelling resistance of ferritic steels with a creep resistance in high temperature conditions at least equal to the austenitic steels. They found their application for fuel cladding of several GEN IV reactors [1–4].

With respect of the positive experience of ODS materials, new or alternate pathway to create iron-based alloys reinforced with a fine dispersion of nitrides - *Nitride-Dispersion-Strengthened steels (NDS)* – are envisaged and tested. In this case, the material could benefit of the stability of nitrides particles [5]. In order to elaborate these new materials, several elaboration ways can be envisaged. Among them, nitriding could lead to a minimization of the production costs, thus avoiding expensive mechanical alloying step required in the case of ODS steels.

An attempt to produce such NDS materials has been realised within the *aXtrem project* leaded by CEA Saclay and launched by the *Agence Nationale de la Recherche (ANR)*. The main objective of the project is the development of advanced materials reinforced by stable dispersion of nanoparticles (oxides and nitrides) dedicated to cladding elements of the so-called Sodium Fast Reactor. In order to improve or to give for the first time an understanding of the basic mechanism at the origin of the formation of nano-reinforcement in Oxide-Dispersion-Strengthened (ODS) and Nitride Dispersion Strengthened (NDS) steels and to qualify their possible application (from research to development), several research groups: *CEA SRMA* (Saclay), *EDF MMC* (Les Renardières), *Laboratoire Léon Brillouin* (Saclay), *CNRS* - Groupe de Physique des matériaux (Rouen) and industrial partners: *AREVA NP* (Lyon), *Nitruvid Bodycote* (Argenteuil), *Sotep*, (Issoudun), join their efforts in the project. In this program, complementary techniques such as Atom Probe Tomography (APT),

Transmission Electron Microscopy (TEM) and Small Angle Neutron Scattering (SANS) are used to fully characterize, at very fine scale ODS and NDS materials.

The present Ph.D. work has been performed in this aXtrem framework and is mainly devoted to the characterization of ODS and NDS materials using the Atom Probe Tomography [6–9]. The characterization of the microstructure after each step of the elaboration process (such as mechanical milling, nitridation, extrusion etc… as well as after annealing at various temperatures), gives key information for the understanding of the nanoclusters formation mechanisms which is necessary for the optimization of the elaboration process.

The present report is divided into 4 chapters. The first chapter describes the innovative nuclear systems issue from the Generation IV Forum, focusing on their severe service conditions. More details are given for the SFR concept and specificities for materials of cladding elements. A first half of the chapter is devoted to ODS, their development and physical metallurgy. More details are given on the oxide nanoparticles, structure, composition as well as their formation mechanism. The second half of the chapter is devoted to NDS steel. Possible ways of elaboration, experience in the past as well as today's opportunities are discussed.

The second chapter reports the description of the studied materials, their elaboration conditions, and the methods used in this work. The basic concepts of APT technique, the explanation of data treatment methods as well as the difficulties associated to the specific case of ODS steels, will be discussed. MatCalc and ThermoCalc softwares were also used in this work in order to estimate the expected microstructure as a function of the chemical composition and heat treatment patterns. Their basic principles and the parameters that were used for modeling are described.

The third chapter provides an atomic scale description of two Oxide Dispersion Strengthened ODS materials. The first one is a model alloy that is characterized in the as-milled condition. As the second one is concerned, it is an industrial ODS steel designed by CEA [10]. A more complete study of the three following states is presented: as-milled, annealed and consolidated. These results associated to results coming from different techniques (from other laboratories, TEM [10–12], SANS [12]) are compared. This general description of the material allows to give some scenario for the observed microstructural evolution.

The forth chapter deals with the microstructural data obtained on Nitride Dispersion Strengthened steels (NDS). The characterisation of NDS material produced by mechanical alloying (MA NDS) is firstly reported. In a second part, the results of the study of NDS material produced by nitriding process are given. Both materials were characterized after different treatments: initial state (as-milled or as-nitrided), after subsequent annealing treatments (up to 1000°C) as well as in the hot extruded state.

Finally a conclusion summarises all this study, gives some tendencies for ODS or NDS structural formation and evolution and gives some perspectives on the elaboration ways used here and production of nanostructured materials.

References:

[1] K.L. Murty, I. Charit, Journal of Nuclear Materials 383 (2008) 189–195.

[2] S. Ukai, S. Mizuta, T. Yoshitake, T. Okuda, M. Fujiwara, S. Hagi, T. Kobayashi, Journal of Nuclear Materials 283-287 (2000) 702–706.

[3] S. Ukai, M. Harada, H. Okada, M. Inoue, S. Nomura, S. Shikakura, K. Asabe, T. Nishida, M. Fujiwara, Journal of Nuclear Materials 204 (1993) 65–73.

[4] J.S. Cheon, C.B. Lee, B.O. Lee, J.P. Raison, T. Mizuno, F. Delage, J. Carmack, Journal of Nuclear Materials 392 (2009) 324–330.

[5] L.E. Kindlimann, G.S. Ansell, Metall and Materi Trans B 1 (1970) 507–515.

[6] D. Blavette, A. Bostel, J.M. Sarrau, B. Deconihout, A. Menand, Nature 363 (1993) 432–435.

[7] D. Blavette, B. Deconihout, A. Bostel, J.M. Sarrau, M. Bouet, A. Menand, Rev. Sci. Instrum. 64 (1993) 2911.

[8] M.K. Miller, R.G. Forbes, Materials Characterization 60 (2009) 461–469.

[9] A. Menand, E. Cadel, C. Pareige, D. Blavette, Ultramicroscopy 78 (1999) 63–72.

[10] Y. de Carlan, J.-L. Bechade, P. Dubuisson, J.-L. Seran, P. Billot, A. Bougault, T. Cozzika, S. Doriot, D. Hamon, J. Henry, M. Ratti, N. Lochet, D. Nunes, P. Olier, T. Leblond, M.H. Mathon, Journal of Nuclear Materials 386-388 (2009) 430–432.

[11] F. Delabrouille, Rapport H-T27-2010-00646-FR. Caractérisation Au Microscope Electronique En Transmission D'alliages NDS Et ODS (ANR AXTREM), 2010.

[12] M. Ratti, Développement De Nouvelles Nuances D'acier Ferritiques/martensitiques Pour Le Gainage D'élément Combustible Des Réacteurs à Neutrons Rapides Au Sodium. Thèse, Institut Polytechnique de Grenoble, 2009.

Chapter 1.
Development of nano-reinforced F/M steels

I. Generation IV nuclear reactors

Grow of energy demands and understanding of the link between global warming and carbon emissions cause to search alternative large-scale power sources. From that point of view, nuclear energy is an attractive source of energy. It allows production of low-cost energy and simultaneously reduces greenhouse gas emissions in 20-75 times [1] (see *Figure 1.1*) in comparison to natural gas power sources (the cleanest fossil fuel available).

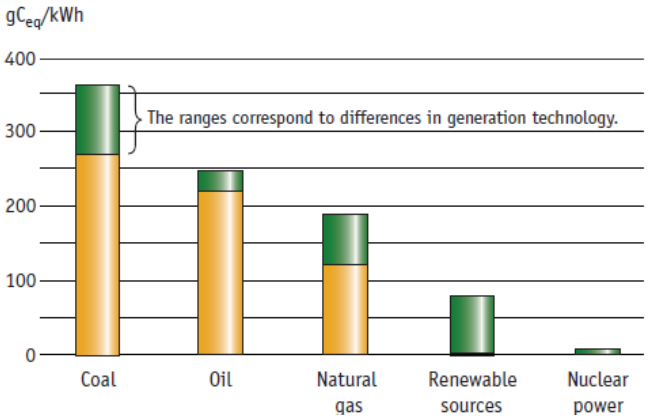

Figure 1.1. Greenhouse gas emissions from electricity generations by different sources [1].

It meets more than 20% [2] of the world's demand for electricity today. Further advances in nuclear energy system designs can broaden the opportunities for the use of nuclear energy. To explore these opportunities, the U.S. Department of Energy's Office of Nuclear Energy, Science and Technology has engaged governments, industries, and the research community worldwide in a wide-ranging discussion on the development of next-generation of nuclear energy systems, known as "Generation IV". This has resulted in the formation of the Generation-IV International Forum (GIF). Member countries of GIF are interested in jointly defining the future of nuclear energy. Generation IV refers to the development and demonstration of one or more nuclear energy systems that would satisfy to the following conditions [3]:

- ***sustainability*:** the systems should offer efficiency in the use of the natural resources, minimize environmental impact and minimize wastes (in terms of mass, radio toxicity, residual power, etc.);

- ***economics:*** the generating cost should be competitive compared with other energy sources and the capital investment cost should be low enough for the nuclear system under development to remain accessible to a large number of countries;
- ***safety and reliability*****:** it is obligatory that future reactors perform at least as well in terms of safety and reliability as current reactors. In particular, a key focus is elimination, as far as possible, of the need for public evacuations from areas outside nuclear sites in the event of an accident;
- ***resistivity*** to proliferation risks and likely to be easily protected from external attack.

For the moment, six reactors designs could reach the Gen IV goals [4]:

Molten salt reactor (MSR) is one of the thermal reactors. In many designs, the nuclear fuel is dissolved in the molten fluoride that serves as a coolant. The fluid becomes critical in a graphite core, which serves as moderator.

Supercritical-Water-Cooled Reactor (SCWR) is also a thermal spectrum reactor. It uses supercritical water (water at a temperature and pressure above its critical point, containing both properties of the liquid and the gas) as moderator and coolant.

Very-High-Temperature Reactor (VHTR) is a thermal reactor that uses a graphite moderator. The outlet temperature, ~ 1000°C envisaged by reactor design, allows to increase thermal efficiency.

Gas-Cooled Fast Reactor (GFR) is a fast neutron spectrum helium-cooled reactor with outlet temperature of 850°C. Radiation to high doses does not make helium radioactive in comparison to other possible coolants.

Lead-Cooled Fast Reactor (LFR) is a fast neutron reactor with molten lead or lead-bismuth eutectic coolant.

Sodium-cooled fast reactor (SFR) is fast neutron sodium-cooled reactor with closed fuel cycle for efficient management of actinides and conversion of fertile uranium.

Schematic overview and relevant information about six selected reactors is represented in *Figure 1.2*. The detailed description of the mentioned systems can be found in [4,5]. Most of these designs are generally not expected to be available for commercial construction before 2040 [6].

Thermal ***Fast***

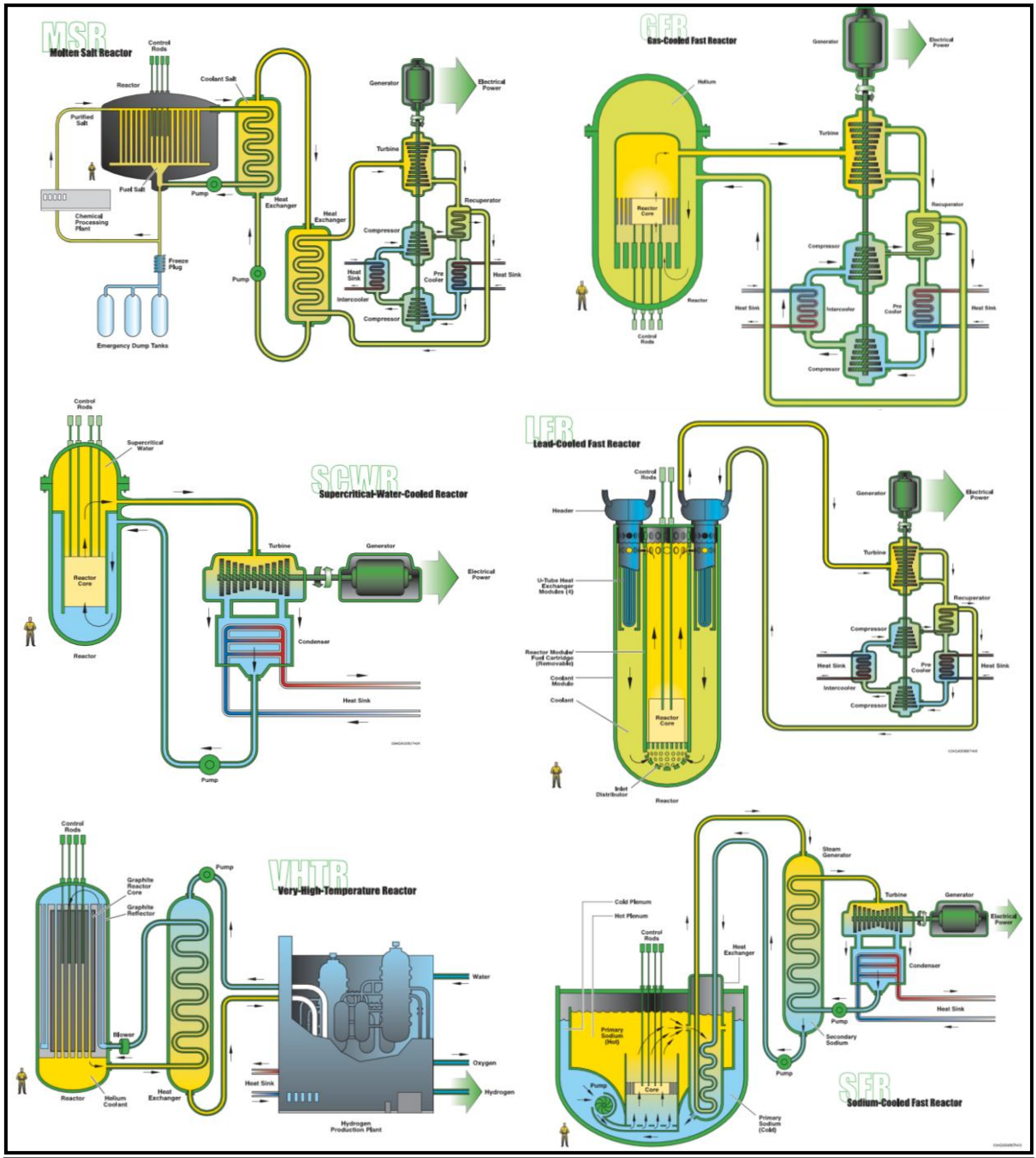

	Neutron spectrum	Coolant	Temperature (°C)	Fuel	Fuel cycle	Size(s) (MWe)
Sodium-cooled fast reactors (SFR)	Fast	Sodium	550	U-238 and MOX	Closed	50, 1700
Very high temperature gas reactors (VHTR)	Thermal	Helium	1000	UO_2 prism or pebbles	Open	275
Gas-cooled fast reactors (GFR)	Fast	Helium	850	U-238	Closed	300, 1500
Supercritical water-cooled reactors (SCWR)	Thermal or fast	Water	625	UO_2 or MOX	Open (thermal) or closed (fast)	1700
Lead-cooled fast reactors (LFR)	Fast	Pb or Pb–Bi	480–800	U-238	Closed	10–100, 600
Molten salt reactors (MSR)	Epithermal	Fluoride salts	700–800	UF in salt	Closed	1000

Figure 1.2. Schematic overview of the different Generation IV reactors [4,6]. Reference information is also presented [6].

Despite the differences among proposed concepts of Gen IV reactors (*Figure 1.2.*), the envisaged operation conditions for all these systems are rather challenging for structural materials. As it can be seen in *Figure 1.3,* the operating temperature of currently operating reactors (Gen II) does not exceed 400°C, whereas for Gen IV it is much higher. In addition, higher neutron doses than in Gen II, are expected for some of these systems (LFR, MSR, SFR).

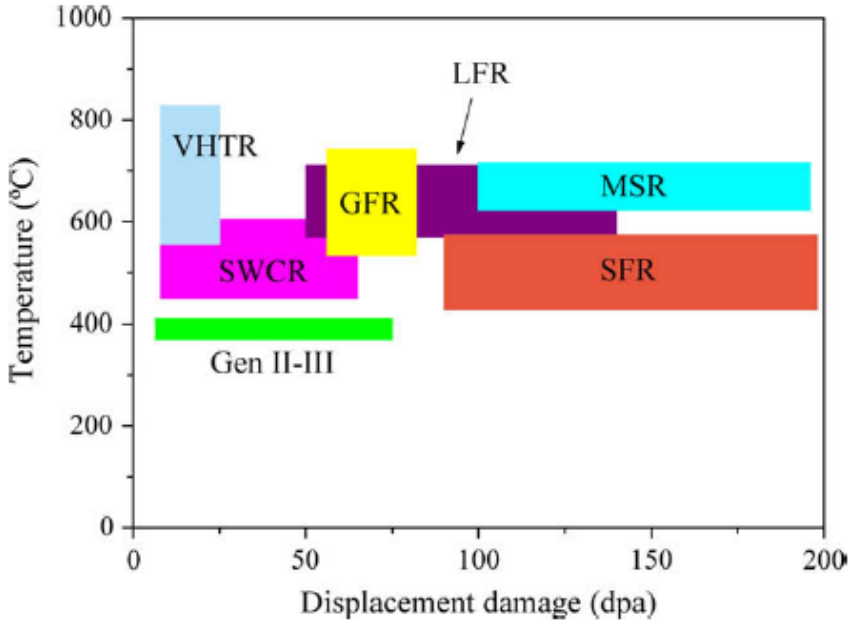

Figure 1.3. Overview of operating temperatures and displacement damage dose regimes for structural materials in current (generation II) and proposed future (Generation IV) fission energy systems. The six Gen IV fission systems are Very High Temperature Reactor (VHTR), Super Critical Water Reactor (SCWR), Lead Fast Reactor (LFR), Gas Fast Reactor (GFR), Sodium Fast Reactor (SFR) and Molten Salt Reactor (MSR) after [7].

Among the other GEN IV designs, SFR reactors may not require so much developments since significant experience already exist (prototypes have been operated: Joyo and Monju in Japan, BN600 in Russia and Phénix in France). SFR gained due to its closed fuel cycle and excellent potential for actinide management, including resource extension. Also, economics, safety and proliferation resistance are among its advantages. Recently, in the framework of Generation IV initiative, Fast Sodium Reactor is chosen as a priority reference design by many countries. France also has announced and confirmed the decision to build a prototype of SFR scheduled for operation in 2020 [8].

However, the operation conditions of SFR (as well as other Gen IV innovative systems) may be a major obstacle for the viability of existing materials employed for core elements. Core materials of concern are fuel components such as the cladding (*Figure 1.4*). The cladding keeps the fuel and products of fission reaction isolated from coolant (liquid Na). The

SFR cladding will be subjected to temperatures from 400 to 600°C and neutron doses up to 200 dpa. In addition cladding is surrounded by corrosive liquid Na that may have negative effect on material. The integrity of the fuel pins strongly depends on whether the cladding can withstand the irradiation environment.

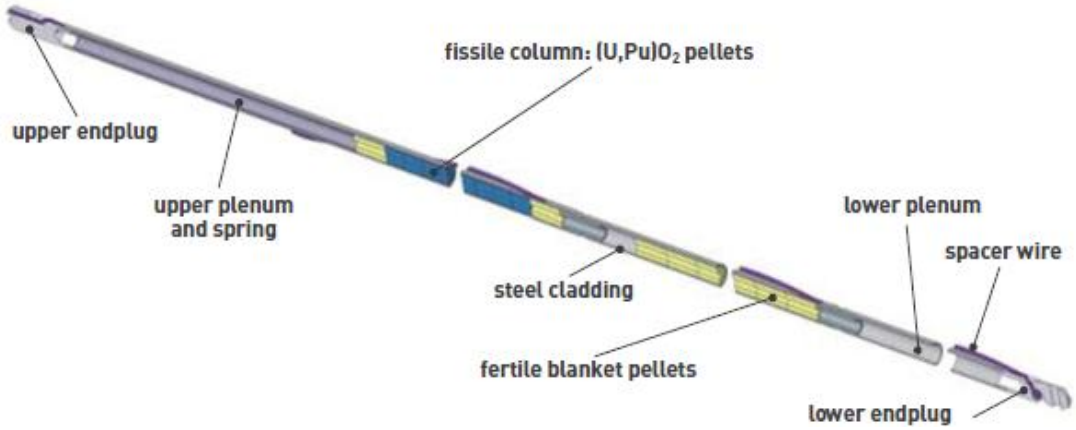

Figure 1.4. Fuel pin of Sodium Fast Reactor and its main components [9].

In this context, the aXtrem program has been launched by the Agence Nationale de la Recherche (ANR). It is devoted to development of advanced materials for application in extreme conditions such as cladding elements of Sodium Fast Reactor. The present work is done in the framework of this program. More details about the participants can be found in the Appendix 1.

The possible candidates for cladding elements of SFR are described in the following section.

II. Materials requirements and possible candidates for Sodium Fast Reactors

Materials used in the core components, in the particular case of cladding elements of SFR, should satisfy the following requirements [10–12]:

- mechanical properties of material (tensile strength, ductility, creep resistance, fracture toughness) should remain acceptable after ageing;
- dimensional stability under irradiation, whether under stress (irradiation creep or relaxation) or without stress (swelling, growth);
- physical and chemical compatibility with the coolant;
- other criteria for the materials are their costs to fabricate and to assemble.

All these requirements must be satisfied under normal operating as well as in accidental conditions. These demands are similar to materials used in the current commercial reactors, but are actually much more demanding for Gen IV [13].

Different metallic materials are envisaged for cladding application in SFR. They are discussed below.

II.1. Austenitic steels

This type of materials was selected for the cladding elements of first generation of fast reactors [14,15]. For this purpose, *304* and *316* steels were used. They are chosen based on their good corrosion and thermal creep resistance. The high temperature mechanical strength, good fabrication technology and abundant experience are also among their advantages. However, they are subjected to significant void swelling induced by radiation [16]. It has been improved by adding stabilizing elements, varying chemical composition and applying cold work. For cladding, as an example, 316Ti steel has been changed by austenitic 15/15Ti, exhibiting better swelling resistance. But use of latter one is also limited by swelling at high doses, as it can be seen on *Figure 1.5*. In addition, influence of radiation provokes the depletion of Cr from grain boundaries, making these materials sensitive to corrosion issues [17–19].

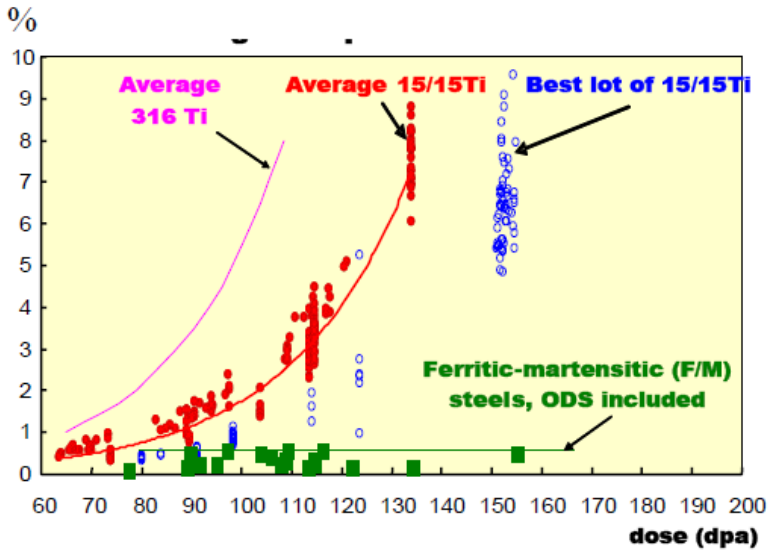

Figure 1.5. Hoop deformation of different grades of austenitic Phénix claddings and ferritic/martensitic (F/M) materials versus dose at temperatures between 675 and 825 K after [11].

II.2. Ferritic/Martensitic (F/M) steels

These materials offer more advantages and are potential candidates for SFR claddings as well as for other Gen IV designs [14,15]. Commercial ferritic/martensitic steels based on 9-12%Cr exhibit the highest swelling resistance in comparison with austenitic steels (*Figure 1.5*). This low swelling response appears to be a generic property of ferritic alloys [20,21]. In addition these materials have high thermal conductivity and low thermal expansion. A limitation to the use of ferritic–martensitic steels is their creep resistance at temperatures (400-600°C) desired in the Gen IV systems. One approach to extend the range of operation temperatures of F/M steels is reinforcing the F/M lattice by stable dispersion of nanoparticles.

II.3. Nano-reinforced steels

One example of such nano-reinforced steels may be Oxide Dispersion Strengthened steels (ODS). These materials are presently achieve increasing attention and currently considered as cladding materials for SFR and several types of Gen IV systems [22,23].

These materials show remarkable properties due to high density (~10^{23} to ~10^{24} m^{-3}) of nanometre scale oxide particles (1-10 nm in diameter) dispersed in Fe-Cr matrix. These nano-oxides are found to be extremely resistant to coarsening (even during ageing at 900°C for times up to 3000 h [24,25]). They act as i) obstacles to dislocation motion [26], providing high creep strength in the range of interest [27–30] for SFR application and ii) sinks for radiation induced point defects, providing good radiation resistance [31–34].

Properties of such ODS steels strongly depend on microstructure that requires close control over nanoparticles density, size, interfacial properties, etc.

Elaboration way, influence of chemical composition and elaboration parameters on final microstructure, as well as study of nano-oxides will be discussed in next section.

III. Elaboration process of ODS

ODS steels are usually produced by complex powder metallurgy technique: mechanical alloying (MA). This process is a dry, high energy ball-milling process, where elemental or pre-alloyed powders (Fe, Cr etc…) are milled together with oxide dispersoid and subsequently mechanically homogenized [31–35]. After MA the powder is consolidated by powder metallurgical processes, as Hot Isostatic Pressing (HIP) or Hot Extrusion (HE). Then

different recrystallization and cold- warm-working heat treatments are applied to produce final form such as tube [40,41]. Schematic elaboration route for iron-base ODS is shown on Figure *1.6*.

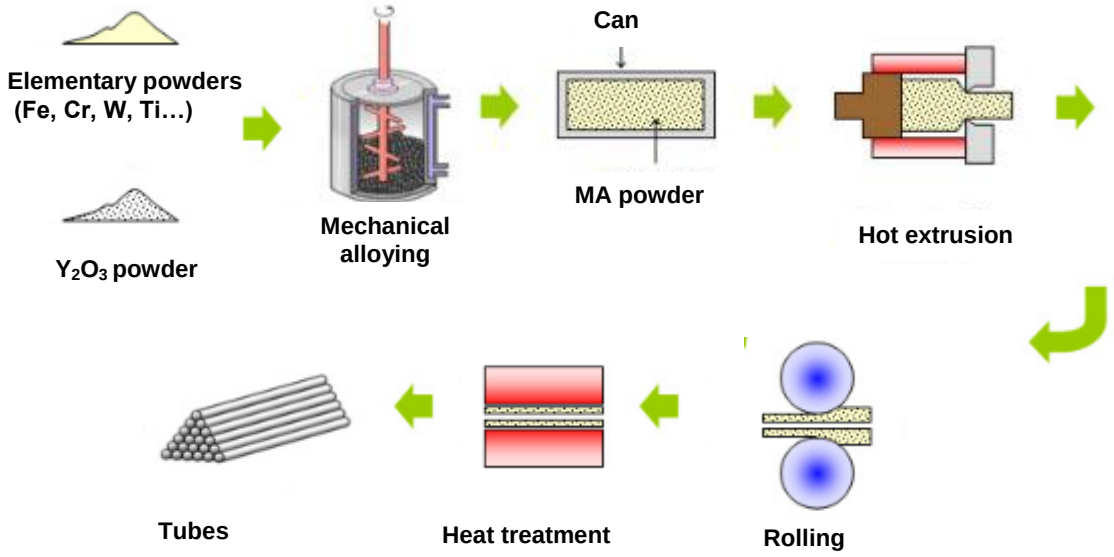

Figure 1.6. Basic scheme of ODS production after [42].

III.1. Mechanical Alloying process

During MA, the powder particles are repeatedly deformed (flattened), fractured and cold welded. When two balls collide, some amount of powder is trapped between them. This impact plastically deforms the powder resulting in work hardening and fracture. New surfaces are created, providing cold welding. In the early stages of MA, a large range of particles sizes develops. They have a characteristic layered structure consisting of different combinations of initial constituents. At certain stage, the fracture dominates over cold welding. As the deformation caused by balls is still acting, the structure of particles is steadily refine, but the size do not change (stays constant). Finally, the interspacing between particles reduces and the number of layers in the particles increases. A steady state particle size is reached when welding balances fracture. At this stage, the internal structure of the particles is steadily refined. Within a short time, the crystallite (or grain) size is refined to the nanometre scale.

In addition, high energy ball milling results in the formation of crystal defects such as dislocations, vacancies, stacking faults. The presence of this defect structure enhances the diffusivity of elements that increases alloying of the different elements.

The structures that develop during high energy ball-milling are highly dependent on the process variables and the nature of powder components. These include type and energy of mills, milling medium, temperature and atmosphere, the weight ratio of ball to the powder, etc. [37]. A brief description of the different parameters is given below.

→*Atmosphere.* To prevent the contamination of powder during alloying, it is usually performed in an inert atmosphere. Argon is the usual gas [39–42], however hydrogen is also used [47,48].

→*Temperature of milling.* This is an important parameter, since it enhances the diffusion process which is involved in formation of alloy phases. A slight increase of the temperature during milling may occur [37,39].

→*Time of mechanical alloying.* It influences the final structure. Usually, the chosen time of milling is sufficient to achieve a steady state between fracture and cold welding of the powder particles. If the powder is milled for longer times, formation of undesirable phases as well as increase of the contamination level of the powder may occur. The time of mechanical alloying is usually 48 hours [43,46,49] for conventional ODS.

→*Ball to powder mass ratio (BPR).* This parameter has significant influence on the rate of decrease of the crystallite size during MA process. Different values are reported in literature: *5:1* [50], 10:1 [51]. The 20:1 BPR [52] value is recommended to achieve the desired alloying in a reasonable time.

→*Milling equipment.* Different types of high energy milling equipment are used to produce mechanically alloyed powders. More detailed description of the different mills available for MA was done by Suryanarayana in [37]. An *attritor* (*Figure 1.7* (a)) is very often used in conventional production of ODS [25,43,45,53]. It consists of a vertical drum with impellers inside. Impellers are located at right angles with respect to each other. A motor rotates the impellers, which in turn cause to move milling balls in the drum. As a result, impacts between balls with powder, container wall, impellers, agitator shaft, lead to powder size reduction. In industrial attritor large quantities of powder (0.5-40 kg) can be milled at a time.

Another popular mill is *planetary ball mill* (*Figure 1.7* (b)) [48,54]. It has such a name due to the planet-like movement of its vials. It has another principle of work. In this system vials are located on rotating support disk. Special drive mechanism causes them to rotate around their own axes. The support disc rotates in opposite direction in relation to vials. The

centrifugal force caused by both: i) vials rotating around their own axes and ii) support disc rotating, acts on powder in the vials [37]. Centrifugal forces alternately act in like and opposite directions resulting in powder size reduction.

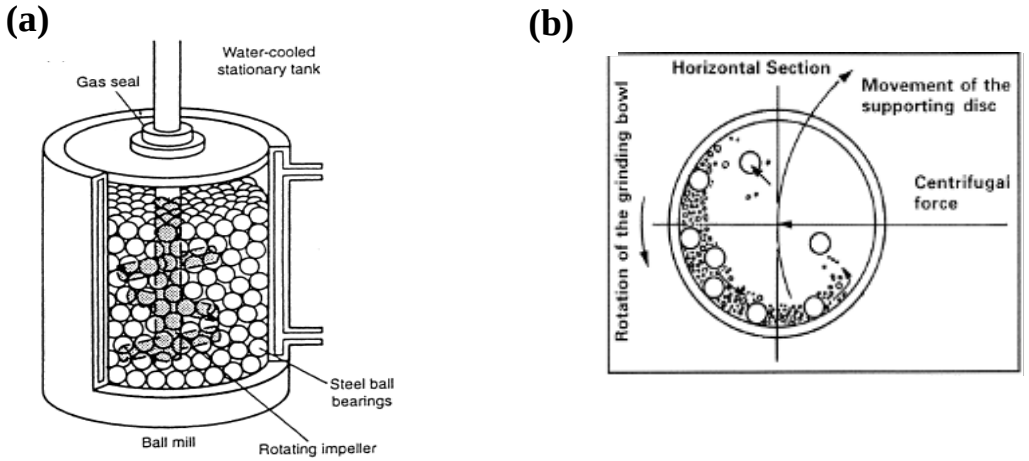

Figure 1.7. Attritor (a) and planetary (b) ball mill

III.2. Consolidation of powder and additional TMT

The consolidation procedure has a very important influence on the microstructure. As it was mentioned above, the consolidation of the powder usually involves either hot extrusion (HE) or hot isostatic pressing (HIP) [55].

Before hot extrusion, the ground powders are loaded into a soft steel can, outgassed and sealed. The can, afterwards, is pre-heated to the extrusion temperature 850-1150°C [43,46,51] and then forced through a reducing die. Extrusion creates high shear and compressive forces which are responsible for the densification of the material.

As in hot extrusion, HIP requires powders to be contained in a vacuum sealed soft steel can. Then, isostatic pressure is applied to powders at temperature 850-1150°C [56] resulting in nearly fully dense powders [57].

From practical point of view hot extrusion is more attractive due to lower cost and possibility to produce larger amounts of material. However, consolidation by hot extrusion produces anisotropic elongated (along hot extrusion direction) and textured grains [23,41]. That leads to anisotropy in mechanical properties [41]. To decrease the anisotropy postextruded *Thermo Mechanical Treatment (TMT)* are usually applied. They include sequences of cold and warm working following by softening-recrystallization heat treatments.

HIP is more interesting resulting in nearly isotropic characteristics of the material.

III.3. Microstructure and influence of elaboration parameters

ODS steels is designed with body-centered cubic (bcc) matrix (which is less sensitive to swelling issues in comparison to face-centered cubic austenitic type matrix), reinforced by dispersion of nano-oxides. Presently, different ODS steels are being developed for fission and fusion applications in Japan –F4, K1, K4, K3 [22,43,58], in Europe - Fe-18Cr-1W-0.3Ti [54,59], Eurofer [60] and in United States 12YWT and 14YWT [27,51,61]. These ODS contain different amounts of Cr (9-20 wt.%). Major part of them contains Ti and W as well as other alloying elements (Mo, Ni, Mn, V, C, Ta, Al).

The current understanding of the microstructures of current ODS steels, the effect of composition and key processing parameters are discussed below.

a) Ferritic or ferritic/martenticitic (F/M) matrix

Due to the different chromium content, ODS steels may have different microstructures:

→ODS steels that contain between 9 and 12 wt.% of Cr, (see Fe-Cr phase diagram in *Figure 1.8*) have *martensitic structure*. These steels are austenitic above 800°C. Martensitic transformation occurs during the quench from the austenitic temperature down to room temperature. After such treatment, the microstructure consists of laths with a very high density of dislocations and the material is extremely hard (and brittle) [62]. A tempering heat treatment must be given to provide a partial recovery of the dislocation network. *Martensitic 9-12 %Cr ODS* can be used for application in a temperature range below 800°C in order to avoid high temperature phase transformation into austenite [13].

→ODS steels containing more than 12 wt.% of Cr, present a fully ferritic matrix up to the melting temperature (see Fe-Cr phase diagram in *Figure 1.8*). This type of materials is envisaged for application in extended range of temperatures up to 1100°C in comparison to martensitic ODS steels [59].

In order to decrease the degree of anisotropy in the direction of extrusion (if hot extrusion is used) for *ferritic* MA-ODS steel, recrystallization process may be used [64]. However, this is not so easily achievable. Up to now, all worldwide efforts are directed to overcome “bamboo-like grain structure and a strong deformation texture” [23] observed after hot extrusion in ferritic ODS steels.

From that point of view, martensitic ODS steels are more attractive since controlling the grain structure is possible by inducing α → γ phase transformation. Such a way allows to significantly reduce the anisotropy of the microstructure after HE [23].

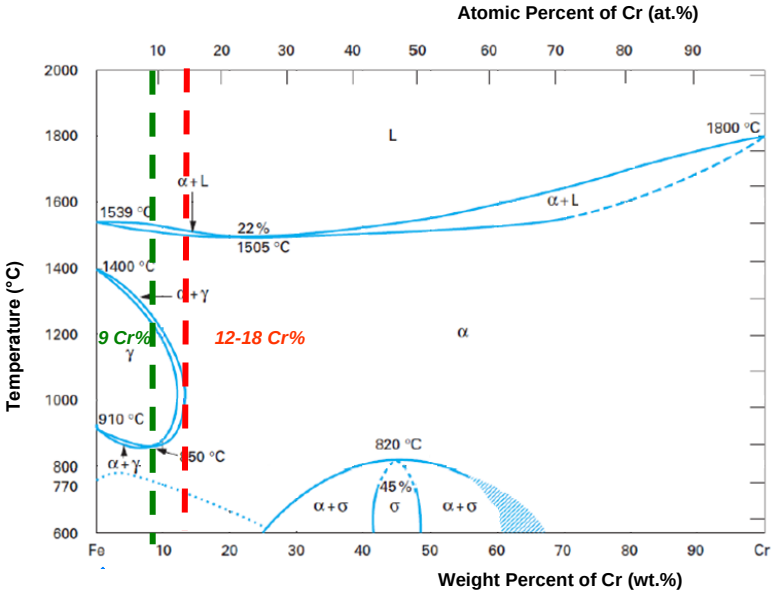

Figure 1.8. Fe-Cr phase diagram [63]. Due to Cr content ODS steel are divided into martensitic (9-12wt.% Cr) and ferritic (>12wt.%Cr).

In addition to that, Cr content in ODS materials is responsible for corrosion resistance. This is particularly important in the case of cladding tube of SFR. A thin and stable layer of chromium oxide forms on the surface, thus increasing the resistance of the material to corrosion issues. The minimum concentration of chromium necessary to obtain an effective passive layer is ~11 wt.% [65]. An increase of the chromium content beyond this level would result in a further increase of corrosion resistance. From that point of view, a ferritic material with high chromium content is preferred.

However, high Cr ferritic ODS steel with Cr concentrations in the range of 14-22 wt.% can be subjected to hardening and embrittlement after ageing in the region of ~400-550°C, temperatures potentially important for technological applications [66,67]. Indeed, an increase in yield and tensile strengths and reduction in ductility appear due to the formation of the α' phase (Cr-rich ferrite). This process is well known as the "475°C embrittlement".

Hence, the Cr content is one of the key parameters to be further optimized in order to get the best corrosion resistance in corrosive environment with favourable mechanical properties.

Concerning other alloying elements, the main objectives are to avoid formation of long life radioactive nuclides. So normally, low activation elements are preferably used. Such

elements as Nb and Mo are not desirable. They are replaced by W (and Ta in some cases). Alloying elements or impurities such as Ni, Cu, Co, Ag or Al also should be kept as low as possible. The content of C should be kept as low as possible in the case of ferritic ODS steels. A small amount of C (300 ppm[1]) may result in austenite formation at high temperatures [65]. The most commonly used alloying elements in ODS and their effects are summarised in *Table 1. 1*.

Table 1. 1. Effect of alloying additions (the most commonly used elements are shown)

Cr	Ferrite stabilizer, corrosion resistance
Ti	Grain refinement, participation in nanoclusters and solution strengthening
W	Solid solution strengthening [68], ferrite stabilizer [69].
Mo	Solid solution strengthening, ferrite stabilizer [69] less used due to high activation by neutrons
Ni, Mn	Austenite stabilizers [69]. Increase toughness [69,70].
C	Austenite stabilizer [65], enhance Ni effect [71].

b) Dispersion of oxides particles

In order to obtain a fine dispersion of nanometer scale oxides particles in a consolidated ODS material, 0.25-0.5 wt.% of Y_2O_3 [25,72–76,66,77] dispersoid is usually added to Fe-Cr matrix during MA. Yttria is known as one of the most stable oxides. As an example, Y_2O_3 has the highest heat of formation which is 1906.7 $kJ.mol^{-1}$, in comparison to other oxides such as Al_2O_3, SiO_2, ThO_2 TiO_2 with heats of formation respectively of 1678.2, 910.9, 1227.6, 944.1 $kjmol^{-1}$ at 25°C [78]. In addition, iron and yttrium are immiscible, so it also contributes to the stability of Y_2O_3 oxide in iron chromium alloys [71].

Ukai et al. [23] have studied the effects of yttria content (up to 0.56 wt.%) on strength properties and ductility of hot extruded Fe-13Cr-3W-0.5Ti ODS steel. The tensile strength along extrusion direction as well as creep rupture strength increases with increase in Y_2O_3 content, whereas total elongation decreases. So the amount of Y_2O_3 (0-0.56 wt.%) should be a

[1] *Ppm – one part per million - is a unit to describe small values of miscellaneous dimensionless quantities. It denotes one part in 10^6 or 1/1.000.000 × 100% = 0.0001%*

compromise between strength and ductility characteristics of ODS steel. The creep rupture strength saturated at about 0.4 wt.% of Y_2O_3.

The positive effect of Ti addition together with Y_2O_3 into Fe-Cr matrix during MA was shown by Ukai et al. [23]. Ti participates with yttrium oxide particles forming Y-Ti-O complex oxides resulting in finer size. As a consequence, an increase of the creep rupture strength is observed.

This result was confirmed by different works. Ramar et al. [79] compared the distribution of particles by TEM in ODS Eurofer 97 (with and without Ti). He concluded that the addition of Ti results in smaller size of nanoparticles (~20 nm and ~ 7 nm respectively without and with Ti addition). Miller et al. [61], using Atom Probe Tomography, compared the distribution of particles in 12YW and Ti-containing 12YWT ODS steel. He concluded that a higher number density (1.4×10^{24} m^{-3}) of smaller sized (r=2.0 nm) particles is observed in Ti-containing 12YWT in comparison to 12YW (3.9×10^{23} m^{-3}, r=2.4 nm).

Finally, Ratti et al. [80], using Small Angle Neutron Scattering, compared the behaviour of Fe-18Cr-1W ODS powders, with addition of 0.8wt.% Ti and without, upon thermal treatments (850, 1000, 1300°C/1h). He showed that the nano-phases formed in powders with some titanium are much more resistant to coarsening than the phases formed in the material without titanium.

After MA and subsequent thermo-mechanical treatment (TMT), microstructure of ODS steel have been characterized by different techniques mainly by Transmission Electron Microscopy (TEM) and Atom Probe Tomography (APT). It is found that the nature (chemistry and structure) of dispersed oxide particles in Fe-Cr matrix varies in a wide range. Summary of observed oxides in different ODS steels are shown in *Table 1. 2.*

In the case of Ti-containing ODS steels, TEM studies have shown variants of fine complex oxides, including pyrochlore $Y_2Ti_2O_7$, Y_2TiO_5, and $YTiO_3$. Y_2O_3 is found in ODS alloys that do not contain Ti. Nanoparticles also have been characterized by APT. As an example in MA 957 or Fe-14CrYWT they appear as clusters enriched in Y-Ti-O in comparison to the matrix, but containing significant amount of Fe and Cr (*Table 1. 2*). The measured compositions by APT indicated that they differ from complex oxides $Y_2Ti_2O_7$, Y_2TiO_5 and $YTiO_3$. Their (Ti+Y)/O ratios range between 1.1 and 1.3.

Table 1. 2. Summary of data concerning the nature of oxides in different ODS steels. Equipment that is used for characterization, size of analysed nano-oxides and their structure is reported. In case of APT, chemical composition is reported (at.%, balance is iron).

Grades	***Equipment***	***C, wt%***	***Size, nm***	***Structure***
Fe-18CrWTi [81]	EFTEM HRTEM	0.3 Ti	20-30	Y_2O_3, $Y_2Ti_2O_7$, PyrOrtho
Eurofer 97+Y_2O_3[79]	HRTEM	-	10-30	Y_2O_3
Fe-9CrWVTaTi +Y_2O_3 [82]	TEM (EELS)	0.5 Ti	~10	~ $Y_2Ti_2O_7$
Eurofer 97+Y_2O_3 [83]	HRTEM	-	~12	Y_2O_3
K1 [58]	TEM (EDS), XRD	0.28 Ti	~3.7	$Y_2Ti_2O_7$
MA 957 [84]	APT	0.9 Ti	1.4	Y-Ti-O rich nanoclusters: Fe-1.7±1.7 Cr, 32.9±5.3 Ti, 15.4±7.3 Y, 39.9±6.9 O, 0.02±0.2 Mo
14YWT [51]	APT	0.4 Ti	~2	Y-Ti-O-rich nanoclusters: Fe-1.2±1.1 Cr, 42.2±5.6 Ti, 7.5±4.3 Y, 43.5±5.3 O
14YWT [48]	HRTEM	0.3 Ti	~10	$YTiO_3$
12YWT [49]	APT	0.4 Ti	2-5	Y-Ti-O-rich nanoclusters: Fe-13.66±0.52Cr, 3.03±0.26 Ti, 0.86±0.14 Y, 2.89±0.25 O, 0.78±0.13 W
Fe-16Cr0.1Ti [85]	TEM (EDX)	0.1 Ti	~9	$Y_2Ti_2O_7$ Y_2TiO_5
Eurofer [53]	APT	-	~2-10	Y-O rich particles: Fe-11.77±0.97Cr, 4.63±0.27Y, 10.98±0.55O, 0.96±0.13Mn, 0.71±0.13 Ta, 2.91±0.09V, 0.5±0.03W, 0.92±0.08Si, 0.68±0.04N, 0.05±0.06 C, 0.02P, 0.03Co

This disagreement between APT and TEM is mainly due to the difference of the size of the analyzed particles. APT observations generally focused on very small oxides particles less than few nanometres in diameter, whereas TEM (EDS) mainly focused on larger oxide particles with about several tens of nanometres in diameter. Recent work of Sakasegawa by TEM on MA 957 tries to clarify this point [86]. He reveals that different types of oxides are present in MA 957 and their nature depends on their size (*Figure 1.9 (a, b)*):

i) Big particles (>35 nm) are TiO_2 particles, with a low Y content;

ii) Particles with sizes from 15 nm to 35 nm are stoichiometric $Y_2Ti_2O_7$ oxydes (mainly observed by TEM).

iii) Small particles (2 to 15 nm) are non-stoichiometric Y-,Ti-,O-enriched clusters (designated as $Y_xTi_yO_z$ and mainly characterized by APT).

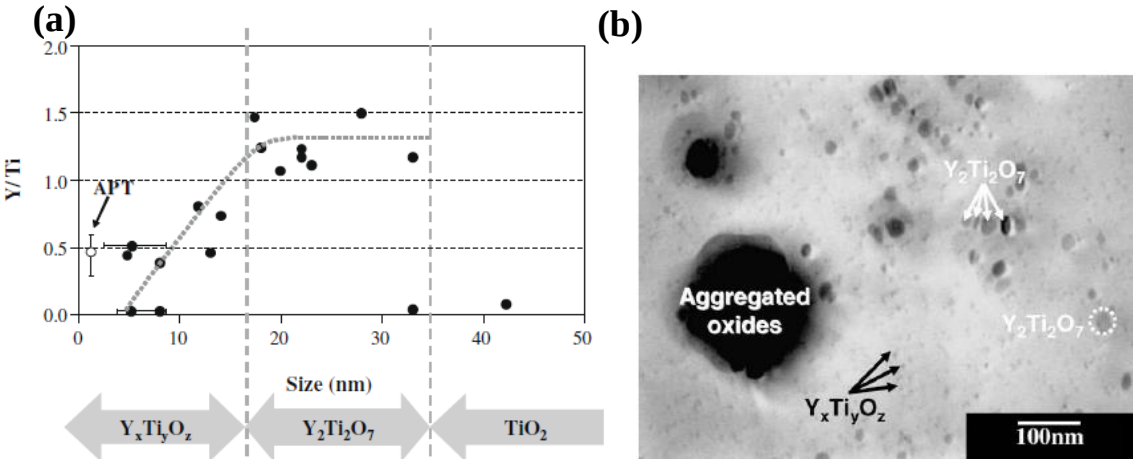

Figure 1.9. (a) Y over Ti concentration in oxide particles detected in MA 957 as a function of their size after TEM and XRD. Three regions are shown: 1) biggest particles are TiO_2, >35 nm, 2) $Y_2Ti_2O_7$ complex oxides with sizes between 15-30 nm and 3) the smallest $Ti_xY_yO_z$ nanoclusters, with sizes from 2 to 15 nm (b) TEM image of extraction replica of MA 957, showing different populations of oxides [86].

Further discussion will focus on these smallest non-stoichiometric $Y_xTi_yO_z$ rich clusters (as defined in [86]). It should be mentioned that different terminologies (particles, clusters, nanofeatures, precipitates etc.) are used by different researchers or groups. This is sometime confusing. In this work and in future discussion, to separate them from larger $Y_2Ti_2O_7$, Y_2TiO_5, $YTiO_3$ complex oxides, we define them as Ti-Y-O rich nanoparticles or clusters (Y-O-rich particles or clusters in case of ODS steel without Ti).

These nanoparticles appear with significantly higher number densities (10^{23}-10^{24} m^{-3} in accordance to APT) and smaller sizes (less than 5 nm). It has been experimentally confirmed that they play a major role in oxide dispersion strengthening of the steel [44]. Due to nanometric size they are mainly studied by APT. It is already mentioned that these nano-clusters contain a significant amount of Fe and Cr. The level of Fe estimated by APT and reported by different researches varies in wide range. As an example, the same 12YWT ODS have been characterized in as-processed condition by different groups. The reported level of Fe in these nanoclusters varies from ~78 at.% of Fe by Larson [49], ~56 at.% [61] and 4 at.% [25] by Miller.

Another example is the APT study of the Eurofer ODS steel [53] (which does not contain Ti). Significant variations of chemical composition of nanoparticles in the size range of 5 to 10 nm are reported by the author. The Fe concentration inside nanoparticles decreases with

increasing size and no Fe is found at the core of large particles (10 nm). In addition, the core of 10 nm particles consists of Y, O, Mn and Si with M:O ratio ~0.72+/-0.15. The core is likely to have Y_2O_3 stoichiometry as it is also confirmed by TEM .

Thus, at the moment it is unclear if these variations are coming from materials or APT technique (APT artefacts will be described in Chapter 2) and the methods used to evaluate concentrations? Additional work is needed to clarify the nature and composition of the nanoclusters using advanced high resolution tools.

Another interesting feature of these small nanoparticles is observed. According to Marquis [87], nano-oxides observed by APT in different ODS steels (MA 957, Fe-12Cr model alloy and Eurofer) may have a core shell structure (*Figure 1.10*).

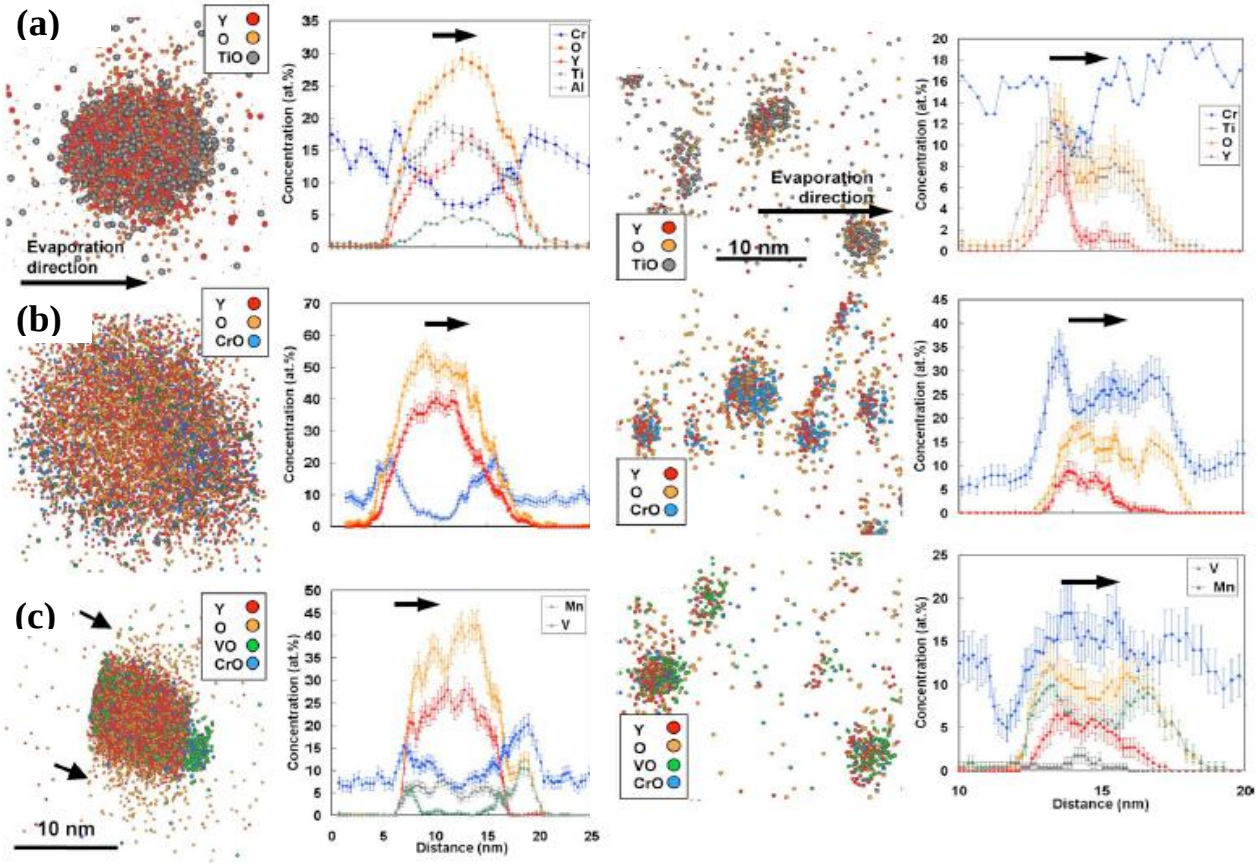

Figure 1.10. 3D reconstructions of oxide particles and concentration profiles through them. Particles with larger sizes (~8 nm, left side) and smaller (~4 nm, right side) are shown for comparison: (a) MA 957, after hot extrusion ~1150°C; (b) ODS Fe-12C alloy, HIPed at 750°C/2h and annealed at 750°C/4h; and c) Eurofer, annealing at 1050°C/30min, tempered at 750/2h [87].

The nanoparticles in MA 957 consist of an Y, Ti, Al and O rich core and a Cr rich shell. In ODS Fe-12Cr, the core is composed of Y and O while shell is also enriched in Cr and finally in Eurofer, an yittria-rich core, surrounded by Cr-rich and V-rich shell is found for all

oxide particles. The presence of a shell is observed independently of the size (4-8 nm) of these nanofeatures [87]. However, in the case of larger particles (8 nm and more), the shell structure is visible all around the core. To rationalize the existence of these core–shell structures, Marquis suggested that since the structure of oxide nanoparticles is similar in three studied ODS (Y rich core with solute rich shells), they may be governed by common thermodynamic properties (interfacial energy between the oxide nanoparticle and surrounding matrix). The particles may have high nucleation barrier and the presence of the shell would decrease the interfacial energy, favoring their nucleation.

Presence of a Cr rich shell in similar Fe-12Cr ODS model alloy have been confirmed by TEM (STEM, EELS, EFTEM) investigations [88,89]. The reported thickness of the Cr-rich shell is ~1-3 nm. In addition, this shell is still present after prolonged annealing times (during 24 and 96 h at 750°C) (*Figure 1.11*). EFTEM analyses performed on ODS annealed during 96 h, do not revealed any significant difference in thickness of the Cr-rich shell in comparison to particles after annealed during 4 hours.

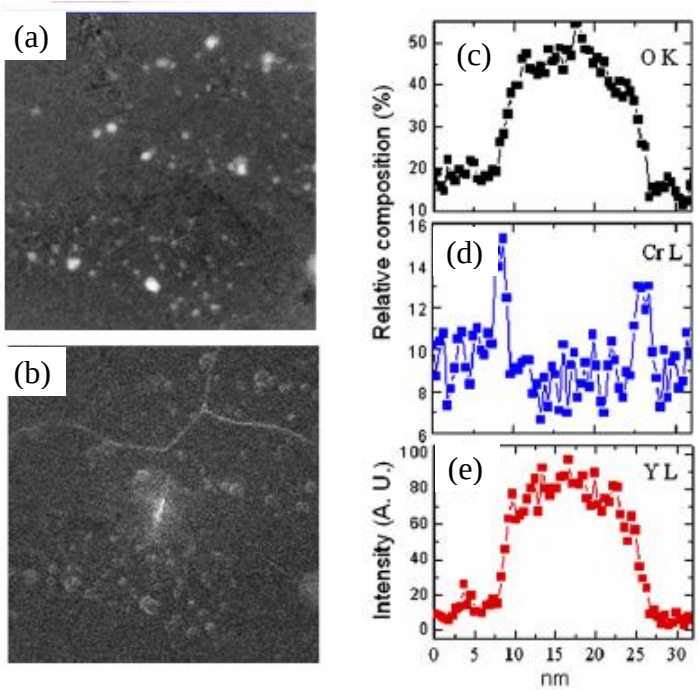

Figure 1.11. Core/shell structure of nanoscale oxide particles in an ODS Fe-12 wt.%Cr alloy as revealed by EFTEM. Elemental maps (a) Y $N_{2,3}$ and (b) Cr $L_{2,3}$ for ODS model alloy after annealing at 750°C during 96 hours. (c, d) EELS and (e) EDS O K, Cr L and Y L elemental profiles across nanoparticles in the ODS alloy after annealing at 750°C during 24 hours [89].

V-and Cr-enriched shells are also observed around all investigated particles by TEM (EDS/EELS) in Eurofer ODS [90].

Taking into account difficulties of quantification of chemical composition by TEM, these results are in good agreement with results reported by E. Marquis [87].

However, the same MA 957 ODS has been studied by Miller et al. [91] in the as-received state and after isothermal annealing treatments up to 24 h at 1300°C (by APT). This author does not report any information about the presence of a core shell structure!

Hsiung et al [43,92,93] studied by HRTEM the interfacial structure of nanoparticles in Fe-16Cr-4Al-2W-0.3Ti (designated as K3) mechanically alloyed with 0.3 wt.% of Y_2O_3. After hot extrusion at 1100°C and additional annealing at 1050°C/1h, the sizes of the studied particles vary from 1.7 to 30 nm. A structure with an $Y_4Al_2O_9$ core associated with a shell has been observed in both large and small nanoparticles, *Figure 1.12*. However, in contrast to the previous reported core-shells structures (by Marquis [87], Castro [89], Klimenkov [90]), the author shows that the shell is amorphous. The author suggests that amorphous shell results in a partial crystallization of amorphous nanoparticles during consolidation, whereas amorphization of these oxides particles appear during MA process. The core/shell structure disappears after prolonged annealing treatment (900°C/168 h) for particle with diameter larger than 20 nm, indicating that these core/shell structures are far from chemical equilibrium.

The same structure of crystallize core and amorphous shell is found in hot extruded (1107°C) Fe-20Cr-4.5Al-0.34Ti+0.5 wt.% of Y_2O_3 (designated as MA 956) ODS steel. In this case significantly thicker shell is observed in comparison to K3.

By comparing the HRTEM observations for K3 and MA 956 materials with results of Marquis [87], the author suggest that the content of these solute-enriched shells may differ and depend on the initial composition of the ODS steel. He suggests that $Y_4Al_2O_9$ and $YAlO_3$ core forms in the case of Al-containing K3 and MA materials, Y_2TiO_5 and $Y_2Ti_2O_7$ may form in the case of Ti-containing ODS steel and Y_2O_3 may form in the case of Eurofer that do not contain either Al nor Ti. It is supposed that shell forms as a result of solutes depletion from the core during crystallization of the particles upon annealing. The formation mechanism proposed by the author to rationalize the existence of these core-shell structures are discussed in details in next section.

As a conclusion, core shell/structure of nanoparticles are observed by different research groups in different ODS materials and by different techniques (APT, HRTEM). However, there is no clear understanding about the origin and the nature of these core/shell structures. At the moment the influence of particles sizes, times of ageing as well as different alloying elements in ODS steel on the stability of these dual core/shell structures is not clear. Further experimental work is needed.

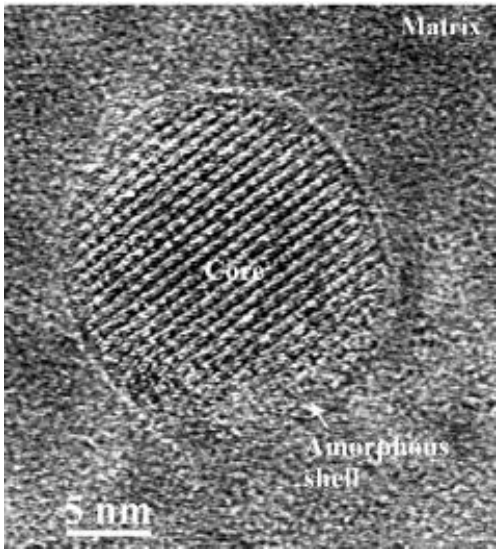

Figure 1.12. HRTEM images of a large nanoparticle (> 20 nm) observed in K3: incoherent interface associated with a core/shell structure [43].

c) Mechanism of formation of nanoparticles

Different analytical devices such as X-ray diffraction (XRD), Small Angle Neutron Scattering (SANS), Transmission Electron Microscopy (TEM) and Atom Probe Tomography (APT) are used to study processes that occur during mechanical alloying and during subsequent TMT in ODS materials. Points of view of different research groups who studied the formation of nanoclusters are reported in the following paragraphs.

Some works show that the formation mechanism of nanoclusters in ODS steel is a two stages process:

i) Fragmentation, decomposition/dissolution of initial Y_2O_3 during mechanical alloying step in the metallic matrix; The matrix is an homogeneous solid solution of Fe, Cr, Y and O;

ii) Precipitation of the nanoclusters occurs during annealing and following thermo-mechanical treatments.

An example is the work of Okuda et al. [94] who studied the change of behaviour of a Fe-13Cr alloy during mechanical alloying (with 3wt.% of Y_2O_3) and subsequent annealing treatments. Another example can be the study of Alinger et al. [56] on Fe-14Cr ODS steels. He confirmed that Y_2O_3 dissolution in Fe-14Cr alloy matrix is the dominating process during MA, resulting in a highly supersaturated solid solutions.

Studies by Larson [49], Miller [51] and Yamashita [95] are also in this direction. However, it should be mentioned that in their works, APT investigations of ODS material are performed only in the final state, passing over investigation of material immediately after MA step. Their conclusions are mainly based on size differences of nano clusters in final state and the initial size of Y_2O_3 powder (~2 nm for nanoclusters in as-received state and 17-31 nm for initial Y_2O_3 powder [51]) introduced during MA process. Another argument is that, the chemical composition of nanoclusters estimated by APT, is more consistent with TiO than Y_2O_3 stoichiometry.

However, some other groups of researchers show that the formation mechanism of these nano-oxides is not limited to dissolution/precipitation mechanisms as reported above. Among them, recent work by Brocq [96,97] on Fe-14Cr-2W-0.25Ti ODS showed that the role of mechanical alloying appears to be more complex. It could be summarised as follow:

i) Dissolution of primary oxide and nucleation of first nanoclusters can occur simultaneously during ball-milling;

ii) Nucleation and growth of nanoclusters continue after subsequent annealing.

The nano-oxides formed this way can be controlled through variation of ball-milling parameters (intensity, temperature and atmosphere) and annealing parameters (duration and temperature). However it should be mentioned that specific conditions of ball milling (reactive ball milling: YFe_3 and Fe_2O_3 are used as reactants) are used for this study. Nevertheless, the possibility that nanoclusters in conventional ODS can originate from the same mechanism are not excluded.

An alternative formation mechanism of nano-oxides is suggested by Hsiung et al [43,92,93]. HRTEM investigations of Fe-16Cr-4Al-2W-0.3Ti ODS (designated as K3) in its final state, revealed some $Y_2Al_2O_9$ crystallite (in the core) surrounded by an amorphous shell. Based on this observation, the author suggests that the formation mechanism of nanoparticles may include three stages (*Figure 1.13.)*:

(a) During MA, fragmentation of initial Y_2O_3 particles occurs resulting in finely-dispersed (nano or sub-nano) fragments;

(b) During continued MA process, agglomeration and amorphization of fragments mixed with matrix material occurs. This initiate the formation of some clusters and agglomerates (designated as [MYO], M: alloying elements) in the Fe-Cr matrix;

(c) Subsequent annealing leads to crystallization of the amorphous oxide agglomerates larger than 2 nm with the formation of an oxide nanoparticles (with a complex-oxide core and solute-enriched (M) shell). Agglomerates or clusters that are smaller than 2 nm remain amorphous.

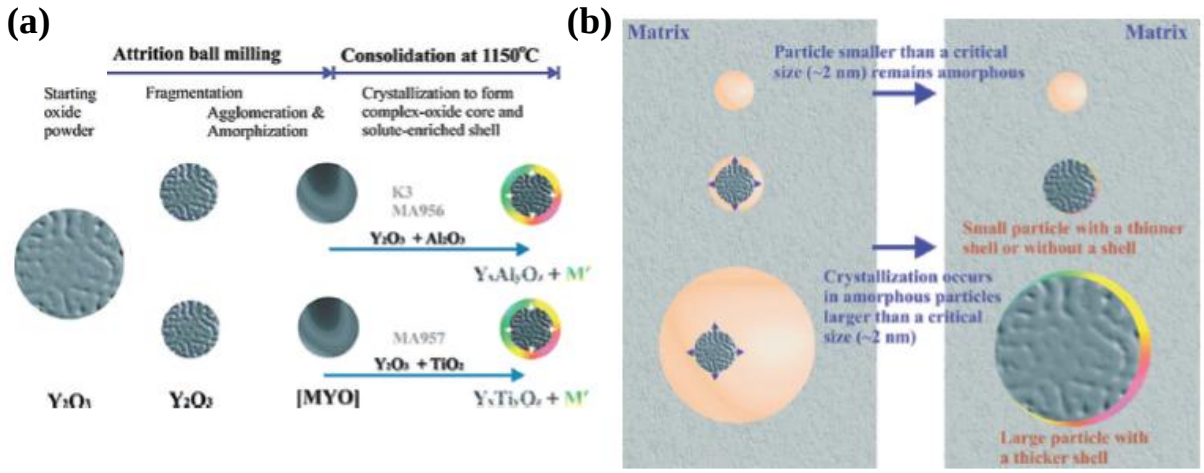

Figure 1.13. Schematic illustrations of (a) the three-stage mechanism for the formation of oxide nanoparticles containing a core/shell structure during MA and consolidation for Al as well as for Ti-containing ODS steel. (b) Size effect on the formation of core/shell structures in oxide nanoparticles. A solute-enriched shell can form in particles larger than 2 nm when solute depletion rate from the core is greater than solute diffusion rate from the oxide/matrix interface during the crystallization stage; a particle smaller than 2 nm remains amorphous [92].

d) Influence of the elaboration parameters on the microstructure of ODS

Elaboration parameters (time of milling, atmosphere, type of mill, conditions of consolidation etc.) may influence the final microstructure of ODS steel. It should be mentioned that elaboration parameters for commercial alloys and for a large part in scientific articles are only limited to the strict minimum, i.e. it is impossible to compare! Thus a detailed summary of the influence of parameters at each stage of elaboration process is difficult.

The effects of mechanical alloying (MA) conditions on oxygen contamination have been investigated by Ohtsuka et al [98]. It was shown that excess oxygen (defined as the total content of oxygen in the steel minus the oxygen coming from Y_2O_3) is a very important parameter along with Y_2O_3 and Ti additions that may result in coarser nanoparticles and as a result reduce mechanical properties of the material. Oxygen content was drastically reduced by the application of a high purity Ar atmosphere during MA process.

Also, he studied the influence of different amounts of excess O on the microstructure of a 9Cr-ODS (Ti-containing) steel [45]. He showed that when the atomic ratio between excess oxygen and titanium in the steel is close to 1, finer and denser distribution of oxide particles (r=2 nm) can be achieved resulting in higher temperature strength.

Miller et al. [51] studied by APT the influence of different milling times 40 and 80h on the microstructure of ball milled 14YWT ODS. The milling is performed in attritor (Zoz Simolayer CM) under argon atmosphere. No residual parts of Y_2O_3 powder are observed in the as-milled state indicating that, it has fully dissolved in Fe-Cr matrix during milling process. No significant difference is observed between 40 and 80 h of milling.

The study of the influence of the consolidation temperature is reported in several works. A systematic study by SANS has been performed by Alinger et al. [56]. The effects of consolidation temperature on nanoclusters size (r), number density (N), volume fraction (f) and hardness (DPH) in MA 14YWT is shown on *Figure 1.14* (a).

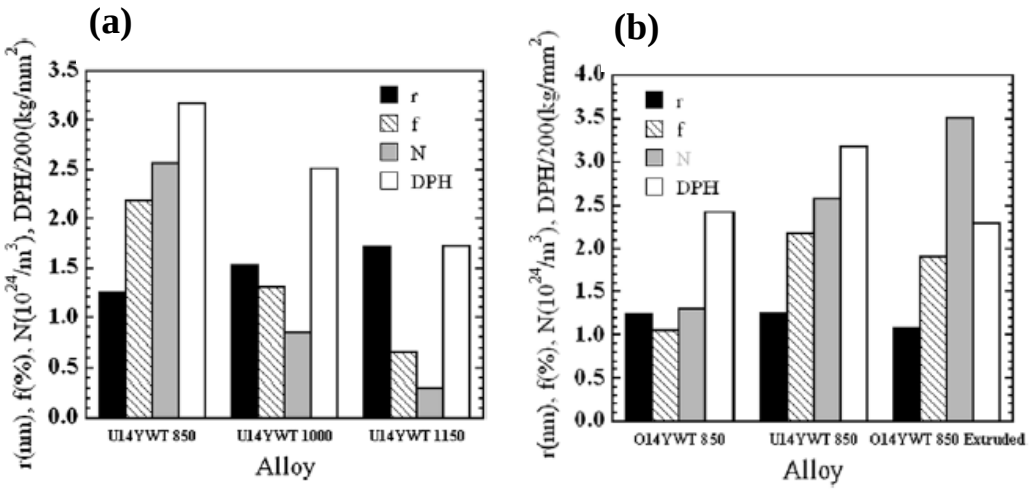

Figure 1.14. SANS data for 14WYT (on the figures designated as U14YWT and O14YWT indicating that Spex and attritor ball mills are respectively used) showing effect of: (a) HIP consolidation temperature (850, 1000 and 1150°C) on radius (r), volume fraction (f), number density (N) and Vickers hardness (DPH) of nanoparticles and (b) consolidation by HIP and HE at 850°C.

Consolidation is performed by HIP at different temperatures: 850, 1000 and 1150°C. As it can be seen from the figure, the nanoclusters number density as well as volume fraction decreases, whereas radius increases, with increasing consolidation temperature. The hardness decreases (from 635 to 344 kg mm^{-3}) with increasing the HIP temperature from 850 to 1150°C. In addition, the effects of consolidation by HIP and hot extrusion have been compared. The nanoclusters number density (3.5×10^{24} m^{-3}) is higher in hot extruded alloy in comparison to HIP one (1.2×10^{24} m^{-3}), whereas their size is approximately the same.

Another study has been conducted by Hoelzer et al [44]. The Fe-14Cr-3W-0.4Ti wt.% ODS alloy was hot extruded at different temperatures (850 and 1175°C). A high number density of 2-nm size Ti-, Y-, and O-rich nanoclusters was observed after HE at 850°C, whereas a lower number density of predominantly $Y_2Ti_2O_7$ oxide particles are observed after extrusion at 1175°C. These results are, in general, consistent with Alinger´s conclusions, showing that higher consolidation temperature results in larger radius as well as lower number density of nanoparticles.

Dou et al [99] by TEM, also studied this point for hot extruded Fe-15.5Cr-2W-0.1Ti-4Al ODS steel. His results are also consistent with Alinger's [56]. He shows that reduction of hot extrusion temperature from 1150 to 1050°C lead to significant decrease of grain size, as well as nanoparticles number density increases (from 1.72×10^{23} to 9.2×10^{23} m^{-3}) and their size decreases to about half (from 6.7 to 3.2 nm).

All listed studies show a common trend. Lower temperature of consolidation results in higher number density of nanoparticles as well as smaller size. The other parameters vary from study to study and general trends are difficult to give.

Influence of Hot Isostatic Pressing (HIP) and Hot Extrusion (HE) on final microstructure and properties of ferritic Fe–14Cr, 2W, 0.3 Ti, $0.3Y_2O_3$ ODS steel have been studied by Unifantowicz et al [48]. In both cases, mechanical alloying is performed in planetary ball mill in hydrogen atmosphere. After the powder is degassed at 400°C/2h, it is heated to consolidation temperature 1100°C/1h and finally extruded in a 500 t press. In the case of HIP material, after canning and degassing, consolidation is performed in Ar atmosphere by applying a pressure of 200MPa for 4 h at 1150°C. Afterwards both consolidated materials are subjected to the same heat treatment: 850°C/1h. The TEM investigations revealed, fairly equiaxed grains (having a mean diameter in the range of 40–80nm) and a high number density of nano-sized oxide particles in both materials. The nanoparticles appear with higher number

density (17.4×10^{23} m^{-3}) and higher radius (r=4 nm) in the case of the HE material in comparison to the HIP one (9.3×10^{23} m^{-3}, r=2 nm). This result is also consistent with Alinger's [56] observation who also studied the influence of HIP and HE consolidation on the microstructure of 14YWT ODS. As for mechanical properties are concerned, the ODS steel produced by HE exhibits much higher tensile strength and hardness at low to moderate temperatures, as compared to the steel fabricated by Hot Isostatic Pressing. It is linked with an important work hardening effects and also a higher number density of nano-sized oxides particles in the HE state in comparison to the HIP material (*Figure 1.15*).

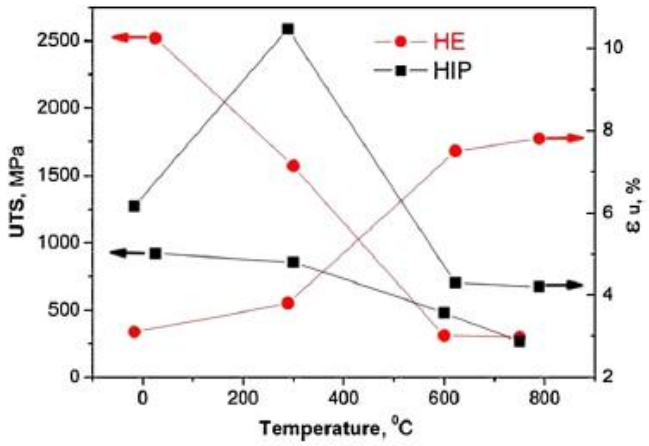

Figure 1.15. Ultimate tensile strength (UTS) and uniform elongation (ε_u) versus test temperature for ferritic Fe–14Cr-2W-0.3Ti-0.3Y_2O_3 ODS steels consolidated either by hot extrusion (HE) or hot isostatic pressing (HIP).

However, at higher temperatures, both steels have similar tensile strength. It is important to note, that micropores are found in both consolidated materials. They are twice larger in the case of the HIP steel (0.42 μm), as compared to the HE steel (0.26 μm).

III.4. Partial conclusion

Advanced nuclear reactors (Gen 4 and fusion) will operate at higher temperatures and higher irradiation doses in comparison to nowadays reactors. Operation conditions of these advanced nuclear reactors are challenging for structural materials. Among the materials that are potentially capable to operate at high temperatures while being resistant to high neutron fluxes are Oxide Dispersion Strengthened steels. These materials consist of ferritic/martensitic (F/M) matrix that is resistant to radiation swelling and fine dispersion of nanometre scale oxides. These nanometre scale particles are stable at elevated temperatures. They are responsible for high temperature creep strength properties of ODS steel (serve as an

obstacle for dislocation movement). In addition they are improving resistance to irradiation by providing a high number density of trapping sites.

Today many different ODS grades are elaborated. They are produced by mechanical alloying, using Y_2O_3 powder milled with Fe-Cr matrix, followed by consolidation and different thermo-mechanical treatments. It is widely accepted that precipitation of Y-Ti-O rich nanophases occurs during Hot Extrusion (HE) or Hot Isostatic Pressing (HIP) processes while mechanical milling mainly causes the dissolution of the initial Y_2O_3 powder. However, limited amount of works were performed in order to characterise ODS powders in the as-milled state. It can be expected that dissolution and nucleation mechanism may vary as a function of alloy chemistry and processing parameters.

ODS steels can contain various types of oxides: i) large TiO_2 oxides, ii) stoichiometric $Y_2Ti_2O_7$ oxides, iii) non-stoichiometric Ti-Y-O enriched nano-clusters,

Reported results are very promising, however many questions still need to be answered. The nature of smallest nano-oxides is not fully understood. Determination of the composition and structure of these particles would provide insight into possible mechanisms of formation and help to develop methods to further optimise processing of desired alloy structures. The nanoscale character of the features requires a combination of complementary techniques such as Small Angle and Neutron Scattering (SANS), Transmission Electron Microscopy (TEM) and Atom Probe Tomography (APT).

An attempt to answer some of these questions is performed in this current Ph.D work.

From another point of view, alternative to ODS materials may give different advantages. One of such solution may be the Nitride Dispersion Strengthened steel. These materials are described in following section.

IV. Nitride Dispersion Strengthened (NDS) alloys

Taking into account the positive experience of ODS steels, development of alternative solutions could be envisaged. In particular, the oxides could be replaced by another stable phase. Nitride Dispersion Strengthened steels (NDS) can be obtained using a dispersion of nanometric nitrides such as TiN. In this case, a high stability is expected at elevated temperatures [100,101].

Dispersion strengthening of ferritic/martenstic (F/M) matrix by nitrides can be obtained by different techniques, depending the way nitrogen is introduced:

(i) nitriding of a steel containing strong nitride forming elements (Cr, Ti, V ect.);

(ii) mechanical alloying with further thermo-mechanical treatments.

These two approaches are detailed in the next section.

The procedure for the elaboration of materials can be significantly simplified (avoiding the expensive MA step), especially if the nitriding process is performed on the final tube. In that case, the amount of elaboration steps would be reduced resulting in a minimization of the fabrication cost. If a homogeneous NDS material could be produced, it may be significantly easier (in comparison to ODS [102,103]) to control the recrystallization process during TMT.

Therefore, NDS materials seem to be very promising. All advantages and weaknesses should be carefully evaluated in order to define if these materials can be worthy alternative to ODS.

IV.1. NDS elaboration by nitriding

a) Principle

Nitriding involves the diffusion of nitrogen into the surface layers of low carbon steel at elevated temperature. This surface treatment is usually applied to improve the fatigue resistance [104], wear resistance [105,106] and corrosion properties [106]. As it is shown on *Figure 1.16*, surface nitriding usually results in the formation of two layers: a *compound* and a *diffusion* layers. The compound layer, located at the surface, is made of iron nitrides [107]. The improvement of the tribological and anticorrosion properties is mainly attributed to this layer.

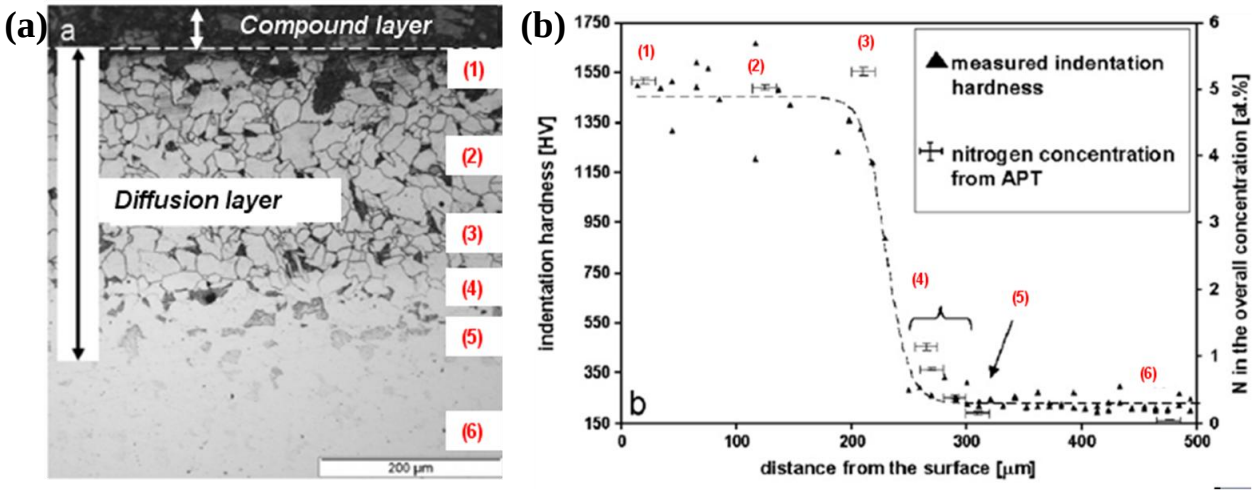

Figure 1.16. (a) Optical micrograph of the nitrided zone observed in Fe–5 wt%Cr after [108]. (b) Hardness profile and nitrogen concentration at different positions from the surface. The positions of the interest are marked from (1) to (6) in the micrograph as in the profile.

Enhancement of the fatigue properties is ascribed to the diffusion zone. In the diffusion zone, nitrogen is dissolved interstitially. If the iron matrix contains some alloying elements, their high affinity with nitrogen (Cr, Ti, Al, V) may promote nitrides formation.

Various nitriding processes exists, depending on the medium used to bring nitrogen. Today the nitriding processes are:

Gas nitriding. A nitrogen rich gas, usually ammonia (NH_3) is used as a donor. When ammonia comes into contact with the heated work piece (>480°C), it dissociates into nitrogen and hydrogen. The nitriding potential, which determines the rate of introduction of nitrogen into the surface, is determined by the NH_3 concentration at the work surface and its rate of dissociation.

Salt bath nitriding. A nitrogen containing salt, such as cyanide (CNO), is used as a nitrogen donor medium. The component(s) is placed in a molten salt bath and is heated to get a hard nitride layer on the surface.

Plasma nitriding. The work piece is placed in a vacuum vessel, where an atmosphere containing nitrogen is introduced. A voltage is applied between the work piece (cathode) and the vessel wall (anode). It results in ionization of gas atoms which are accelerated toward the work piece. This ion bombardment cleans the surface and provides active nitrogen. Nitrogen can diffuse into the work piece under the effect of temperature which is controlled by the heating system. A key difference between gas and ion nitriding is the mechanism used to

generate nitrogen at the surface of the metal. A schematic representation of an ion nitriding furnace is shown in *Figure 1.17.*

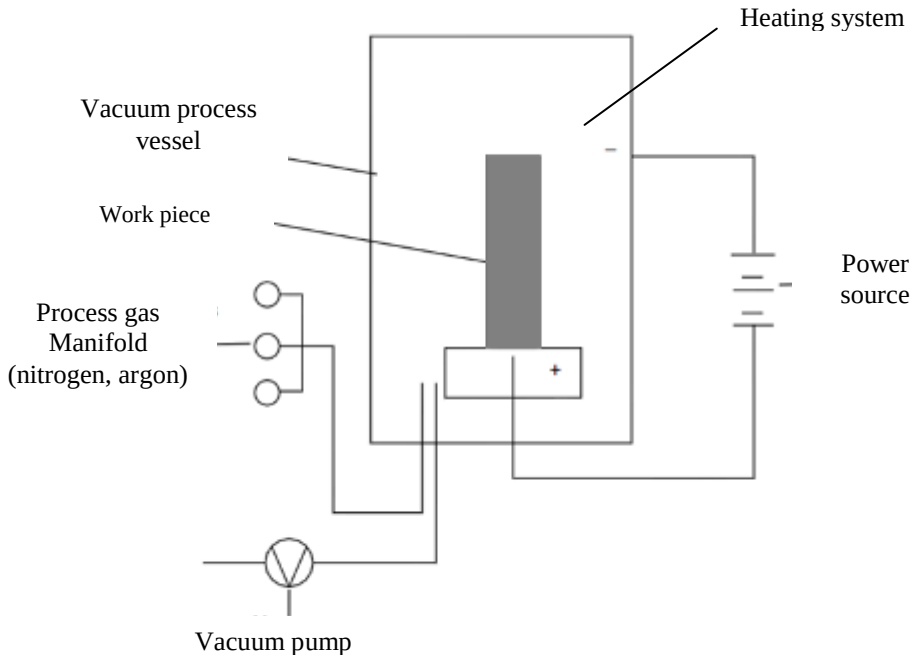

Figure 1.17. Simple schematic representation of a plasma (ion) nitriding furnace system after [109].

Among the several plasma based surface modification processes, plasma nitriding is considered as the most industrially adopted method.

b) NDS production since 80`s

Nitride-Dispersion-Strengthened Steels has been already envisaged for nuclear application in 1980s. Their development was performed mainly by two companies. The first is United *Kingdom Atomic Energy Authority (AEA, UK).* Its activity was focused on developing reactor technologies for the nuclear power stations. The second one is *the Garrett Corporation, (USA).* Its activities are mainly concentrated on Aircraft Engineering and Aerospace Technology. Results of their investigations are mainly available in patents. Another scientific group – Swedish Institute of metals research - also performed several attempts in order to reinforced austenitic matrix with a fine dispersion of TiN particles.

A summary of different ways used to produce Nitride Dispersion Strengthened steels since 1980s is represented in *Table 1. 3.* Some of these studies were not primarily focused on nitride investigation (morphology, microstructure, size etc.) but aimed improvement of mechanical properties (Patents). The nitriding was used for powder, strip, sheet as well as for

tubes. The austenitic, ferritic and F/M materials were nitrided. Only gas nitriding was applied. It was always realised in two steps:

i) Nitriding in the temperature range (815 to 1200°C);

ii) Denitriding treatment at high temperature (T>1000°C) to remove excess of CrN and to convert Ti into TiN.

Several important conclusions can be drawn:

- Uniform distribution of TiN particles [100,110,111] have been obtained with relatively small sizes (*Table 1. 3.),* producing a dispersion hardened steel [110,111].

- Resulting microstructure is strongly dependent on nitriding parameters. High nitriding temperatures (815 to 1200°C) result in an increased diffusion of alloying elements making difficult the control of the nitriding process. From one hand, if the nitriding time is extended greatly beyond the time needed to react all of the Ti excess CrN forms and further denitriding treatment can lead to the pore formation [100,112]. From another hand, if time was not sufficient, it resulted in non uniform microstructures through the cross-section (resulting in unnitrided core).

- The range of maximum service temperatures of nitrided parts have been limited by nitrided temperature.

Many ways of production, equipment and technology have been changed since then. Taking into account new possibilities, production way can be re-evaluated.

As an example, plasma nitriding can be an alternative to gas nitriding as proposed by AEA in the past. It offers many advantages such as close control, not only of temperature but also of gas composition, pressure heating rate and process time. Shorter process time is achievable, due to higher nitrogen concentration available on the surface. Due to such technique, nitrogen incorporation can be achieved at considerably lower temperature (~400°C). Further homogenization would occur during thermal treatment (before consolidation in case of powders). So, precipitation of nitrides (TiN) can be expected at lower temperature (600-700°C) in comparison to what was already studied (800-1200°C).

Such nitriding treatment has been realized in the framework of the ANR “aXtrem” program in collaboration with Nitruvid-Bodycote. Plasma nitriding of Fe-Cr-Ti powder have performed at T~400°C. The first results devoted to characterisation of this material are presented in the Ph.D.

Table 1. 3. Summary of nitriding ways for NDS production (research ~ 1980s). Information is available from patents and conventional scientific literature. OM –Optical microscopy, X-Ray-X-ray diffraction, TEM- Transmission electron microscopy.

Reference	Composition/state	Process	Characterisation techniques	Observation
Kindlimann and Ansell [100]	316 austenitic stainless steel (Fe-18Cr-12Ni-2.0Ti wt.%) (Strip)	a) gas nitriding at 870-1210°C (NH_3) b) denitriding treatment	TEM, X-ray	Cubic TiN particles (non coherent with matrix), have Bain orientation relationship [113].
Swedish institute for metals research [110]	316L austenitic stainless steel (Fe-17.4Cr-12.8 Ni+0.7Ti+1.2Mn wt.%) (Powder)	a) gas nitriding at 900°C (N_2+5%H); b) hot extrusion of cans filled with powder at 1150°C	OM, TEM ?	Two homogeneous distributions of TiN nitrides are observed [114]. Mean radii ~10 and 50 nm. The number densities are respectively 10^{21} and 10^{20} m^{-3}
Swedish institute for metals research [111].	316L austenitic steel (Fe-18.13.9Ni+0.6wt.%Ti) (Powder)	a) gas nitriding at 900-1100°C (pure N_2); b) hot extrusion at 1200°C.	SEM, TEM (EDX)	Nitriding at higher temperature (1000°C) gives two distributions of Ti-containing particles (R~150 and R~10 nm), nitriding at lower temperature (900°C) results in more homogeneous size distribution of particles (R~25 and R~1 nm).
The Garett corporation. Patent4.464.207and 0.008.228 [112,115]	Ferritic steel (type 409 or 439) (Fe-11/19Cr-0.5Ti wt.%) (light gauge-strip or sheet)	a) gas nitriding at 815-980°C (NH_3 or N_2); b) denitriding treatment in H_2 at 1000°C	?	Plate-like TiN shape
AEA [116] Patent 4.846.899	F/M steel (Fe-9/12Cr+2.5Ti wt.%) (strip, sheet, tube or powder)	a) gas nitriding at 1050-1200°C (in fully austenitic state); precipitation of nitride within matrix and b) converting to the ferrtic, or ferritc/martensitic form during cooling	?	Resulting dispersoid is too coarse to make any strengthening effect

c) Mechanism of formation of nitrides

The formation of nitrides in iron during nitriding is an issue with a long history. Precipitates shape, size, coherency with matrix, orientational relationship (OR) as well as plastic and elastic deformations of the matrix needed to nucleate and coarsen the precipitates have been studied by Jack [101,113,117] and Mittemeijer [118,119].

Due to the large affinity of some alloying elements (Cr, Ti, V, Mo etc.) with nitrogen, these elements easily form thin and stable platelets on the {100} faces of the bcc lattice, thus influencing the mechanical properties. In most cases after nitriding of Fe-Cr and Fe-Ti systems, TiN and CrN plate-like precipitates form. They develop with the nitride platelet faces parallel to the $\{0\ 0\ 1\}_{\alpha\text{-Fe}}$ ferritic planes [100,108,120,121]. The platelets are oriented with respect to the ferrite matrix according to the Bain (also known as Baker-Nutting) orientation relationship (OR) given by:

$$\{0\ 0\ 1\}_{\alpha\text{-Fe}} \,//\, \{0\ 0\ 1\}_{\text{nitride}};\ [1\ 0\ 0]_{\alpha\text{-Fe}} \,//\, [1\ 1\ 0]_{\text{nitride}}$$

Schematic representation of the Bain OR is shown on *Figure 1.18.* Following the Bain OR, the expansion in the (011) α-Fe plane is typically less than 5% and is higher than 45% in the direction perpendicular to this plane. That defines the plate-like structure of precipitates.

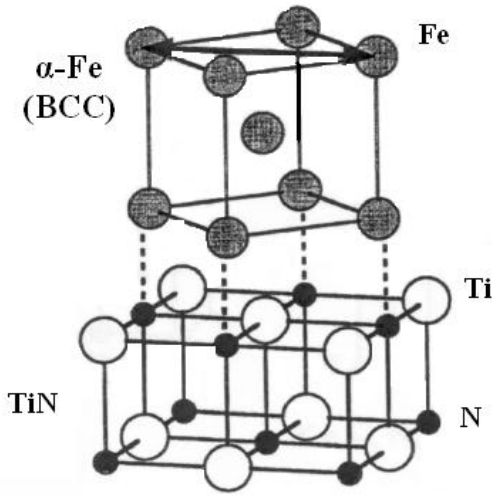

Figure 1.18. Schematic representation of the Bain (or Baker-Nutting) orientation relationship between a titanium nitride particle and the ferrite matrix after [122].

However, up to now, the initial stage of precipitate formation is under debate. It was proposed by Jack [117], that there is a sequence of steps upon nitriding of Fe-Ti, Fe-Cr, Fe-Mo, Fe-W systems before equilibrium precipitates is formed. They are the following:

i. first, metastable intermediate Fe-M-N-enriched clusters (or mixed GP zones as defined in [123]), where M=Cr, Ti, Mo or V are formed.

ii. after nitriding these metastable clusters transforms into stoichiometric stable MN phase.

Not all stages are observed in all alloys. As an example, in Fe-Cr alloys, equilibrium f.c.c. CrN precipitates have been identified even in the initial stages of the nitriding [124].

In order to clarify that point, investigation of the initial stage of formation as well as the evolution of precipitates upon heat treatments in cold rolled Fe-4Ni-2Ti (wt.%) and Fe-4Ni-3Cr (wt.%) alloys have been performed by Chechenin et al [123]. The nitriding is performed on thin foils in NH_3/H_2 atmosphere, in the temperature range 300-600°C, during 1-24h. XRD and TEM (HRTEM) investigations revealed:

- Small (dimensions 2.5 a_{TiN}×2.5 a_{TiN} ×0.5 a_{TiN}) coherent Ti(Fe)N clusters (probably GP-zone type) are formed during nitriding at 300°C in Fe-4Ni-2Ti alloy.
- Further annealing at higher temperatures result in growth of lateral dimensions of these clusters. In addition, these GP-like-clusters loose Fe and become stoichiometric TiN precipitates.

However, no evidence of precipitate formation is observed in Cr-containing alloy at 300°C, whereas at 400 °C thin (1 to 2 monolayers) and wide (more that 5 a_{CrN}) platelets are found. No evidence of formation of any GP-like clusters (pre-precipitation stage) is found at any stage for Fe-4Ni-3Cr alloy.

These results are in agreement with the work of Jack in the case of the Fe-Ti system [117] and Mortimer [124] for Fe-Cr system.

Another open question is the microstructure of nitrided layers. A number of investigations were conducted for Fe-Cr alloys [108,118–120,125–127], showing two precipitate morphologies:

- In the initial stage very small (nanometric [108,123,125]), Cr-N precipitates appear. This stage is associated with high hardness, caused by field strains, initiated by misfit between nitrides and α-Fe matrix.
- On prolongated nitriding, coarsening of nitrided zone appears. Either (a) the growth of nitrided particles with loss of coherency at the matrix/cluster interface or (b) by discontinuous coarsening, where the fine Cr nitride particles are replaced by a lamellar

morphology consisting of nitride and ferrite lamellae [119]. It has been suggested that the driving force for the discontinuous coarsening of MeN nitride depends on the amount of Me [126]. Recently, lamellar morphology is reported for Fe-V [128] alloy.

Both coarsening reactions can occur simultaneously and may lead to a decrease of hardness, which is most pronounced for lamellar microstructure.

IV.2. NDS elaboration by Mechanical Alloying

As it was already mentioned at the beginning of the section, nitriding is not the only way envisaged for NDS production. Mechanical alloying with subsequent consolidation of powder may also be considered as an alternative to nitriding way. Like in the case of ODS, the idea of the method is the following:

i) Introduction of "nitride donor" (Y_2O_3 in case of ODS) into Fe-Cr matrix during mechanical alloying process.

ii) Stimulation of precipitation of nitrides (TiN) after further heat treatments (consolidation of a powder).

An important question is the way of introduction of "nitride donor" during MA process. Several possibilities can be suggested:

a) MA of Fe-Cr that contains Ti in solid solution with CrN, Cr_2N or Fe_xN. Further heat treatment converts necessary amount of nitrogen to react with Ti and form TiN precipitates. This way has been proposed by *Atomic Energy Authority (AEA, UK)* [129].

b) MA of Fe-Cr powder with TiN and further heat treatment could lead to formation of TiN particles.

c) MA can be performed for Fe-Cr powder that contains nitrogen in solid solution with Ti powder (in the form of TiH_2). Further heat treatments should result in precipitation of TiN. This way has never been explored before and represents a new solution. This way has been realised in the framework of the present ANR program and studied in the current Ph.D. work.

The dissolution kinetics of Fe_xN, Cr_2N, TiN and TiH_2 reinforcements in Fe-Cr matrix during MA have been studied by Ratti et al. [130] using neutron and X-ray diffraction. MA during 48 h is performed in all cases. It is concluded that the behaviour of all these reinforcements during MA is different. As an example, TiN do not dissolve in Fe-9Cr matrix

during milling. Concerning Cr_2N, the author does not give any conclusions indicating that further study is needed. In the case of Fe_XN and TiH_2, dissolution during 48 h occurs.

In case of NDS elaboration by mechanical alloying several advantages can be envisaged:

- At least several solutions for nitrogen incorporation during MA can be suggested (in contrast to ODS production, where commonly, only Y_2O_3 is used). These solutions can offer some additional advantages in term of stability, i.e. they can be less stable and dissolution may occur more easily (in comparison to stable Y_2O_3);
- Homogeneous dispersion of strengthening particles (well known attribute of MA).
- Significant experience gained form ODS production.

IV.3. Partial conclusions

Nitride Dispersion Strengthened Steels can have different advantages and could be an alternative to ODS, replacing oxides by a fine and dense dispersion of nitrides. NDS materials have been already envisaged for nuclear application in 1980s. Taking into account options suggested in the past and new possibilities that are available nowadays, dispersion of nitrides inside Fe-Cr matrix can be achieved by two ways: plasma nitriding and mechanical alloying. Characterisation of such kind of materials in as-recieved state (as well as at elevated temperature and irradiation) is needed at all levels as almost no database is available at the moment in comparison to ODS steel.

In the framework of the ANR aXtrem program, ferritic Fe-18CrWT NDS steels are elaborated by both mechanical alloying and plasma nitriding methods. The aim of the current work is to provide a systematic study of the microstructural evolution at each step of the elaboration process (initial state and subsequent heat treatments up to 1000°C) by means of Atom Probe Tomography.

The studied materials and experimental technique used in this program and Ph.D will be described in the next chapter.

V. Bibliography of Chapter 1

[1] Nuclear Energy Agency (NEA) 'Nuclear Energy Today': URL www.oecd-Nea.org/Html/Pub/Nuclearenergytoday/Welcome.html, (2005).

[2] M.M. Abu-Khader, Progress in Nuclear Energy 51 (2009) 225–235.

[3] European nuclear society, www.euronuclear.org/1-information/generation-IV.htm (2004).

[4] T. Abram, S. Ion, Energy Policy 36 (2008) 4323–4330.

[5] Gen IV International forum, http://www.gen-4.org/Technology/systems/index.htm (2010).

[6] G. Van Goethem, M. Hugon, V. Bhatnagar, P. Manolatos, M. Deffrennes, Nuclear Engineering and Design 237 (2007) 1486–1502.

[7] J.G. Marques, Energy Conversion and Management 51 (2010) 1774–1780.

[8] G.L. Fiorini, A. Vasile, Nuclear Engineering and Design 241 (2011) 3461–3469.

[9] Clefs Cea n.55 'Nuclear systems of the future Generation IV', http://www.cea.fr/var/cea/storage/static/gb/library/Clefs55/contents.htm (2007).

[10] K.L. Murty, I. Charit, Journal of Nuclear Materials 383 (2008) 189–195.

[11] P. Yvon, F. Carré, Journal of Nuclear Materials 385 (2009) 217–222.

[12] B. Raj, K.B.S. Rao, Journal of Nuclear Materials 386-388 (2009) 935–943.

[13] O.N.E. Agency, Structural Materials for Innovative Nuclear Systems (SMINS): Workshop Proceedings, Karlsruhe, Germany, 4-6 June 2007, OECD Publishing, 2008.

[14] J.S. Cheon, C.B. Lee, B.O. Lee, J.P. Raison, T. Mizuno, F. Delage, J. Carmack, Journal of Nuclear Materials 392 (2009) 324–330.

[15] I. Shibahara, N. Akasaka, S. Onose, H. Okada, S. Ukai, Journal of Nuclear Materials 212-215, Part 1 (1994) 487–491.

[16] F.A. Garner, M.B. Toloczko, B.H. Sencer, Journal of Nuclear Materials 276 (2000) 123–142.

[17] P.R. Okamoto, L.E. Rehn, Journal of Nuclear Materials 83 (1979) 2–23.

[18] J.M. Titchmarsh, S. Dumbill, Journal of Nuclear Materials 227 (1996) 203–219.

[19] S. Bruemmer, E. Simonen, P. Scott, P. Andresen, G. Was, J. Nelson, Journal of Nuclear Materials 274 (1999) 299–314.

[20] E. Little, Materials Science and Technology, 22 5 (2006).

[21] E.A. Little, Journal of Nuclear Materials 87 (1979) 11–24.

[22] S. Ukai, S. Mizuta, T. Yoshitake, T. Okuda, M. Fujiwara, S. Hagi, T. Kobayashi, Journal of Nuclear Materials 283-287 (2000) 702–706.

[23] S. Ukai, M. Harada, H. Okada, M. Inoue, S. Nomura, S. Shikakura, K. Asabe, T. Nishida, M. Fujiwara, Journal of Nuclear Materials 204 (1993) 65–73.

[24] P. Miao, G.R. Odette, T. Yamamoto, M. Alinger, D. Klingensmith, Journal of Nuclear Materials 377 (2008) 59–64.

[25] M.K. Miller, D.T. Hoelzer, E.A. Kenik, K.F. Russell, Intermetallics 13 (2005) 387–392.

[26] J. Malaplate, F. Mompiou, J.-L. Béchade, T. Van Den Berghe, M. Ratti, Journal of Nuclear Materials In Press (2011).

[27] R.L. Klueh, J.P. Shingledecker, R.W. Swindeman, D.T. Hoelzer, Journal of Nuclear Materials 341 (2005) 103–114.

[28] T. Hayashi, P.M. Sarosi, J.H. Schneibel, M.J. Mills, Acta Materialia 56 (2008) 1407–1416.

[29] M.B. Toloczko, D.S. Gelles, F.A. Garner, R.J. Kurtz, K. Abe, Journal of Nuclear Materials 329-333 (2004) 352–355.

[30] R.L. Klueh, P.J. Maziasz, I.S. Kim, L. Heatherly, D.T. Hoelzer, N. Hashimoto, E.A. Kenik, K. Miyahara, Journal of Nuclear Materials 307-311 (2002) 773–777.

[31] I.-S. Kim, J.D. Hunn, N. Hashimoto, D.L. Larson, P.J. Maziasz, K. Miyahara, E.H. Lee, Journal of Nuclear Materials 280 (2000) 264–274.

[32] P. Pareige, M. Miller, R. Stoller, D. Hoelzer, E. Cadel, B. Radiguet, Journal of Nuclear Materials 360 (2007) 136–142.

[33] H.S. Cho, R. Kasada, A. Kimura, Journal of Nuclear Materials 367-370 (2007) 239–243.

[34] M.S. El-Genk, J.-M. Tournier, Journal of Nuclear Materials 340 (2005) 93–112.

[35] C.C. Koch, J.D. Whittenberger, Intermetallics 4 (1996) 339–355.

[36] C. Suryanarayana, Materials Park, OH: ASM International 7 (1998) 80.

[37] C. Suryanarayana, Progress in Materials Science 46 (2001) 1–184.

[38] C. Suryanarayana, E. Ivanov, V. Boldyrev, Materials Science and Engineering: A 304-306 (2001) 151–158.

[39] P.R. Soni, Mechanical Alloying: Fundamentals and Applications, Cambridge International Science Publishing, 1999.

[40] C. Capdevila, H.K.D.H. Bhadeshia, Advanced Engineering Materials 3 (2001) 647–656.

[41] S. Ukai, M. Harada, H. Okada, M. Inoue, S. Nomura, S. Shikakura, T. Nishida, M. Fujiwara, K. Asabe, Journal of Nuclear Materials 204 (1993) 74–80.

[42] Japan Atomic Energy Agency, Http://www.jaea.go.jp/english/news/p06101302/index.shtml (2006).

[43] L. Hsiung, M. Fluss, S. Tumey, J. Kuntz, B. El-Dasher, M. Wall, B. Choi, A. Kimura, F. Willaime, Y. Serruys, Journal of Nuclear Materials 409 (2011) 72–79.

[44] D.T. Hoelzer, J. Bentley, M.A. Sokolov, M.K. Miller, G.R. Odette, M.J. Alinger, Journal of Nuclear Materials 367-370 (2007) 166–172.

[45] S. Ohtsuka, S. Ukai, M. Fujiwara, T. Kaito, T. Narita, Journal of Nuclear Materials 329-333 (2004) 372–376.

[46] S. Ukai, T. Nishida, H. Okada, T. Okuda, M. Fujiwara, K. Asabe, J. Nucl. Sci. Technol. 34 (1997) 256–263.

[47] Z. Oksiuta, N. Baluc, Journal of Nuclear Materials 386-388 (2009) 426–429.

[48] P. Unifantowicz, Z. Oksiuta, P. Olier, Y. de Carlan, N. Baluc, Fusion Engineering and Design In Press (2011).

[49] D. Larson, P. Maziasz, I. Kim, K. Miyahara, Scripta Materialia 44 (2001) 359–364.

[50] A. Ramar, Z. Oksiuta, N. Baluc, R. SchÃ¤ublin, Fusion Engineering and Design 82 (2007) 2543–2549.

[51] M.K. Miller, K.F. Russell, D.T. Hoelzer, Journal of Nuclear Materials 351 (2006) 261–268.

[52] C.-L. Chen, Y.-M. Dong, Materials Science and Engineering: A 528 (2011) 8374–8380.

[53] C.A. Williams, E.A. Marquis, A. Cerezo, G.D.W. Smith, Journal of Nuclear Materials 400 (2010) 37–45.

[54] M. Couvrat, L. Chaffron, D. Nunes, P. Bonnaillie, M.H. Mathon, M. Perrut, Solid State Phenomena 172-174 (2011) 721–726.

[55] H.V. Atkinson, S. Davies, Metallurgical and Materials Transactions A 31 (2000) 2981–3000.

[56] M.J. Alinger, G.R. Odette, D.T. Hoelzer, Acta Materialia 57 (2009) 392–406.

[57] Z. Livne, A. Munitz, J.C. Rawers, R.J. Fields, Nanostructured Materials 10 (1998) 503–522.

[58] R. Kasada, N. Toda, K. Yutani, H.S. Cho, H. Kishimoto, A. Kimura, Journal of Nuclear Materials 367-370 (2007) 222–228.

[59] Y. de Carlan, J.-L. Bechade, P. Dubuisson, J.-L. Seran, P. Billot, A. Bougault, T. Cozzika, S. Doriot, D. Hamon, J. Henry, M. Ratti, N. Lochet, D. Nunes, P. Olier, T. Leblond, M.H. Mathon, Journal of Nuclear Materials 386-388 (2009) 430–432.

[60] M. Klimiankou, R. Lindau, A. Möslang, Journal of Nuclear Materials 367-370 (2007) 173–178.

[61] M.K. Miller, E.A. Kenik, K.F. Russell, L. Heatherly, D.T. Hoelzer, P.J. Maziasz, Materials Science and Engineering A 353 (2003) 140–145.

[62] L. Schäfer, M. Schirra, K. Ehrlich, Journal of Nuclear Materials 233-237 (1996) 264–269.

[63] P.J. Cunat, Aciers inoxydables, critères de choix et structures, Techniques de l'Ingénieur, M4540, (2000).

[64] S. Ukai, M. Fujiwara, Journal of Nuclear Materials 307-311 (2002) 749–757.

[65] M. Durand-Charre, Microstructure of Steels and Cast Irons, Springer, 2004, p.305, 323.

[66] C. Capdevila, M.K. Miller, I. Toda, J. Chao, Materials Science and Engineering: A 527 (2010) 7931–7938.

[67] J.S. Lee, C.H. Jang, I.S. Kim, A. Kimura, Journal of Nuclear Materials 367-370 (2007) 229–233.

[68] H. Hadraba, B. Fournier, L. Stratil, J. Malaplate, A.-L. Rouffié, P. Wident, L. Ziolek, J.-L. Béchade, Journal of Nuclear Materials 411 (2011) 112–118.

[69] R.L. Klueh, Elevated-Temeperature Ferritic and Martensitic steels, Http://www.ornl.gov/~webworks/cppr/y2001/rpt/121054.pdf (2004).

[70] V. Vodárek, A. Strang, Scripta Materialia 38 (1997) 101–106.

[71] M. Alinger, On the Formation and Stability of Nanometer Scale Precipitates in Ferritic Alloys During Processing and High Temperature Service. Thesis, University of California, 2004.

[72] R. Lindau, A. Möslang, M. Schirra, P. Schlossmacher, M. Klimenkov, Journal of Nuclear Materials 307-311 (2002) 769–772.

[73] A. Alamo, V. Lambard, X. Averty, M.H. Mathon, Journal of Nuclear Materials 329-333 (2004) 333–337.

[74] M. Klimenkov, R. Lindau, A. Möslang, Journal of Nuclear Materials 386-388 (2009) 557–560.

[75] I. Monnet, P. Dubuisson, Y. Serruys, M.O. Ruault, O. KaÏtasov, B. Jouffrey, Journal of Nuclear Materials 335 (2004) 311–321.

[76] A. Alamo, J.L. Bertin, V.K. Shamardin, P. Wident, Journal of Nuclear Materials 367-370 (2007) 54–59.

[77] C. Capdevila, M.K. Miller, K.F. Russell, J. Chao, J.L. González-Carrasco, Materials Science and Engineering: A 490 (2008) 277–288.

[78] T.C. Totemeier, C.J. Smithells, Smithells Metals Reference Book, Butterworth-Heinemann, 2004, p. 8-1.

[79] A. Ramar, N. Baluc, R. Schäublin, Journal of Nuclear Materials 386-388 (2009) 515–519.

[80] M. Ratti, D. Leuvrey, M.H. Mathon, Y. de Carlan, Journal of Nuclear Materials 386-388 (2009) 540–543.

[81] C. Cayron, A. Montani, D. Venet, Y. Carlan, Journal of Nuclear Materials 399 (2010) 219–224.

[82] M. Klimiankou, R. Lindau, A. Möslang, Micron 36 (2005) 1–8.

[83] M. Klimiankou, R. Lindau, A. Möslang, Journal of Crystal Growth 249 (2003) 381–387.

[84] M.K. Miller, D.T. Hoelzer, E.A. Kenik, K.F. Russell, Journal of Nuclear Materials 329-333 (2004) 338–341.

[85] H. Kishimoto, R. Kasada, O. Hashitomi, A. Kimura, Journal of Nuclear Materials 386-388 (2009) 533–536.

[86] H. Sakasegawa, L. Chaffron, F. Legendre, L. Boulanger, T. Cozzika, M. Brocq, Y. de Carlan, Journal of Nuclear Materials 384 (2009) 115–118.

[87] E.A. Marquis, Applied Physics Letters 93 (2008) 181904.

[88] S. Lozano-Perez, V. de Castro Bernal, R.J. Nicholls, Ultramicroscopy 109 (2009) 1217–1228.

[89] V. de Castro, E.A. Marquis, S. Lozano-Perez, R. Pareja, M.L. Jenkins, Acta Materialia In Press (2011).

[90] M. Klimenkov, R. Lindau, A. Möslang, Journal of Nuclear Materials 386-388 (2009) 553–556.

[91] M.K. Miller, D.T. Hoelzer, E.A. Kenik, K.F. Russell, Journal of Nuclear Materials 329-333 (2004) 338–341.

[92] L.L. Hsiung, M.J. Fluss, S.J. Tumey, B.W. Choi, Y. Serruys, F. Willaime, A. Kimura, Phys. Rev. B 82 (2010) 184103.

[93] L.L. Hsiung, M.J. Fluss, A. Kimura, Materials Letters 64 (2010) 1782–1785.

[94] T. Okuda, M. Fujiwara, J Mater Sci Lett 14 (1995) 1600–1603.

[95] S. Yamashita, S. Ohtsuka, N. Akasaka, S. Ukai, S. Ohnuki, Philosophical Magazine Letters 84 (2004) 525.

[96] M. Brocq, Synthèse Et Caractérisation D'un Acier ODS Préparé Par Un Procédé Inspiré Du Broyage Réactif - Etude De L'influence Des Conditions De Broyage Et Recuit. Thèse, Université de Rennes, Ph.D, 2010.

[97] M. Brocq, B. Radiguet, S. Poissonnet, F. Cuvilly, P. Pareige, F. Legendre, Journal of Nuclear Materials 409 (2011) 80–85.

[98] S. Ohtsuka, S. Ukai, M. Fujiwara, T. Kaito, T. Narita, Journal of Physics and Chemistry of Solids 66 (2005) 571–575.

[99] P. Dou, A. Kimura, T. Okuda, M. Inoue, S. Ukai, S. Ohnuki, T. Fujisawa, F. Abe, Journal of Nuclear Materials 417 (2011) 166–170.

[100] L.E. Kindlimann, G.S. Ansell, Metall and Materi Trans B 1 (1970) 507–515.

[101] D.H. Jack, Acta Metallurgica 24 (1976) 137–146.

[102] Rapport CEA-R-5918. Lambard V. Développement D'une Nouvelle Nuance Martensitique ODS Pour Utilisation Sous Rayonnement à Haute Température, Thèse De Doctorat, Université Paris Sud Orsay, 2000.

[103] Rapport CEA-R-5675. Réglé H. Alliages Ferritiques 14/20% De Chrome Renforcés Par Dispersion D'oxydes, Thèse De Doctorat, Université Paris Sud Orsay, 1994.

[104] Frank E., W. Rembges, H. Harig, Harterei-Tech. Mitt. 38 8 (1983) 110–115.

[105] B. Podgornik, J. Vizintin, O. Wanstrand, M. Larsson, S. Hogmark, Surface and Coatings Technology 120-121 (1999) 502–508.

[106] Y. Xi, D. Liu, D. Han, Surface and Coatings Technology 202 (2008) 2577–2583.

[107] E.J. Mittemeijer, A.B.P. Vogels, P.J. Schaaf, Journal of Materials Science 15 (1980) 3129–3140.

[108] P. Jessner, R. Danoix, B. Hannoyer, F. Danoix, Ultramicroscopy 109 (2009) 530–534.

[109] D. Pye, Practical Nitriding and Ferritic Nitrocarburizing, illustrated ed., ASM International, 2003.

[110] L. Yue-Zhu, L. Arnberg, S. Savage, Materials Science and Engineering 98 (1988) 531–534.

[111] A. Johansson, L. Arnberg, P. Gustafson, S. Savage, 46 (1991) 65.

[112] L.E. Kindlimann, Dispersion Strengthened Ferritic Stainless Steel, U.S. Patent 4464207, 1984.

[113] D.H. Jack, Materials Science and Engineering 13 (1974) 19–27.

[114] Y.Z. Li, L. Arnberg, Rep. IM-2143, Swedish Institute of Metals, Stockholm, (1986).

[115] L.E. Kindlimann, Internally Nitrided Ferritic Stainless Steels, and Methods of Producing Such Steels, U.S. Patent 0008228, 1979.

[116] A.G. Wilson, Nitride Dispersion Strengthened Steels and Method of Making, U.S. Patent 4846899, 1989.

[117] K.H. Jack, Scan. J. Met., 1, 195 (1972).

[118] E.J. Mittemeijer, J. Heat Treating 3 (1983) 114–119.

[119] R.E. Schacherl, P.C.J. Graat, E.J. Mittemeijer, Metall and Mat Trans A 35 (2004) 3387–3398.

[120] G. Miyamoto, A. Yonemoto, Y. Tanaka, T. Furuhara, T. Maki, Acta Materialia 54 (2006) 4771–4779.

[121] K.S. Jung, R.E. Schacherl, E. Bischoff, E.J. Mittemeijer, Surface and Coatings Technology 204 (2010) 1942–1946.

[122] R.G. Nooning, Effect of stabilizing elements on the precipitation behavior and phase stability of type 409 ferritic stainless steel. Thesis, University of Pittsburg, (1999).

[123] N.G. Chechenin, A.R. Chezan, C.B. Craus, D.O. Boerma, L. Niesen, P.M. Bronsveld, J.T.M. Hosson, Metall and Mat Trans A 33 (2002) 3075–3087.

[124] Mortimer, B., Grieveson, P., Jack, K.H., 1, (1972) 203–209.

[125] N.G. Chechenin, P.M. Bronsveld, A. Chezan, C.B. Craus, D.O. Boerma, J.T.M. de Hosson, L. Niesen, Phys. Stat. Sol. (a) 177 (2000) 117–125.

[126] N.E.V. Díaz, R.E. Schacherl, L.F. Zagonel, E.J. Mittemeijer, Acta Materialia 56 (2008) 1196–1208.

[127] G. Miamoto, A. Yonemoto, Y. Tanaka, T. Maki, T. Furuhara, ISIJ International 47 (2007) 1491.

[128] S.S. Hosmani, R.E. Schacherl, E.J. Mittemeijer, Acta Materialia 53 (2005) 2069–2079.

[129] E.G. Wilson, Production of Nitride Dispersion Strengthened Alloys, U.S. Patent 4708742, 1987.

[130] M. Ratti, Développement De Nouvelles Nuances D'acier Ferritiques/martensitiques Pour Le Gainage D'élément Combustible Des Réacteurs à Neutrons Rapides Au Sodium. Thèse, Institut Polytechnique de Grenoble, 2009.

Table of content

Chapter 2. Materials, experimental and simulation techniques 46

I. Materials 46

I.1. ODS model alloy 47

I.2. ODS steel 48

I.3. Mechanically alloyed NDS steel (MA NDS) 49

I.4. Nitrided NDS 50

II. Atom Probe Tomography (APT) 52

II.1. Principle 52

II.2. Laser assisted field evaporation 56

II.3. Experimental devices and their performances 57

II.4. Particular case of ODS and NDS materials 60

a) Determination of experimental parameters 60
b) Isotope overlaps 64
c) Methods for APT data treatment 69
d) Local magnification effect 71

III. Modelling of precipitation kinetics with MatCalc and Thermocalc softwares 79

III.1. Theory of precipitation kinetics 79

III.2. Modelling of precipitation kinetics with MatCalc 80

a) Precipitate nucleation 80
b) Evolution of radius and composition of precipitates 81
c) Evaluation of interfacial energies 82

III.3. Used parameters for MatCalc calculations 83

III.4. ThermoCalc software 84

IV. Conclusions of the Chapter 2. 86

V. Bibliography of the Chapter 2 87

Chapter 2. Materials, experimental and simulation techniques

This work is a part of the ANR aXtrem devoted to development of ferritic steel reinforced by nano-particles, for nuclear application in extreme conditions. Basically, two kinds of materials are studied. The first one is an Fe-based Oxide Dispersion Strengthened steel. ODS steels are currently under intense investigation all over the world as they are considered as reference solution for application such as cladding elements in GEN IV reactors.

Taking into account the positive experience of ODS materials, iron-based alloys reinforced by a fine dispersion of nitrides (Nitride Dispersion Strengthened steels) could also be promising. NDS steels, elaborated by two different ways: mechanical alloying and plasma nitriding are investigated in this work. In the first section, studied materials, their production route and state in which they are characterized are detailed.

Characterization of microstructure at very fine scale, near atomic level, after different steps of elaboration process as well as after annealing at various annealing treatments is needed to get a better understanding of basic laws of nanoparticle formation and evolution. To do so, Atom Probe Tomography is used [1–4]. Two types of Atom Probes are used to get accurate compositional measurements and rather good statistics for nanoparticles characterization. Main principle, used devises, chosen experimental conditions and appeared difficulties are described in the second section.

Thermodynamic and kinetic computer modelling has successfully established itself as an important tool for alloy design and predictions of precipitation behaviour. In this work, MatCalc and ThermoCalc softwares are used to estimate the expected microstructure as a function of chemical composition and heat treatment pattern. MatCalc and Thermocalc, their basic principles and used parameters for modelling are presented is the third section.

I. Materials

Studied materials are mainly high chromium Fe-18Cr-1W ferritic steels reinforced either by small dispersion of oxides or nitrides. In addition Fe-9Cr ODS model alloy with higher level of Y_2O_3 is also studied.

They are all obtained by introducing either Y or Ti and/or N or O in the pre-alloyed powder. All pre-alloyed powders are elaborated by atomisation in Aubert & Duval Company.

The elaboration ways used for production of ODS and NDS are detailed below for each material. In all cases, a thermal treatment and consolidation step are performed in *Commissariat à l'énergie atomique* (CEA, SRMA/LTMEX), Saclay.

I.1. ODS model alloy

This model alloy is elaborated in two steps. First, a Fe-9Cr-1W pre-alloyed powder is mechanically alloyed with 10 wt.% of titanium hydrate (TiH_2) during 48 hours. Then, Fe-9Cr-1W-10Ti powder is again mechanically alloyed with 10 wt.% of Y_2O_3 during 48 hours. Mechanical alloying (MA) are performed in CEA (SRMA/LTMEX), Saclay. In both cases MA is performed in planetary ball mill (Fritsch P-6). Milling parameters are:

- Atmosphere: gas argon.
- Milling speed: 400 rpm.
- Ratio of the mass of the balls to the powder m_{balls}/m_{powder}: 1,20.
- Direction of rotation is changed each cycle. One cycle consists in 15 minutes of milling and 20 minutes of vessel cooling. The final MA consists of 48 hours of milling and 64 hours of cooling (total sequence of 192 cycles).
- Balls: diameter 20 mm made of stainless steel.

The nominal composition of ODS model alloy is given in the *Table 2.1*.

Table 2.1. Nominal composition of ODS model alloy. Balance is iron.

	Cr	**W**	**TiH_2**	**Y**	**O**
wt.%	9	1	10	$10Y_2O_3$	
at.%	7.45	0.29	11.0	4.8	7.1

Such model alloy with very high level of oxide-like element can provide useful information about dissolution mechanism of yittria and reaction occurring during milling. This alloy was firstly studied by X-ray and neutron diffraction in Laboratoire Léon Brillouin (LLB) in CEA Saclay. X-ray diffraction analysis on single powder grain was performed in synchrotron Soleil [5–7], thanks to specific sample preparation method developed in GPM (see details in Appendix 2-d.). In addition, to these diffraction methods, Atom Probe Tomography was used to get information about solute distribution in the as-milled powder.

I.2. ODS steel

This ferritic ODS steel is elaborated by mechanical alloying of pre-alloyed Fe-18Cr-1W-0.3Ti powder with 0.6 wt.% of Y_2O_3 powder (SRMA code F20). Mechanical alloying is performed by Plansee Company in an industrial attritor. Mechanical alloying is performed under hydrogen atmosphere. Conditions of MA are confidential so precision on experimental parameters of the process is unknown.

After, as-milled powder is pre-heated to the "consolidation temperature" of 1100°C and then hot extruded into bars. The next step is hot rolling (20% reduction), performed at 700°C. Finally, hot extruded bars are additionally annealed at 1050°C during 1h.

In order to get information on clustering kinetics, the as-milled powder is also annealed at 850°C during 1 hour. Annealing is performed in hydrogen atmosphere. After heat treatment the powder is air cooled.

Nominal compositions of ODS steel are detailed in *Table 2.2.*

Table 2.2. Nominal composition of ODS steel (F20). Balance is iron.

	Cr	**Ti**	**Si**	**Mn**	**W**	**Ni**	**Y**	**O**
wt.%	18	0.3	0.15	0.3	1	0.3	0.6 Y_2O_3	
at.%	19.2	0.35	0.30	0.30	0.30	0.28	0.30	0.44

In order to get information about the formation mechanism of oxides in this steel, the material was studied in the final state (so called "hot extruded" sample) but also just after the mechanical alloying step ("as-milled" sample). It gives information about dissolution process during milling and the "initial" state for oxide nucleation. The powder that was annealed at 850°C/1h is called further "annealed".

The material has been characterized in the framework of the project by different techniques in three states: after MA, annealing and hot extrusion. Small-Angle Neutron Scattering experiments have been conducted by M.H. Mathon, M.Perrut and M.Ratti at Laboratoire Léon Brillouin in CEA Saclay [7,8]. Investigations by Transmission Electron Microscopy [9–11] were also performed. Mechanical properties of the ODS steel have been extensively studied in the framework of the Ph.D. work of M. Ratti [7].

I.3. Mechanically alloyed NDS steel (MA NDS)

NDS steels were elaborated following two distinct ways. The first one is mechanical alloying. In this case, pre-alloyed powder Fe-18Cr-1W-0.14N is mechanically alloyed with 0.5 wt.% of titanium hydrate (TiH_2) in laboratory attritor ball mill. Mechanical alloying is performed in CEA (SRMA/LTMEX), Saclay. Initial sizes of pre-alloyed powder and TiH_2 are 100 μm and 100 nm respectively. Parameters of milling are the following:

- Atmosphere: gas argon.
- Milling time: 10 hours.
- Milling speed: 400 rpm.
- The ratio of the mass of the balls to the powder m_{balls}/m_{powder}: 15.
- Balls: stainless steel 440

Nominal composition of MA NDS steel is detailed in *Table 2.3*.

Table 2.3. Nominal composition of Fe-18Cr-1W-0.14N NDS steel (J12). Balance is iron.

	Cr	W	N	Ti
wt.%	18	1	0.14	0.5 (TiH_2)
at.%	19	0.30	0.54	0.57

In order to study the precipitation process (nucleation, growth as well as coarsening stages) as-milled powder is subjected to different annealing treatments at 600, 700, 850, 1000°C, during 1hour. Annealing is performed under hydrogen atmosphere. After annealing powders are air cooled.

In order to get bulk material, as-milled powder is degassed at 300°C during 10 hours, then pre-heated at 800°C/1h and finally hot extruded (SRMA code J12).
The APT characterisations were performed after on the following states:

- as-milled state;
- annealed at 600°C during 1h;
- annealed at 700°C during 1h;
- annealed at 850°C during 1h;
- annealed at 1000°C during 1h;
- consolidated state.

Like ODS steel, the MA NDS was studied by both SANS [8] and TEM [11]. Since the elaboration way to produce NDS steel have never been performed before, a patent was created by M. Ratti and Y. de Carlan [12].

I.4. Nitrided NDS

One of the advantages of NDS compared to ODS is the possibility to avoid complex step of mechanical alloying when nitrogen is introduced by simple nitriding process. In this work, a pre-alloyed Fe-18Cr-1W-0.75Ti powder is plasma nitrided by Bodycote-Nitruvid Company.

The aim of the treatment is to introduce nitrogen in a quantity sufficient to reach the core of biggest particles. The level of nitrogen is a function of the temperature and duration of the treatment as well as the chemical activity of nitrogen and hydrogen mixture. The desirable level of nitrogen ranges between 1000 and 2000 ppm in weight.

Nitriding of 1.4 kg of powder has been performed in rotating drum, shown in *Figure 2.1* (a). In order to mix the powder during nitriding, impellers have been implemented in the drum, *Figure 2.1* (b).

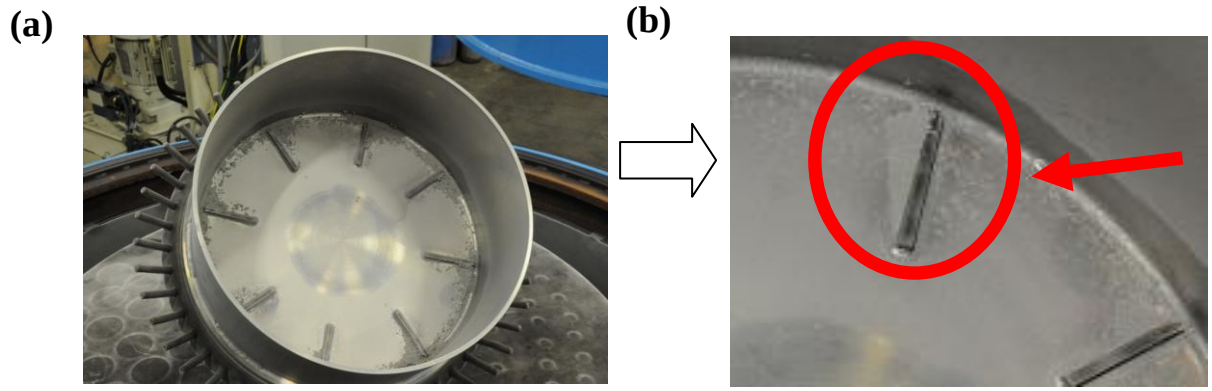

Figure 2.1. Rotary drum (inclined at 45°) where nitriding treatment is conducted [13,14] (a) full view, (b) impellers with powder.

The nitriding conditions that were used by Bodycote-Nitruvid Company are:

- Atmosphere of N_2 (30%)/H_2 (70%);
- Nitriding time: 15 hours;
- Temperature: 400°C;

The measurement of the temperature during nitriding of powder was performed by pyrometer[1]. Up to 1700 ppm in weight of nitrogen is incorporated during nitriding, value close to the expected one: 2000 ppm in weight. Nominal composition of nitrided NDS steel is given in *Table 2.4.*

Table 2.4. Nominal composition of nitrided NDS steel (SRMA code J22). Balance is iron.

	Cr	**W**	**Ti**	**N**
wt.%	18	1	0.8	0.17
at.%	19.1	0.30	0.86	0.67

Before consolidation, as-nitrided powder is sealed in a can and subjected to an homogenization treatment during 10 days at a temperature of 400°C. The purpose of the treatment is to get a more uniform distribution of nitrogen. The consolidated material is obtained after hot extrusion at 800°C (SRMA code J22). After hot extrusion material is air cooled.

The characterisation using the APT technique was performed on the following states:

- as-nitrided state;
- annealed at 600°C during 1h;
- annealed at 700°C during 1h;
- consolidated state.

[1] *Pyrometer – is a non-contacting device that measures thermal radiation. Can be used to determine the temperature of an object's surface.*

II. Atom Probe Tomography (APT)

II.1. Principle

Atom Probe is described as a field ion microscope (FIM) equipped with a time-of-flight mass spectrometer and position sensitive detector (*Figure 2.2*.).

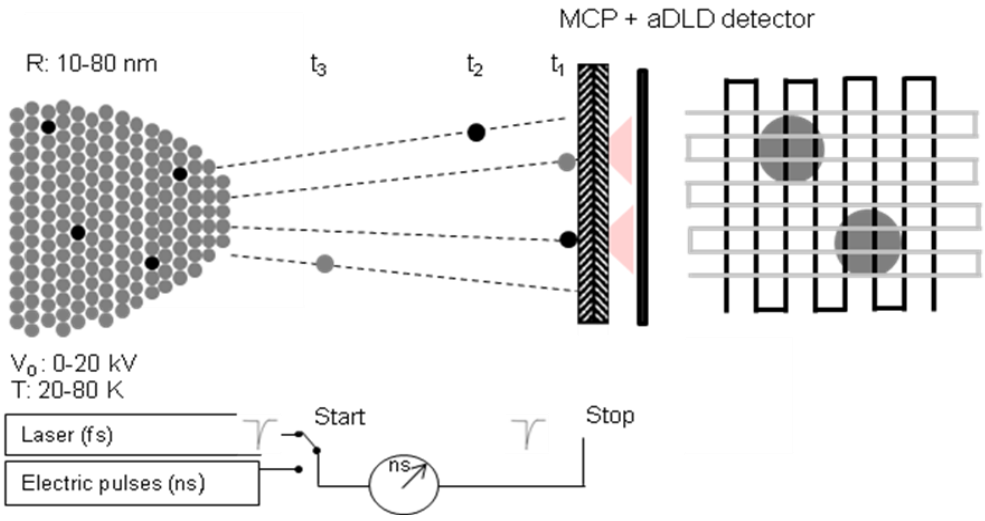

Figure 2.2. Schematic representation of an APT (R – radius of the tip, T – temperature of analyse, V_0- voltage applied to the tip, t_1, t_2, t_3 –flight times of an atoms evaporated from the tip, MCP - micro channel plates, aDLD - advanced Delay Line Detector).

A sharp cryogenically-cooled needle-shaped specimen (end radius, *R*, smaller than 50 nm) is introduced into an ultrahigh vacuum chamber (10^{-10} mBar). A positive voltage V_0, (several kilovolts) is then applied to the specimen. Thus, an electric field, *E* (given by $E = V_0/\beta R$ (equation 2.1)) is created at the apex of a specimen. β is a geometrical factor with a value between 2 and 8 [15].

In the presence of an electric field, atoms at the surface of a tip are ionised, *Figure 2.3*. The field evaporation rate *k* due to the presence of the field is given by the Arrhenius-type equation [3]:

$$k = \nu \exp \frac{-Q(E)}{k_b T} \qquad (2.2.)$$

where Q(E) is the field evaporation activation energy, k_b is the Boltzmann constant, *T* the applied temperature and υ is vibration frequency of the surface atoms on the tip.

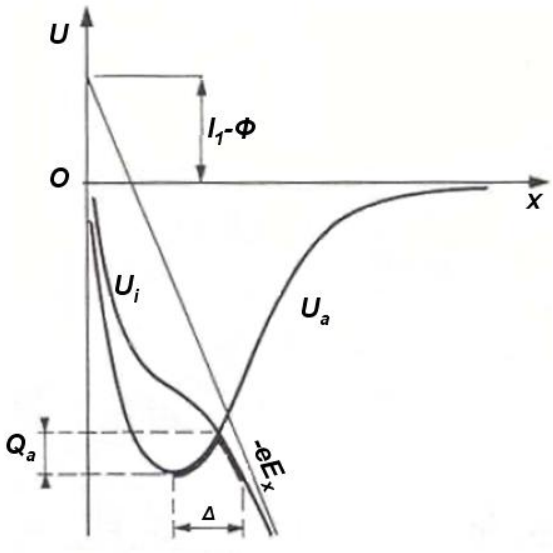

Figure 2.3. Potential energy diagrams for atom (U_a) and ion (U_i) on the surface of a sample under an electric field [16].

After the atom is ionized, it flies towards a detector. The chemical nature of the evaporated ions is then determined by time of flight mass spectrometry. The time of flight is the time between the electrical (or Laser) pulse that initiate the ionisation and the impact of the ion into the detector (micro channel plates and aDLD).

The mass-over-charge ratio, *m/n*, of ions is then deduced from the applied voltage, $V_{total}=V_o+V_p$ (with V_o and V_p standing and pulse voltages) and the time of flight, *t*, by using the energy balance relationship:

$$\frac{m}{n} = 2e(V_0 + V_p) \times \left(\frac{t}{L}\right)^2 \tag{2.3.}$$

where *m* is the ion mass, *n* is the ion charge state (1^+, 2^+...), *e* is the electron elementary charge and *t* and *L* the flight time and length.

The data collected during an experiment are represented in the form of a mass spectrum, showing the number of detected ions as a function of their mass-over-charge ratio (given in atomic mass units, amu). Each peak could be identified and associated to the corresponding element or its isotopes or combination (molecular ions). The concentration of an element *i*, in the analyzed volume is given in atomic percent by:

$$C_i = \frac{N_i}{N_t} \tag{2.4.}$$

where N_i is the number of atoms of the element i and N_t is the total number of atoms in the volume. The uncertainty of the concentration estimate due to counting statistics given by:

$$2\sigma = 2\sqrt{\frac{C(1-C)}{N_t}} \tag{2.5.}$$

The detector on which evaporated ions arrive is a position sensitive Advanced Delay Line Detector (aDLD) [17]. It consists in two microchannel plates (located in front of aDLD detector), which amplify the signals by creating electron bundle for each ion (see *Figure 2.2.*). This electron bundle creates electric signal in vertical and horizontal wire windings. The electrical signal propagates up to the end of each wire. The recording of signals in each wire end allows to measure difference of propagation delay between the top, the bottom, the left and the right of the detector and to deduce accurately the position of impact. The aDLD also allows the deconvolution of coordinates if group of ions arrive at the same time.

Once the position of ion impacts *(x, y)* on the detector is known, the coordinate of the atoms at the specimen surface may be computed by inverse projection. As shown in *Figure 2.4*, the image magnification is given by:

$$G = \frac{L}{(m+1)R} \tag{2.6.}$$

where *m* is the image compression factor related to the position of the projection point *P*. *R* is the tip radius and *L* is the free flight length of an ion (the estimated specimen to detector distance).

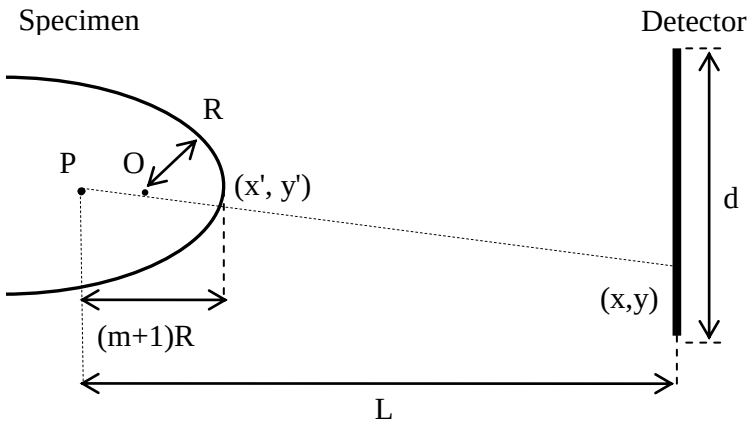

Figure 2.4. Shows that the derivation of atom positions from impact coordinates simply involves a point projection P.

The x' and y' coordinates of the position of the ion in the specimen for an analysis along the specimen axis may be expressed as:

$$x' = \frac{x}{G} \text{ and } y' = \frac{y}{G} \tag{2.7.}$$

where x and y are the coordinates of an ion impact on the detector. As the material is field evaporated layer by layer, a 3D reconstruction of the analyzed volume can be made. In practice the third coordinate, z, is deduced from the number of detected ions, N. A small increment of depth coordinate, Δz, corresponding to the ΔN evaporated atoms is given by formula:

$$\Delta z = \frac{\Delta N \Omega_i}{Q d^2} \times G^2 \tag{2.8.}$$

where Ω_i is the atomic volume of the i^{th} ion, Q *is* the detection efficiency of the detector and d is the diameter of the detector.

The typical detection efficiency of an Atom Probe is about 50 to 60% (about 50 to 40% of arriving ions are lost). The loss is mainly due to some ions striking the interchannel regions of microchannel plates. These atoms are being lost in a random way, so this effect does not affect the quantitative measurements of composition.

The depth resolution is determined by the screening distance of the electric field at the specimen surface. Usually, it is around 0.1 nm in conductive materials. This value is comparable to the typical lattice interplanar distances. The best spatial resolution is achieved along the depth of analysis and lattice planes of a crystalline materials are usually resolved if their normal is close to the direction of analysis.

On the other hand, in a cristallographic plane, perpendicular to the direction of analysis, the image of the lattice is "blurred". The lateral resolution is of several angstroms. The physical limit is mainly controlled by the ion-optical aberrations. With the typical magnification G of an Atom Probe (about 10^6), an error in the position of ion impact equal to 1 mm (caused for example by trajectory aberrations of the evaporating ions in the close vicinity of the specimen surface) lead to uncertainties in the range $0.2 - 0.5$ nm. In addition to a detection efficiency of 60%, these two effects are enough to blur the lattice structure. Deeper discussion concerning spatial resolution of an Atom Probe can find in the recent work of Gault et al [18].

Another important characteristic of an Atom Probe is its mass resolution. It characterizes the capability of an instrument to resolve two neighbouring peaks on the mass spectrum. It is convenient to define the mass resolution as the ratio between the peak position (in amu) and the peak width at 10% of its height. Mass resolution depends on the type of AP and on experimental conditions. This will be discussed in a next section.

II.2. Laser assisted field evaporation

As it was shown in previous section, conventional Atom Probes use electrical pulses in order to evaporate surface atoms. In this case, analysis of materials that are brittle under the applied electric field (which is the case of ODS and NDS samples obtained from powder grains), could be very difficult. Indeed, these electrical pulses submit the material to cyclic stress that frequently leads to the rupture of the specimen [19].

In the 1980`s Tsong and co-wokers designed a pulsed Laser Atom Probe (PLAP) [20,21]. This work was done on the basis of one-dimentional Atom Probe that differs from 3DAP by much smaller field of view and the use of the detector non sensitive to the position. In the PLAP, because of duration of Laser pulses (nanosecond or subnanosecond) the evaporation field of atoms was strongly thermally assisted. It was shown that the peak temperature of the specimen under nanosecond Laser pulse can reach 500 K [22]. In that case, the spatial resolution has been degraded due to surface diffusion of atoms prior their field evaporation.

Since 2004, a new generation of Atom Probes, using femtosecond Laser pulses have been developed in the GPM laboratory [19,23]. In this case poor conductive materials (ceramics, oxide layers, etc…) as well as brittle samples can be analysed [24,25]. Another significant advantage is the higher mass resolution of the Laser assisted TAP in comparison to electrical [26].

As it was already mentioned, the evaporation of an atom is assisted either by i) increasing the electric field at the tip surface (case of applied electrical pulses) or ii) by increasing the temperature. Since few years, many efforts have been devoted to the understanding of physical processes involved in field evaporation under action of femtosecond Laser. Up to now, two models are generally accepted:

(i) *Thermal pulse model (TMP).* According to this model, a part of the Laser pulse energy is absorbed in a fine area close to the tip apex, generating a localised thermal spike.

This temperature rise can initiate field evaporation by thermal activation during 1 to 10 ns [27,28].

(ii) *Optical rectification model (OR).* In this case, non linear response of the material is considered. Interaction of the Laser with the material generated non symmetric vibration of the electrons at the surface of the specimen. Thus, an electric field, sufficient to promote field evaporation of surface atoms is generated. The pulsed field induced by the OR may act exactly as a voltage pulse applied to the tip with sub-picoseconds duration [29,30].

Recently, J. Houard and F. Vurpillot [31,32] have demonstrated that Laser assisted field evaporation is clearly a thermal process in case of metals. Mechanisms occurring in the insulators or semi-conductors are still under investigation.

II.3. Experimental devices and their performances

Experiments are carried out with two different Atom Probes: *Laser-Assisted Tomographic Atom Probe (LATAP)* and *Laser-Assisted Wide Angle Tomographic Atom Probe (LAWATAP).* Both of them are equipped with an advanced Delay Line position sensitive Detectors (aDLD).

Laser-Assisted Tomographic Atom Probe (LATAP) is known for its high mass resolution that is achieved due to long distance between position sensitive detector and the specimen (~40 cm). However, this technique allows a small volume of material to be analysed (up to $20\times20\times200$ nm^3), limiting statistics. This instrument is equipped with a Ti:Sa femtosecond Laser. Pulse length is 400 fs and the pulse repetition rate is equal to 2 kHz.

As for the Laser-Assisted Wide Angle Tomographic Atom Probe (LAWATAP), it is equipped with a diode-pumped ytterbium femtosecond Laser with a pulse repetition rate of 100 kHz [23]. Undoubted benefit of this modification of TAP is that larger volume of materials can be analysed (up to $60\times60\times200$ nm^3) in comparison to LATAP. It is achieved by reduction of the distance between position sensitive detector and the specimen (~20 cm). However, the shorter flight-path lengths of ions lead to the degradation of the mass resolution. The comparison of mass resolution of the LATAP and LAWATAP can be observed on *Figure 2.5.*

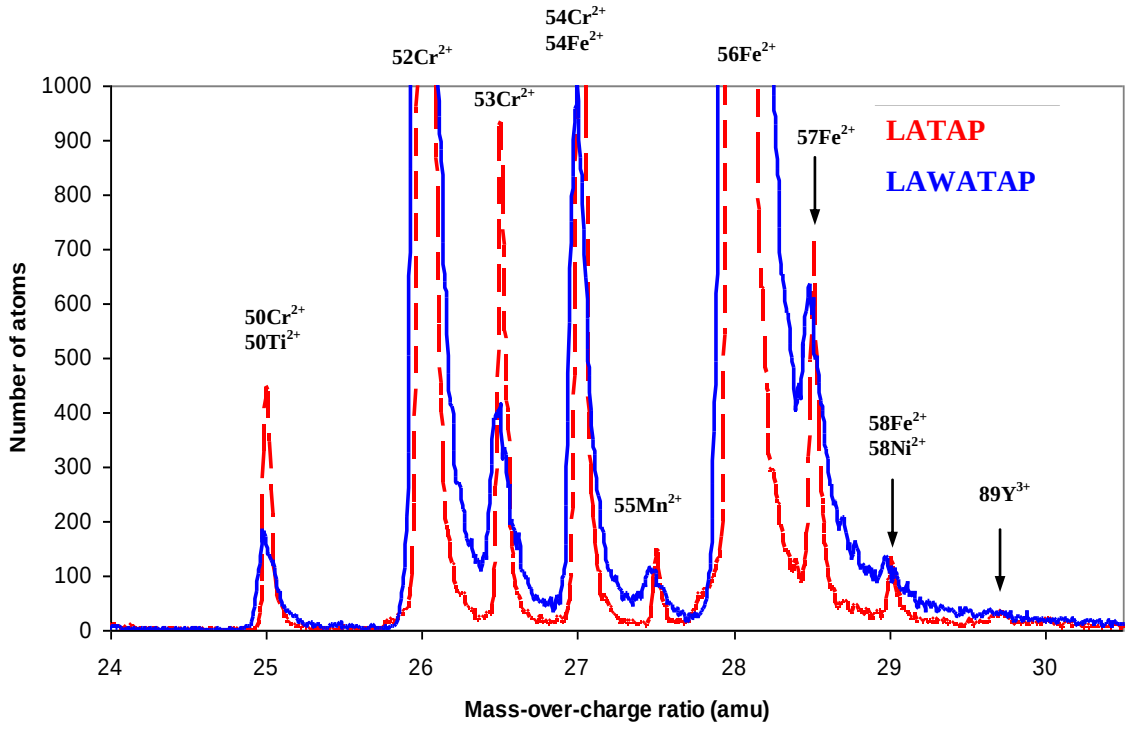

Figure 2.5. Mass spectra obtained by Laser-Assisted Tomographic Atom Probe (LATAP) (dashed red line) and Wide Angle Laser-Assisted Tomographic Atom Probe (LAWATAP) (blue line) for hot extruded ODS steel (~330 000 at). For LATAP data $\frac{M}{M_{10\%}}(56Fe^{2+}) = 215$ *and for LAWATAP data* $\frac{M}{M_{10\%}}(56Fe^{2+}) = 100$.

In *Figure 2.5*, mass resolution $\frac{M}{M_{10\%}}$ of the major iron isotope ($56Fe^{2+}$) is 215 for LATAP and 100 for LAWATAP experiments. In the case of LATAP, mass resolution is sufficient to separate most of the peaks. Only peaks of $56Fe^{2+}$ and $57Fe^{2+}$ are not separated. These conditions are sufficient to extract accurate measurements. In the case of LAWATAP, the mass resolution is not high enough and some difficulties may appear for $55Mn^{2+}$, $89Y^{3+}$, $58Fe^{2+}$, $58Ni^{2+}$ peaks for example. Accurate global compositional measurements are not possible in majority of cases for these elements since their concentrations would be underestimated.

However, LAWATAP can be used to study chemical composition of isolated nanoparticles. The mass spectrum corresponding to nanoparticles is represented on *Figure 2.6.*

Mass resolution in this case allows to indentify Y^{3+} ions at 29.6 amu and TiO^{2+} molecular ions at 31-33 amu located in the tail of the majoritary $56Fe^{2+}$ peak. As a consequence, chemical composition of these nanoparticles can be defined.

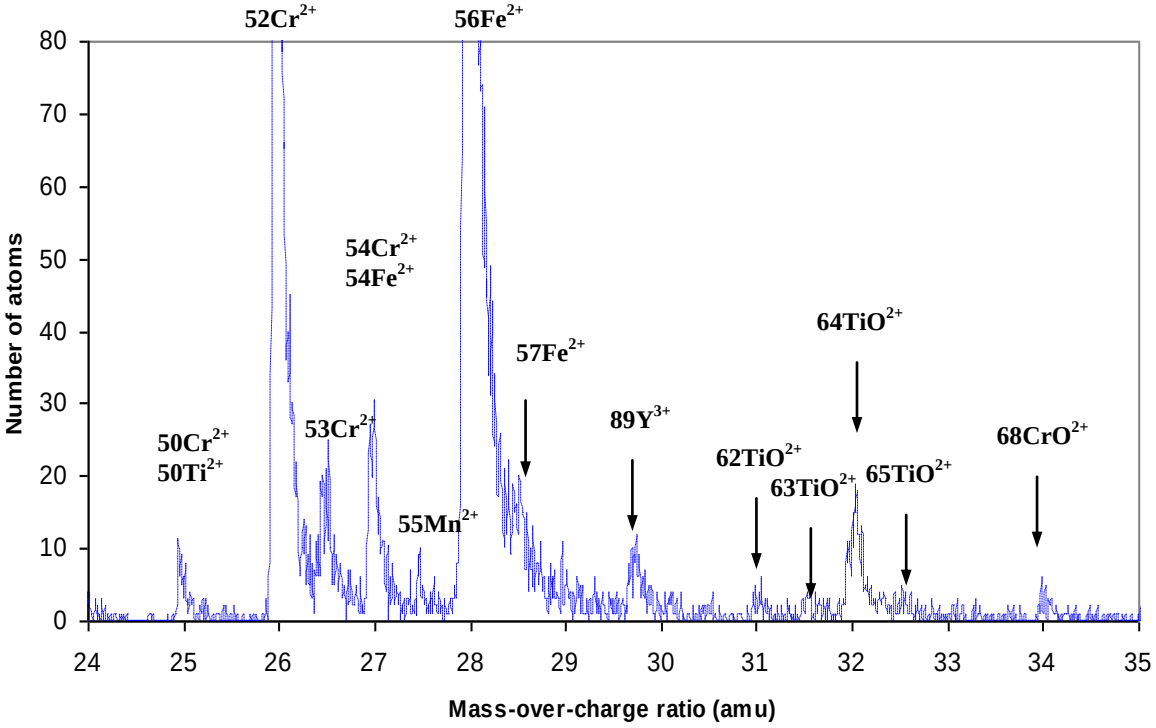

Figure 2.6. Mass spectra represented for isolated nanoparticles of hot extruded ODS steel by Wide Angle Laser-Assisted Tomographic Atom Probe (LAWATAP).

Both techniques have also been compared. The chemical composition of nanoparticles in hot extruded ODS steel was calculated with data coming from LATAP and LAWATAP mass spectra. The comparison is shown in *Figure 2.7.* As it can be seen from the graph, there is a good agreement whatever is the Atom Probe.

In this work, the combination of these two techniques was used. In order to get the most accurate composition measurements LATAP was preferably used. In order to get sufficient statistics for nanoparticles size, number density as well as chemical compositions LAWATAP was used.

Observations and different hypothesis used for the calculation of the chemical compositions in these ODS and NDS materials are now discussed in following sections.

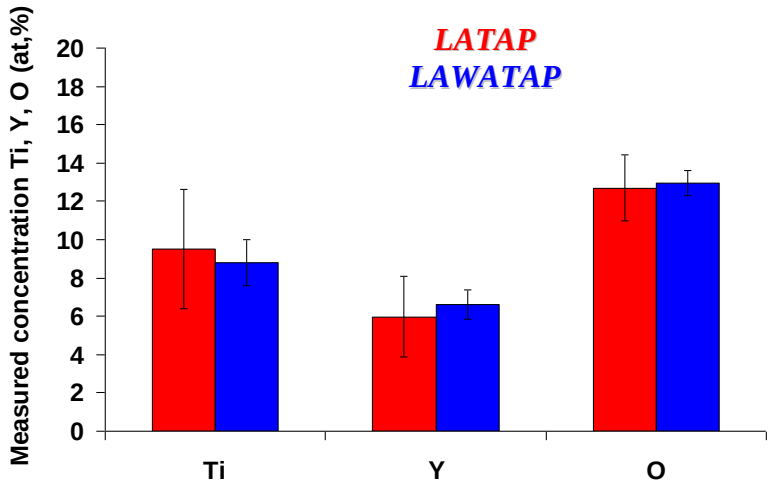

Figure 2.7. Comparison of chemical composition estimated for nanoparticles in ODS steel by Laser-Assisted Tomographic Atom Probe (LATAP) and Wide Angle Laser-Assisted Tomographic Atom Probe (LAWATAP).

II.4. Particular case of ODS and NDS materials

a) Determination of experimental parameters

In order to get reproducible and reliable results during APT analysis, it is important to set correctly experimental conditions. Temperature, Laser wavelength and pulse fraction are important parameters influencing results.

Laser wavelength. Two different Laser wavelengths were available on LATAP and LAWATAP at the beginning of this work: λ=1030 nm (infrared) and λ=515 nm (green). It is clearly established that for ferritic materials, green Laser pulses give largely better mass resolution than infrared. Thus, 515 nm wavelengths were used in all experiments.

Temperature effect. The temperature of the sample during analysis may have different consequences. First, the risk of sample breaking increases when the temperature decreases. However, by increasing the temperature, mass resolution and spatial resolution are affected and additional effect such as preferential evaporation[2] may bias the chemical composition

[2] *This effect happens when elements have different field of evaporation. If the standing voltage of the specimen is too high, elements with lower field of evaporation will preferentially evaporate during the time between the pulses. This effect can be avoided by increasing the pulse fraction (which results in a decrease of standing voltage) or decreasing the temperature (differences in evaporation fields are normally decreases with decreasing of the temperature).*

measurements. Best compromise between mass resolution and tip fracture are obtained for temperature in the range of 80K and 50K for LATAP and LAWATAP analysis, respectively.

Equivalent pulse fraction of the Laser. In the electrical mode, the pulse fraction, α, is equal to $\frac{V_p}{V_o}$, where V_p and V_o are respectively pulse and standing voltages. In Laser mode, an *equivalent pulse fraction*, giving the effect of the Laser pulse is given by:

$$\frac{V_t - V_o}{V_o} \tag{2.9}$$

where V_t and V_o are respectively electric voltages necessary to ionize surface atoms without or with pulse.

Pulse fraction is determined experimentally in the following way. At fixed value of evaporation rate, the standing voltage necessary to evaporate the sample at a given Laser energy is measured. This measurement is done for different values of the Laser energy, *E*. The dependence V_0 versus *E* is linear. The linear fit of experimental points gives an estimation of the voltage V_t (for zero Laser energy). The Laser energy applied to the tip depends on the pulse repetition rate of a Laser (that differs for LATAP and LAWATAP and is respectively 2 and 100 KHz) and size of Laser spot. An example of pulse fraction measurements (in terms of Laser power) is represented on *Figure 2.8.*

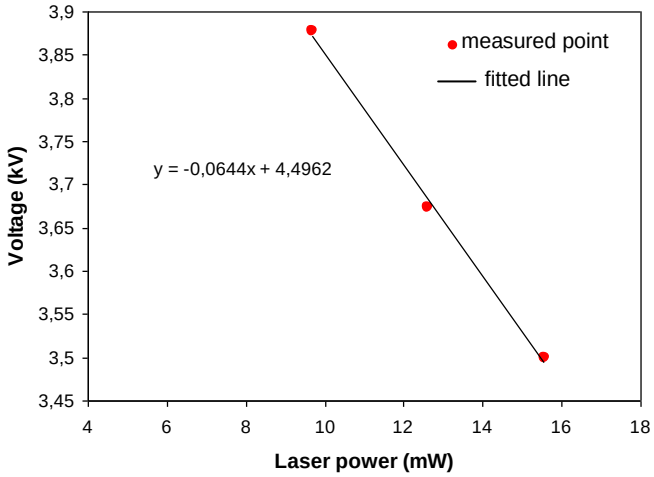

Figure 2.8. Standing voltage necessary to evaporate ions as a function of the Laser power. Red points represent experimental values of the Laser power (LAWATAP). The cross of fitted line with y axis corresponds to the voltage, V_t, that is needed to evaporate an atom without Laser pulses.

The obtained parameters V_t (cross with y axis) and k (slope), gives the Laser power P_α. for a desired pulse fraction α using formula:

$$P_\alpha = -\frac{\alpha V_0}{(\alpha+1)k} \tag{2.10}$$

The above procedure is common for LATAP and LAWATAP pulse fraction measurements.

Different values of pulse fraction 5, 15, 25 % were tested in order to determine the best experimental parameters. A constant temperature of 80K was used. Mass spectra of three analyses obtained by LATAP are shown on *Figure 2.9*. As it can be seen, a pulse fraction of 25% allows to give a high resolution mass spectrum.

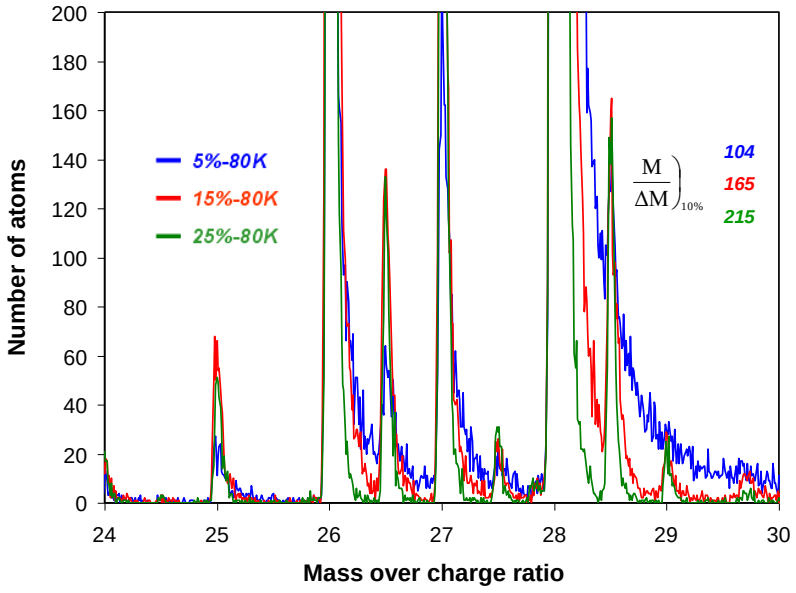

Figure 2.9. Mass spectra of three analyses performed on as-milled ODS steel by LATAP. Different conditions are used: pulse fraction of 5, 15 and 25% are tried. Temperature is fixed at 80K. Pulse fraction of 25% allows separate all the peaks.

Further, in order to exclude preferential evaporation effects, the influence of pulse fraction (15-25%) in the temperature range 80-50K on chemical compositions have been tested. The chemical compositions under these conditions are presented in *Table 2.5*. No preferential evaporation effects are observed. Reliable chemical compositions can be obtained in the temperature range T≤80K. Thus, following from different compromises pulse fraction of the Laser is set at 25% whereas the temperature in experiments ranges between 80-50 K.

Table 2.5. Influence of analyse temperature and pulse fraction on chemical compositions measured in as-milled ODS steel by LATAP. Different analyse conditions are tested: 1) 25% at 80K, 2) 15% at 80K and 25% at 50K. Balance is Fe. Standard deviations are given by 2σ. Compositions are calculated for 80 000 at.

	Cr	**W**	**Ni**	**Mn**	**Si**	**Y**	**O**	**Ti**	**C**
wt.%	**18**	**1**	**0.3**	**0.3**	**0.15**	**0.6 Y_2O_3**		**0.3**	**-**
at.%	**18.7**	**0.295**	**0.28**	**0.30**	**0.29**	**0.28**	**0.43**	**0.3**	**-**
25%- 80K	18.4	0.09	0.16	0.35	0.88	0.25	0.70	0.38	0.03
2σ	0.3	0.03	0.03	0.05	0.07	0.04	0.07	0.05	0.01
15%-80K	18.8	0.25	0.18	0.31	1.0	0.35	0.54	0.28	0.05
2σ	0.3	0.04	0.03	0.04	0.1	0.04	0.06	0.04	0.02
25%- 50K	19.8	0.14	0.20	0.34	0.81	0.28	0.43	0.24	0.04
2σ	0.3	0.03	0.03	0.05	0.07	0.04	0.05	0.04	0.02

Parameters for 3D reconstruction. Parameters for the 3D reconstruction are also very important in order to obtain the best visualization of the analysed volume and estimate the best sizes and morphologies of the nanoparticles.

For the 3D reconstruction of the analysed volume, it is necessary to know the magnification, G, given by the expression (2.6). As the specimen is field evaporated, the radius R normally increases thus decreasing the magnification. The specimen radius is deduced from the evaporation voltage *V* owing to the relation:

$$R = \frac{V}{E\beta} \tag{2.11}$$

where *E* is the field of evaporation at the apex of the specimen and β is a constant related to the shape of the specimen. So, in order to calculate the magnification, two parameters have to be known: *m* and $E\beta$. These values can easily be determined with the field ion microscopy or with results obtained near a well-known crystallographic pole ((h,k,l) known).

In this latter case, if one is able to index the crystallographic pole (and, hence, the Miller indexes of planes), then the real interatomic spacing between two planes is known. As an example, the (110) pole is observed in MA NDS steel (bcc, white area on the picture) on *Figure 2.10* (a).

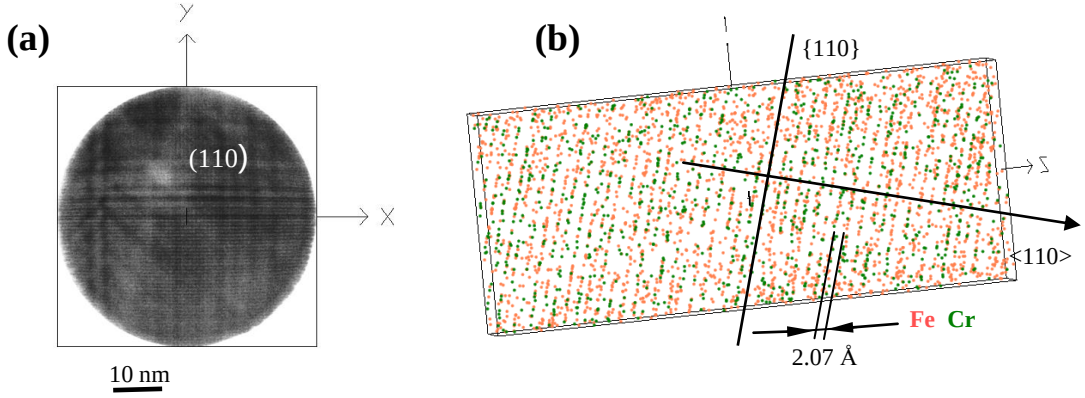

Figure 2.10. Reconstruction 3D of MA NDS steel, with reconstruction parameters Eβ=14.5 and μ+1=1.45. (a) Top view showing the pole (110) and (b) crystallographic planes resolved near pole. Interplane distance in bcc Fe is ~2.02Å that is in good corresponds to the value, obtained by TAP (2.07Å).

The reticular spacing in this case is 2.02 Å. Adjusting the distance between planes to the real one by playing with the reconstruction parameters, allows to find the appropriate set of parameters, *Figure 2.10* (b). This method was used in the current work. The set of reconstruction parameters for these materials using LATAP and LAWATAP is shown in *Table 2.6.*

Table 2.6. Reconstruction parameters used in the work for ODS and NDS materials.

Parameter	***ODS and NDS***	
	LATAP	*LAWATAP*
m+1	1.45	1.45
Eβ	14.5-16.5	14.5-16.5
Detection efficiency,%	0.58	0.60

b) Isotope overlaps

Isotope overlaps occur when two or more isotopes with the same mass-over-charge ratio are detected. In this case it becomes impossible to distinguish them and special attention must be paid in order to avoid incorrect compositional measurements.

The peaks that are identified on mass spectra as well as isotope overlaps in ODS and NDS materials are reported in *Table 2.7*. The numbers are deduced from the natural abundance when overlapping between peaks occurs.

Table 2.7. List of isotopes and molecular ions corresponding to peaks observed in ODS and NDS materials. Natural abundances are also shown. Overlapping peaks of different elements are defined by the same colour.

ODS			NDS		
Elements	**Mass (amu)**	**Natural abundance (%)**	**Elements**	**Mass (amu)**	**Natural abundance(%)**
C^+/C^{2+}	6/12	100	C^{2+}/C^+	6/12	100
Si^{2+}	14/14.5/15.0	92.2/4.67/3.1	Al^{3+}/Al^{2+}	9/13.5	100
O^+ or O_2^{2+}	16	100	Si^{2+}	**14**/14.5/15.0	92.2/4.67/3.1
Ti^{2+}	23/23.5/24/24.5/**25**	8.0/7.3/73.8/5.5/5.4	O^+ or O_2^{2+}	**16**	100
Cr^{2+}	**25**/26/26.5/**27**	4.35/83.8/9.5/2.36	Ti^{3+}	15.33/15.67/**16.0**/16.33/16.67	8.0/7.3/73.8/5.5/5.4
Fe^{2+}	**27**/28/28.5/**29**	5.8/91.72/2.2/0.28	AlO^{2+}	21.5	100
Mn^{2+}	27.5	100	Ti^{2+}	23/23.5/24/24.5/**25**	8.0/7.3/73.8/5.5/5.4
Ni^{2+}	**29**/30/30.5/**31**/**32**	68.1/26.2/1.14/3.63/0.93	Cr^{2+}	**25**/26/26.5/**27**	4.35/83.8/9.5/2.36
TiO^{2+}	**31**/31.5/**32**/32.5/**33**	8.0/7.3/73.8/5.5/5.4	Fe^{2+}	**27**/28/28.5/**29**	5.8/91.72/2.2/0.28
O_2^+	**32**	100	Ni^{2+}	**29**/**30**/**30.5**/**31**/**32**	68.1/26.2/1.14/3.63/0.93
CrO^{2+}	**33**/34/34.5/35	4.35/83.8/9.5/2.36	TiN	**30**/**30.5**/**31**/**31.5**/**32**	8.0/7.3/73.8/5.5/5.4
Y^{3+}, Y^{2+}	**29.7**/**44.5**	100	TiO^{2+}	**31**/**31.5**/**32**/32.5/**33**	8.0/7.3/73.8/5.5/5.4
YO^{2+}/YO^+	**52.5**/**105**	100	O_2^+	**32**	100
Cr^+	**50**/52/53/**54**	4.35/83.8/9.5/2.36	CrN^{2+}	**32**/**33**/33.5/34	4.35/83.8/9.5/2.36
Fe^+	**54**/56/57/**58**	5.8/91.72/2.2/0.28	Cr^+	**50**/52/53/**54**	4.35/83.8/9.5/2.36
Mn^+/Mn^{2+}	27.5/55	100	Fe^+	**54**/56/57/**58**	5.8/91.72/2.2/0.28
Ni^+	**58**/**60**/61/**62**/**64**	68.1/26.2/1.14/3.63/0.93	Mn^+/Mn^{2+}	27.5/55	100
TiO^+	**62**/63/**64**/65/66	8.0/7.3/73.8/5.5/5.4	Ni^+	**58**/**60**/**61**/**62**/**64**	68.1/26.2/1.14/3.63/0.93
W^{3+}	**60**/60.7/61/61.3/**62**	0.14/26.4/14.4/30.6/28.4	TiN^+	**60**/**61**/**62**/**63**/**64**	8.0/7.3/73.8/5.5/5.4
CrO^+	66/68/69/**70**	4.35/83.8/9.5/2.36	TiO^+	**62**/**63**/**64**/65/**66**	8.0/7.3/73.8/5.5/5.4
FeO^+	**70**/72/73/74	5.8/91.72/2.2/0.28	CrN^+	**64**/**66**/67/68	4.35/83.8/9.5/2.36
TiO^{2+}	78/79/80/81/82	8.0/7.3/73.8/5.5/5.4	W^{3+}	**60**/60.7/61/61.3/**62**	0.14/26.4/14.4/30.6/28.4
W^{2+}	90/91/91.5/92/93	0.14/26.4/14.4/30.6/28.4	W^{2+}	90/91/91.5/92/93	0.14/26.4/14.4/30.6/28.4
WO^{2+}	98/99/99.5/100/101	0.14/26.4/14.4/30.6/28.4	WN^{2+}	97/97.5/98.5/99/100	0.14/26.4/14.4/30.6/28.4

Example: the simple case of isotopes overlap, common for both ODS and NDS materials are discussed. The same mass-over charge ratio 27 amu appears for $\mathbf{54Cr^{2+}}$ and $\mathbf{54\ Fe^{2+}}$ (see *Figure 2.11*). In that case, the total number of ions at 27 amu ($\mathbf{X_{total}}$), is equal to the number of **Cr** from the last isotope ($\mathbf{X_{Cr}^4}$) and atoms from the first isotope of **Fe** ($\mathbf{X_{Fe}^1}$). $\mathbf{X_{Cr}^4}$ can be estimated from other $\mathbf{Cr^{2+}}$ isotopes at 25, 26, 26.5 amu, which represents respectively 4.35, 83.8 and 9.5 % of chromium:

$$\mathbf{X_{Cr}^4}=(\mathbf{X_{Cr}^1}+\mathbf{X_{Cr}^2}+\mathbf{X_{Cr}^3})\times 2.4/(4.35+83.8+9.5),$$

where $\mathbf{X_{Cr}^1}$, $\mathbf{X_{Cr}^2}$,$\mathbf{X_{Cr}^3}$ is the number of detected ions located at 25.26 and 26.5 amu. Then the **Cr** isotopes at 27 amu can be calculated as:

$$\mathbf{X_{Cr}^4}=(\mathbf{X_{total}}-\mathbf{X_{Cr}^4}).$$

Similar deconvolution procedure is systematically used for $\mathbf{50Ti^{2+}/50Cr^{2+}}$ and $\mathbf{58Fe^{2+}/58Ni^{2+}}$ isotope overlaps.

Particular cases of isotopes overlaps in ODS and NDS materials are further detailed. In ODS materials, the deconvolution of peaks located just after the iron peak between 30 and 34 amu is difficult. A mass spectrum obtained in an ODS steel is represented in *Figure 2.11*.

As it can be seen, the difficulties are connected with the overlapping of peaks which are important for the compositions, such as: $\mathbf{62TiO^{2+}/62Ni^{2+}}$ at 31, $\mathbf{64TiO^{2+}/16O^{2+}/64Ni^{2+}}$ at 32 amu. An uncertainty may be introduced in such case concerning minor elements such as Ti, O important in this study.

In this work, the chemical composition of nanoparticles is calculated following these assumptions and hypothesis:

(a) the oxygen ions can be present at the 16 amu in the form of $\mathbf{O^+}$ or $\mathbf{O_2^+}$. However, since there is no possibility to separate contributions of each ($\mathbf{O^+}$ or $\mathbf{O_2^+}$), the compositions have been calculated following two assumptions: i) all ions at 16 correspond to $\mathbf{O^+}$ or ii) to $\mathbf{O_2^+}$. However, the found difference between both assumptions does not exceed standard deviation. So, finally only one value ($\mathbf{O^+}$) will be presented.

b) no $\mathbf{Ni^{2+}}$ atoms located at 30, 30.5, 31, 32 amu, since **Ni** is not associated with nanoparticles;

c) to separate overlaps at 32 amu, for as-milled powder, two hypotheses are used: i) only $\mathbf{O_2^+}$ atoms are located at 32 amu without any $\mathbf{TiO^{2+}}$ atoms, ii) only $\mathbf{TiO^{2+}}$ is located at 32

amu without $\mathbf{O_2^+}$. So, chemical compositions of nanoparticles will be presented owing to both assumptions (showing minimum and maximum level of **Ti**). For annealed and hot extruded powder chemical composition of particles will be calculated taking into account $\mathbf{TiO^{2+}}$ molecular ions located at 32 amu (presence of $\mathbf{TiO^{2+}}$ molecular ions at 31, 31.5, 32, 32.5, 33 is clearly seen on mass spectrum, see on *Figure 2.11*.

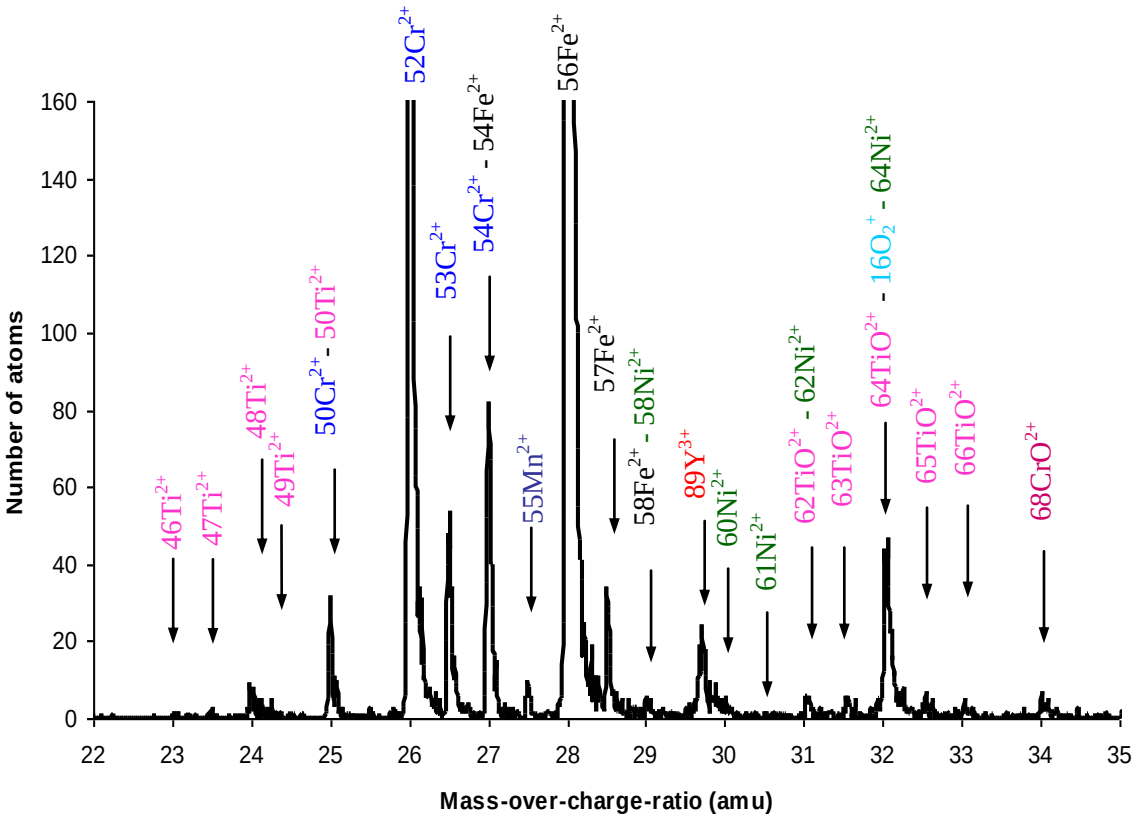

Figure 2.11. Mass spectrum of a hot extruded ODS steel obtained with LATAP.

As MA NDS steel are concerned, a mass spectrum of MA NDS steel annealed at 850°C/1h is shown on *Figure 2.12* (a, b).

As it can be seen on *Figure 2.12* (a, b), there is an overlap between $\mathbf{62TiN^{2+}/62TiO^{2+}/62Ni^{2}}$ at 31, $\mathbf{63TiN^{2+}/63TiO^{2+}}$ at 31.5, $\mathbf{64TiN^{2+}/64TiO^{2+}/64Ni^{2+}}$ at 32 amu (*Figure 2.12* (b)). In this case, chemical composition of particles is calculated following these assumptions:

(a) Only **N** atoms are located at 14 amu (no **Si** atoms);

(b) No **Ni** atoms are located at 30, 30.5, 31, 32 amu. **Ni** is not associated to nanoparticles.

(c) $\mathbf{TiN^{2+}}$ and $\mathbf{TiO^{2+}}$ overlap between 30 and 33 amu is deconvoluted in accordance to Ti natural abundances. The total number of ions at 31 amu ($\mathbf{X_{total}}$), is equal to the number of **TiN** ($\mathbf{X_{TiN}^3}$) and the first isotope of **TiO** ($\mathbf{X_{Si}^1}$). $\mathbf{X_{TiN}^3}$ can be estimated from two others $\mathbf{TiN^{2+}}$ isotopes at 30 and 30.5 amu which represent respectively 8.0 and 7.3 %:

$$\mathbf{X_{TiN}^3} = (\mathbf{X_{TiN}^1}+\mathbf{X_{TiN}^2}) \times 79.3/(8.0+7.3),$$

where $\mathbf{X_{TiN}^1}$ and $\mathbf{X_{TiN}^2}$ is a number of detected ions located at 30 and 30.5 amu. Then the **TiO** isotopes located at 31 amu can be calculated as:

$$X_{TiO}^1 = X_{total} - X_{TiN}^3.$$

Similarly, the **TiN** and **TiO** overlaps at 31.5 and 32 amu can be separated.

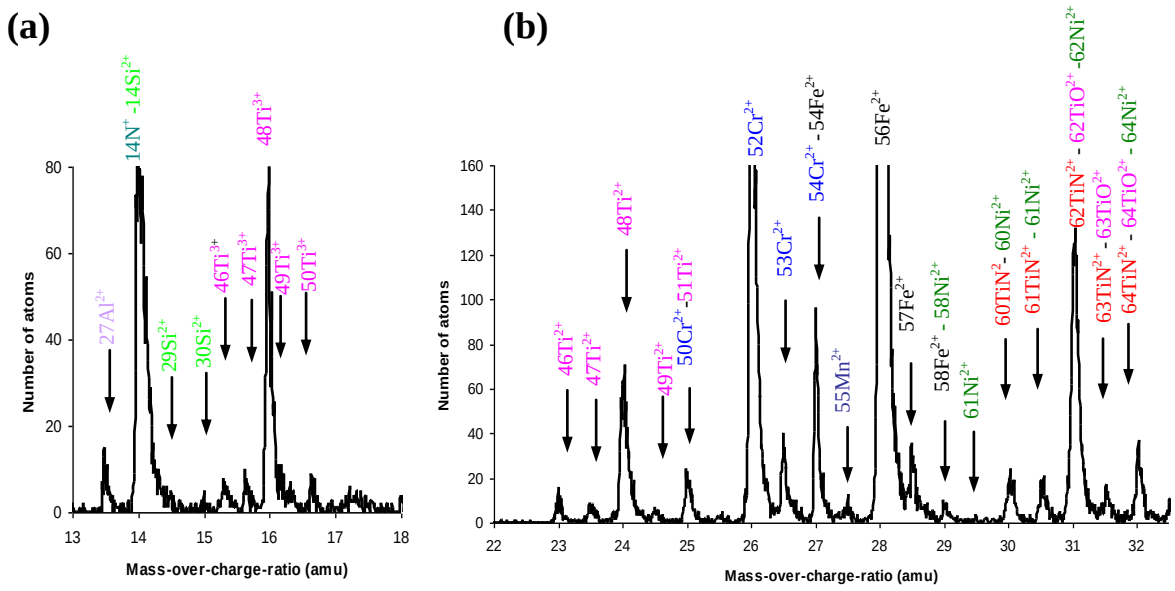

Figure 2.12. Mass spectrum of MA NDS steel after annealing at 850°C/1h. Intervals of mass spectrum (a) from 13 to 18 and (b) from 22 to 32 amu are represented.

Concerning as-nitrided NDS steel, a mass spectrum of a powder after annealing at 700°C/1h is shown on *Figure 2.13*.

The calculation of chemical composition of nanoparticles follows these assumptions:

(a) Only **N** atoms are located at 14 amu (no **Si** atoms);

(b) No $\mathbf{Ni^{2+}}$ atoms are located at 30, 30.5, 31, 32 amu.

(c) Deconvolution of overlap between **$64CrN^{2+}$** and **$64TiN^{2+}$** is conducted due to natural abundances of **Cr** and **Ti** in agreement with the procedure discussed above (for **$64TiO^{2+}$/$64TiN^{2+}$** or **$54Cr^{2+}$/54 Fe^{2+}).**

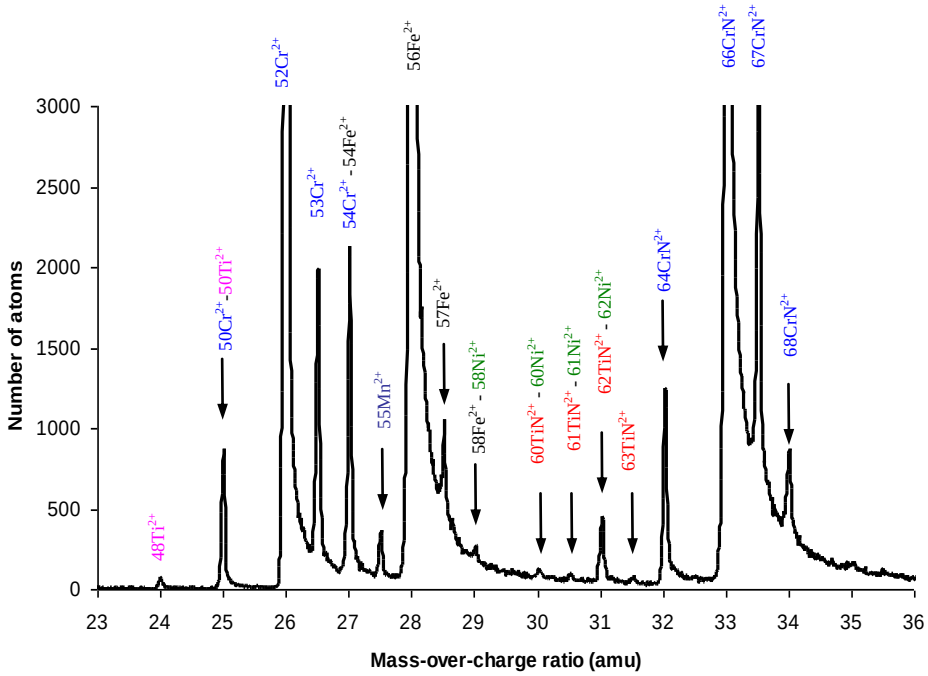

Figure 2.13. Mass spectrum of nitrided NDS steel after annealing at 700°C/1h by LAWATAP. Interval from 23 to 36 amu is shown.

c) Methods for APT data treatment

The data treatment procedure, in general, is similar for all materials and consists of several steps:

(a) Measurement of the global chemical composition of the analysed volume;

(b) Investigation of solute distributions in analysed volumes. If clusters are not visible (simply by eyes), then statistical tests are used. The assumption of a random distribution of solute atoms (Cr, Ni, Mn, W, Si, etc.) is tested using the statistical test described in Appendix 3-a. Two results are possible:

(i) Statistical test confirms that the distribution of solute atoms in the analysed volume is random. In this case the analysed volume is considered as a part of matrix.

(ii) Statistical test indicates that the distribution of given solute atoms (Y, O in ODS as an example) is not random. In this case, a cluster detection algorithm (see Appendix 3) is used.

If nanoparticles are detected, they are subjected to further characterization in terms of size, chemical composition and number density.

Size of nanoparticles is given by a Guinier radius [16]. Guinier radius represent the actual size of a feature and defined by the formula $R_g = \sqrt{5/3} l_g$, where l_g is radius of gyration, i.e. radius of hypothetical body that have all his mass concentrated at a single distance from its centre of mass ($\bar{x}, \bar{y}, \bar{z}$). In three dimensions, this hypothetical body is a spherical shell. In APT experiment it is usually determined using the formula:

$$l_g = \sqrt{\frac{\sum_{i=1}^{n} (x_i - \bar{x})^2 + (y_i - \bar{y})^2 + (z_i - \bar{z})^2}{n}} \qquad (2.12)$$

where x_i, y_i, z_i are the spatial coordinated of each atoms.

The Guinier radius is derived from 3DAP software for each individual nanoparticle after "iso position" and "erosion" according to the procedure detailed in Appendix 3-b,c.

Chemical composition of nanoparticles is calculated from small sampling boxes placed well inside the nanoparticle (so called core measurements). The size of the box is adjusted taking into account the geometry of each individual particle. Such measurements allow to avoid the introduction of matrix atoms close to the nanoparticle/matrix interface.

Number density of nanoparticles in an analysed volume N_v, is estimated from the total number of atoms N_t, number of nanoparticles N_p, taking into account the detection efficiency of the detector, ζ, and the average atomic volume of the material, Ω, i.e. $N_v = Np\zeta / \Omega N_t$. Uncertainty $\Delta\rho$ of number density N_v is estimated as:

$$\Delta\rho = \frac{N_v}{\sqrt{N_p}} \qquad (2.13)$$

The chemical composition of the matrix is also estimated. It is derived from the total number of atoms in the analysed volume minus the total number of atoms contained in nanoparticles (if no other features are present in the volume (dislocation, grain boundary, etc…).

One of the most common diagrams for data analysis is the construction of a composition profile. The first step in order to create a composition profile is to select a volume within the three-dimensional data set from which the composition profile is desired. The shape of this selected volume may either be a cylinder or a rectangular parallelepiped depending on the type of the feature to analyze. The size and the position of this selected volume are then carefully adjusted by the user until the desired volume is enclosed. Once the parallelepiped or cylinder is correctly positioned, it is divided into small slices perpendicular to its long axe. The size of the slices may be defined in terms of distance. The concentration of specie in each slice is then measured as following:

$$c^i = \frac{N_s^i}{N_t} \tag{2.14}$$

where N^i_s is the number of ions of solute *i*, and N_t is the total number of ions detected in the sampling volume. The uncertainty (ΔC) on measured concentration depends on the size of the sample (quantity of collected atoms (N)) and on the concentration of chemical specie. It is given by:

$$\Delta c = 2\sigma \text{ where } \sigma = \sqrt{\frac{c_i(1-c_i)}{N_t}} \tag{2.15}$$

d) Local magnification effect

Differences in fields of evaporation between the matrix and a second phase are usually observed in decomposed materials. The difference of fields of evaporation between two phases provokes a local variation of the sample radius. This latter variation may modify the ions trajectories during the very first moments of their flight from the specimen surface to the detector [33,34]. It leads to trajectory aberrations, especially near interfaces and results in the so called *local magnification effects*. Trajectory aberrations and their influences on chemical compositions is the subject of numerous studies [34–36]. However, this artefact is still not fully understood or more precisely not so well reproduced or simulated.

The local magnification effect is illustrated in *Figure 2.14* (a - d*)*. It represents the result of the simulations of ion impacts on the detector [33]. For a particle with a higher field of evaporation (compared to the field of evaporation of the matrix), ions from the particle fall outside the particle and a depleted zone forms close to the interface (*Figure 2.14* (c)*)*. In

contrast, for a particle with a lower field of evaporation, the image of the nanoparticle is compressed and ions coming from the surrounding matrix fall into the particle (*Figure 2.14* (d)). The local magnification can consequently modify the morphology, dimensions of precipitates and introduce bias in the measured chemical composition. These effects have been observed in the studied ODS and NDS materials and are discussed below.

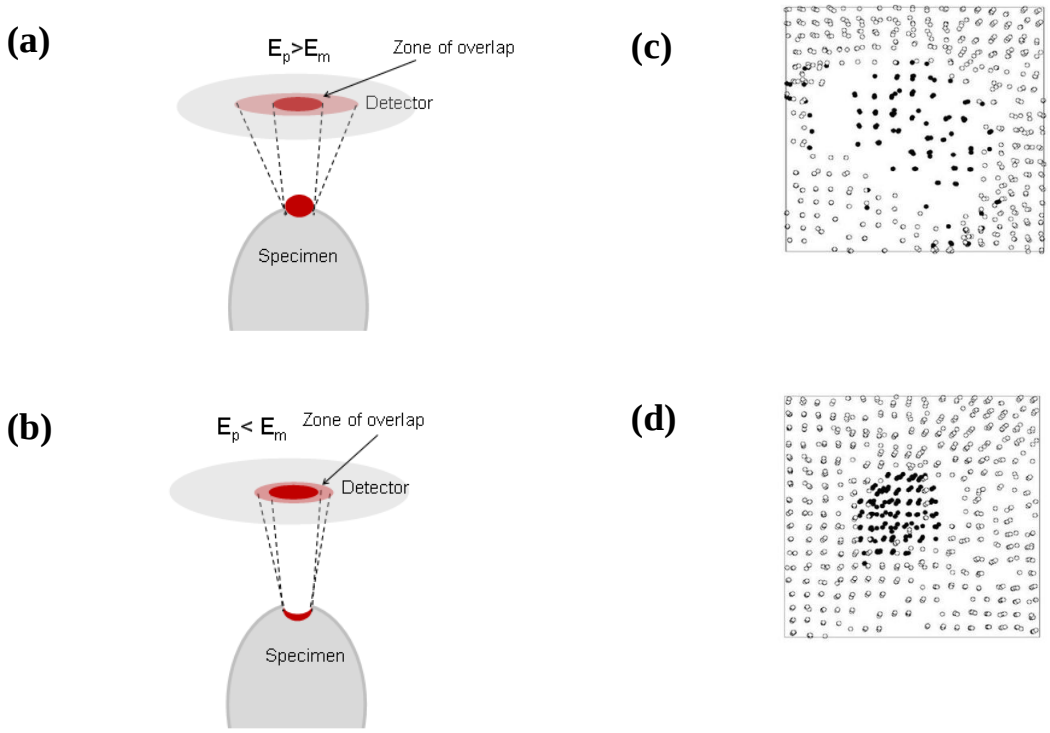

Figure 2.14. Schematic representation of local magnification effects in case of evaporation of ***(a)*** *high-field precipitate;* ***(b)*** *low-field precipitate; Simulation of impact images for binary AB alloy containing a spherical β particle (eight interatomic distances). β phase is pure in B and its environment is pure in A. These two simulated images are cross sections of reconstructed precipitates with* ***(c)*** $E_{prec} > E_{matrix}$ *and* ***(d)*** $E_{prec} < E_{matrix}$*: B atoms are in black and A are in gray. The images are reproduced from [36,37].*

An indication of the presence of the local magnification effect during an analysis is the detection of a local change in the *atomic density* (i.e. number of atoms per unit of a volume) in the nanoparticles compared to matrix. Nanofeatures in ODS steels generally exhibit a lower field of evaporation than the surrounding matrix ($\varepsilon_p < \varepsilon_m$) [36]. In the present work, an atomic density inside the nanoclusters is higher (up to 2.5-3 times) than in the surrounding matrix. Up to now the contribution of matrix atoms to the nanoclusters is not accurately determined. A PhD work is in progress on this topic.

The situation is completely different in the case of nitrides observed in NDS steel. According to variation of atomic density, Ti-N-rich particles seem to have a higher field of

evaporation than the surrounding matrix ($\varepsilon_p > \varepsilon_m$). Indeed, the atomic density inside the particles is lower than in the surrounding matrix (up to 5 times!).

In order to evaluate the contributions of local magnification effects on the compositions in the case of "low and high field" particles, modelling was used. A model developed by F. Vurpillot [38] and M. Gruber [39], allows to simulate the field evaporation of atoms from a tip apex and to calculate ion trajectories. The general principle of the model is described in Appendix 4. The results are treated with the same tools as in APT. Calculations adapted to the case of ODS and NDS were performed by Constantinos Hatzoglou in University of Rouen (Master and PhD work). The parameters chosen for calculations are:

- Nanoparticles are spherical with different sizes, R_{core}= 0.5 to 2.0 nm (*Figure 2.15*);
- Two kinds of nanoparticles are simulated with core-shell structure and without.

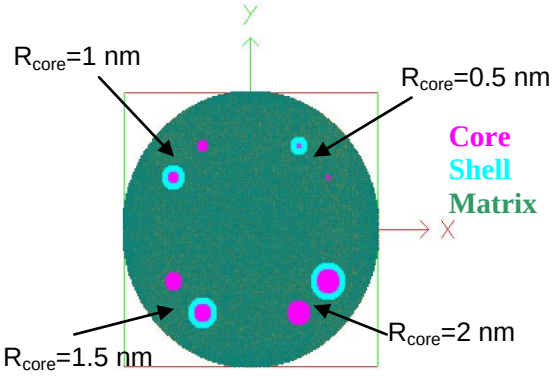

Figure 2.15. Initial configuration of nanoparticles before simulated field evaporation is shown. R_{core} varies from 0.5 to 2.0 nm. Particles with and without core shell structure is shown.

- The shell around the core consists of pure Cr atoms (100%);
- The thickness of a shell is assumed to be similar for all sizes of nanoparticles (0.5 nm);
- The chemical species are determined by their evaporation fields. However, the values of evaporation fields of oxygen, nitrogen as well as molecular ions (TiO, YO, TiN etc.) is not known. In addition, the values of evaporation fields of Fe, Ti, Y and Cr [16] are known only in the case of a pure Fe matrix. Since it is not possible to have accurate value of field of evaporation, the relative evaporation fields are estimated in comparison to Fe (*Table 2.8*). Finally, it is considered that in first approximation, the simulated nanoparticles consist of pure A element, dispersed in Fe-18Cr matrix, supposed pure Fe here.

Table 2.8. Field of evaporation of Fe, Cr, Y and Ti [16].

Elements	**Fe**	**Cr**	**Ti**	**Y**
Evaporation field: E_i ($V.nm^{-1}$)	33	29	26	23.5
Relative evaporation field: E_i	1	0.8	0.8	0.7

- Two types of nanoparticles have been modelled: with lower evaporation field $\varepsilon_A = \frac{E_A}{E_{Fe}} = 0.7$ and with higher evaporation field $\varepsilon_A = \frac{E_A}{E_{Fe}} = 1.4$, where E_A and E_{Fe} are field of evaporation of Fe and element A respectively. The values ε_A (0.7 or 1.4) correspond to nanoparticles in ODS or nanoparticles in NDS with atomic density inside nanoparticles close to the experimentally observed ones (*Figure 2.16*).

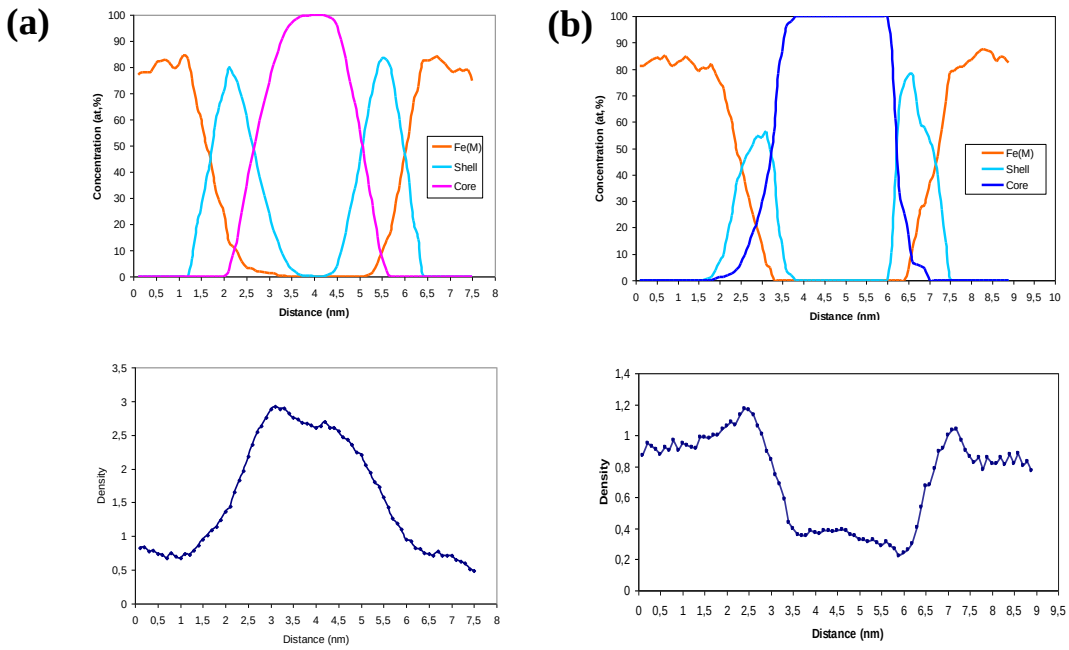

Figure 2.16. Profiles through simulated nanopartilces with core-shell structure R_{core}=2.0 nm, showing concentration (above) and relative atomic density (below) for (a) low field with $\varepsilon_A = 0.7$ and (b) high field with $\varepsilon_A = 1.4$ particles. Profiles build in evaporation direction with sampling box 1.0×1.0×1.0 nm^3.

The 3D representation of nanoparticles before field evaporation and after are shown in *Figure 2.17* (a-d) in the case of $\varepsilon_A = 0.7$.

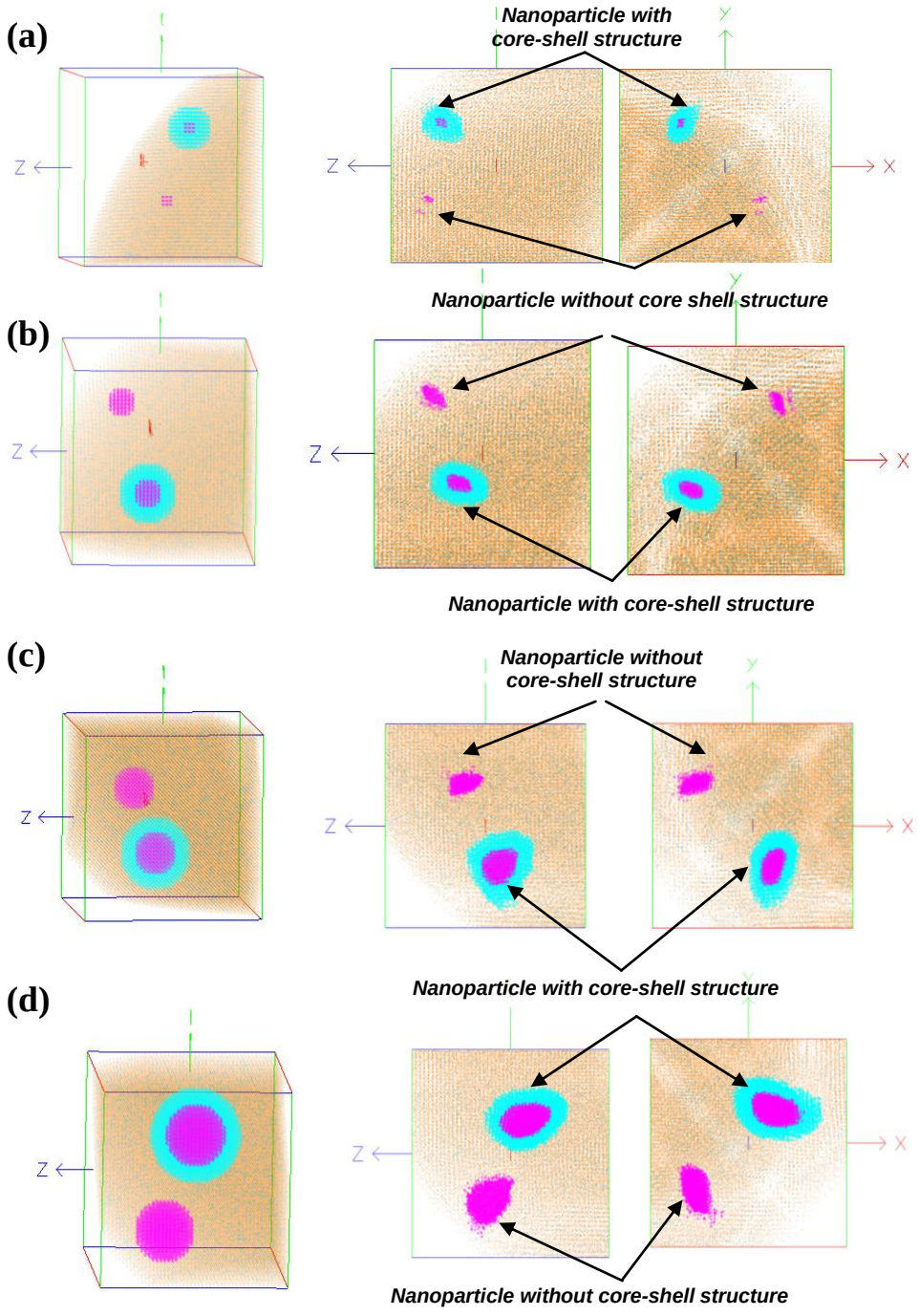

Figure 2.17. Modelling of APT analyse for low-field ($\varepsilon_A = 0.7$) nanoparticles with R_{core} (a) 0.5 nm, (b) 1.0 nm, (c) 1.5 nm and (d) 2.0 nm. Particles with and without core shell structure is shown. Cores of both are composed of pure element A. Initial configuration (left) and reconstruction after analyse (right).

Before simulated field evaporation all particles have perfectly spherical shape. However, after field evaporation nanoparticles (whatever the size is and with or without core shell structure) are deformed. Their lateral dimension is slightly compressed as it can be expected for low evaporation field particles. The chemical composition in the core of the particles is given in *Table 2.9.*

Table 2.9. Core chemical composition of simulated low field ($\varepsilon_A = 0.7$) nanoparticles as a function of their size. Particles with core shell structure and without are treated. Composition is calculated inside of core in the box (0.7×0.7×0.7 nm^3). All compositions are in at.%.

R_{core}	**0.5 nm**	**1 nm**	**1.5 nm**	**2.0 nm**
Composition without core shell				
A	35.0±12.3	86.0±5.3	91.8±3.7	94.0±3.4
Fe	53.3±12.9	11.0±4.8	6.8±3.4	5.0±3.0
Cr	11.7±8.3	2.9±2.6	1.3±1.6	1.0±1.4
Composition with core shell				
A	22.2±7.5	87.8±5.2	100	100
Fe	-	-	-	-
Cr	-	-	-	-
Shell	77.8±7.5	12.2±5.2	-	-

It is seen from the table, in the case of a low field nanoparticles with R_{core}=0.5 nm, that a significant amount of Fe and Cr is measured when the core shell structure is absent. When the radius increases up to 2 nm, their amount measured in the core decreases, however still some quantity is measured.

In the case of a core-shell structure, significant amount of shell atoms is measured in the core of relatively small nanoparticle, R_{core}=0.5 nm. Smaller amount of shell atoms is measured when R_{core}=1.0 and no shell atoms is measured for nanoparticle with R_{core}=1.5 and 2.0 nm.

In all cases, for low field nanoparticles (except nanoparticles with core-shell structure with R_{core}=1.5 and 2.0 nm) the core measurements may be biased.

3D representations for as high-field nanoparticles before and after field evaporation are shown in *Figure 2.18* (a-d). As an example, nanoparticles with R_{core}=0.5 nm, with core shell and without, are deformed after evaporation (*Figure 2.18* (a)). Their lateral dimensions are

slightly elongated as it can be expected in high evaporation field particles. In particles with core shell structure, atoms belonging to shell and core are completely mixed. No more core shell structure can be detected after simulated evaporation. Particle without core shell structure are also completely mixed with the matrix.

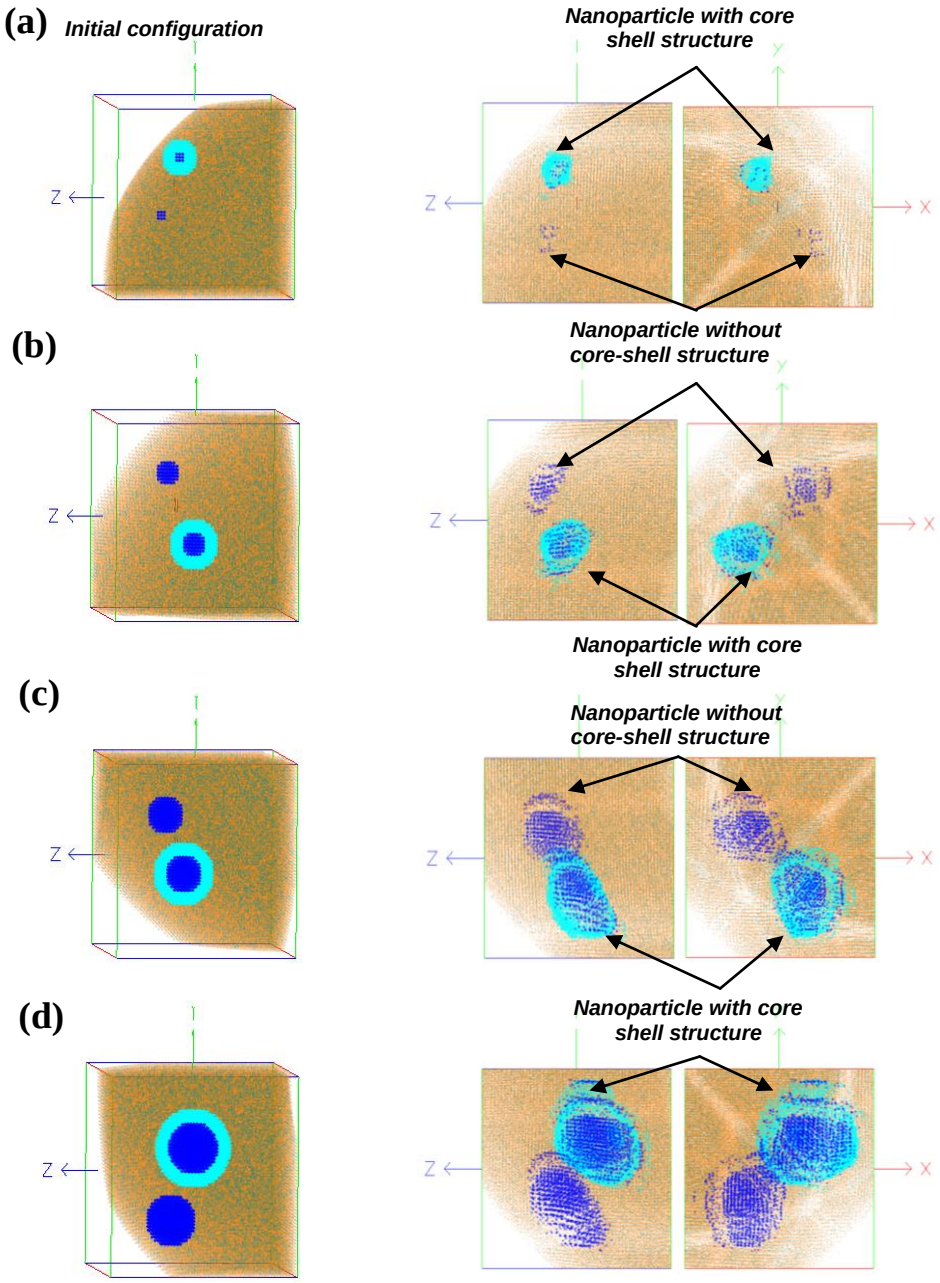

Figure 2.18. Modelling of APT analyse on high-filed ($\varepsilon_A = 1.4$) nanoparticles with R_{core} (a) 0.5 nm, (b) 1.0 nm, (c) 1.5 nm and (d) 2.0 nm dispersed. Particles with and without core shell structure is shown. Cores of both are composed of pure element A. Initial configuration (left) and reconstruction after analyse (right).

A field evaporation process of slightly bigger spherical nanoclusters with R_{core}=1.0, 1.5 and 2 nm has been modelled (*Figure 2.18* (b-d)). It is clearly seen that after field evaporation the shape is no more spherical. Both types of nanoparticles are deformed like in previous case. In the case of core-shell structure, atoms belonging to shell and core are partially mixed, but core shell structure is still seen. The chemical composition in the core as a function of the particle size is presented in *Table 2.10.*

Table 2.10. Core chemical composition of simulated high field nanoparticles ($\varepsilon_A = 1.4$) as a function of their size. Particles with core shell structure and without are treated. Composition is calculated inside of core in the box ($0.7 \times 0.7 \times 0.7$ nm^3). All compositions are in at.%.

R_{core}	0.5 nm	1 nm	1.5 nm	2.0 nm
Composition without core shell				
A	50.0±29.0	100	100	100
Fe	50.0±29.0	-	-	-
Cr	-	-	-	-
Composition with core shell				
A	42.8±37.4	100	100	100
Fe	-	-	-	-
Cr	-	-	-	-
Shell	57.0±37.4	-	-	-

In the case of small nanoparticles (R_{core}=0.5 nm), with core shell structure or without, a significant amount of Fe and shell atoms is measured. Thus, composition measurements are not correct in these cases. The chemical composition measured in the larger nanoparticles (R_{core}=1, 1.5 and 2 nm respectively), consists of 100 at.% of A in both cases (with or without core-shell structure).

As a conclusion, well-known artefacts appear during the field evaporation of low-field and high-field particles in APT analyses. These effects affect the reconstruction of the nanoparticles leading to slight change of their dimensions. In addition, according to the modelling, the core compositions measured in low field nanoparticles seems to be modified in almost all studied cases (except nanoparticles with core-shell structure, having R_{core}=1.5 and 2.0 nm). The situation is completely different in the case of high field nanoparticles with R_{core}> 1nm, where concentration measurement seems unbiased (true composition).

III. Modelling of precipitation kinetics with MatCalc and Thermocalc softwares

III.1. Theory of precipitation kinetics

Precipitation occurs when the content of alloying elements, at a given temperature, exceeds the solubility limit. In that case, a second phase is formed. In the case of low supersaturation, the precipitation process can be divided into three main stages: nucleation, growth and coarsening. The chronological sequence of the evolution of precipitate characteristics (mean radius, volume fraction, and interparticle distance) during these three stages is schematically represented in *Figure 2.19*.

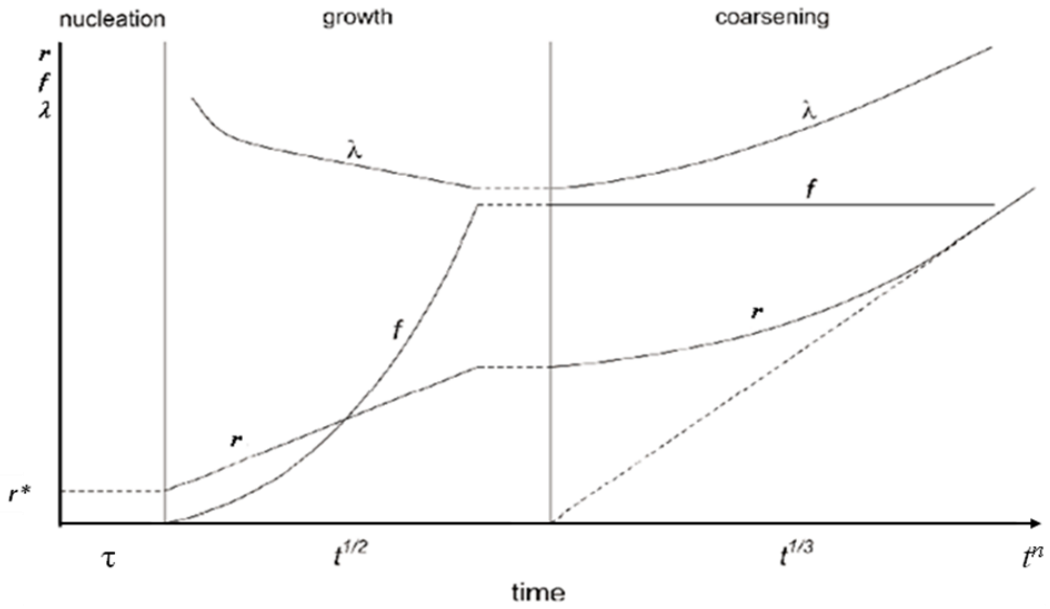

Figure 2.19. The chronological sequence of the evolution of precipitate volume fraction f, diameter d and inter-particle spacing λ for isothermal annealing during the nucleation, growth and coarsening stage after [40] .

Nucleation. During the nucleation stage, stable nuclei, bigger than a critical size *r**, are formed. The time needed to form these critical nuclei is called incubation time, *τ*.

Growth. Nuclei which have reached the critical size are thermodynamically stable and can continue to grow. The nuclei grow by attaching atoms diffusing towards its surface and therefore depleting the matrix until the equilibrium volume fraction is reached. During the growth stage, both volume fraction and precipitate size increase with time. The growth of

precipitates is mainly controlled either by the rate at which atoms are brought to the interface by diffusion, or the rate at which they cross the interface. This process usually follows a $t^{1/2}$ dependency.

Coarsening. Coarsening of precipitates, also called Ostwald ripening, is the last stage of precipitation. It is very important for the long term creep strength. When the coarsening sets in, no new particles nucleate, but the largest ones grow at the expense of the smaller ones at a nearly constant volume fraction, *f*. This process results in fewer but larger particles. Ostwald ripening is driven by the total decrease of the interfacial energy, as few coarse particles have a smaller surface area compared to a corresponding amount (in volume) of small particles. The asymptotic time dependency of precipitate size is usually proportional to $t^{1/3}$.

III.2. Modelling of precipitation kinetics with MatCalc

A theoretical approach has been recently developed by Kozeschnik and his group for simulation of precipitation kinetics in multi-components alloys systems [41–43]. The model of evolution of precipitates structure derived by means of application of the thermodynamic extremum principle [44]. In combination of Classical Nucleation Theory (CNT), the evolution of the radii and chemical composition of individual precipitates in multi-component system can be obtained. This model is implemented in the software MatCalc [41,43]. In addition, it provides access to thermodynamic and kinetic data, i.e. multi-component chemical potentials and mobilities based on CALPHAD type databases [137]. The numerical model used in MatCalc is briefly reviewed here.

The model for simulation of precipitation kinetics that are implemented in software MatCAlc consists of two major parts, i.e. module for precipitates nucleation and a module for the evolution of radius and chemical composition of precipitates.

a) Precipitate nucleation

Precipitate nucleation in solid-state systems can be described by classical nucleation theory (CNT). In accordance to this theory, the transient nucl eation rate J is given as:

$$J = Z\beta^* N_0 \exp\left(-\frac{\Delta G^*}{kT}\right)\exp\left(-\frac{\tau}{t}\right) = J_s \exp(-\frac{\tau}{t}) \qquad (2.16)$$

where J_s is steady state nucleation rate, N_0 represents the total number of potential nucleation sites, Z is the Zeldovich factor, β^* is the atomic attachment rate, k is the

Boltzmann constant, T is the temperature, τ is the incubation time and t is time. G^* is the critical nucleation energy.

For application to multi-component systems, the mathematical formulation has been recently extended [41]. *Table 2.11*, summarizes the multi-component expressions for nucleation.

Table 2.11. Expressions for multi-component precipitate nucleation after [45].

Quantity	description	value	comment
Z (dimensionless)	Zeldovich factor	$\left[\frac{-1}{2\pi kT}\frac{\partial^2 \Delta G}{\partial n^2}\Big\vert_{m^*}\right]^{1/2}$	n, number of atoms in the nucleus
β^* (s^{-1})	Atomic attachment rate	$\frac{4\pi r^{*2}}{a^4 \Omega}\left[\sum_{i=1}^{n}\frac{(c_{ki}-c_{oi})^2}{c_{oi}D_{oi}}\right]^{-1}$	r^*, radius of critical nucleus a, atomic distance Ω, molar volume, c_{ki}, c_{0i}, element concentrations in precipitate/matrix interface, D_{0i}, diffusivities in the matrix
ΔG^* (J)	Critical nucleation energy	$\frac{16\pi}{3}\frac{\gamma^3}{F^2}$	F– effective driving force, γ – interfacial energy
r^* (m)	Critical radius	$\frac{2\gamma_k}{F}$	
τ (s)	Incubation time	$\frac{1}{2\beta^* Z^2}$	

b) Evolution of radius and composition of precipitates

Once a precipitate is nucleated, its further growth is evaluated from the evolution equations for multi-component precipitation derived in ref [41]. These expressions have been summarized and discussed recently by Kozeschnik [42]. The total Gibbs free energy of a system with m spherical precipitates and n components is expressed as:

$$G = \sum_{i=1}^{n} N_{0i}\mu_{0i} + \sum_{k=1}^{m}\frac{4\pi r_k^3}{3}\left(\lambda_k + \sum_{i=1}^{n} c_{ki}\mu_{ki}\right) + \sum_{k=1}^{m} 4\pi r_k^2 \gamma_k \qquad (2.17)$$

where, N_{0i} and μ_{oi} are number of moles and chemical potential of component i in the matrix; μ_{ki} and c_{ki} are the chemical potential and the concentration of component i in the precipitate k; r_k is the radius of precipitate k, γ_k is the interfacial energy contributions. The first term from the left, is the sum of the chemical potentials of all atoms in the matrix. The middle term is

the precipitate volume related part of the Gibbs energy. The left term takes the interface between precipitate and matrix into account.

In thermodynamic equilibrium, the Gibbs free energy is a minimum. Since real systems during heat treatments are in a highly non-equilibrated state, driving forces exist for an evolution of the precipitate microstructure such that G is minimized. Three dissipative processes have been considered in MatCalc software:

Q_1: Migration of interfaces with mobility, M_k,

Q_2: Diffusion of all atoms inside the precipitates;

Q_3: Diffusion of all atoms in the matrix

with

$$Q_1 = \sum_{k=1}^{m} \frac{4\pi r_k^2}{M_k} \tag{2.18}$$

$$Q_2 = \sum_{k=1}^{m} \sum_{i=1}^{n} \frac{4\pi RT r_k^5 c_{ki}^2}{45 c_{ki} D_{ki}} \tag{2.19}$$

$$Q_3 = \sum_{k=1}^{m} \sum_{i=1}^{n} \frac{4\pi RT r_k^3 (\rho_k (c_{ki} - c_{0i}) + r_k c_{ki} / 3)^2}{c_{0i} D_{0i}} \tag{2.20}$$

The Gibbs free energy dissipation rate G, is given by sum of these three terms

$-G = Q_1 + Q_2 + Q_3$. With the total Gibbs free energy and the corresponding dissipation terms, the thermodynamic extremum principle [44] is applied and a linear system of rate equations for the change of radius and chemical composition of each individual precipitate is obtained. Further details about the model and the numerical treatment of the evolution equations are given in [41–43].

c) Evaluation of interfacial energies

The interfacial energy γ and effective driving force F are dominant quantities in the simulation of nucleation and growth of precipitates. These quantities appear during evaluation of critical nucleation energy ΔG^* (see *Table 2.11*). In contrast to F, which can be estimated from thermodynamic databases, γ is not accessible by direct experimental measurement and is often considered as fitting parameter. In MatCalc, γ is determined from the "nearest-

neighbour broken-bond model" [46]. Based on assumption that pairwise bonding between neighbouring atoms, γ is related to the solution enthalpy ΔE_{sol} of precipitate with:

$$\gamma = \frac{n_s z_s}{N z_L} \times \Delta \mathrm{E_{sol}} \tag{2.21}$$

where z_L is the number of nearest neighbours per atom, z_s the number of broken bonds across the interface per atom. n_s denotes the number of atoms per m^2 interface and N is the Avogadro constant. E_{sol} is estimated from thermodynamic databases with:

$$\Delta E_{sol} = \frac{\partial H}{\partial f_P} \tag{2.22}$$

where H denotes the molar system enthalpy and f_p is the precipitate phase fraction.

III.3. Used parameters for MatCalc calculations

Most quantities in eq. (2.16) are either thermodynamic quantities or kinetic quantities related to the diffusivity of the atoms. Some of them can be obtained from independent thermodynamic and kinetic databases. In contrast, the number of potential nucleation sites, N_0, strongly depends on the microstructure of the material and the type of heterogeneous nucleation sites. This feature requires consideration of the material microstructure, i.e. grain and subgrain size and dislocation density. These parameters are rarely known and present case is not an exception.

Matcalc simulations were performed at CEA, Saclay under guidance of ***Stéphanie HOLLNER (Ingénieur post-doc CEA Saclay).*** To model the precipitation kinetics with MatCalc the following parameters have been used.

Chemical composition that was used for modeling is Fe-18Cr-0.14N-0.5Ti (wt.%), that is a simple case of MA NDS steel. Real MA NDS steel was produced by mechanical alloying of Fe-18Cr-0.14N matrix with TiH_2. In accordance to that, the simulations are based on the hypotheses that all nitrogen and titanium introduced during mechanical alloying are in solid solution. Nucleation sites are dislocations and grain boundaries. Since the dislocation density in mechanically alloyed system is not known, the dislocation density is chosen 10^{14} (m^{-2}) like in [40]. Since the real grain sizes are not known, the approximate values have been derived from SEM pictures during APT sample preparation. Following grain sizes were tried: 600°C/1h -80 nm, 700°C/1h- 100 nm, 850°C/1h – 900 nm, 1000°C/1h – 1000 nm. One step

thermal cycles that correspond to annealing during 1 hour at 600, 700, 850 or 1000°C were simulated. Script used for simulation of TiN precipitation is presented in Appendix 5. Results of calculations will be discussed in Chapter IV.

III.4. ThermoCalc software

Thermocalc has been used for phase diagram calculation of the studied systems [47]. Thermocalc is based on the application of equilibrium thermodynamics. Basically, there are two approaches that can be followed: one based on the minimization of Gibbs energy, the other being a derivative equivalent based on the solution of sets of non-linear equations. The main non-linear equations involved are the "equilibrium relationships": the relationships for balanced chemical reactions between the end-members of phases that are in equilibrium with each other:

$$0 = \Delta G_o + \mathrm{R}T \ln K \qquad (2.24)$$

In the equation (2.24), ΔG_o is the Gibbs energy of the reaction between the pure end-members in the same structure as the phases in which they occur, K is the equilibrium constant, in terms of the activities of the end-members in their phases, T is temperature, and R is the gas constant.

Thermocalc calculations were performed by ***Dany Lemarchand and Nicolas Masquelier in GPM, Rouen.*** Compositions used for simulation are presented in *Table 2.12*. Calculations were done for two temperatures: 600 and 1000°C.

For MA NDS steel the composition used in simulation is Fe-19Cr-0.57Ti-0.54N-0.3W-0.3Mn-0.3Si (at.%). The results of simulations are reported in *Table 2.12*.

Table 2.12. ThermoCalc calculations for MA NDS powder. Two temperatures 600 and 1000°C is used.

Phases	**TiN (FCC)**	**Laves-phase (Fe, Cr, W)**	**σ phase (Fe, Cr)**	**Ferrite (BCC)**
600°C	1%	0.3%	2.6%	96.1%
1000°C	1%	-	-	99%

Fcc phase that corresponds to TiN precipitates is expected after annealing at both temperatures (mass fraction is 1.0%). In addition significant amount of σ phase (mass fraction 2.6%) as well as Laves-phase (mass fraction 0.3%) are also expected at low temperature

(600°C/1h). TiN particles and ferrite, as predicted by ThermoCalc, can only be achieved at higher annealing temperature.

For nitrided NDS steel the composition used in ThermoCalc simulation is Fe-17.3Cr-0.26Ti-0.20W-0.6Si-N (at.%). In one case, the content of nitrogen used for simulation is 1 at.%. In a second case, the content of nitrogen was ~11.0 at.%. This content corresponds to measured chemical composition of as-nitrided powder after APT experiment. The results of simulations are reported in *Table 2.13* and *Table 2.14*.

Table 2.13. ThermoCalc calculations for nitrided NDS powder. Two temperatures 600 and 1000°C is used. Nitrogen content is 1 at.%.

Phases	**TiN (FCC)**	**Cr_2N (HCP)**	**Ferrite (BCC)**	**Austenite (FCC)**
600°C	0.5%	2%	97%	-
1000°C	0.6%	-	25%	74%

When small (~1 at.%) of nitrogen are introduced during nitriding treatment, the predicted microstructure of the material are composed of TiN (FCC) and Cr_2N (HCP) phases dispersed in ferrite at low temperature. After annealing at higher temperature, slightly higher mass fraction of TiN is expected. However, the matrix in this case is a combination of ferrite and austenite.

In the case of a large nominal amount of nitrogen in the Fe-18Cr matrix, a large content of CrN and Cr_2N is predicted by ThermoCalc after annealing at lower temperature. The predicted microstructure of the material is fully austenitic with CrN precipitates after annealing at higher temperature.

Table 2.14. ThermoCalc calculations for nitrided NDS powder. Two temperatures 600 and 1000°C is used. Nitrogen content is ~11.0 at.%.

Phases	**CrN (FCC)**	**Cr_2N (HCP)**	**Ferrite (BCC)**	**Austenite(FCC)**
600°C	14%	13%	73%	-
1000°C	22%	-	-	78%

IV. Conclusions of the Chapter 2.

Two types of materials are investigated in the work. The first one is a Fe-based Oxide Dispersion Strengthened steel that is currently under intense investigation worldwide (reference solution for application such as cladding elements in GEN IV reactors). Based on ODS positive experiences, a second type of materials, Nitride Dispersion Strengthened steels, have been elaborated in the framework of the ANR AXTREM program. Two different elaboration routes have been used: mechanical alloying and plasma nitriding.

To get a better understanding of the basic processes at the origin of nanoparticle formation and evolution in both ODS and NDS materials, characterization of microstructure at very fine scale after different steps of elaboration process is needed. The main experimental tool that will be used here is the Atom Probe Tomography. Two different types of Atom Probes will be used in this work and have been presented. As for any techniques, some artefacts may affect the results. They have been presented here and their modelling gives some information on the nature and the quantification of the bias.

In addition, thermodynamic and kinetic computer modelling is also used in parallel to APT to follow the precipitation kinetics. A comparison of experimental and modelling will thus be possible.

In following chapter, experimental results devoted to characterisation of ODS materials are described. NDS will be described in the fourth chapter.

V. Bibliography of the Chapter 2

[1] D. Blavette, A. Bostel, J.M. Sarrau, B. Deconihout, A. Menand, Nature 363 (1993) 432–435.

[2] D. Blavette, B. Deconihout, A. Bostel, J.M. Sarrau, M. Bouet, A. Menand, Rev. Sci. Instrum. 64 (1993) 2911.

[3] M.K. Miller, R.G. Forbes, Materials Characterization 60 (2009) 461–469.

[4] A. Menand, E. Cadel, C. Pareige, D. Blavette, Ultramicroscopy 78 (1999) 63–72.

[5] L. Toualbi, M. Ratti, G. André, F. Onimus, Y. de Carlan, Journal of Nuclear Materials 417 (2011) 225–228.

[6] L. Toualbi-Bénévise, Mécanismes Mis En Jeu Lors De La Mécanosynthèse Des ODS : Apport De La SAT Et De La Diffraction De Rayons X Et De Neutrons. Présentation. Materiaux Conférence, Nant, 18-22 October, 2010.

[7] M. Ratti, Développement De Nouvelles Nuances D'acier Ferritiques/martensitiques Pour Le Gainage D'élément Combustible Des Réacteurs à Neutrons Rapides Au Sodium. Thèse, Institut Polytechnique de Grenoble, 2009.

[8] M.H. Mathon, Bilan Des Caractérisation Des Alliages NDS Par Diffusion De Neutrons Aux Petits Angles. Présentation. ANR AXTREM Réunion, Saclay, 27 Septembre, 2011.

[9] C. Cayron, A. Montani, D. Venet, Y. Carlan, Journal of Nuclear Materials 399 (2010) 219–224.

[10] Y. de Carlan, J.-L. Bechade, P. Dubuisson, J.-L. Seran, P. Billot, A. Bougault, T. Cozzika, S. Doriot, D. Hamon, J. Henry, M. Ratti, N. Lochet, D. Nunes, P. Olier, T. Leblond, M.H. Mathon, Journal of Nuclear Materials 386-388 (2009) 430–432.

[11] F. Delabrouille, Rapport H-T27-2010-00646-FR. Caractérisation Au Microscope Electronique En Transmission D'alliages NDS Et ODS (ANR AXTREM), 2010.

[12] M. Ratti, Y. De Carlan, Method for Manufacturing Reinforced Alloy Through Scattering of Nitride Nanoparticles, Patent WO/2011/061435, 2011.

[13] L. Poirier, B. Stauder, Traitement Thermochimique Assisté Plasma En Vue Du Renforcement Par Dispersion De Nitrures: Cas De Poudre Et De Produit Massif. Présentation. ANR AXTREM Réunion, Saclay, 27 Septembre, 2011.

[14] Quatriéme réunion d'avancement du projet ANR aXtrem, Rouen. Rapport, 2009.

[15] M.K. Miller, A. Cerezo, M.G. Hetherington, G.D.W. Smith, Atom Probe Field Ion Microscopy, Clarendon Press, 1996.

[16] M. K. Miller, Atom-probe Tomography: Analysis at the Atomic Level, Kluwer Academic/Plenum, New York, 2000.

[17] G. Da Costa, F. Vurpillot, A. Bostel, M. Bouet, B. Deconihout, Rev. Sci. Instrum. 76 (2005) 013304.

[18] B. Gault, M.P. Moody, F. De Geuser, A. La Fontaine, L.T. Stephenson, D. Haley, S.P. Ringer, Microsc. Microanal. 16 (2010) 99–110.

[19] B. Gault, F. Vurpillot, A. Vella, M. Gilbert, A. Menand, D. Blavette, B. Deconihout, Rev. Sci. Instrum. 77 (2006) 043705.

[20] G.Kellogg, T.Tsong, J. Appl. Phys. 51 (1980) 59.

[21] T. Tsong, S. McLane, T.Kinkus, Rev. Sci.Instr 53 (1982).

[22] H.F. Liu, T.T.Song, Rev.sci.Instr. 55 (1974).

[23] B. Deconihout, F. Vurpillot, B. Gault, G. Da Costa, M. Bouet, A. Bostel, D. Blavette, A. Hideur, G. Martel, M. Brunel, Surf. Interface Anal. 39 (2007) 278–282.

[24] B. Gault, A. Menand, F. de Geuser, B. Deconihout, R. Danoix, Appl. Phys. Lett. 88 (2006) 114101.

[25] M. Gilbert, F. Vurpillot, A. Vella, H. Bernas, B. Deconihout, Ultramicroscopy 107 (2007) 767–772.

[26] B.Gault, Physique De L'évaporation Par Effet De Champ Assistée Par Impulsions Laser Ultracourtes - Application à La Sonde Atomique. Thèse. Université De Rouen, 2006.

[27] H. Liu, T. Tsong, Rev. Sci. Instrum. 55 (1984).

[28] A. Cerezo, G.D.W. Smith, P.H. Clifton, Appl. Phys. Lett. 88 (2006) 154103.

[29] B. Gault, A. Vella, F. Vurpillot, A. Menand, D. Blavette, B. Deconihout, Ultramicroscopy 107 (2007) 713–719.

[30] A. Vella, B. Deconihout, L. Marrucci, E. Santamato, Phys. Rev. Lett. 99 (2007) 046103.

[31] J. Houard, A. Vella, F. Vurpillot, B. Deconihout, Phys. Rev. B 81 (2010) 125411.

[32] F. Vurpillot, J. Houard, A. Vella, B. Deconihout, J. Phys. D: Appl. Phys. 42 (2009) 125502.

[33] F. Vurpillot, A. Bostel, D. Blavette, Appl. Phys. Lett. 76 (2000) 3127.

[34] M.K. Miller, M.G. Hetherington, Surface Science 246 (1991) 442–449.

[35] A. Morley, G. Sha, S. Hirosawa, A. Cerezo, G.D.W. Smith, Ultramicroscopy 109 (2009) 535–540.

[36] D. Blavette, F. Vurpillot, P. Pareige, A. Menand, Ultramicroscopy 89 (2001) 145–153.

[37] E.A. Marquis, J.M. Hyde, Materials Science and Engineering: R: Reports 69 (2010) 37–62.

[38] F. Vurpillot. Thèse, Université de Rouen, 2001.

[39] M. Gruber, Thèse. Université De Rouen. In Progress.

[40] I. Holzer, Modelling and Simulation of Strengthening in Complex Martensitic 9-12% Cr Steel and a Binary Fe-Cu Alloy, Graz University of Technology, 2010.

[41] J. Svoboda, F.D. Fischer, P. Fratzl, E. Kozeschnik, Materials Science and Engineering A 385 (2004) 166–174.

[42] E. Kozeschnik, J. Svoboda, P. Fratzl, F.D. Fischer, Materials Science and Engineering A 385 (2004) 157–165.

[43] E. Kozeschnik, J. Svoboda, F.D. Fischer, Calphad 28 (2004) 379–382.

[44] L. Onsager, Phys. Rev. 37 (1931) 405.

[45] E. Kozeschnik, I. Holzer, B. Sonderegger, Journal of Phase Equilibria and Diffusion 28 (2007) 64–71.

[46] B. Sonderegger, E. Kozeschnik, Metallurgical and Materials Transactions A 40 (2009) 499–510.

[47] ThermoCalc Software. User's guide.Stockholm, Sweden, 1995-2008, (1995).

Table of content

Chapter 3. Oxide Dispersion Strengthened Steels 90

I. ODS model alloy 91

I.1. Investigation of as-milled state 91

a) Microstructure 91
b) Evaporation artifacts 94
c) Chemical composition of Y-Ti-O-rich and Fe-rich phases 99

I.2. Discussion 103

I.3. Partial conclusions 107

II. ODS industrial steel 108

II.1. Global chemical composition 108

II.2. Nanoparticles study 110

a) Distribution, number density and size 110
b) Chemical composition 112
c) Interfacial structure of nanoparticles 115

II.3. Discussion 117

a) Comparison between APT, SANS and TEM results 117
b) Composition of nanoparticles 121
c) Formation mechanism of nanoparticles in ODS steel 125

II.4. Partial conclusions 127

III. Bibliography of Chapter 3 128

Chapter 3. Oxide Dispersion Strengthened Steels

As it was shown in Chapter 1, elaboration of ODS steels usually includes a mechanical alloying step. During this process Y_2O_3 dispersoids are introduced into steel matrix. It is widely accepted that during this process Y_2O_3 dissolved and nucleation of nano-oxides occurs during following annealing treatments [1, 2]. Despite on the fact that this schematic scenario is often used, it is not so clear whether and how far these single Y_2O_3 crystals get crushed during MA process. In this context, one of the objectives of the present work is to contribute to the study of the dissolution mechanism occurring during elaboration of ODS steels by mechanical alloying. For that purpose, ODS model alloy with a high content of yttria (10 wt.%) is studied. In addition to APT, this material also has been characterized by X-ray and neutron diffraction in Laboratoire Léon Brillouin (CEA/CNRS) [3–6].

In addition to this model alloy, an industrial ferritic ODS steel elaborated by CEA [7] is also studied. This material is studied in as-milled state, after annealing at 850°C during 1 hour and in hot extruded state. As already mentioned, in the framework of ANR program, this ODS steel has been characterized by TEM and SANS [6]. Thus a comparison between all techniques will be possible.

I. ODS model alloy

I.1. Investigation of as-milled state

ODS model alloy has been prepared by ball milling in two steps: firstly FeCrW pre-alloy powder has been mechanically alloyed with 10 wt.% of TiH_2 (48 h) and secondly 10 wt.% of Y_2O_3 powder has been added by MA (48 h) to FeCrW-10Ti alloy. Three analyses were performed on three different powder grains. In all experiments the analyses are conducted at 80K. The information about experiments is reported in *Table 3.1*. The observed microstructure is detailed below.

Table 3.1. Experiments performed for ODS model alloy by APT.

APT	***Number of analyses***	***Number of analyzed atoms***
LATAP	1	240 000 at
LATAP	1	230 000 at
LAWATAP	1	5.10^6

a) Microstructure

3D reconstruction of ODS model alloy is represented on *Figure 3.1* (a-b). The figure reveals that two phases are present. Concentration profiles of Fe, Cr, Ti, Y, O elements are shown on *Figure 3.1* (c). As it can be seen, one phase corresponds to a Fe+Cr rich phase. W, Si, Mn and C are also associated. The second phase corresponds to a Y+O rich phase with in a less extent Ti enrichment. Fe and Cr are clearly depleted. This phase will be further defined as the Y-Ti-O-rich phase.

Owing to the 3D reconstruction, a geometrical characteristic of these phases (Fe-Cr-rich and Y-Ti-O-rich phases) could be their thicknesses (λ): $\lambda_{Y\text{-}Ti\text{-}O}$ for Y-Ti-O phase and λ_{Fe+Cr} for the Fe+Cr-rich phase. The concentration profile (*Figure 3.2*) gives $2 < \lambda_{Y\text{-}Ti\text{-}O} < 5.5$ nm and $8 < \lambda_{Fe} < 10$ nm. The thickness of the stacking sequence range between: $9 < \lambda < 12$ nm.

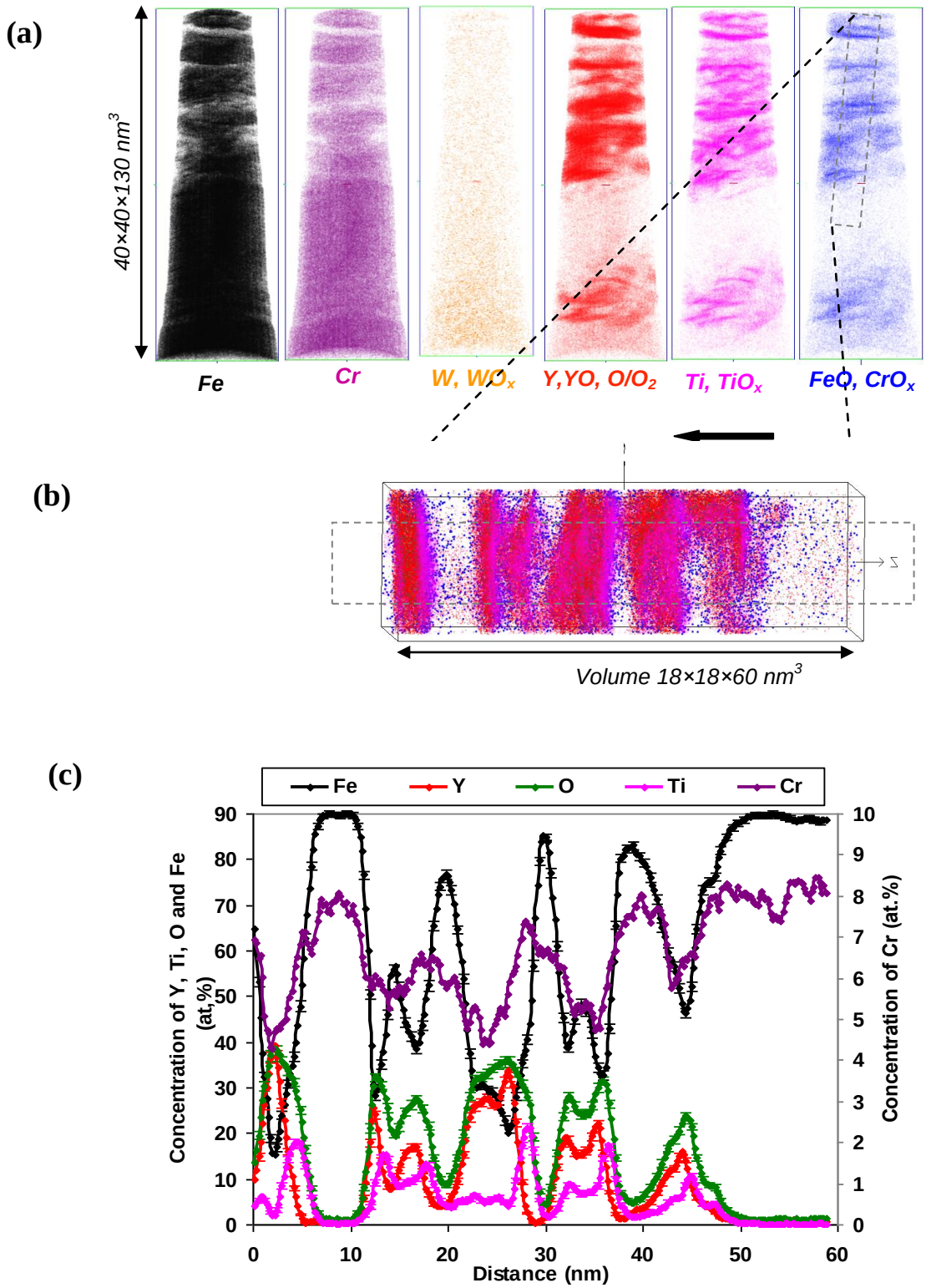

Figure 3.1. 3D reconstruction of ODS model alloy analysed by LAWATAP. (a) Only main elements (Fe, Cr, W, Ti, Y, O) and molecular ions (YO, TiO_x, FeO, CrO_x, WO_x) are shown. Analyzed volume is 40×40×130 nm^3. (b) Zoom on selected volume in (a). ***Y, YO, Ti, TiO, O/O$_2$, FeO, CrO$_x$*** *elements are shown. (c) Concentration profiles generated from a volume in (b). Concentrations of main elements:* ***Fe, Cr, Y, Ti*** *and* ***O*** *are shown in at.%. Profile is obtained from a 12×12×60 nm^3 volume with steps of 0.2 nm.*

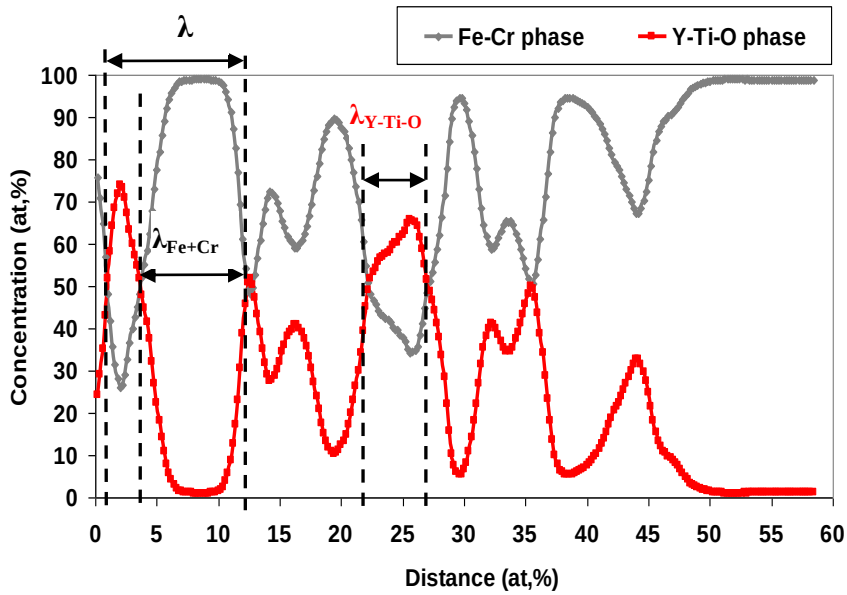

*Figure 3.2. Profile generated from a volume in Figure 3.1 (b). Characteristic lengths of Y-Ti-O – $\lambda_{Y\text{-}Ti\text{-}O}$ and Fe-Cr-rich phases and Fe-rich phases – λ_{Fe+Cr} are shown. Fe, Cr, Mn, Si, C, W species are associated with **Fe-Cr-rich phase** while Y, YO, O/O_2, Ti, TiO_x, FeO, CrO_x with **Y-Ti-O phase**. Profile is 12×12×60 nm^3 with step of 0.2 nm.*

A similar two-phase microstructure was also observed in a different analysis (LATAP analyse, see *Figure 3.6*) while a one phase structure, corresponding to Fe-Cr-rich phase has been observed in the last experiment, *Figure 3.3*. This non homogeneous microstructure can be explained simply looking at the microstructure observed during APT tip preparation in SEM / FIB (*Figure 3.4*). Different contrasts (bright and dark) clearly reveal that a two phase structure is present. The shape of both phases is not well defined and irregular. From SEM picture it is clear that, the dimensions of these phases vary between tens of nanometres to several micrometers. So, the dimensions of these phases, can explain the different microstructures observed by 3DAP.

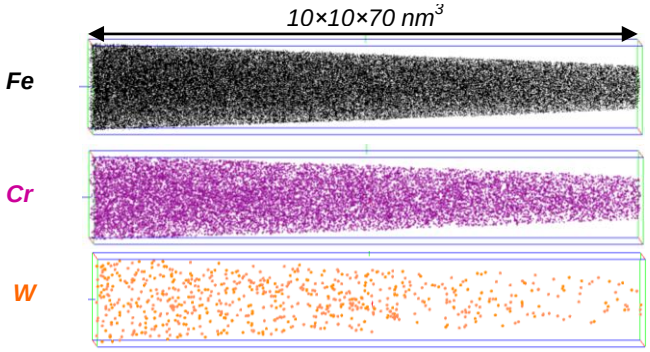

Figure 3.3. 3D reconstruction of ODS model alloy analysed by LATAP. Fe, Cr, W are shown. No presence of Y-Ti-O-rich phase is observed. Analyzed volume is 10×10×70 nm^3.

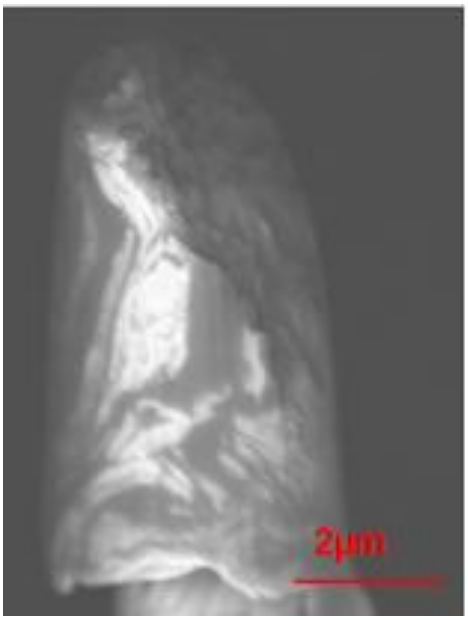

Figure 3.4. SEM image of APT sample preparation by Focused Ion Beam (annular milling). Two contrasts are clearly observed indicating that two phases are observed.

b) Evaporation artifacts

In the 3DAP reconstructions of ODS model alloy, a shift between Ti and Y atom positions is observed, as shown in *Figure 3.1* (c). It should be mentioned that, the major part of Y and almost all Ti are detected as molecular ions. They are bonded with O in the form of TiO, TiO_2 and YO. In addition, CrO, CrO_2 and FeO molecular ions are also observed. Thus, in order to study the Y/Ti shift in more details, concentration profiles showing only YO, TiO_x, FeO and CrO_x molecular ions are shown on *Figure 3.5* (a-c).

The YO and $TiO+TiO_2$, FeO, $CrO+CrO_2$ peaks correspond to the Y-Ti-O rich phase on the concentration profile. The shifts of TiO, TiO_2 molecular ions relatively to YO are clearly seen in the z direction (direction of analysis). The same observation is done for CrO, CrO_2 and FeO molecular ions.

The shift between these ions is estimated as follow. First, the distance between YO and TiO_x top peaks, *d*, are determined (as indicated in *Figure 3.5* (a)). Then, the width of each YO, TiO and TiO_2 peaks (namely L_{YO} and L_{TiOx}) at half maximum height is estimated and the difference between these values $(L_{TiOx} - L_{YO})$ is calculated. All these characteristics (*d*, L_{YO}, L_{TiOx} *and* $L_{TiOx} - L_{YO}$) are summarized in *Table 3.2*. *d* varies from 0.2 to 2.1 nm and $(L_{TiOx} - L_{YO})$ varies from -0.9 to 0.7 nm. As it can be seen from *Figure 3.5* (a), in one case the TiO_x peak is absent in comparison to corresponding YO peak (peak 4 on the figure).

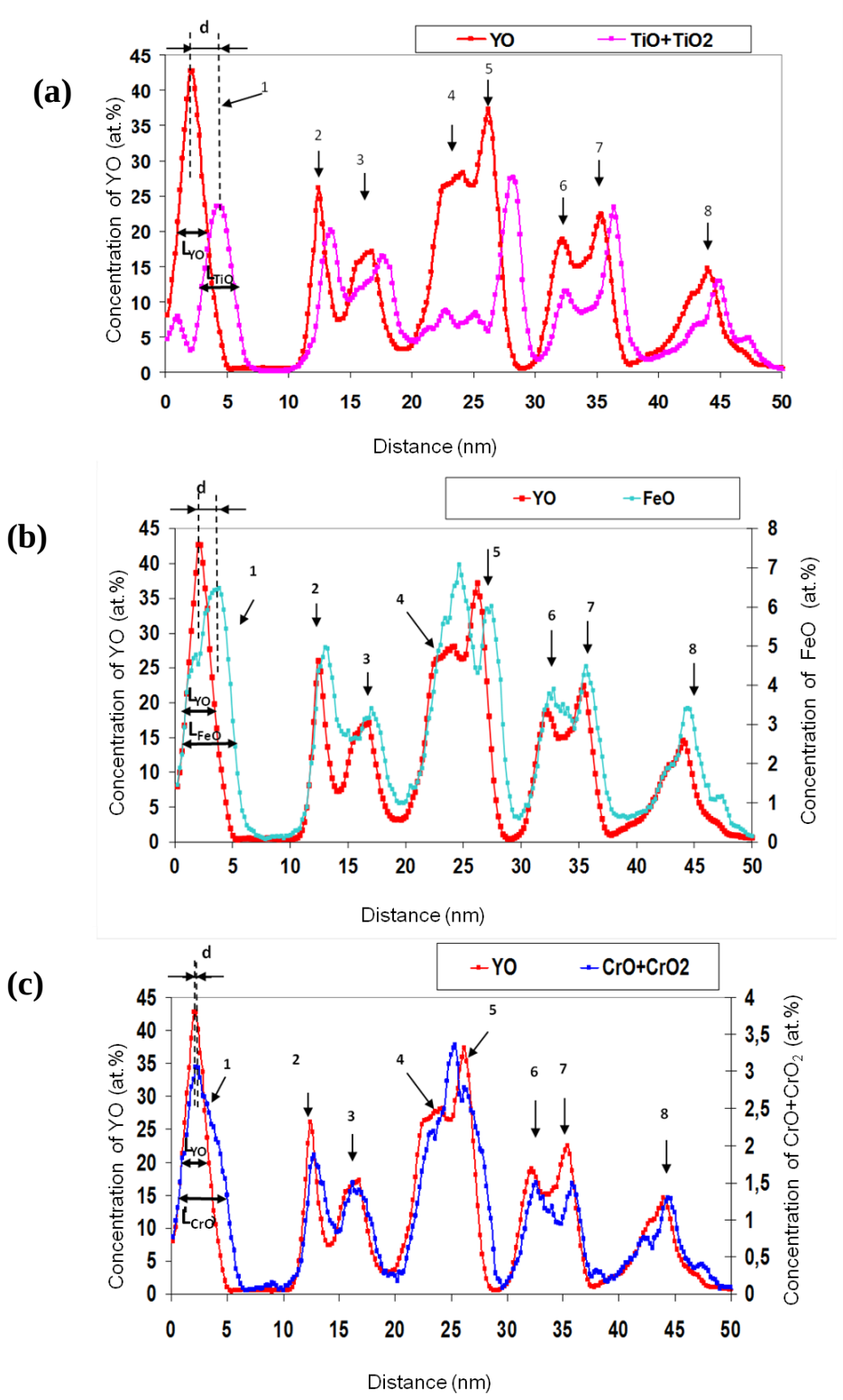

*Figure 3.5. Profiles generated in a volume shown in Figure 3.1 (b). Only YO (in red) and (a) **TiO+TiO₂** (pink), (b) **FeO** (blue) and (c) **CrO+CrO₂** (deep blue) molecular ions are shown. Decay of TiO_x, FeO and CrO_x molecular ions relatively YO in z direction is clearly seen. d – decay in z between tops of the YO and TiO_x, FeO, CrO_x peaks respectively. L_{YO}, L_{TiOx}, L_{FeO} and L_{CrOx} are widths of YO, TiO_x, FeO and CrO_x molecular ions measured at half of the maximum height of each peak on the profile. Profile is 12×12×60 nm³ with step of 0.2 nm.*

As far as FeO, CrO and CrO_2 are concerned on *Figure 3.5* (b-c)), the characteristics are summarized in *Table 3.3* and *Table 3.4*. In the case of FeO, *d* varies from 0.4 to 1.6 nm. These values show that the decay between FeO and YO peaks is smaller than between TiO_x and YO peaks. In addition, FeO peaks are slightly larger than YO ones, which is not the case for TiO_x. Finally, for CrO, CrO_2 and YO shifts, *d* varies from 0.2 to 0.5 nm. One can note that the shifts between CrO, CrO_2 and YO are smaller in comparison to TiO, TiO_2 and FeO.

Table 3.2.Characteristics of TiO, TiO_2 decay relatively YO molecular ions observed in ODS model alloy. d is difference between YO and TiO_x tops, L_{YO} and L_{TiOx} width of the peak at half of its maximum height.

№ peak	**d (nm)**	**L_{YO} (nm)**	**L_{TiOx} (nm)**	**L_{TiOx} -L_{YO} (nm)**
1	2.1	2.2	2.8	0.6
2	0.9	1.1	1.25	0.15
3	1	2.45	2.0	0.45
4	-	2.3	-	-
5	2	1.2	1.9	0.7
6	0.2	1.1	1.0	-0.1
7	1	1.1	1.1	0
8	1	3.0	2.1	-0.9

Table 3.3. Characteristics of FeO molecular ions decay relatively YO molecular ions observed in ODS model alloy. d is difference between peaks of YO and FeO peaks, L_{YO} and L_{FeO} width of the peak at half of its maximum height.

№ peak	*d (nm)*	*L_{YO} (nm)*	*L_{FeO} (nm)*	*L_{FeO} - L_{YO} (nm)*
1	1.6	2.2	4.1	1.9
2	0.6	1.1	1.6	0.5
3	0.4	2.45	1.9	-0.55
4	0.9	2.3	2.1	0.2
5	0.7	1.2	1.4	0.2
6	0.9	1.1	2.3	1.2
7	0.4	1.1	1.3	0.2
8	0.5	3.0	2.6	-0.4

Table 3.4.Characteristics of CrO and CrO_2 molecular ions decay relatively YO molecular ions observed in ODS model alloy. d is difference between peaks of YO and CrO, CrO_2 peaks, L_{YO} and L_{CrO} width of the peak at half of its maximum height.

№ peak	*d (nm)*	*L_{YO} (nm)*	*L_{CrOx} (nm)*	*L_{CrOx} - L_{YO} (nm)*
1	0.2	2.2	4.2	2.0
2	0.3	1.1	1.9	0.8
3	0.5	2.45	2.2	-0.25
4	-	2.3	-	-
5	0.5	1.2	1.6	0.4
6	0.4	1.1	1.5	0.4
7	0.3	1.1	1.3	0.2
8	0.4	3.0	3.1	0.1

Similar two phase structure is observed in LATAP experiment shown on *Figure 3.6* (a). Composition profile built perpendicularly to Y-Ti-O-rich phase shown on *Figure 3.6* (b) does not reveal any decay of TiO, TiO_2, CrO, FeO molecular ions relatively YO. However, it should be keep in mind that in this case, the interfaces between Y-Ti-O and Fe-Cr rich phases are not perpendicular to the evaporation direction of the tip (like in case of LAWATAP analyse, *Figure 3.1* (b)). As a result, the directions of composition profiles relatively direction of analyse are not the same in both experiments. Thus, the decay of TiO, TiO_2, CrO, FeO may appear depending on the orientation of Y-Ti-O-rich phase relatively direction of analyse.

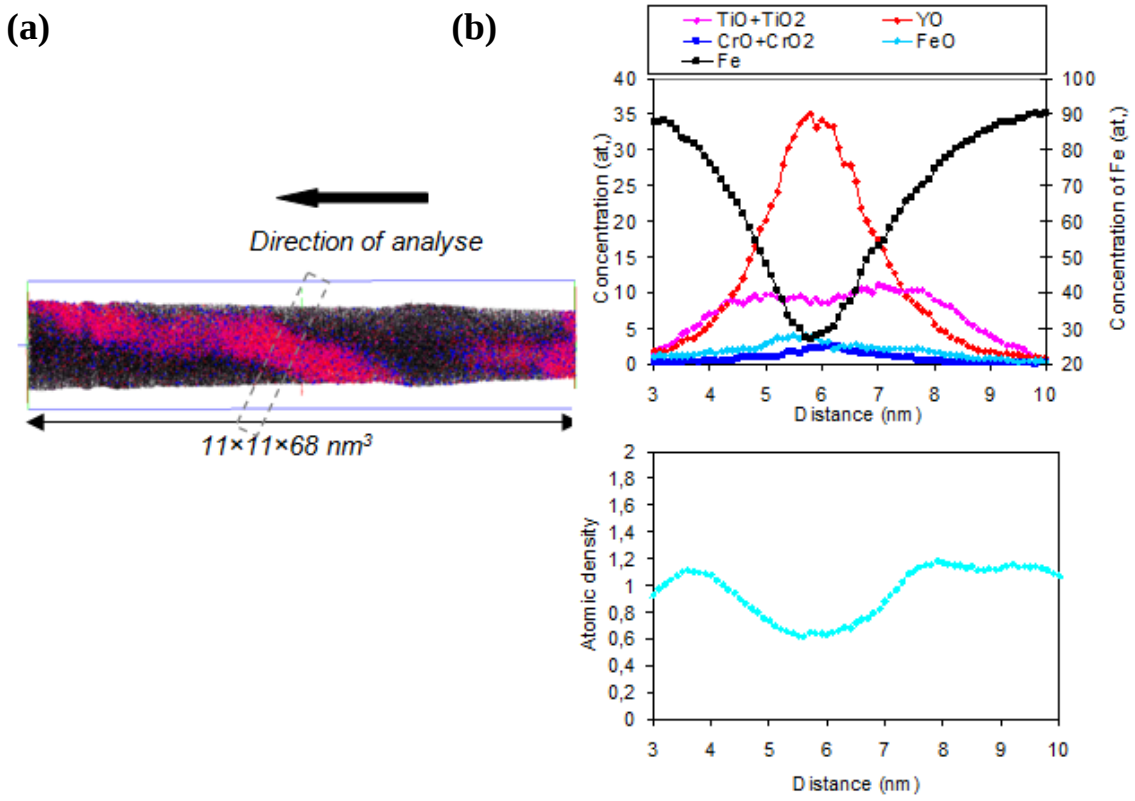

*Figure 3.6. ODS model alloy analysed by LATAP. (a) 3D reconstruction of analysed volume. Two phase structure is observed: Fe-Cr phase and Y-Ti-O rich phases are shown. Only **Fe, Cr** and **Y, YO, O, Ti, TiO_x, FeO, CrO_x** is shown. (b) Concentration profile (above) generated in a volume as indicated by dashed rectangle in (a). The shift of TiO molecular ions in z direction relatively YO is not observed in this case. Decrease of atomic density (below) associated with Y-Ti-O-rich phase, indicating that the higher evaporation field is required in comparison to matrix. Sampling size of profile is 5×5×0.1 nm^3.*

On the overall, such TiO_x and FeO, CrO_x shifts in the z direction (seen only in one LAWATAP experiment) can be related to the preferential retention effect. This effect arises when one element (or molecular ion) has a higher field of evaporation than others. In order to describe this effect, let us consider a binary alloy with A and B elements having different fields of evaporation such as $E_B<E_A$. Two different cases may be considered, as reported in

Figure 3.7. In the first case (case 1, on *Figure 3.7*), if the field at the tip apex is high enough, all ions have the same evaporation probability at (V_0+V_p). This may be achieved by applying faster pulse repetition rates, lower temperature of analyse as well as lower standing field and higher pulse fraction. In second case, if the field at the tip apex (V_0+V_p) is too low, then A atoms could stay at the surface while B elements will be evaporated (case 2, on the *Figure 3.7*).

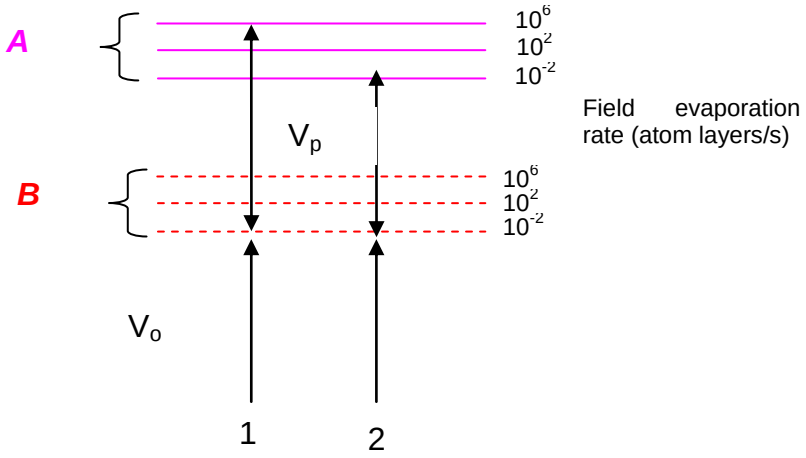

Figure 3.7. Schematic diagram of the field evaporation rate as a function of specimen temperature for A-B binary alloy, after [8]. Constant temperature is considered. In case 1, conditions of analyse allowing to get equal field evaporation probability at (V_0+V_p) for both elements are shown. In case 2, the increase of electric field (V_0+V_p) is too low to induce evaporation of element A (that is more difficult to field evaporate in comparison to B).

The latter effect could occur in the case of ODS model alloy, when Y-Ti-O-rich phases reach the surface of the sample. The affinity between Ti, Y, Fe and Cr with O is high. As it is shown in *Table 3.5*, the enthalpy of formation of oxide is higher for Y, Ti and slightly lower for Cr and Fe. As a consequence, their dissociation is difficult and they appear as molecular ions. The values of the field of evaporation are only known for Fe, Cr, Ti, Y ions embedded in pure Fe matrix [8]. There is no data for molecular ions (TiO, YO, CrO, ...). From the observation of TiO_x, CrO_x and FeO behaviour in our experiments, it is suggested that the field required to evaporate TiO_x as well as FeO and CrO_x is higher in comparison to YO molecular ions. Such a difference may be the reason of the shifts described previously.

The previously described effects are taken into account for chemical composition measurements of Y-Ti-O –rich phases. Indeed, if care is not taken Ti as well as O atoms may be lost, resulting in their underestimation. The methods used for calculation of chemical composition are detailed below.

Table 3.5. Heat of formation of pure binary oxides (at 25°C) [9].

Oxide composition	***ΔH_f (kJ/mol (Oxide))***	***ΔH_f (kJ/mol O)***
Y_2O_3	1906.7	636
TiO	542	542
TiO_2	944.1	472
CrO_2	582.8	291
Cr_2O_3	1130.40	376
Fe_3O_4	1899.1	474
Fe_2O_3	821.9	274

c) Chemical composition of Y-Ti-O-rich and Fe-rich phases

In order to ensure a reliable method for the composition measurements, chemical compositions have been measured in two different ways. In the first case, Y-Ti-O rich phases have been isolated from the matrix using the "iso position" method (see Appendix 3). The measurements were performed within regions where the concentration of Ti+Y+O (at.%) exceeds 30 to 35 at.% ($C_{threshold}$). A schematic representation of the procedure is shown on *Figure 3.8* (a).

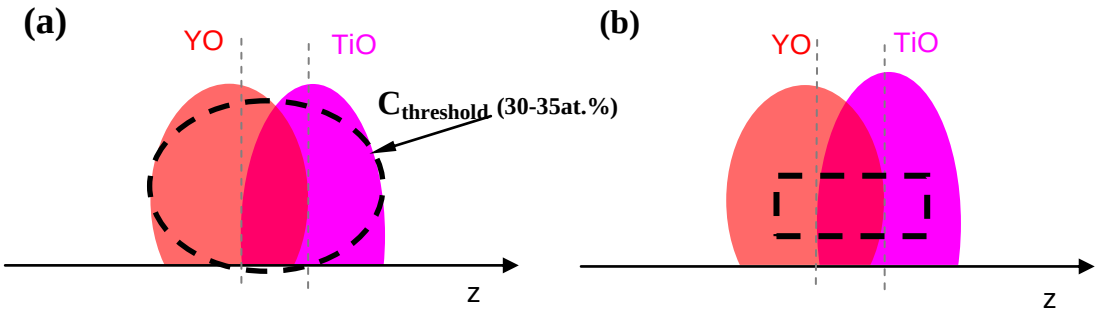

Figure 3.8. Schematic representation of concentration measurements of Y-Ti-O rich nanophases in ODS model alloy. Concentration measurements are performed (a) after "iso position" procedure, inside regions where concentration of Ti+Y+O is more than $C_{threshold}$ and (b) in small boxes located in these Y-Ti-O phases. YO and TiO molecular ions are represented in red and in pink respectively.

In the second case, small boxes were located in the particles as schematically indicated in *Figure 3.8* (b). The size of the box has been adjusted to the dimensions of the particle, of the order 5×5×5 nm^3 on the average. Compositions obtained using these two methods are compared in *Table 3.6* and *Table 3.7*. From both tables, a good agreement is observed

between both methods. So, two ways are further considered since both of them give reliable concentration measurements.

Table 3.6. Chemical compositions of Y-Ti-O-rich phases in ODS model alloy measured by LAWATAP. The composition is measured by "iso position" method. For comparison the nominal composition is also reported. The composition is calculated in accordance to the assumption that O_2 ions located at 32 amu. The values are in at.%. Error bars are given by the standard deviation 2σ. Y/O and (Y+Ti)/O ratios are also shown.

Elements	Fe	Cr	Y	Ti	O	Y/O	(Y+Ti)/O
Nominal (at.%)	**-**	**7.45**	**4.8**	**11.0**	**7.1**	**-**	**-**
1	**32.7**	**3.5**	**24.1**	**6.9**	**32.2**	**0.75**	**0.96**
2σ	*0.4*	*0.2*	*0.3*	*0.2*	*0.4*	*0.03*	*0.05*
2	**26.3**	**3.4**	**25.6**	**7.9**	**36.4**	**0.70**	**0.92**
2σ	*0.2*	*0.1*	*0.2*	*0.1*	*0.2*	*0.01*	*0.02*
3	**32.2**	**3.9**	**19.5**	**11.3**	**32.6**	**0.60**	**0.94**
2σ	*0.3*	*0.2*	*0.3*	*0.2*	*0.3*	*0.02*	*0.03*
Mean	**28.2**	**3.5**	**24.3**	**8.4**	**35.2**	**0.69**	**0.93**
2σ	*0.1*	*0.1*	*0.2*	*0.1*	*0.2*	*0.02*	*0.03*

Table 3.7. Chemical compositions of Y-Ti-O-rich phases in ODS model alloy measured by APT. Composition is measured in boxes located in Y-Ti-O-rich phases. 1-7 measurements correspond to LAWATAP (see Figure 3.1) and 8 to LATAP (Figure 3.6) analyses. For comparison the nominal composition is also reported. The composition is calculated in accordance to assumption that O_2 ions located at 32 amu. The values are in at.%. Error bars are given by the standard deviation 2σ. Y/O and (Y+Ti)/O ratios are also shown.

Elements	Fe	Cr	Y	Ti	O	Y/O	(Y+Ti)/O
Nominal (at.%)	**-**	**7.45**	**4.8**	**11.0**	**7.1**	**-**	**-**
1	**21.6**	**3.1**	**27.7**	**9.3**	**37.7**	**0.73**	**0.98**
2σ	*1.6*	*0.8*	*1.7*	*1.2*	*1.6*	*0.10*	*0.25*
2	**29.6**	**3.0**	**28.0**	**4.4**	**34.7**	**0.80**	**0.94**
2σ	*1.6*	*0.6*	*1.6*	*0.7*	*1.6*	*0.10*	*0.23*
3	**20.0**	**3.2**	**31.3**	**5.5**	**39.6**	**0.79**	**0.93**
2σ	*1.3*	*0.6*	*1.3*	*0.7*	*1.4*	*0.10*	*0.20*
4	**24.9**	**2.9**	**26.9**	**6.0**	**38.8**	**0.69**	**0.85**
2σ	*1.3*	*0.5*	*1.3*	*0.7*	*1.4*	*0.10*	*0.20*
5	**22.2**	**2.9**	**25.1**	**8.8**	**40.7**	**0.62**	**0.83**
2σ	*1.3*	*0.6*	*1.4*	*0.9*	*1.5*	*0.10*	*0.20*
6	**25.9**	**3.7**	**22.9**	**9.7**	**37.4**	**0.62**	**0.87**
2σ	*1.2*	*0.6*	*1.2*	*0.8*	*1.3*	*0.10*	*0.20*
7	**33.9**	**3.3**	**19.6**	**11.1**	**31.4**	**0.63**	**0.96**
2σ	*1.7*	*0.8*	*1.5*	*1.1*	*1.6*	*0.11*	*0.22*
8	**32.4**	**10.4**	**17.7**	**13.0**	**25.5**	**0.70**	**1.21**
2σ	*4.4*	*2.9*	*3.6*	*3.2*	*4.1*	*0.37*	*0.61*
Mean	**25.2**	**3.2**	**26.0**	**7.7**	**37.4**	**0.70**	**0.90**
2σ	*0.5*	*0.2*	*0.5*	*0.3*	*0.6*	*0.05*	*0.10*

From these measurements, it can be seen that: some Cr and Fe is present in these Y-Ti-O-rich phases. Cr concentration is rather constant, about 3.0 at. %, and the level of Fe varies from 20 up to 33.9 at.%. As it was shown on concentration profiles (*Figure* 3.5 (b, c)), some CrO, CrO_2 and FeO molecular ions are associated with Y-Ti-O-rich phases. It indicates that a part of Fe and Cr atoms are originally present in the Y-Ti-O-rich phases. On the other hand, introduction of Fe and Cr due to 3DAP artefacts cannot be excluded (see Chapter 2, section

II.4 (d)) [10,11]. However, considering the size of Y-Ti-O rich phases (λ_{TiO} > 2nm) and the results given by the field evaporation model (chapter 2), the level of matrix atoms artificially incorporated in the core of Y-Ti-O rich phases could be rather low. In addition, other parameters given in the tables, the ratios Y/O and (Y+Ti)/O, are not biased by field evaporation artefacts.

Y and O concentrations vary from 17.7 up to 31.3 at.% and from 25.5 up to 40.7 at.% respectively. The detected concentration of Ti varies from 4.4 up to 13.0 at.%. (Ti+Y)/O ratio varies from 0.83 up to 1.21 with a mean value of 0.93±0.02. The Y/O ratio varies from 0.60 up to 0.80 with a mean value of 0.69 ± 0.01. This value is close to the Y/O ratio corresponding to the original Y_2O_3 powder (0.67). Thus, it seems that these Y-Ti-O rich phases correspond to remnants of the original Y_2O_3 powder with Fe, Cr and Ti that were incorporated during milling.

In order to investigate the dissolution of Y and O, as well as Ti into Fe-Cr rich phase, concentrations of Y, O and also Ti have been measured in the matrix. The matrix measurements were done in boxes located at different distances from Y-Ti-O rich phases as indicated in *Figure 3.9*. The matrix concentrations, owing to their place of measurement, are summarized in *Table 3.8*.

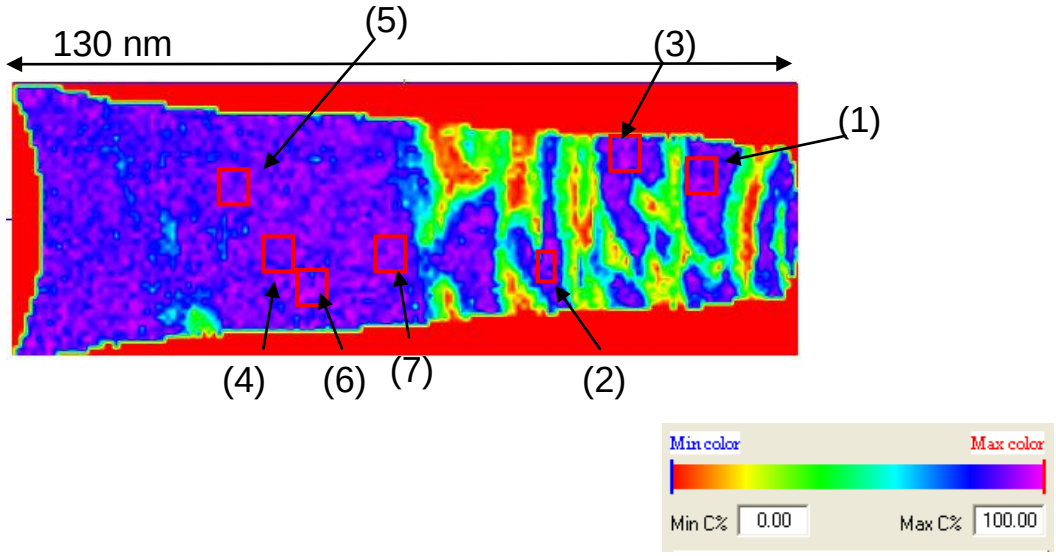

Figure 3.9. Fe iso-concentration map of ODS model alloy, showing the places (red boxes) where measurements of matrix composition are done. The higher concentrations are in deep blue and the lower in green and red (see scale on the right side of the picture). Number of boxes (1-7) corresponds to the number of measurements in the Table 3.8.

Table 3.8. Chemical compositions of Fe-Cr rich phase measured by APT in ODS model alloy. In total, the matrix composition is measured on three different powder grains. LAWATAP measurements in places indicated on Figure 3.9, corresponds to 1-7 analyses. Matrix measurements are also performed for two LATAP analyses. In one (shown on Figure 3.6), matrix composition is calculated by similar way and corresponds to 8-11 analyses. In second one (shown on Figure 3.3), the composition is calculated for Fe-Cr rich phase and corresponds to 12 analyse. For comparison the nominal composition is also reported. The composition is calculated in accordance to assumption that O_2 ions located at 32 amu. Standard deviations are 2σ. The values are in at.%.

Elements	Fe	Cr	Si	Mn	W	C	Y	Ti	O
Nominal (at.%)	**Bal.**	**7.45**	**-**	**-**	**-**	**-**	**4.8**	**11.0**	**7.1**
1	**88.7**	**9.9**	**0.04**	**0.33**	**0.22**	**0.08**	**0.11**	**0.32**	**0.70**
2σ	*0.9*	*0.9*	*0.06*	*0.17*	*0.14*	*0.08*	*0.10*	*0.17*	*0.25*
2	**90.3**	**7.7**	**0.16**	**0.31**	**0.15**	**0.08**	**0.39**	**0.08**	**0.80**
2σ	*1.6*	*1.5*	*0.22*	*0.31*	*0.22*	*0.16*	*0.35*	*0.16*	*0.50*
3	**89.9**	**7.2**	**0.24**	**0.33**	**0.24**	**0.06**	**0.24**	**0.34**	**1.5**
2σ	*1.5*	*1.3*	*0.24*	*0.28*	*0.24*	*0.12*	*0.24*	*0.29*	*0.59*
4	**90.2**	**8.6**	**0.19**	**0.18**	**0.13**	**0.03**	**0.11**	**0.10**	**0.36**
2σ	*0.6*	*0.6*	*0.09*	*0.08*	*0.07*	*0.03*	*0.07*	*0.06*	*0.12*
5	**90.1**	**8.6**	**0.19**	**0.26**	**0.25**	**0.05**	**0.07**	**0.08**	**0.35**
2σ	*0.6*	*0.6*	*0.09*	*0.10*	*0.10*	*0.04*	*0.05*	*0.05*	*0.12*
6	**90.9**	**8.2**	**0.22**	**0.27**	**0.14**	**0.04**	**0.01**	**0.01**	**0.28**
2σ	*0.5*	*0.5*	*0.09*	*0.10*	*0.07*	*0.03*	*0.02*	*0.02*	*0.10*
7	**90.7**	**8.1**	**0.10**	**0.16**	**0.18**	**0.02**	**0.09**	**0.08**	**0.54**
2σ	*0.6*	*0.5*	*0.60*	*0.08*	*0.08*	*0.03*	*0.06*	*0.06*	*0.15*
8	**86.4**	**10.1**	**0.22**	**0.22**	**0.22**	**0.04**	**0.39**	**0.33**	**1.50**
2σ	*2.3*	*2.0*	*0.31*	*0.31*	*0.31*	*0.42*	*0.38*	*0.39*	*0.81*
9	**88.6**	**9.4**	**0.37**	**0.16**	**0.19**	**0.11**	**0.06**	**0.22**	**0.80**
2σ	*0.9*	*0.8*	*0.17*	*0.11*	*0.12*	*0.09*	*0.07*	*0.13*	*0.25*
10	**88.8**	**8.70**	**0.38**	**0.25**	**0.47**	**0.09**	**0.09**	**0.12**	**1.18**
2σ	*1.9*	*1.7*	*0.38*	*0.30*	*0.42*	*0.20*	*0.20*	*0.21*	*0.67*
11	**85.1**	**11.7**	**0.22**	**0.43**	**0.11**	**0.22**	**0.01**	**0.40**	**1.70**
2σ	*2.3*	*2.1*	*0.30*	*0.43*	*0.22*	*0.30*	*0.01*	*0.41*	*0.85*
12	**89.5**	**9.5**	**0.27**	**0.15**	**0.16**	**0.13**	**0.01**	**0.05**	**0.05**
2σ	*0.2*	*0.2*	*0.03*	*0.02*	*0.02*	*0.02*	*0.01*	*0.01*	*0.01*
Mean	**89.7**	**8.85**	**0.20**	**0.23**	**0.19**	**0.07**	**0.08**	**0.12**	**0.48**
2σ	*0.23*	*0.22*	*0.03*	*0.04*	*0.04*	*0.02*	*0.03*	*0.03*	*0.06*

As it can be seen in *Table 3.8*, the matrix concentration is different from the nominal one. A significant lower amount of Ti, O and Y are measured. Si, Mn, W and C are also detected. In the Fe-Cr-rich phase, Fe varies from 85.1 to 90.9 at.% and Cr from 7.2 to 11.7 at.%. Fluctuations of Y, Ti and O elements are also observed from one place to another. As an example, smaller amounts of Ti, Y and O are measured in box number 5 and 6 located far from Y-Ti-O rich phases in comparison to boxes 1, 2 and 3 located closer (see *Figure 3.9*). In general, the Ti, Y and O concentrations vary from 0.01 to 0.40 at.%, 0.01 to 0.39 at.% and 0.05 to 1.7 at.%, respectively. It must be mentioned that Y and O are almost immiscible in bcc iron (their equilibrium solubility limits are 0.029 at.% [12] and 0.06 [13] respectively at

800°C). If to consider measured mean concentrations in the matrix (*Table 3.8*), they exceed the equilibrium values reported above. In contrast, Ti has a reasonable solubility in iron (>3.0 at.% at 800°C [14]). However a significant smaller amount of Ti is detected in the matrix of ODS model alloy. It should be mentioned that in multicomponent system, the Ti solubility limit given above, may change. Supersaturation of the matrix in Y and O is not surprising since capacity of ball milling to extend the solubility limits have been demonstrated [15].

Finally it should be mentioned that, the supersaturation of the matrix is more pronounced for O (0.48 ± 0.06 at.%) comparing to Y (0.08 ± 0.03 at.%) and Ti (0.12 ± 0.03 at.%). First principles calculations by Fu et al [1, 16], show that O form strong bonds with vacancies. Therefore, the higher solubility of O in bcc iron is possible due to its strong interaction with vacancies introduced during the MA process.

As a comment, the results from the 12th analyse in *Table 3.8*, show smaller Y and O concentrations. The values are more comparable to solubility limits, whereas again a significant smaller amount of Ti is measured. A good agreement with the nominal composition of the FeCrW pre-alloy powder without addition of TiH_2 and Y_2O_3 is found. So, it can be assumed that, in that specific experiment, no TiH_2 nor Y_2O_3 dissolution occur.

I.2. Discussion

The same ODS model alloy was also analysed by neutron and X-ray diffraction (XRD) at different stages of mechanical alloying and subsequent annealing treatments [5, 6].

Concerning the first stage, when FeCrW prealloyed powder is mechanically alloyed with TiH_2, no characterisation by APT is available. The results of X-ray as well as neutron diffraction at this step show that peaks corresponding to TiH_2 decrease with milling time and disappear after 48 hours. From these results the dissolution of a major part of TiH_2 in the Fe-9CrW matrix [6] is supposed.

At second stage, FeCrW-Ti powder is mechanically alloyed with Y_2O_3. Both neutron diffraction [5,6] and APT results are available. Neutron diffraction shows that the intensity of the signal corresponding to the Y_2O_3 decreases with milling time. A single phase (alpha Fe) is observed after 24 h of milling. The authors suggest two possible mechanisms for Y_2O_3 diffraction peaks diminution [5,6]: i) fragmentation with subsequent dissolution of Y_2O_3 powder into Fe-rich matrix resulting in the formation of a supersaturated solid solution and ii)

fragmentation of initial Y_2O_3 with amorphization of Y-O regions that do not contribute to diffraction.

Our APT investigations clearly show that the microstructure is composed of two phases: i) Y and O enriched phases associated to Ti and ii) Fe-Cr rich phase supersaturated in Y and O. Therefore, the hypothesis of a complete dissolution of Y_2O_3 in the matrix [5, 6] is not supported here. The APT results cannot give information about the hypothesis that Y-Ti-O rich regions could be amorphous, as suggested by neutron diffraction results [5, 6]. However, it was shown by Kimura [17], that mechanical alloying up to 100 h of Fe-24Cr with 15 Y_2O_3 wt.% results in a microstructure composed of nano-grains of iron surrounded by amorphous layer of Y and O atoms. The amorphization of Y_2O_3 powder (milled alone as well as dispersed in Ni-based alloy) has been also observed by Begin-Colin et al [18] and Ruhle and Steffens [19]. It must be keep in mind that in all listed works, different milling conditions (mills, intensities, ball to powder weight ratio, etc…) as well as different compositions of materials (mainly Y_2O_3, without Ti addition) are involved. To conclude about amorphization of these Y-Ti-O-rich phases specific TEM investigation is needed.

Another important observation can be given owing to APT results. As it can be seen from profiles on *Figure* 3.6 (b), a decrease of the atomic density is detected where Y-Ti-O-rich phase is present. It indicates, as previously explain, that Y-Ti-O rich phase is a high evaporation field phase compared to the matrix (Fe-Cr-rich phase). But, this is not the case for small nanoparticles observed in the ODS steels MA with 0.2-0.5 wt.% of Y_2O_3. These nanoparticles (as in MA957, Fe-12Cr ODS and Eurofer [20]) after heat treatment exhibit low evaporation field. This suggests, that Y-Ti-O-rich phases observed in as-milled ODS model alloy and Ti-Y-O rich nanoparticles in Ti-containing ODS alloys do not have the same nature.

Concerning the second phase (Fe+Cr matrix), the thickness measured by APT varies from 8 to 10 nm and 15 nm is estimated from neutron diffraction. A significant reduction (up to 10^3 times) of the Fe powder is achieved (initial sizes (100 μm [6])) by mechanical alloying. As revealed by APT, the composition of this phase may vary depending on the distance from Y-Ti-O-rich phase. On one hand, it may correspond to the nominal composition of the FeCrW powder without addition of TiH_2 and Y_2O_3 reinforcements (0.01±0.01, 0.05±0.01 and 0.05±0.01 at.% respectively for Y, Ti and O), i.e. indicating that MA does not occur. On the another hand, the composition of this Fe-Cr-rich phase may contain some Y (0.08±0.03 at.%), Ti (0.12±0.03 at.%) and O (0.48±0.06 at.%) in the surrounding of Y-Ti-O rich phases.

It is reported from neutron diffraction that a small part of Y and O can be dissolved in the bcc iron because of the slight change (0.00023 Å) of the lattice parameter (2,86800±0.00039 and 2,86823±0.00005 Å respectively [5,6]) observed between 0 and 48h of MA. Since Y is significantly larger than O, it may be assumed that the distortion of the bcc crystalline lattice can be mainly caused by the Y dissolution. The application of the Vegard`s law [21] indicates that the difference of 0.00023 Å, can be caused by a dissolution of approximately 0.03±0.02 at.% of Y. Within experimental uncertainties, this is in good agreement with the APT value: 0.08±0.03 at.%. It should be also mentioned that neutron diffraction suggests an average evolution of the lattice parameter depending on the materials whereas APT shows that saturation of Y and O in Fe-Cr phase is not homogeneous and occurs next to Y-Ti-O rich phases. Therefore, these facts can further reduce the differences between neutron diffraction and APT results.

The ODS model alloy has been also studied by X-ray diffraction after annealing treatments (950-1300°C/1h) [6]. Clear signals have been detected corresponding to $YTiO_3$, Y_2O_3 and TiO phases. However, only Y-Ti-O-mixed regions have been observed by APT in as-milled condition (FeCrWTi+Y_2O_3). So, taking into account results of XRD it can be assumed that: i) during subsequent annealing Y-Ti-O rich phase transforms into $YTiO_3$, Y_2O_3 and TiO rich phases; ii) the microstructure observed in as-milled state is not homogeneous at micrometer scale. Along with Y-Ti-O rich phases, the existence of Ti-rich and Y-O-rich regions with low density ($>10^{22}$ m^{-3}) is possible. To clarify this point, APT investigation of the material in as-milled state as well after annealing treatment should go further.

The following discussion is devoted to the possible scenario to explain phase formation in this ODS model alloy under ball milling conditions. The evolution of the microstructure of materials under ball milling [22–24] can be described from the theory of "driven alloys" developed for materials under irradiation [25]. The microstructure of MA ODS model alloy may results of a dynamic competition between two phenomena that occurs at some stage of the MA process:

i) on one hand, mechanical forces induced by plastic deformation and ballistic displacements tend to bring the system towards a random solid solution regardless the chemical nature of atoms;

ii) on the other hand, thermodynamic driving forces tend to lead the system towards equilibrium.

Here, the first process could lead to amorphization of Y_2O_3, partial dissolution of Y and O in the ferritic matrix and incorporation of Fe and Cr into the Y and O rich phase. In addition to this chemical mixing, crystallites size decreases during MA. However, since the solubility limit of Y and O into Fe is very small, a large part of Y and O remains in a separate phase. In addition, due to the strong affinity of Ti for O, this element can migrates to the Y and O rich phase. Indeed, it should be kept in mind that during mechanical alloying a high number of defects is introduced [15,26,27] in the system and the temperature may increase [19,28] allowing diffusion. Finally, during subsequent annealing, formation of well-defined oxides occurs. The presence of different types of oxides (as revealed by diffraction techniques) could be linked with the heterogeneous structure resulting from MA. These mechanisms are schematically represented in *Figure 3.10*.

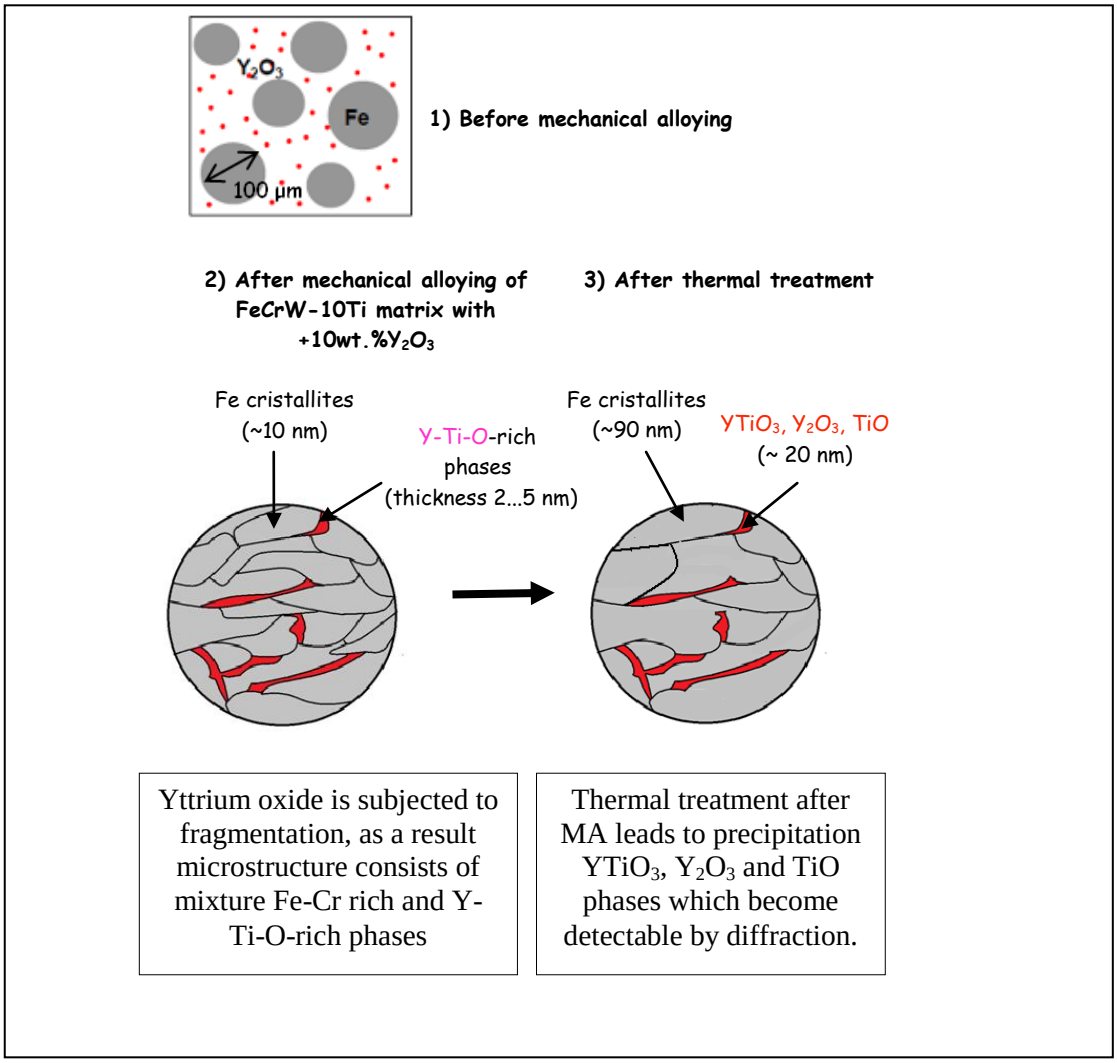

Figure 3.10.Shematic representation of Oxides formation mechanism in ODS model alloy (after [6]).

I.3. Partial conclusions

ODS model alloy was studied in the framework of the ANR aXtrem project by Atom Probe Tomography. Material was produced by mechanical alloying of FeCrW pre-alloyed powder with 10 wt.% of TiH_2 and 10 wt.% of Y_2O_3. Characterization by APT was compared to results by X-ray and neutron diffraction [5, 6]. The main conclusions are the following:

- APT revealed a two phase structure: i) Fe-Cr-rich phase and ii) Y-Ti-O-rich phase, with Y, O and in less extent Ti content close to the proportion introduced into material.
- A formation mechanism for ODS model alloy can be suggested: i) mechanical alloying results in fragmentation and amorphisation of initial Y_2O_3 powder associated to a surrounding supersaturation in Y and O into Fe-Cr rich matrix. ii) Strong affinity between Ti, Y and O results in the formation of Y-Ti-O-rich phases. iii) Further heat treatment stimulates the precipitation of $TiYO_3$ and Y_2O_3 and TiO phases [5,6].

II. ODS industrial steel

ODS steel was produced by MA in an industrial attritor and was characterized by APT in as-milled, annealed at 850°C during 1h and hot-extruded states. Information about the different APT experiments performed on this steel are reported in *Table 3.9***.**

Table 3.9. APT experiments performed for ODS industrial steel.

Material state	APT	Number of analyses	Number of analyzed atoms
As-milled powder	LATAP	4	$1.9\ 10^6$
	LAWATAP	3	30.10^6
Annealed at 850°C/1h powder	LATAP	3	750 000
	LAWATAP	1	15.10^6
Consolidated material	LATAP	2	600 000
	LAWATAP	2	10.10^6

In this first part, the global chemical compositions calculated in all studied conditions are presented and discussed. A more detailed description of the microstructure is reported in a second section. In all studied conditions nanometre scale nanoparticles are observed. The nanoparticles are described in terms of size, number density and chemical composition. These APT results will be compared with SANS [6] and TEM [6, 29] results. At the end, formation mechanism of nanoparticles in ODS steel are discussed.

II.1. Global chemical composition

The global chemical composition corresponds to the chemical composition of the total analysed volume, i.e. including matrix and nanoparticles. The mean global composition for each condition was measured from at least two different powder grains or bulk rods. Global chemical compositions of as-milled, annealed 850°C/1h powders and hot extruded material are shown in *Table 3.10*.

As it can be seen from *Table 3.10* fluctuations of Cr, Ni and W are detected from one analyse to another in the as-milled powder. In addition, a small and constant amount of C is found. In the case of the annealed ODS material (850°C during 1h), fluctuations of Ti, Y, O and Si are observed from one experiment to another. In hot extruded material fluctuations of Cr, Ti, Y, O and Si are also detected.

Table 3.10. Global chemical compositions of ODS steel in as-milled, annealed and hot extruded state measured by LATAP. Nominal chemical composition is also shown for comparison. Compositions are in at. %. Balance is iron. Uncertainties are the standard deviation 2σ. All analyses are performed on different powder grains or bulk rods.

	Cr	Ti	Y	O	Si	Ni	Mn	W	C
nominal	**19.2**	**0.35**	**0.29**	**0.44**	**0.30**	**0.28**	**0.30**	**0.30**	**-**
As-milled powder									
1	**19.0**	**0.33**	**0.25**	**0.34**	**0.82**	**0.13**	**0.32**	**0.13**	**0.02**
2σ	*0.2*	*0.03*	*0.03*	*0.03*	*0.04*	*0.02*	*0.03*	*0.02*	*0.01*
2	**19.5**	**0.28**	**0.21**	**0.32**	**1.00**	**0.17**	**0.29**	**0.19**	**0.03**
2σ	*0.2*	*0.02*	*0.02*	*0.03*	*0.04*	*0.02*	*0.02*	*0.02*	*0.01*
3	**19.8**	**0.28**	**0.25**	**0.38**	**0.99**	**0.20**	**0.30**	**0.24**	**0.03**
2σ	*0.2*	*0.02*	*0.02*	*0.02*	*0.03*	*0.02*	*0.02*	*0.02*	*0.01*
4	**18.7**	**0.35**	**0.25**	**0.37**	**1.0**	**0.17**	**0.29**	**0.17**	**0.04**
2σ	*0.2*	*0.03*	*0.03*	*0.03*	*0.05*	*0.02*	*0.03*	*0.03*	*0.01*
Annealed at 850°C/1h									
1	**19.2**	**0.16**	**0.18**	**0.51**	**0.41**	**0.18**	**0.29**	**0.20**	**0.04**
2σ	*0.3*	*0.02*	*0.03*	*0.04*	*0.04*	*0.03*	*0.04*	*0.03*	*0.02*
2	**18.8**	**0.25**	**0.32**	**0.54**	**0.98**	**0.18**	**0.29**	**0.22**	**0.03**
2σ	*0.2*	*0.02*	*0.02*	*0.02*	*0.03*	*0.02*	*0.02*	*0.02*	*0.01*
3	**19.0**	**0.16**	**0.21**	**0.42**	**0.87**	**0.17**	**0.27**	**0.24**	**0.03**
2σ	*0.2*	*0.02*	*0.02*	*0.03*	*0.03*	*0.02*	*0.02*	*0.02*	*0.01*
Hot extruded steel									
1	**20.6**	**0.36**	**0.42**	**0.71**	**1.80**	**0.14**	**0.29**	**0.19**	**0.07**
2σ	*0.2*	*0.03*	*0.03*	*0.03*	*0.05*	*0.02*	*0.02*	*0.03*	*0.01*
2	**21.1**	**0.25**	**0.26**	**0.46**	**1.0**	**0.15**	**0.28**	**0.20**	**0.06**
2σ	*0.2*	*0.02*	*0.02*	*0.02*	*0.40*	*0.02*	*0.02*	*0.02*	*0.01*

An average of all these compositions is reported in *Table 3.11*. In all cases, a significant excess of Si and depletion of Ni and W are observed in comparison to nominal values. In the as-milled powder, a slight depletion in Ti, Y and O is measured. As far as all elements are concerned, the mean chemical composition of material is in relatively good agreement with the nominal one.

After annealing at 850°C during 1h, the Ti depletion is more pronounced, in comparison to as-milled condition. However, an excess in O is measured. This could be explained by an oxidation of the powder during the annealing treatment. In the hot extruded state, a slight excess in Cr and Si is found in comparison to the previously reported cases. The excess in Ti and O is more pronounced than in the annealed state. As it will be shown later Y, Ti and O species form nanoparticles. The average fluctuations of Ti, Y and O depend on the size and the number density of these nanoparticles in the analysed volumes.

Table 3.11. Mean chemical composition of as-milled, annealed and hot extruded powder measured by LATAP. Compositions are in at. %. Balance is iron. Uncertainties are the standard deviation 2σ.

	Cr	Ti	Y	O	Si	Ni	Mn	W	C
nominal	**19.2**	**0.35**	**0.29**	**0.44**	**0.30**	**0.28**	**0.30**	**0.30**	**-**
As-milled	**19.6**	**0.30**	**0.25**	**0.36**	**0.98**	**0.18**	**0.30**	**0.21**	**0.03**
2σ	*0.1*	*0.01*	*0.01*	*0.01*	*0.02*	*0.01*	*0.01*	*0.01*	*0.03*
Annealed at 850°C/1h	**18.9**	**0.21**	**0.27**	**0.50**	**0.84**	**0.18**	**0.29**	**0.22**	**0.03**
2σ	*0.1*	*0.02*	*0.02*	*0.02*	*0.02*	*0.02*	*0.02*	*0.02*	*0.01*
Hot extruded state	**20.9**	**0.31**	**0.34**	**0.59**	**1.45**	**0.14**	**0.28**	**0.22**	**0.07**
2σ	*0.2*	*0.02*	*0.02*	*0.03*	*0.04*	*0.02*	*0.02*	*0.02*	*0.01*

II.2. Nanoparticles study

As it was previously mentioned, nanoparticles are observed in all studied conditions in the ODS industrial steel. These particles are characterized in terms of size, number density and chemical composition below.

a) Distribution, number density and size

The spatial distribution of the main elements in as-milled, annealed at 850°C/1h and extruded conditions are shown on *Figure 3.11* (a-c). As it can be seen from the figure, in all studied conditions the distributions of Y, YO, O, FeO and CrO species are not random. These species and molecular ions form nanoparticles in the 3D images. Ti and TiO are also associated, excepted in the as-milled condition, where the contribution of this ions is less pronounced.

An example of nanoparticles detected is shown in *Figure 3.12* (1-3). It is worth noticing that the nano-particles in the as-milled state are diluted and not always well-defined (roughness of the interface). In contrast, nano-particles observed after subsequent annealing and hot extrusion have spherical shape. As it was suggested by Klimiankou et al. [30], the solute diffusion occurring during heat treatments results in the minimisation of the surface energy of the nanoparticles resulting in more spherical shape.

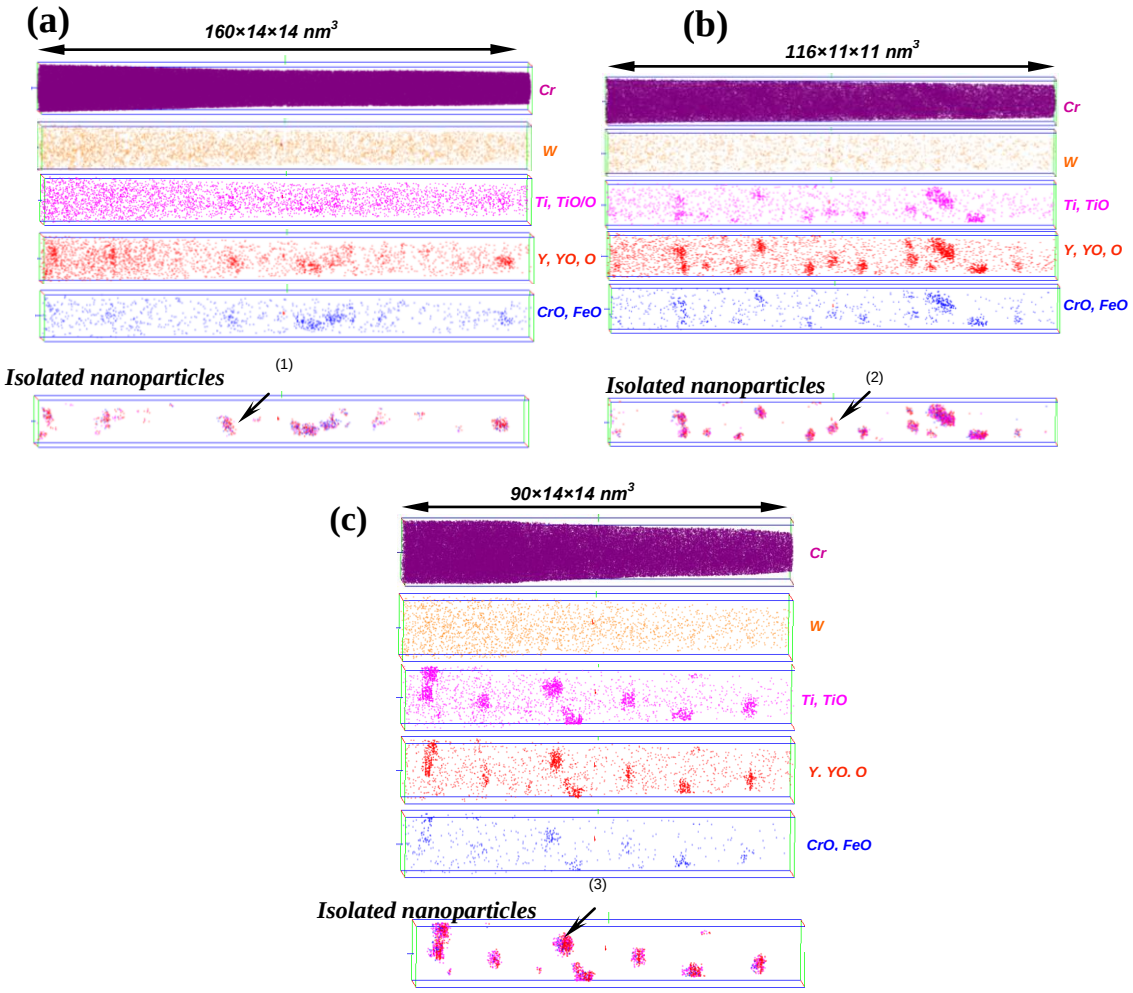

Figure 3.11. 3D reconstructions of ODS steel studied by LATAP in (a) as-milled, (b) annealed at 850°C during 1h and (c) hot extruded condition. Cr, W, Ti, TiO, Y, YO, O, FeO, CrO species are shown. In all cases distributions of Y, YO, O, FeO and CrO are associated with nanoparticles. Isolated nanoparticles using a cluster detection algorithm are also shown. Zooms on particles indicated by arrows (1, 2, 3) are depicted respectively on Figure 3.12.

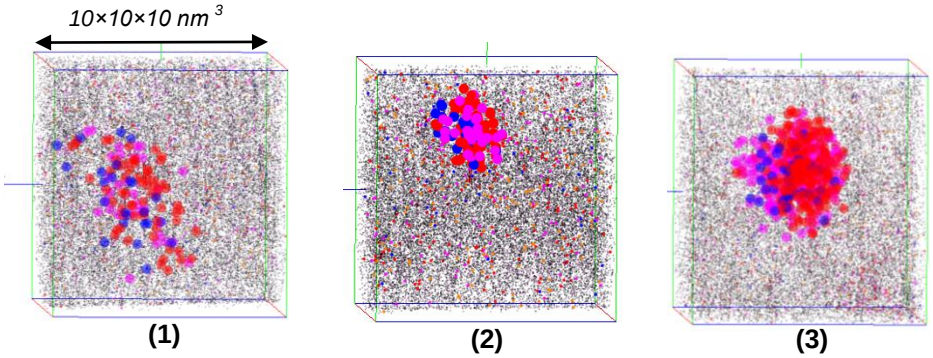

Figure 3.12. Zoom on a typical particles detected by APT in ODS steel (1) in as-milled state, (2) after annealing at 850°C during 1h and (3) in hot extruded state. Cr and Fe atoms are represented in black, W in orange, CrO and FeO in blue, Ti and TiO in pink and Y, YO and O in red. Solute atoms in the matrix are represented by spheres with relative size equal to 1 and solute atoms in the nanoparticles by spheres of the relative size equal to 4. (Cr and Fe are represented as dots). Volume of 10×10×10 nm^3 is shown for each particle.

The size distributions of the nanoparticles as a function of their number densities are reported on *Figure 3.13* for each condition.

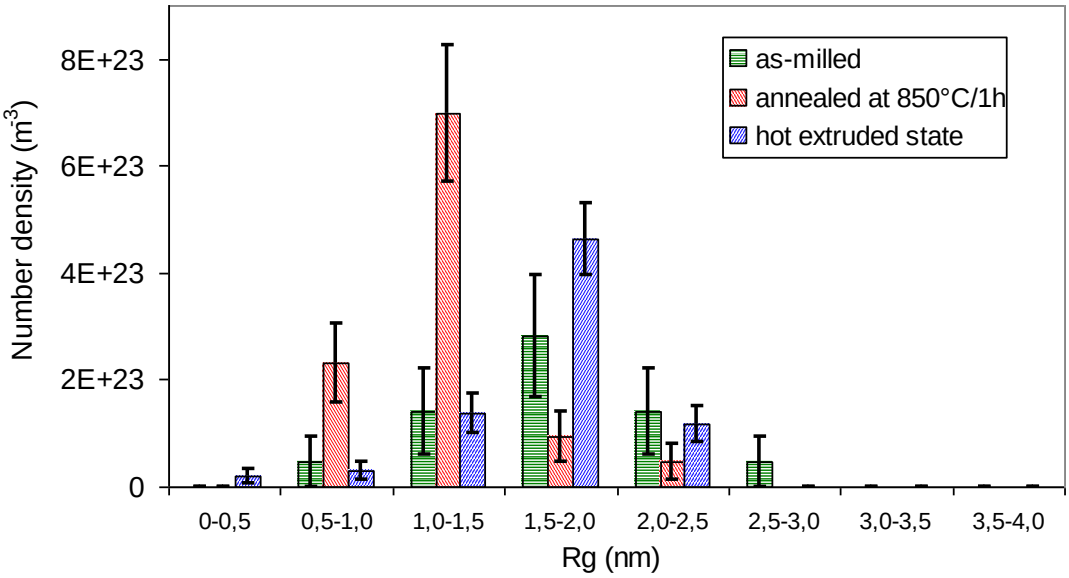

Figure 3.13. Size distribution of nanoparticles as the function of number density is shown in ODS steel in as-milled, annealed at 850°C as well as in hot extruded condition. (14, 50 and 70 nanoparticles are characterized respectively). Incertitude on number density, N_v, is given by $\Delta\rho = \frac{N_v}{\sqrt{N_p}}$*, where N_p is number of detected nanoparticles.*

It is observed that the Guinier radii of nanoparticles in all analysed conditions vary between 1 to 2.5 nm. The mean Guinier radius of nanoparticles in as-milled state is **1.8 nm** (-0.8/+1.2) and their mean number density is **(7 ± 2)×10^{23} m^{-3}**. The annealing treatment at 850°C during 1h induces a slight decrease of the mean Guinier radius down to **1.35 nm** (-0.35/+0.75) and a slight increase of their mean number density **(1.2±0.2)×10^{24} m^{-3}**. For the hot extruded condition, the mean radius of nanoparticles is **1.8 nm** (-1.3/+0.5) and the number density is **(7 ± 0.6) × 10^{23} m^{-3}**, as in the as-milled condition. The characteristics of these particles (nanometre sizes and high number densities (10^{23}-10^{24} m^{-3})) are comparable to those observed in different Ti-containing ODS alloys (for example MA 957 [31], 12 YWT [32] or 14YWT [2]).

b) Chemical composition

The chemical compositions of nanoparticles in the three states are reported in *Table 3.12*. The enrichment factor, is defined as the ratio of concentration in the cluster over the concentration in the matrix is also given.

Table 3.12. Nanoparticles and matrix compositions measured by APT in as-milled, annealed at 850°C during 1hour and hot extruded ODS steel. Composition for nanoparticles in as-milled state is calculated in accordance to two assumptions (depending on the peak O_2 / TiO which is considered at 32 amu on mass spectrum). Enrichment factor, F (ratio of the concentration in the feature over the matrix concentration) is also reported. Compositions are in at. %. Uncertainties are the standard deviation 2σ.

Elements	As-milled				Annealed at 850°C/1h			Hot extruded		
	Matrix	Nanoparticles TiO	Nanoparticles O_2	F	Matrix	Nanoparticles	F	Matrix	Nanoparticles	F
Fe	**77.7**	**69.9**		**0.90**	**79.7**	**54.2**	**0.70**	**76.8**	**43.3**	**0.60**
2σ	1.0	1.7			**0.2**	1.1		**0.2**	1.2	
Cr	**19.8**	**19.0**		**0.94**	**18.3**	**26.6**	**1.5**	**20.8**	**26.3**	**1.3**
2σ	0.2	1.5		-	0.2	1.0	-	0.2	1.1	-
Ti	**0.25**	**1.6**	**0.55**	**6.4/2.3**	**0.05**	**4.1**	**59**	**0.03**	**8.9**	**297**
2σ	0.02	0.5	0.3	-	0.01	0.4	-	0.01	0.7	-
Y	**0.16**	**4.1**		**25**	**0.04**	**5.5**	**138**	**0.02**	**6.5**	**325**
2σ	0.02	0.7		-	0.01	0.5	-	0.01	0.6	-
O	**0.26**	**4.3**	**5.0**	**16/20**	**0.19**	**8.0**	**50**	**0.10**	**12.9**	**129**
2σ	0.02	0.8	0.8	-	0.02	0.6	-	0.01	0.9	-
Si	0.98	0.91		1.0	0.97	1.0	1.0	1.20	1.20	0.9
2σ	0.03	0.4		-	0.03	0.2	-	0.05	0.3	-
C	0.03	n.s.			0.03	n.s.		0.05	n.s.	-
2σ	0.01				0.01			0.01		-
Ti+Y+O at.%	~10 at.%				~18 at.%			~28 at.%		

First of all, it appears that the levels of Fe and Cr measured inside the nanoparticles are always high (>70 at.%). This situation is similar for ordinary industrial ODS steels where different levels of Fe are reported by APT [33–35]. Indeed, the nanoparticles contain about 70, 55 and 44 at.% of Fe in as-milled, annealed and hot extruded samples respectively. Secondly, the level of Cr is also high, but contrary to Fe, it is significantly higher in annealed and extruded samples (~26 at.%) than in nanoparticles detected in as-milled powder (19 at.%). As it has been explained in Chapter 2 (section II.4 (d)), at least part of Fe and Cr detected into these nanoparticles can be due to trajectory overlaps. Thus, in addition to the measured level of Y, Ti and O in the nanoparticles (*Table 3.12*.), the ratios Y/Ti and (Y+Ti)/O are given on *Figure 3.14* (a, b).

The first point is that nanoparticles are enriched (F>1) in Y, O in all cases (whatever is the assumption about the peak at 32 amu in as-milled powder). The total level of Y, O and Ti is the highest in hot extruded samples (~28 at.%). It is higher in annealed powder (~18 at.%)

than in as-milled powder (~10 at.%). It is worth noticing that the behaviour of Ti differs slightly from the Y and O ones. Indeed, in the as-milled powder the enrichment factor of Ti is rather small (between 2 and 6 depending on the assumption) compared to enrichment factor of Y (25) and O (16 to 20). On the contrary, the enrichment in Ti is comparable to the Y and O enrichment in annealed and hot extruded samples. In other words, these nanoparticles are mainly enriched in Y and O in as-milled powder, whereas they are enriched in Y, O and Ti in other samples. This clearly appears on the *Figure 3.14*, where the ratio O/Ti and Y/Ti strongly decrease with temperature of annealing treatment. The same behaviour is observed for the ratio Y/O. A consequence is that (Ti+Y)/O ratio remains constant.

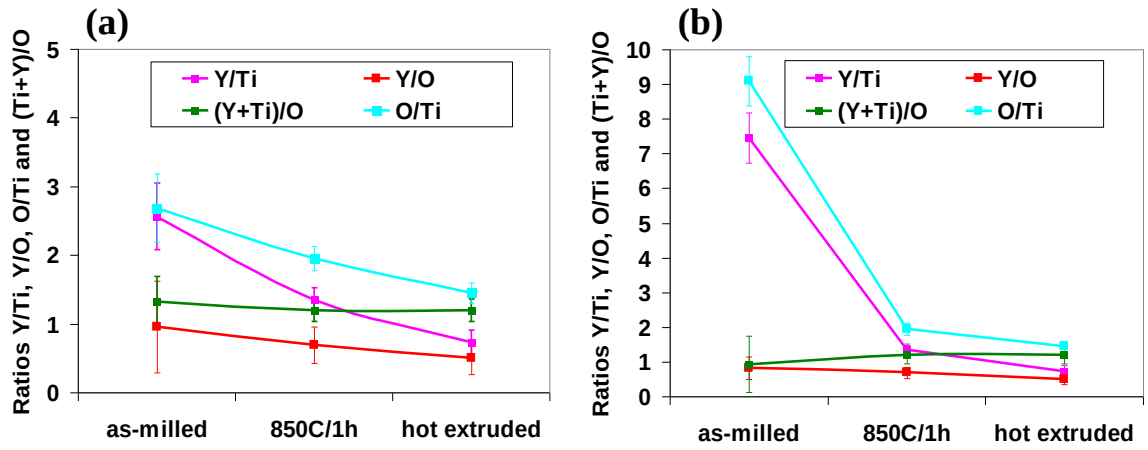

Figure 3.14. Mean Y/Ti, Y/O and (Ti+Y)/O ratios calculated for as-milled, annealed and hot extruded ODS steel (a) chemical composition of as-milled powder calculated in accordance to TiO assumption and (b) to O_2 assumption. In both cases (a, b) the significant enrichment in Ti is evident after subsequent heat treatments.

As far as the matrix composition is concerned, most of the Y, O and Ti are still in solid solution in the matrix in the as-milled powder (64, 72 and 83% respectively). In annealed and hot extruded samples, the higher the annealing temperature is, the lower remaining concentrations of Y, Ti and O in the matrix are. The concentrations of Y measured in the matrix of annealed (0.04±0.01 at.%) and hot extruded (0.02±0.01 at.%) samples are near solubility limit (0.035 and 0.05 at.% at 850 and 1000°C respectively [12]). A significantly less amount of Ti is measured in the matrix in comparison to its expected solubility limit (5.0 at.% 850°C [14]). The deviation from equilibrium binary diagram is possible in multicomponent system. Significant depletion of the matrix is correlated with nanoparticles evolution during annealing and hot extrusion.

However, as it can be seen in the *Table 3.12*, the O content in the matrix remains very high compared to other elements. Indeed, 40% of O detected in annealed powder is still in

solid solution (respectively 24 and 15 % for Ti and Y). In the hot extruded state the ratios are respectively 10, 6 and 17 % for Ti, Y and O. The concentration of O measured in the matrix is largely higher than the solubility limit (which is 0.06 at.% at 800°C [13]). Similar observation is done by Miller et al. [36], reporting the oxygen concentration in the matrix of as-processed 12YWT ODS to be <0.13 at.%. As already mentioned, first principles calculations by Fu et al [1, 16] show that O has strong affinity with vacancies. The high level of O remaining in the matrix could be due to the presence of stable O-V complexes.

c) Interfacial structure of nanoparticles

Core-shell structures of nanoparticles in different ODS steels (characterized by APT) were recently reported (MA957, ODS-Eurofer-97, Fe-12 wt.% Cr ODS [20]). The presence of the shell is reported independently of the size of nanoparticles [20].

In order to get information about the interfacial structure of the particles of this work, concentration profiles were plot through the particles. Two different orientations – perpendicular and parallel to the evaporation direction - were used to build these profiles. Typical profiles for 3 nm diameter particles in as-milled, annealed powders and in hot extruded ODS steel are shown on *Figure 3.15 (a-c)*.

As it is clearly visible in *Figure 3.15 (a-c)*, particles show an enrichment in Y, Ti, O and a depletion of Fe, whatever the profile axis is. Y-Ti-O enrichment is slightly less in the case of the as-milled material in comparison to others. Concerning Fe, the core concentration of these nanoparticles is 70, 50 and 40 at.% respectively for as-milled, annealed and hot extruded state.

For Cr, the situation is more complex, since Cr profiles differ if you consider profile parallel or perpendicular to analysis direction. Indeed, the Cr level in the direction perpendicular to the analysis axis increases in the cluster (as Y, Ti and O). On the contrary, if the profile axis corresponds to the analysis direction, the Cr level is higher at the cluster-matrix interface than in the cluster or in the matrix. It must be mentioned that, in the case of as-milled powder it is difficult to conclude on the Cr enrichment at interface.

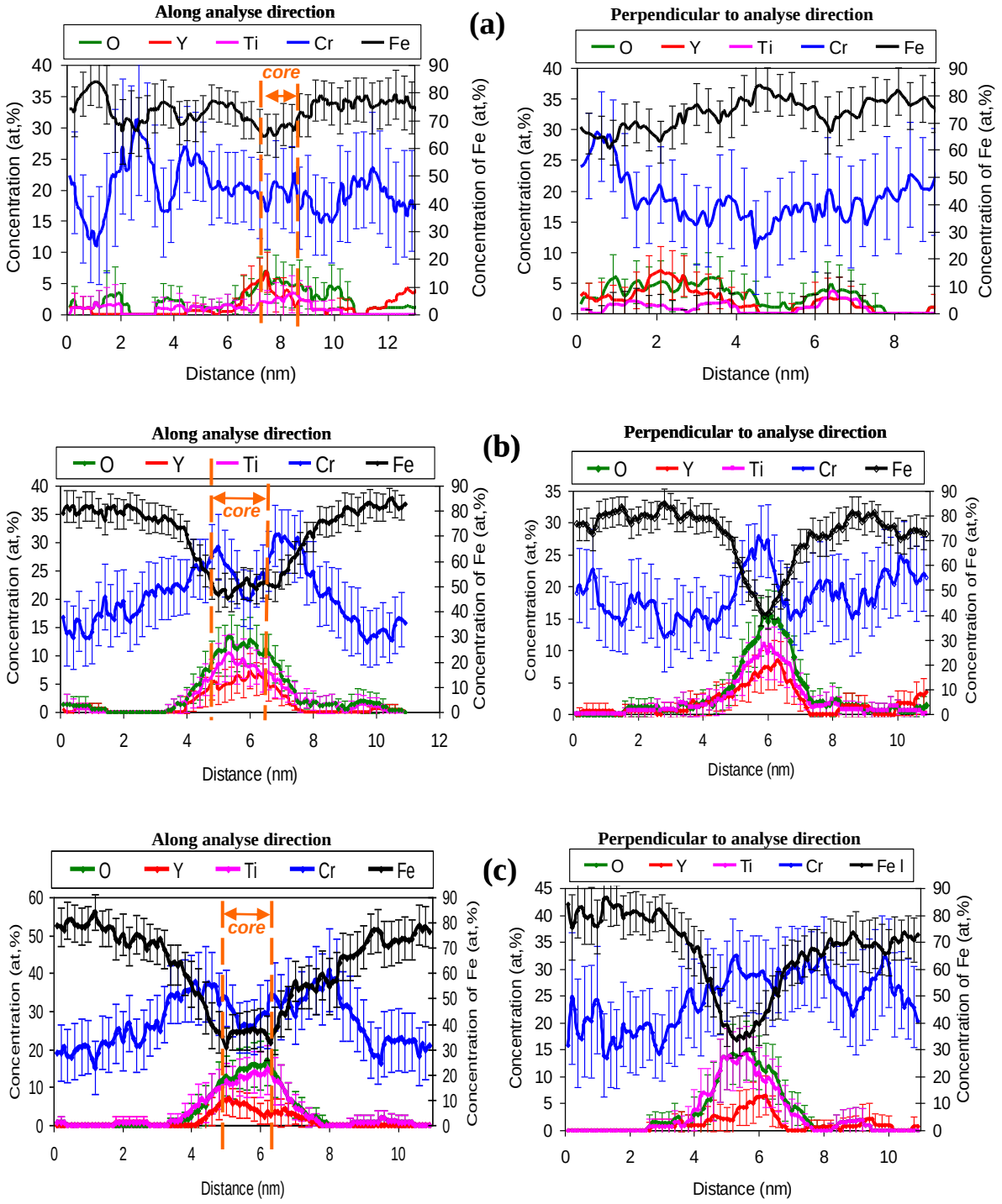

Figure 3.15. Typical concentration profiles through Y-Ti-O enriched nanoparticles observed in (a) as-milled and (b) annealed powders as well as (c) in hot extruded ODS steel. Concentration profiles are built along (left) and in the plane perpendicular to the evaporation direction (right) of the tip. Only Fe, Cr and Ti, Y, O species are shown. Sampling volume is 1,5×1,5×0.1 nm^3.

Such Cr behaviour suggests the existence of a Cr rich shell around a Ti-Y-O-rich core. The difference between Cr profiles along and perpendicular to analysis direction can be qualitatively explained by trajectory overlaps (has been discussed in Chapter 2, section II.4

(d)). As a consequence, the Cr atoms from the shell and Fe atoms from the matrix may be artificially displaced and mixed within nanoparticles. Thus, no clear distinction between Y-Ti-O-rich core and Cr-rich shell is possible (*Figure 3.15* (b-c)) on the profiles perpendicular to analyse axis.

Moreover, the most recent first principles calculations [37] performed for Ti-containing ODS steel, indicate that the presence of Cr in the core of nanocluster is not energetically favoured, i.e. the positive binding energies of Cr with Y and Ti suggest that they would interact repulsively in bcc iron resulting in Cr depletion in the core.

Several hypotheses can explain the existence of a core-shell structure: a) shell may act as interfacial phase, which reduces the surface energy of the particles favouring their nucleation [20,35]. b) Shell may result from a complex formation mechanism that includes solid state amorphization during MA process and crystallization of nanoparticle core during subsequent heat treatments. During the latter process, the formation of solute-rich shells may occur by depletion of the solutes that are not involved in crystallisation reaction [38–40].

II.3. Discussion

a) Comparison between APT, SANS and TEM results

ODS steels were also characterized by SANS [6] and TEM [6,29]. The *Table 3.13*, summarizes the different observations from each technique.

In the as-milled powder, TEM shows that the intragranular microstructure is homogeneous and composed of small nanograins (several hundreds of nanometres in diameter) [29]. However, no nanoparticle is visible. On the contrary, SANS [6] and APT reveal the presence of nanoparticles. According to APT, these objects are not well-defined nanoparticles, but "dilute" features (R_g=1.8±0.2 nm) mainly enriched in Y and O. The SANS data does not give a clear description of their nature. They suggest: (a) remnants from original yttrium oxides, (b) “fragments” of material coming from matrix particles, (c) metastable aggregates of atoms or (d) nanoparticles of point defects caused by milling [6].

The comparison between SANS and APT techniques shows discrepancies in terms of size and number density of these objects. There are several assumptions that can explain these discrepancies:

i) SANS data are treated considering that the shape of these features is spherical [6].

ii) The radius estimated by APT is a Guinier radius. In the case of non-spherical particles the size can be slightly overestimated. In order to estimate the radius of these nanoparticles independently of their shape, equivalent radius, R_{eq}, has been calculated for each particle. It has been calculated from the total number of atoms (N) included in the particle ($R_{eq} = \sqrt[3]{\frac{3NV_{at}}{4\pi Q}}$, where Q is the detection efficiency of the atom probe (0.58) and $V_{at}=a^3/2$ is the atomic volume with the lattice parameter a=0.2866 nm). An average equivalent radius equal to 1.7±0.2 nm has been calculated. So, the possibility that the size of these nanoparticles estimated by Guinier radius (R_g=1.8±0.2 nm) can be significantly overestimated can be rejected.

iii)SANS can "see" nanoparticles (as observed by APT) but also another kind of nanofeatures that remains invisible by APT (as an example point defects clusters).

Concerning powder subjected to annealing at 850°C during 1 hour, TEM reveals change in the internal microstructure in comparison to the as-milled state [29]. A bimodal distribution of grains is observed in this case: small grains (few hundreds of nanometres in diameter) preferentially located in the core of the powder and large grains (several micrometers in diameter) located near the surface. Large oxide particles with sizes from 50 to 100 nm in diameter and low number density are observed in large grains. EDX investigation indicates that these particles are enriched in yttrium. No information has been obtained by APT on these oxides particles.

The small grains contain a high density of dislocations as well as nanometric particles [29]. However, these latter are difficult to characterize because of their small size, near the resolution limit of TEM. Nevertheless, the presence of nanometric objects in this condition is reported by SANS and APT. From the point of view of APT, they are nanometric Y-Ti-O-rich nanoparticles. Both techniques give comparable sizes (R=1.2nm for SANS and R_g=1.35±0.2 nm for APT) and number densities ($1.4\times10^{24}m^{-3}$ for SANS and $1.2\pm0.2\times10^{24}$ m^{-3} for APT). So, in contrast to the as-milled condition, the comparison of sizes and number densities are fully consistent for both techniques.

Table 3.13. Summary of characterization of nano-reinforcements in ODS steel by TEM [6,7,29], *SANS* [6] *and APT.*

	TEM	**SANS***	**APT**
As-milled	• Microstructure inside of powder grain is homogeneous, composed of small nanograins (several hundreds of nanometres). • No nanoparticles are visible [29].	• Presence of small objects non identified • Radius 0.8 nm • Volume fraction 0.4% • Number density 1.9×10^{24} m^{-3}	• Presence of nanoparticles enriched in Y and O • Shape is not well defined • Mean radius 1.8 nm (-0.8/+1.2 nm) • Number density $7\pm2\times10^{23}m^{-3}$
Powder annealed at 850°C/1h	• Bimodal grain distribution (several hundreds of nanometres located in the core and several micrometers located on the surface of the powder) [29]. • Presence of precipitates (50-100 nm) in the large grains with a low number density • Presence of nanometric nanoparticles in small grains [29].	• Presence of nano phases • Radius 1.2 nm • Volume fraction 1% • Number density 1.4×10^{24} m^{-3}	• Presence of precipitates enriched in Y, Ti and O • Shape is spherical • Distribution in space homogeneous • Mean radius 1.35 nm (-0.35/+0.75 nm) • Number density $1.2\pm0.2\times10^{24}m^{-3}$
Hot extruded (final state)	• Elongated in extrusion direction grains (300 nm and 2 μm); • Presence of two populations of particles: a) located on grain boundaries with sizes 10-20 nm and b) homogeneously distributed inside of grains with mean radius 1.8 nm and density 0.8×10^{23} m^{-3}	• Presence of two populations of nano particles with a) mean radius 1.8 nm, number density 3.5×10^{23} m^{-3} and b) mean radius 5 nm and number density ~ 5×10^{21} m^{-3}; • Volume fraction 1.1% (0.85 and 0.25% respectively for R=1.8 and R=5 nm).	• Presence of precipitates enriched in Y, Ti and O • Shape is spherical • Distribution in space homogeneous • Mean radius 1.8 nm (-1.3/+0.5 nm) • Number density $7\pm0.6\times10^{23}m^{-3}$

* From reported by SANS mean radius, R, and volume fractions, F_v, the number density, N_v, was deduced in accordance to formula: $N_v = \frac{f_v}{V}$ where $\boldsymbol{f_v}$ is volume fraction of nanoparticles and $\boldsymbol{V}$ is a volume of a spherical precipitate.

In the hot extruded condition, TEM characterization [6] of the microstructure shows that it is made of very fine grains or ‘‘fibres”. Grains are elongated in the extrusion direction (several microns in longitudinal direction and about 300 nm in thickness), as expected after such a treatment. In addition, a high number density of dislocations, 10^{14}-10^{15} m^{-2}, is reported [6, 41]. Such densities have the same order of magnitude as in tempered martensitic ODS [42].

Different classes of oxides are observed [6, 7]: (a) located mainly on the grain boundaries with sizes from several tens of nanometres, (b) spherical nanoparticles (R=1.85 nm and density 8×10^{22} m^{-3}) homogeneously distributed.

As bigger particles are mainly located at grain boundaries and have a low number density ($<10^{21}$ m^{-3}), no information was obtained by APT (the probability to intercet a particle with such number density is low, especially if the APT tip is prepared in the extrusion direction, where grain size is around several micrometers). According to results of Sakasegawa et al., who showed existence of different populations of oxides depending on their size [43] in MA957, these bigger particles could be $Y_2Ti_2O_7$ or TiO_2 oxides.

The size of the smallest nanoparticles (R=1.85 nm) reported by TEM, are in good agreement with the size (R_g=1.8±0.2 nm) observed by APT. However, there is a discrepancy concerning number density. The density reported by APT is nearly ten times higher ($7\pm0.6\times10^{23}m^{-3}$) than the one reported by TEM ($8\times10^{22}m^{-3}$). Such discrepancy may be explained as following: a) in TEM, the density of nanoparticles is estimated considering a thickness of 100 nm, no direct measurements has been done [6], b) the contrast used for TEM does not always allow to distinguish all the particles and c) particles not visible by TEM are considered in APT data treatment (each nanoparticle containing more than 10 (Y, Ti, O) solute atoms was treated in APT experiments). From another hand, the procedure used for APT data treatment may overestimate the number density, since the nanoparticle fully inside the volume as well as the one on the surface contributes as 1 in the estimation of the number density.

SANS results [6] are consistent with the existence of two size distributions with mean radii R=1.8 nm and R=5 nm. Concerning number density, APT measurements are slightly higher ($7\pm0.6\times10^{23}m^{-3}$) for the hot extruded powder in comparison to SANS data (3.5×10^{23} m^{-3}). The reasons of such discrepancy can be: a) spatial fluctuations of nanoparticles in the

volume that cannot be accounted by APT and b) way of nanoparticle treatment in APT as discussed above.

From APT point of view, these smallest nano-oxides (R_g=1.8±0.2) are non-stoichiometric Ti-Y-O enriched particles.

In general, for nanoparticles observed in the powder annealed at 850°C during 1h and hot extruded material, agreement between TEM, SANS and APT techniques is reasonable.

b) Composition of nanoparticles

The Fe content reported by APT varies significantly in different ODS steels [32, 33, 36]. Relative Fe concentration inside particles in Eurofer ODS decreases with increasing particle size and no Fe is found by APT at the core of largest particles [35]. In our case, two possibilities could be considered: a) the decreasing content of Fe (70, 54 and 43 at.%) as a function of heat treatment could indicate thermodynamic reasons for the presence of the iron, b) some part of Fe can be introduced due to APT artefacts [10,11].

An attempt to quantify the contribution of matrix atoms artificially introduced in particles, due to trajectory overlaps in the vicinity of the interfaces is described below. The calculations are based on simple geometrical considerations and assumptions: a) the nanoparticle contains only Y, Ti and O (C_Y+C_{Ti}+C_O=100 at.%), b) nanoparticles are surrounded by Cr-rich shell (C_{Cr}=100 at.%) with R shell = 0.8 nm (estimated from concentration profile) and c) the matrix are composed only of Fe and Cr with experimentally measured concentrations.

Two basic ways to introduce Fe and Cr are considered, as indicated in *Figure 3.16* (a): i) Fe and Cr from matrix and ii) Cr from Cr-rich shell. The only exception is nanoparticles in as-milled state, where existence of Cr shell is not evident. Thus, the number of atoms coming from the matrix and Cr-rich shell into cluster $N_{cluster}^{artificial}$ can be defined as:

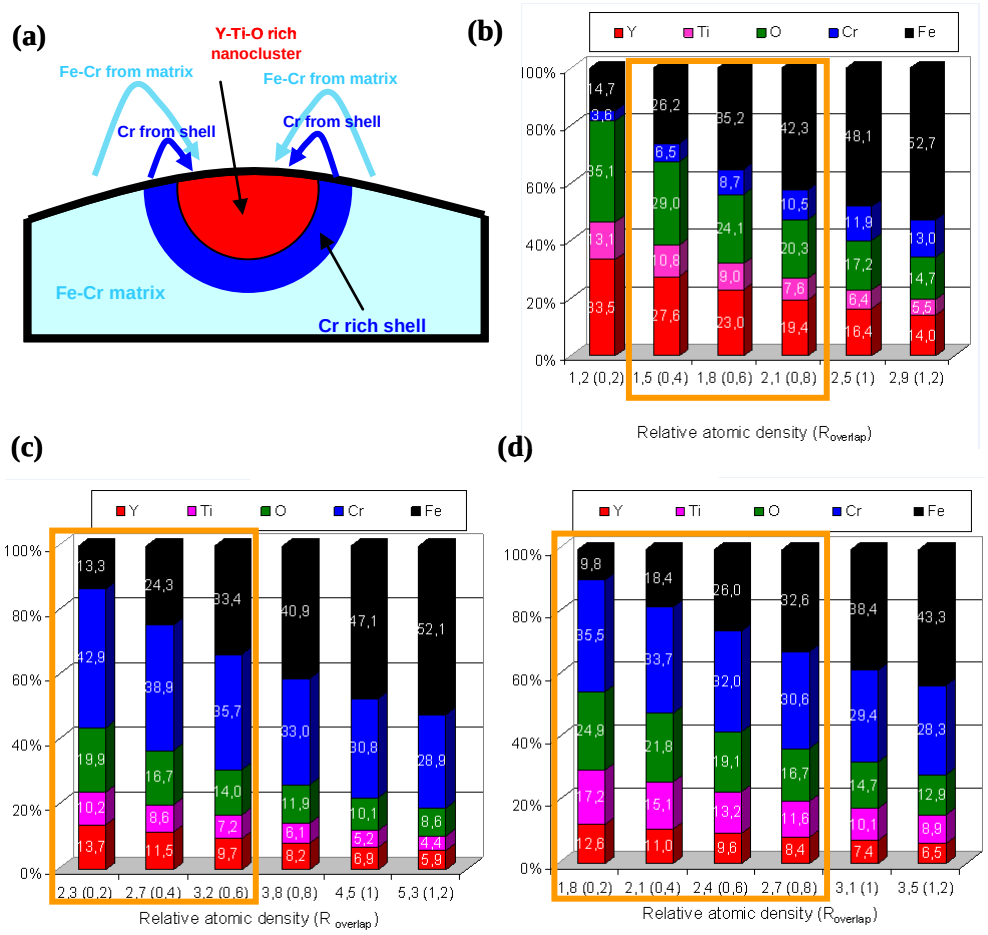

Figure 3.16. (a). Schematic representation of bias introduced in the spherical nanoparticle consisting of Y, Ti and O (C_Y+C_{Ti}+C_O=100 at.%) during field evaporation. (b) Diagrams showing concentration of Fe, Cr that can be artificially introduced in Ti, Y, O rich nanoparticles in (b) as-milled, (c) annealed at 850°C during 1h and (d) hot extruded material as a function of relative atomic density and zone of overlap ($R_{overlap}$ indicated in brackets).

$$N_{cluster}^{artificial} = \eta \frac{C_{Fe}^{matrix}}{V_{at}} V_{overlap} + \eta \frac{C_{Cr}^{matrix}}{V_{at}} V_{overlap} + \eta \frac{C_{Cr}^{Shell}}{V_{at}} V_{shell} \quad (3.1)$$

where $C_{Fe}^{matrix}, C_{Cr}^{matrix}$ are measured concentrations of Fe and Cr in the matrix (taken from *Table 3.12*) and C_{Cr}^{Shell} is the concentration of Cr in the shell (assumed here to be 100 at.%.). V_{at}=a^3/2 is the atomic volume with the lattice parameter a=0.2866 nm. η is the overlap rate, showing how many atoms can be artificially moved from the matrix to nanoparticles, and is equal to 0.3, according to [10]. $V_{overlap}$ is the overlapped zone, that corresponds to the region in the matrix from where Fe and Cr can be introduced in the nanoparticle. This parameter is not known, so it will vary from R=0.4 to 1.2 nm. V_{shell} is the volume of the Cr-rich shell. The

concentration of element, *i*, that is Fe, Cr, Ti, Y and O in the nanoparticle then can be deduced from relation:

$$C_i = \frac{N_i}{N_{cluster}^{real} + N_{cluster}^{artificial}} \tag{3.2}$$

where N_i is the number of chemical specie, *i*, and $N_{cluster}^{real}$ the number of atoms that form the nanoparticle (Y, Ti and O). The results of calculations for as-milled, annealed and hot extruded nanoparticles are reported in *Figure 3.16* (b-d).

As it was previously mentioned the artificially introduced matrix atoms, in particular Fe and Cr, result in an increase of the relative atomic density inside the nanoparticles. In accordance with experimental results, the relative atomic density increases by a factor 2 in nanoparticles in as-milled state and factors 2 and 2.5 in annealed at 850°C during 1h and hot extruded states. So, taking into account the increase of atomic density, several conclusions can be done:

a) the radius of overlapped zone, $R_{overlap,}$ from 0.2 to 0.8 nm give the experimentally observed increase of relative atomic density.

b) around 36-42 at.% of Fe as well as 8.7-10.5 at.% of Cr can be introduced in nanoparticles in as-milled state as a result of the local magnification effect. It should be mentioned that for as-milled nanoparticles, calculations are performed in accordance to assumption that there is no Cr-rich shell around Y-Ti-O-rich nanoparticle (since no clear evidence was observed in experimental data). From these calculations, the content of Fe and Cr that can be artificially introduced into nanoparticles is slightly smaller in comparison to the experimentally measured one (70 and 19 at.% respectively for Fe and Cr).

c) about 10-33 at.% of Fe and 30-46 at.% of Cr can be introduced in nanoparticles after annealing and hot extrusion (resulting in an increase of the relative atomic density from 1.8 to 3.2 times). It should be mentioned that the content of Cr estimated from these calculations are higher than the experimentally observed ones (26.6 and 26.3 at.% respectively in annealed and hot extruded samples). It should be keep in mind that in reality, the concentration of Cr rich shell may be lower than 100 at.%. As a consequence smaller content of Cr atoms would be introduced into Y-Ti-O-rich nanoparticles, decreasing the difference with experimental results.

Therefore, following these calculations the measured level of Fe in the nanoparticles can not be only explained by trajectory overlaps. Some underplaying level of Fe may be present originally in these nanoparticles.

Another kind of calculations may also be done. The main idea is to separate the mixed atoms in the nanoparticles, those which initially contributed to nanoparticle (Y, Ti, O) and those which were in the matrix (Fe, Cr). In the literature different methods for concentration correction were discussed and applied [11, 44]. In our calculations, the increase of the relative atomic density is a key parameter, in accordance to which the number of excess atoms of Fe and Cr that should be removed from clusters is determined. In order to perform a correction, we suppose that: a) the atomic density into particles is the same than the BCC iron one, b) the nanoparticle consists of Y, Ti, O and may contain some true level of Fe and Cr, c) nanoparticles are surrounded by Cr-rich shell (C_{Cr}=100 at.%) with R shell = 0.8 nm excepted in as-milled state and d) the matrix are composed only of Fe and Cr with experimentally measured concentrations.

The compositions of nanoparticles calculated in accordance to the described assumptions are represented in *Table 3.14*. After annealing and hot extrusion, the amount of Cr atoms that "artificially" entered into the nanoparticles exceeds the number of atoms that has been measured by APT. This is the reason, why no Cr is present after correction in the table (*Table 3.14*). It may be concluded that removal of Cr that comes from Cr-rich shell allows keeping relative atomic density equal to 1. In other words, the increase of the relative atomic density observed in nanoparticles may be caused by Cr that comes from the surrounding Cr-rich shell.

Table 3.14. Corrected chemical composition of nanoparticles in as-milled, annealed and hot extruded ODS steel.

	As-milled	Annealed state	Hot extruded state
Fe	67 to 62	59.0 to 42.0	47.0 to 21.6
Cr	18.0 to 17.0	-	-
Y	6.0 to 9.0	13.0 to 18.0	12.0 to 18
Ti	2.4 to 3.5	9.5 to 13.5	17.0 to 25
O	7.0 to 9.0	19.0 to 26.0	24.0 to 35.7
Y+Ti+O	15-22 at%	41-58 at%	53-78 at%

In this case, the amount of Fe that can be present in the nanoparticles remains quite high: 67-62 at.%. It should be mentioned that there is a relatively good agreement with the APT composition, indicating that just small part of Fe is introduced due to local magnification effect. The major part of the measured Fe is originally present in these nanoparticles. The main enrichment of these nanoclusters after subsequent heat treatments appears mainly in terms of Ti (in 4 and 7 times higher after annealing and hot extrusion respectively in comparison to as-milled state) and O (~3 and ~4 times higher respectively for annealed and

hot extruded state) incorporation, whereas just slight enrichment in Y is observed (~2 times higher for both annealed and hot extruded state). As it will be shown below, this can be linked with the fact that Y is the slowest diffuser. In addition, some part of Y (36% owing to APT) is located in Y-O rich nanoclusters just after mechanical alloying step.

c) Formation mechanism of nanoparticles in ODS steel

Different formation mechanisms of nanoparticles have been detailed in Chapter 1 (Section III.3 (c)). In present case, nanometric nanoparticles are observed in the ODS steel just after mechanical alloying step.

Considering the materials that have been studied in this work, a formation mechanism for oxide nanoclusters could be suggested. Mechanical alloying results in: a) dissolution of Y_2O_3 initial oxide inducing supersaturation of Y and O in the matrix (64 and 72 % of Y, O respectively) and b) formation of Y-O-enriched aggregates. These Y-O enriched phases could contain some amount of Ti (up to 1.6±0.5 at.%). However, the origin of YO-rich aggregates is still not clear. Two possibility can be considered: (i) they are produced by the direct transformation (under ball milling conditions) of Y_2O_3 oxide towards Y-O-rich phases or (ii) complete dissolution of Y_2O_3 occurs first and then Y-O-rich phase nucleates. Since Y_2O_3 is very stable oxide (heat of formation of - 1907 $kJ.mol^{-1}$ [9]), milling time and intensity of industrial attritor may not be sufficient fully dissolve it in Fe-Cr matrix. From this point, the hypothesis that MA results in only a partial dissolution of original Y_2O_3 powder seems to be probable. Tendency of Y_2O_3 to amorphization during ball milling process has been widely demonstrated [17–19].

Subsequent annealing or hot extrusion, results in significant depletion of matrix in Y, O and Ti, whereas nanoparticles become more enriched. Y-O nanoparticles in as-milled state, act as nuclei for the formation of the nano-oxide particles. Y, O and Ti are incorporated to these nuclei, resulting in their enrichment. After annealing or hot extrusion, most of Ti and Y are located into nanoparticles. The schematic representation of nanoparticles formation is summarized in *Figure 3.17*.

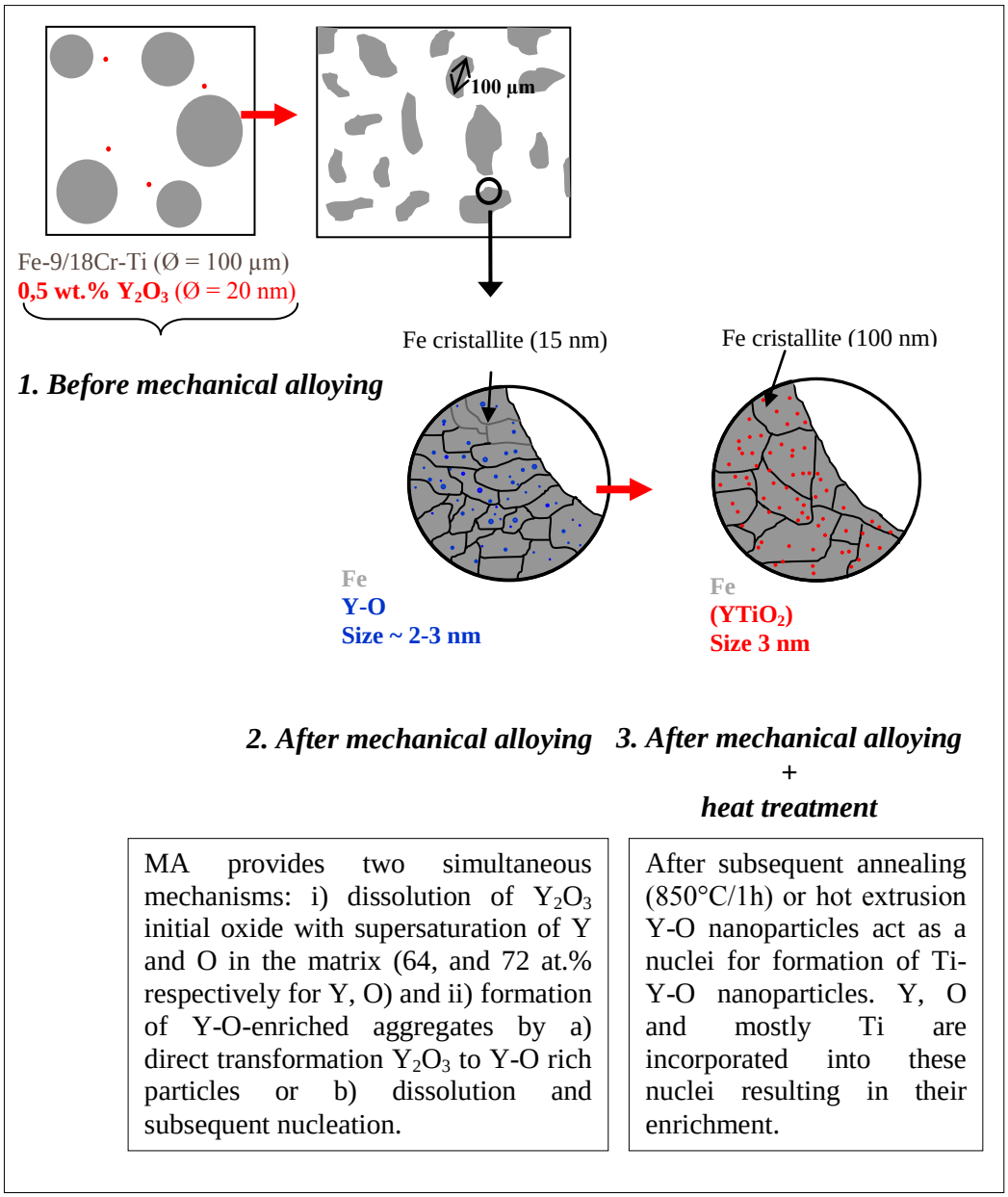

Figure 3.17. Mechanism of nanoparticles formation in ODS steel after [6].

II.4. Partial conclusions

ODS steel was produced by mechanical alloying of FeCrWTi pre-alloyed powder with 0.5wt.% of Y_2O_3 in industrial attritor mill. The microstructure and especially nanoparticles were studied in as-milled, annealed and final hot extruded states by APT. Results are compared to SANS [6] and TEM [6, 7, 41] data. The main conclusions of the work are the following:

- Nanometric particles enriched in Y and O are found in as-milled state. They are nanometric in sizes and have a high density;
- Subsequent annealing or hot extrusion results in the precipitation of ~3 nm in diameter Ti-, Y-, O-enriched nanoparticles.
- Reasonable agreement was found between SANS and APT results in case of annealed at 850°C/1h and extruded powder.

A formation mechanism for ODS steel can be suggested: a) mechanical alloying provides two simultaneous mechanisms: i) dissolution of Y_2O_3 initial oxide (inducing supersaturation of Y and O in BCC matrix) and ii) formation of Y-O-enriched aggregates (more probable remnants of original Y_2O_3 powder); b) during subsequent annealing or hot extrusion, Y-O act as nuclei for the formation of the nano-oxide particles. Y, O and Ti are incorporated to these nuclei, resulting in their enrichment. After annealing or hot extrusion, most of Ti and Y are located in the nanoparticles.

III. Bibliography of Chapter 3

[1] M.K. Miller, C.L. Fu, M. Krcmar, D.T. Hoelzer, C.T. Liu, Front. Mater. Sci. China 3 (2008) 9–14.

[2] M.J. Alinger, G.R. Odette, D.T. Hoelzer, Acta Materialia 57 (2009) 392–406.

[3] L. Toualbi-Bénévise, Mécanismes Mis En Jeu Lors De La Mécanosynthèse Des ODS : Apport De La SAT Et De La Diffraction De Rayons X Et De Neutrons. Présentation. Materiaux Conférence, Nant, 18-22 October, 2010.

[4] L. Toualbi, M. Ratti, G. André, F. Onimus, J. Malaplate, Y. de Carlan, Proceedings of the 14th International Conference on Fusion Reactor Materials, (2009).

[5] L. Toualbi, M. Ratti, G. André, F. Onimus, Y. de Carlan, Journal of Nuclear Materials 417 (2011) 225–228.

[6] M. Ratti, Développement De Nouvelles Nuances D'acier Ferritiques/martensitiques Pour Le Gainage D'élément Combustible Des Réacteurs à Neutrons Rapides Au Sodium. Thèse, Institut Polytechnique de Grenoble, 2009.

[7] Y. de Carlan, J.-L. Bechade, P. Dubuisson, J.-L. Seran, P. Billot, A. Bougault, T. Cozzika, S. Doriot, D. Hamon, J. Henry, M. Ratti, N. Lochet, D. Nunes, P. Olier, T. Leblond, M.H. Mathon, Journal of Nuclear Materials 386-388 (2009) 430–432.

[8] M. K. Miller, Atom-probe Tomography: Analysis at the Atomic Level, Kluwer Academic/Plenum, New York, 2000.

[9] T.C. Totemeier, C.J. Smithells, Smithells Metals Reference Book, Butterworth-Heinemann, 2004.

[10] D. Blavette, F. Vurpillot, P. Pareige, A. Menand, Ultramicroscopy 89 (2001) 145–153.

[11] F. Vurpillot, A. Bostel, D. Blavette, Appl. Phys. Lett. 76 (2000) 3127.

[12] H. Okamoto, JPE 16 (1995) 473–473.

[13] M. Hansen, K. Anderko, 2nd ed, McGraw Hill New York, 1958.

[14] H. Okamoto, Journal of Phase Equilibria 17 (1996) 369–369.

[15] C. Suryanarayana, Progress in Materials Science 46 (2001) 1–184.

[16] C.L. Fu, M. Krcmar, G.S. Painter, X.-Q. Chen, Phys. Rev. Lett. 99 (2007) 225502.

[17] Y. Kimura, S. Takaki, R. Suejima, R. Uemori, H. Tamehiro, ISIJ Int (Iron Steel Inst Jpn) 39 (1999) 176–182.

[18] S. Begin-Colin, G. Le Caër, M. Zandona, E. Bouzy, B. Malaman, Journal of Alloys and Compounds 227 (1995) 157–166.

[19] M. Ruhle, T. Steffens, Zeitschrift Für Metallkunde 83 (1992) 436–440.

[20] E.A. Marquis, Applied Physics Letters 93 (2008) 181904.

[21] A.R. Denton, N.W. Ashcroft, Phys. Rev. A 43 (1991) 3161–3164.

[22] P. Bellon, R.S. Averback, Phys. Rev. Lett. 74 (1995) 1819.

[23] Y. Chen, M. Bibole, R. Le Hazif, G. Martin, Phys. Rev. B 48 (1993) 14.

[24] P. Pochet, P. Bellon, L. Chaffron, G. Martin, MSF 225-227 (1996) 207–216.

[25] P. Bellon, F. Soisson, G. Martin, 3 (1993) 1977–1979.

[26] P.R. Soni, Mechanical Alloying: Fundamentals and Applications, Cambridge International Science Publishing, 1999.

[27] B.Q. Zhang, L. Lu, M.O. Lai, Physica B: Condensed Matter 325 (2003) 120–129.

[28] R.B. Schwarz, MSF 269-272 (1998) 665–674.

[29] F. Delabrouille, Rapport H-T27-2010-00646-FR. Caractérisation Au Microscope Electronique En Transmission D'alliages NDS Et ODS (ANR AXTREM), 2010.

[30] M. Klimiankou, R. Lindau, A. Möslang, Journal of Crystal Growth 249 (2003) 381–387.

[31] M.K. Miller, D.T. Hoelzer, E.A. Kenik, K.F. Russell, Journal of Nuclear Materials 329-333 (2004) 338–341.

[32] M.K. Miller, E.A. Kenik, K.F. Russell, L. Heatherly, D.T. Hoelzer, P.J. Maziasz, Materials Science and Engineering A 353 (2003) 140–145.

[33] D. Larson, P. Maziasz, I. Kim, K. Miyahara, Scripta Materialia 44 (2001) 359–364.

[34] M.K. Miller, K.F. Russell, D.T. Hoelzer, Journal of Nuclear Materials 351 (2006) 261–268.

[35] C.A. Williams, E.A. Marquis, A. Cerezo, G.D.W. Smith, Journal of Nuclear Materials 400 (2010) 37–45.

[36] M.K. Miller, D.T. Hoelzer, E.A. Kenik, K.F. Russell, Intermetallics 13 (2005) 387–392.

[37] D. Murali, B.K. Panigrahi, M.C. Valsakumar, S. Chandra, C.S. Sundar, B. Raj, Journal of Nuclear Materials 403 (2010) 113–116.

[38] L.L. Hsiung, M.J. Fluss, S.J. Tumey, B.W. Choi, Y. Serruys, F. Willaime, A. Kimura, Phys. Rev. B 82 (2010) 184103.

[39] L.L. Hsiung, M.J. Fluss, A. Kimura, Materials Letters 64 (2010) 1782–1785.

[40] L. Hsiung, M. Fluss, S. Tumey, J. Kuntz, B. El-Dasher, M. Wall, B. Choi, A. Kimura, F. Willaime, Y. Serruys, Journal of Nuclear Materials 409 (2011) 72–79.

[41] J. Malaplate, F. Mompiou, J.-L. Béchade, T. Van Den Berghe, M. Ratti, Journal of Nuclear Materials In Press (2011).

[42] R.A. Renzetti, H.R.Z. Sandim, R.E. Bolmaro, P.A. Suzuki, A. Möslang, Materials Science and Engineering: A (2011).

[43] H. Sakasegawa, L. Chaffron, F. Legendre, L. Boulanger, T. Cozzika, M. Brocq, Y. de Carlan, Journal of Nuclear Materials 384 (2009) 115–118.

[44] A. Morley, G. Sha, S. Hirosawa, A. Cerezo, G.D.W. Smith, Ultramicroscopy 109 (2009) 535–540.

Table of content

Chapter 4. Nitride Dispersion Strengthened Steels 131

I. Study of MA NDS steel 131

I.1. Matrix chemical composition 132

I.2. Grain boundaries study 133

a) Powder annealed at 600°C/1h 133
b) Powder annealed at 700°C/1h 135
c) Hot extruded state 136
d) Segregation intensity as a function of temperature 137

I.3. Nanoparticles characterization 138

a) As-milled condition 138
b) Annealing at 600°C/1h 141
c) Annealing at 700°C/1h 144
d) Hot extruded condition (800°C) 146
e) Annealing at 850°C/1h 148
f) Annealing at 1000°C/1h 152

I.4. Discussion 153

a) Chemical composition of nanoparticles 153
b) Precipitation and kinetics 158
c) Comparison between ODS and NDS 162

I.5. Partial conclusion 164

II. Study of nitrided NDS 165

II.1. Characterization of powders 166

a) Powder in as-nitrided state 167
b) Powder annealing at 600°C/1h 168
c) Powder annealing at 700°C/1h 171

II.2. Characterization of consolidated material 175

a) Experiment 1. LATAP 175
b) Experiment 2. LAWATAP 176
c) Experiment 3. LAWATAP 178

II.3. Discussion 180

II.4. Partial conclusions 183

III. Bibliography of Chapter 4 184

Chapter 4. Nitride Dispersion Strengthened Steels

This fourth chapter describes Atom Probe results obtained on the two types of Nitride Dispersion Strengthened steels: the first one is elaborated by mechanical alloying of Fe-18Cr-1W-0.14N powder with TiH_2 (named MA NDS steel) and the second one by plasma nitriding of Fe-18Cr-1W-0.75Ti powder (named nitrided NDS steel). In both cases, APT results will be compared to SANS [1,2] and TEM [3] results obtained in the framework of the ANR project and the formation mechanisms of nitrides will be discussed.

I. Study of MA NDS steel

Powder grains of MA NDS steel are studied in the as-milled state (i.e. directly after mechanical alloying) and after different heat treatments up to 1000°C during 1h, in order to study the formation of nitrides and their stability. In addition, MA NDS steel is studied in the consolidated state, after hot extrusion at 800°C.

As for ODS steel, two complementary Atom Probes were used: the LATAP and the LAWATAP. The summary of different analyses realised are given in *Table 4.1*.

Table 4.1. APT experiments performed on the MA NDS steel in each state.

Materials	APT	Number of analyses	Number of analyzed atoms
As-milled powder	TAP	1	500 000
	LAWATAP	2	12×10^6
Powder annealed at 600°C/1h	TAP	1	200 000
	LAWATAP	1	16×10^6
Powder annealed at 700°C/1h	TAP	1	900 000
	LAWATAP	1	15×10^6
Powder annealed at 850°C/1h	TAP	2	900 000
	LAWATAP	2	7×10^6
Powder after hot extrusion at (800°C)	TAP	1	500 000
	LAWATAP	1	15×10^6
Powder annealed at 1000°C/1h	TAP	1	400 000
	LAWATAP	1	15×10^6

In all analysed conditions, the precipitation of a second phase was detected. In addition, several grain boundaries were observed as well. Results are presented in following way. Firstly, matrix compositions are provided. Afterwards, the results of grain boundary investigations are shown. Then, the information about particles (sizes, number densities and

compositions) are given. All along the chapter, the results will always be presented in the following order: as-milled powder, annealed powders at 600 and 700 during 1h, hot extruded steel (at 800°C) and annealed powders at 850 and 1000°C during 1h.

I.1. Matrix chemical composition

Chemical compositions of the matrix for each state are reported in the *Table 4.2*.

Table 4.2. Matrix composition of MA NDS powders (as-milled, annealed at 600, 700, 850 and 1000°C during 1h) and consolidated steel (by hot extrusion at 800°C) measured by LATAP. Concentrations are in at.%. Balance is iron. O and Al traces are detected but values (not reported) are of the order of the background noise.

	Ti	**N**	**Cr**	**Ni**	**Mn**	**W**	**Si**	**C**
Bulk	**0.57**	**0.54**	**19.0**	**-**	**-**	**0.30**	**-**	**-**
				as-milled powder				
at .%	**0.46**	**0.41**	**18.2**	**0.20**	**0.23**	**0.21**	**0.40**	**0.05**
2σ	*0.02*	*0.02*	*0.2*	*0.03*	*0.02*	*0.02*	*0.02*	*0.01*
				Annealed at 600°C/1h powder				
at .%	**0.10**	**0.11**	**14.9**	**0.18**	**0.12**	**0.13**	**0.40**	**0.02**
2σ	*0.02*	*0.02*	*0.20*	*0.03*	*0.02*	*0.02*	*0.03*	*0.01*
				Annealed at 700°C/1h powder				
at .%	**0.14**	**0.13**	**16.9**	**0.17**	**0.20**	**0.22**	**0.41**	**0.03**
2σ	*0.01*	*0.01*	*0.01*	*0.02*	*0.02*	*0.02*	*0.02*	*0.01*
				Hot extruded state				
at.%	**0.04**	**0.06**	**17.2**	**0.17**	**0.18**	**0.19**	**0.31**	**0.01**
2σ	*0.01*	*0.01*	*0.20*	*0.02*	*0.02*	*0.02*	*0.02*	*0.003*
				Annealed at 850°C/1h powder				
at.%	**0.04**	**0.05**	**19.1**	**0.13**	**0.16**	**0.25**	**0.39**	**0.09**
2σ	*0.01*	*0.01*	*0.12*	*0.01*	*0.02*	*0.02*	*0.02*	*0.01*
				Annealed at 1000°C/1h powder				
at .%	**0.03**	**0.05**	**18.8**	**0.18**	**0.21**	**0.23**	**0.28**	**0.05**
2σ	*0.01*	*0.01*	*0.20*	*0.20*	*0.02*	*0.01*	*0.02*	*0.01*

The matrix composition of as-milled powder is slightly depleted in Ti, N and W in comparison to nominal values. A small amount of C (not expected) is detected.

After annealing at 600 and 700 °C during 1h and after hot extrusion, matrix becomes strongly depleted in Ti and N in comparison to nominal values. This depletion is more

pronounced in the matrix of powders annealed at 850 and 1000°C during 1h. As it will be shown later, Ti as well as N species are involved in the precipitation of the second phase.

The matrixes of powders annealed at 600, 700°C and of the consolidated material are depleted in Cr whereas the concentration of Cr in the matrix of as-milled, annealed at 850 and 1000°C powders is in good agreement with nominal values. These depletions are linked to segregation on grain boundaries described later.

As far as W is concerned, lower concentrations are measured in the matrix for all conditions in comparison to nominal values. Concerning the rest of elements, variations of Ni, Mn and C concentrations are measured from one state to another.

I.2. Grain boundaries study

Grain boundaries (GB) are non-equilibrium features, characterised by an increased energy compared to the perfect lattice of the grain [4]. GB can interact with point defects and solute atoms, resulting in inter-granular segregation or depletion. Such changes in local chemistry may alter properties of GB. So, investigations of such segregations are of technological interest.

Several grain boundaries were observed during APT characterisation of MA NDS steel. They were identified thanks to Cr segregation. Before presenting the results, the method used for the quantification of the GB segregation is defined:

a) Concerning the chemical analysis, composition profiles through GB are plotted perpendicularly to the GB plane. These profiles represent the relative excess of solutes ($C_{boundary}/C_{matrix}$). When particles are present at GB, attention is paid to avoid their presence along the profile.

b) Si and N species are presented together as N(Si) overlap on the mass spectrum.

c) No quantitative data on Ni are given on GB because of the low mass resolution and the too small number of atoms corresponding to each point on the profile (see section II.4 of the Chapter 2).

The segregations observed in MA NDS powders annealed at 600, 700°C during 1h as well as in hot extruded state are described below

a) Powder annealed at 600°C/1h

Individual atom maps, showing GB as well as nanoparticles (dashed grey circles) in powder annealed at 600° during 1h are depicted on *Figure 4.1* (a). From visual inspection, Cr enrichment is clearly seen and traces of W, Ti and N(Si) can be distinguished.

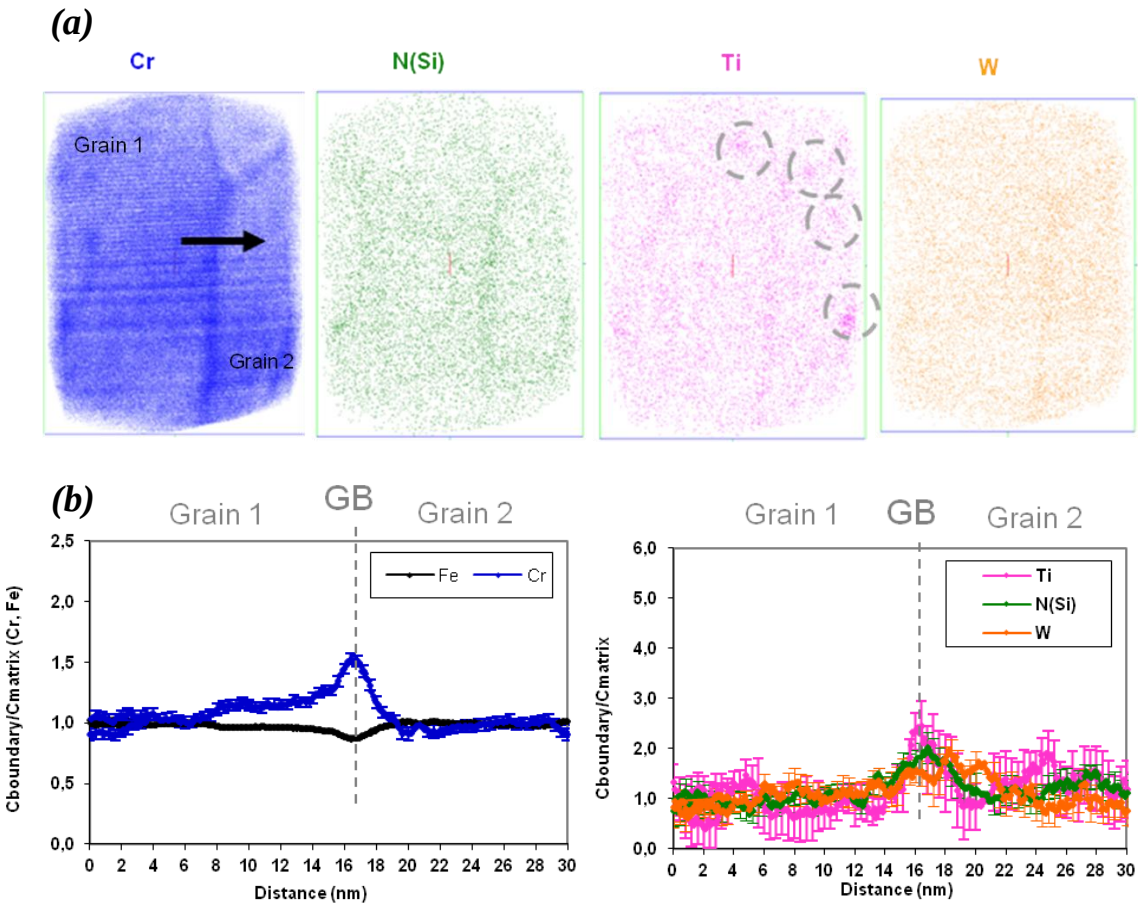

Figure 4.1. Grain boundary observed in MA NDS powder annealed at 600°C during 1h. (a) 3D atom maps are shown for Cr, Ti, W and N(Si) species; Ti-enrichment corresponding to nanoparticles can be seen in Ti map (dashed circles). (b) Variation of $C_{boundary}/C_{matrix}$ measured across the grain boundary plane as indicated by arrow in (a). (Cr and Fe are on the left profile and N(Si), Ti, and W species on the right one). $C_{boundary}$ corresponds to the concentration measured in the sampling volume $6\times8\times1$ nm^3. C_{matrix} is equal to the concentration of the element measured in the matrix.

Composition profile drawn across this grain boundary (as indicated in *Figure 4.1* (a)) confirms Cr enrichment (*Figure 4.1* (b)) as well as enrichment in Ti, N(Si) and W. However, it should be mentioned that concentration profile exhibit asymmetric behaviour with respect to Cr, which segregates up to 10 nm in the grain 1. The maximum peak of W is slightly shifted in comparison to Ti, N(Si) and Cr peaks (*Figure 4.1* (b)). Normally, the highest solute concentrations correspond to GB`s core, however, elastically strained region near GB also can result in significant segregation outside the core [5, 6].

Cr segregation is detected for all studied GBs within this temperature condition. The relative excess of Cr ($C_{boundary}/C_{matrix}$) varies from 1.44 to 1.6. As for Ti, N(Si) and W, enrichments are clearly visible at several GB but not in all cases.

b) Powder annealed at 700°C/1h

3D atom maps showing GBs and nanoparticles in powder annealed at 700°C during 1h are shown *Figure 4.2* (a). The enrichment of Cr, N(Si), Ti, in less extend W and Mn is visible. Composition profiles shown on *Figure 4.2* (b), clearly revealed Cr, Ti, N(Si), W and Mn enrichment on GB as well. As for Cr, like in the previous case (600°C), the relative excess varies from one GB to another. Variations from 1.4 to 2.1 are observed.

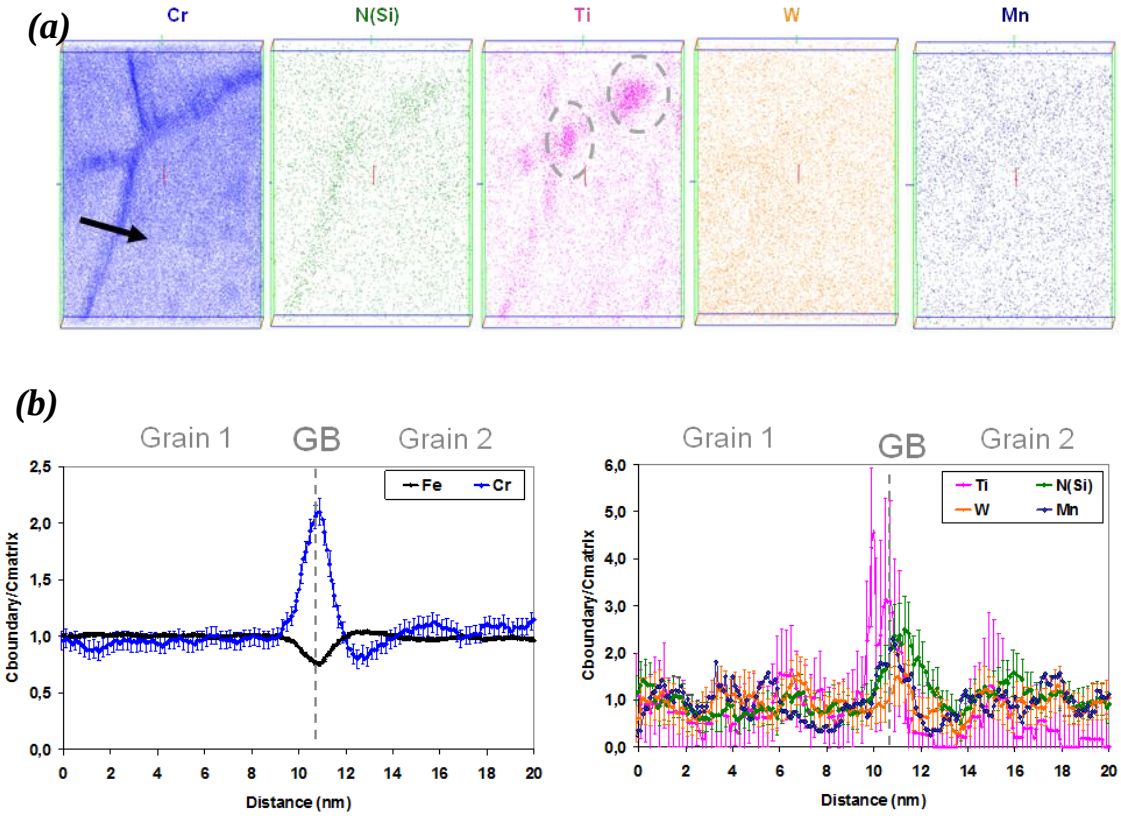

Figure 4.2. Grain boundaries observed in MA NDS powder annealed at 700°C during 1h. (a) 3D atom maps are shown for Cr, Ti, W, Mn and N(Si) species; Ti-enrichment corresponding to nanoparticles can be seen in Ti map (dashed circles) (b) Variation of $C_{boundary}/C_{matrix}$ measured across the grain boundary as indicated by the arrow in (a). (Cr and Fe are on the left profile and N(Si), Ti, Mn and W species on the right one). $C_{boundary}$ corresponds to the concentration measured in a sampling volume of 6×8×1 nm^3. C_{matrix} is equal to the concentration of the element measured in the matrix.

Concerning Ti, W, Mn and N(Si) species (*Figure 4.2* (b)), concentration profile confirmed their enrichment. However, the maximum peak of Ti is shifted up to 1 nm in the direction of Grain 1 relatively GB position. Similar shift of maximum peak can be noticed for N(Si) up to 1.5 nm in the direction of Grain 2. As it was mentioned previously, the solute segregation may occur not only for GB core but also as a result of solute interaction with strained regions next to GB [5, 6]. Taking into account standard deviations, Ti shows the higher excess, in comparison to W, Mn and N(Si) species.

c) Hot extruded state

Only one GB was intercepted in this state. 3D atom maps showing GB observed in hot extruded powder is shown on *Figure 4.3* (a).

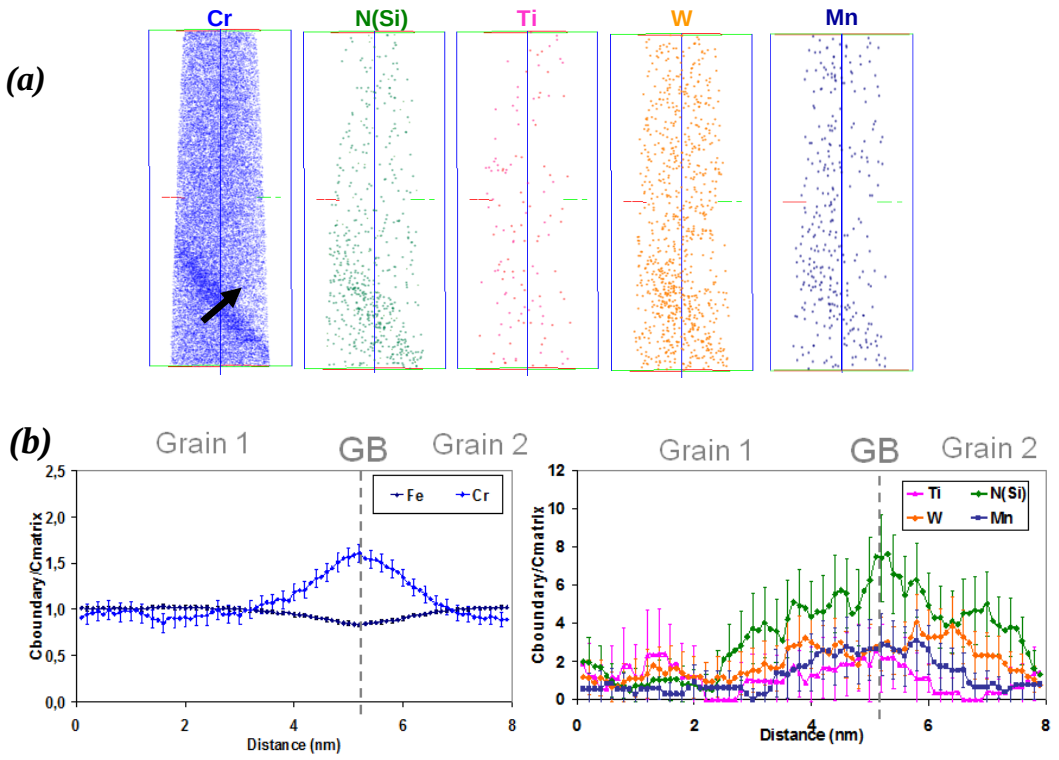

Figure 4.3. Grain boundary observed in MA NDS steel extruded at 800°C. (a) 3D atom maps are shown for Cr, Ti, W and N(Si) species; (b) Variation of $C_{boundary}/C_{matrix}$ measured across the grain boundary as indicated by the arrow in (a). (Cr and Fe are on the left profile and N(Si), Ti, and W species on the right one). $C_{boundary}$ corresponds to the concentration measured in a sampling volume 6×8×1 nm^3. C_{matrix} is the concentration of the element measured in the matrix.

The figure as well as composition profiles (shown on *Figure 4.3* (b)), revealed enrichment of Cr, W, Mn, N(Si), Ti on GB. Taking into account standard deviations, the enrichment of N(Si) on the GB is significantly higher in comparison to Mn, W and Ti.

d) Segregation intensity as a function of temperature

Intergranular Cr segregation is observed in powders annealed at 600 and 700°C during 1h as well as in hot extruded state. This result is consistent with similar observations done in 14YWT and Fe-12Cr wt.% ODS steels [7–9]. In addition to Cr, segregations of W, N, C and O elements on GBs are also reported in 14YWT ODS steels [7,8].

The mean relative excess of Cr ($C_{boundary}/C_{matrix}$) on GBs in MA NDS samples, in the different states is shown on *Figure 4.4*. The mean relative excess is averaged over 4 and 5 GBs for powder annealed at 600 and 700°C respectively. Error bars on the graph represent maximum as well as minimum value of relative excess. Deviations are not shown for hot extruded material since only one GB was observed.

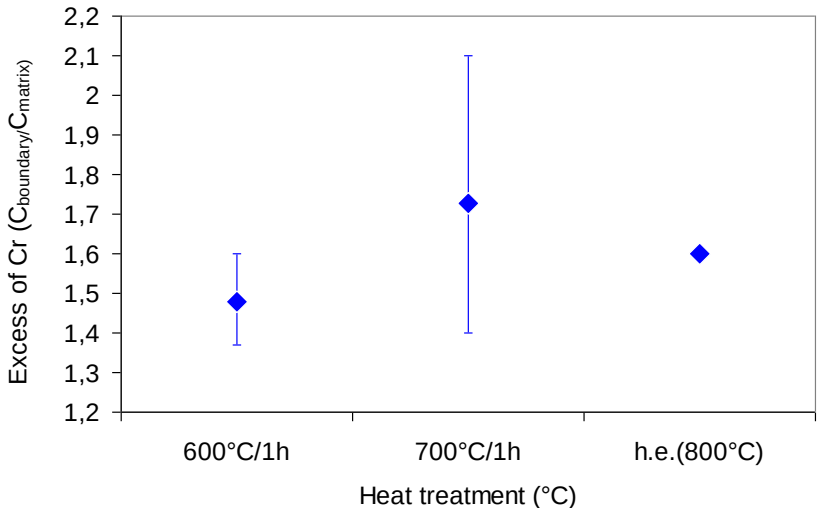

Figure 4.4. Variation of $C_{boundary}/C_{matrix}$ for different GBs observed in MA NDS powder. Different heat treatments are shown. Reported data are averaged from 4 and 5 GBs in powders annealed at 600 and 700°C and one GB in the case of the hot extruded state.

As it can be seen on *Figure 4.4*, there is an increase of the Cr relative excess after annealing at 700°C, in comparison to 600°C. However, significantly higher variations of Cr segregation intensities are measured between different GBs for the same annealing temperature (700°C). It is well known that segregation intensity not only depends of the temperature, but also on the GB type (tilt, twist) and misorientation [4]. Variations of GB characteristics are responsible therefore for non homogeneous GB segregations in the same

metallurgical state. In the present case, since there was no systematic study of the nature and misorientation of GB, the effect of annealing temperature on Cr segregation intensity can not be deduced.

In addition, MA NDS powders are subjected to mechanical alloying, which is known as a highly non-equilibrium process. During this process, non-equilibrium point defects are introduced into material. This super-saturation of point defects (vacancies) can lead to non equilibrium intergranular segregation. Indeed, two basic segregation mechanisms can be distinguished: (a) *equilibrium* and (b) *non-equilibrium* [4, 10]. The basis of equilibrium segregation relies on the existence of crystalline disordered region, boundary or interface, where misfitting impurity atoms can find low-energy sites [11]. Non equilibrium segregation is due to the excess of vacancies which can migrate toward GB where they annihilate. Vacancy fluxes can induce solute fluxes by solute dragging. If the time of annealing is enough, so that diffusion process is allowed to reach full equilibrium, equilibrium redistribution of solutes appears. In the present case, such phenomena can occur during annealing of as-milled powder. Since as-milled powder is subjected to high temperature annealing within short time (1 hour), this time might not be sufficient to reach equilibrium in the system. The observed segregation behaviour in MA NDS steel may be combination of both equilibrium as well as non-equilibrium aspects.

To clarify these points a specific experimental study is needed (but not in the program of this PhD work) to: (i) evaluate segregation intensity depending on GBs nature; ii) study segregation kinetics as a function of longer ageing times as well as varying temperatures.

I.3. Nanoparticles characterization

a) As-milled condition

Small nanoparticles are observed in the as-milled powder (*Figure 4.5* (a, b)). The shape of these nanoparticles is roughly spherical. However, slight elongation in the plane perpendicular to the evaporation direction can be noted. Such a shape can result from local magnification effects [12, 13] occurring during field evaporation of a spherical particle with an evaporation field higher than the matrix one (high field particle). To clarify this point, concentration profiles were plotted through particles. Such profile, oriented parallel to the specimen axis, is shown on *Figure 4.6* (b). An enrichment in Ti, N and O can be clearly seen (*Figure 4.6* (a)). In the Ti, N and O enriched area, the atomic density is 5 times lower than in

the surrounding matrix (*Figure 4.6* (b)). This clearly demonstrates that the particles have high evaporation field.

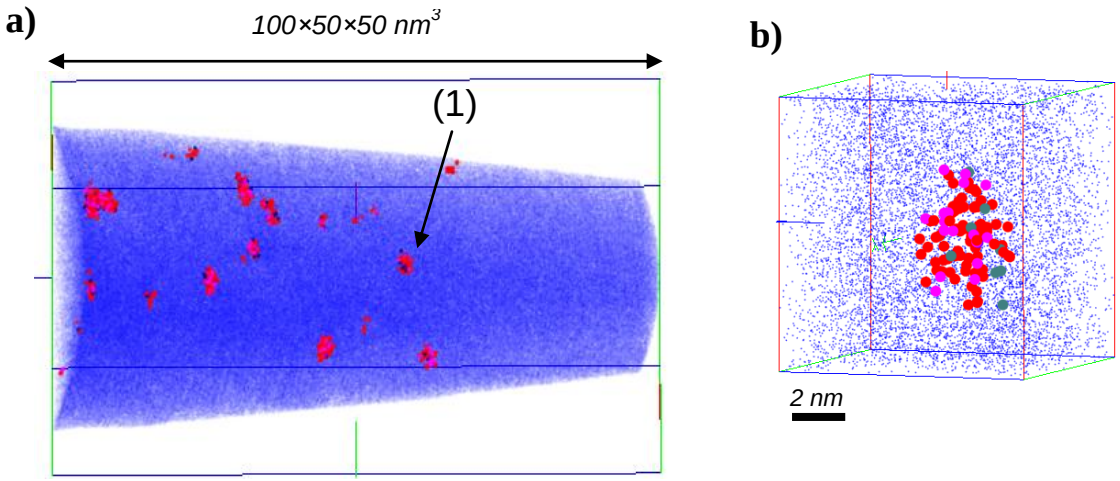

Figure 4.5. 3D representation of MA NDS powder in as-milled state (a) Particles isolated using detection algorithm are shown (Ti, TiN, N, TiO and FeN, CrN species) into the matrix (Cr atoms). The analysed volume is 100×50×50 nm^3. (b) Zoom on indicated nanoparticle in (a) is presented.

As it is explained in Chapter II, local magnification effects may bias chemical compositions, by mixing matrix and cluster atoms near the interface. However, considering that the only difference between particles and matrix is their evaporation fields, the model described in Chapter II (section II.4. (d)) suggests that the measured chemical composition of the core of high field particles bigger than 1 nm in radius is not strongly biased. As it is shown on the profile, the core of particles, even the largest one (R_g=2.2 nm in radius), contains Fe (about 40 at.%). Thus, it can be concluded that particles actually contains Fe in addition to N, Ti and O.

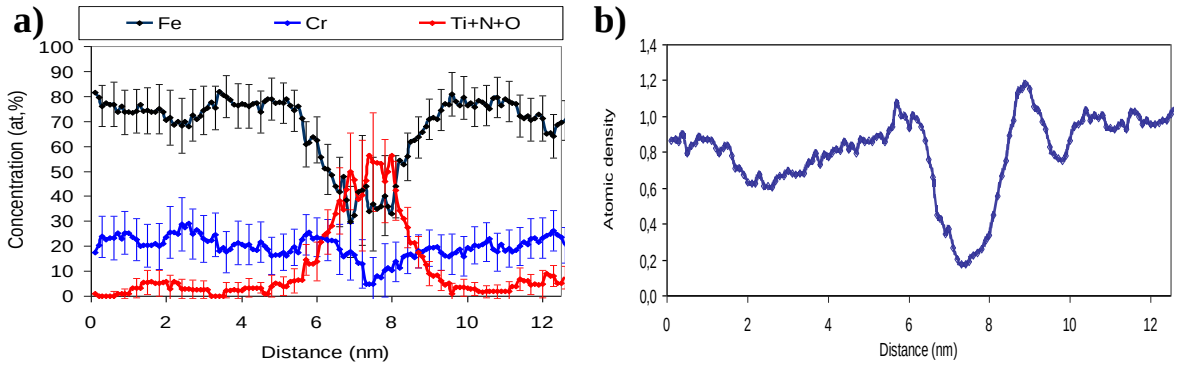

Figure 4.6. Concentration profile drawn through Ti-N rich particle in MA NDS powder (as-milled state). (a) Profile has been drawn along evaporation direction. Ti, N, O species are shown together, Cr and Fe elements are also presented. The Guinier radius of the particle is 2.2 nm. (b) Profile showing a reduction of the relative atomic density inside of particle. Sampling size is 1.5×1.5×1 nm^3.

The measured chemical composition in the core of each cluster (in terms of Ti, N, Cr, O and Fe) as a function of cluster radius is depicted on *Figure 4.7.*

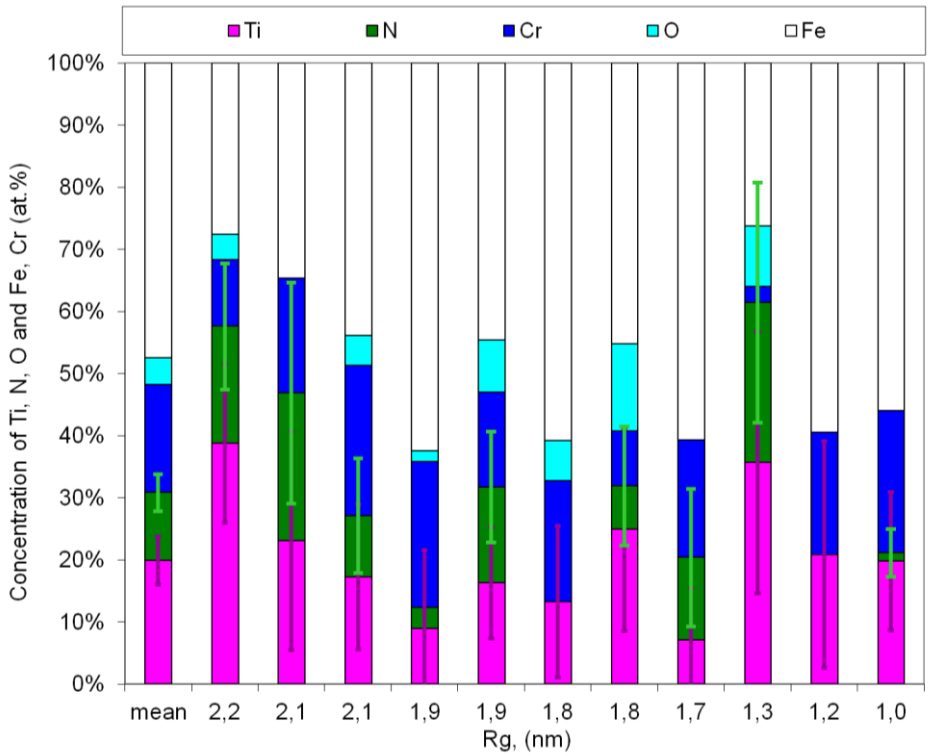

Figure 4.7. Measured composition of nanoparticles observed in MA NDS steel in as-milled state as a function of their size. Compositions are measured in the core of particles. Only Ti, N, O and Fe, Cr (at.%) are shown. For comparison mean chemical composition is also presented.

The measured concentration varies from 7 to 37 at.% for Ti, from 1 to 26 at.% for N and reaches up to 5 at.% for O. This element is probably incorporated into powder grains during elaboration process. The mean measured chemical composition of nanoclusters is (in at.%): **19.3**±3.7 **Ti**, **10.6**±2.9 **N**, **16.8**±3.5 **Cr**, **46**±5.6 **Fe**, **4.2**±2.0 **O**, **1.8**±1.2 **W**. It is worth noticing, that measured chemical composition of these nanoclusters, does not correspond to stoichiometry of TiN nitride. Titanium over nitrogen ratio (**Ti/N**) is **1.8**±0.5.

The Guinier radius of these nanoclusters varies from **1.0** to **2.2 nm** with a mean value of **1.8 nm**. The number density of detected clusters is **$(1.2\pm0.3)\times10^{23}$ m^{-3}**. These values are in agreement with SANS data[1] on smaller sized population of nanoparticles (which are respectively 1.6 nm and 7×10^{22} m^{-3}) [2]. As for second population of nanoparticles, they

[1] *SANS investigations of the MA NDS steel are consistent with two size population of nanoparticles in almost all analysed conditions : as-milled state, annealing up to 850 C and consolidated state. Number density of nanoparticles, Nv, was deduced in accordance to the formula :* $N_v = f_v / V$ *, where V is a volume of spherical particle and fv is the precipitated volume fraction.*

appear with larger sizes (R=4 nm) and lower densities (2.2×10^{21} m^{-3}). Less than half of nanoparticle may be intersected by APT volume of analyse with such density. Thus, no information has been obtained on this population of nanoparticles with APT.

b) Annealing at 600°C/1h

Like in the previous case, nanometric particles are observed in the powder after annealing at 600°C during 1h. 3D reconstruction of isolated nanoparticles is shown on *Figure 4.8* (a). The shape of these particles can be defined as spherical with a slight elongation in directions perpendicular to the analyse axis, as in the as-milled powder. In this sample, GBs are visible thanks to solute segregation. Thus, it appears that about 87 % of the detected nanoparticles are located on GBs. It is known that GBs are favourable nucleation sites, as they reduce activation barrier for nucleation and are diffusion pipes thus enhancing solute diffusion [14]. Representative nanoparticles located on GB and in the matrix are presented on *Figure 4.8* (b).

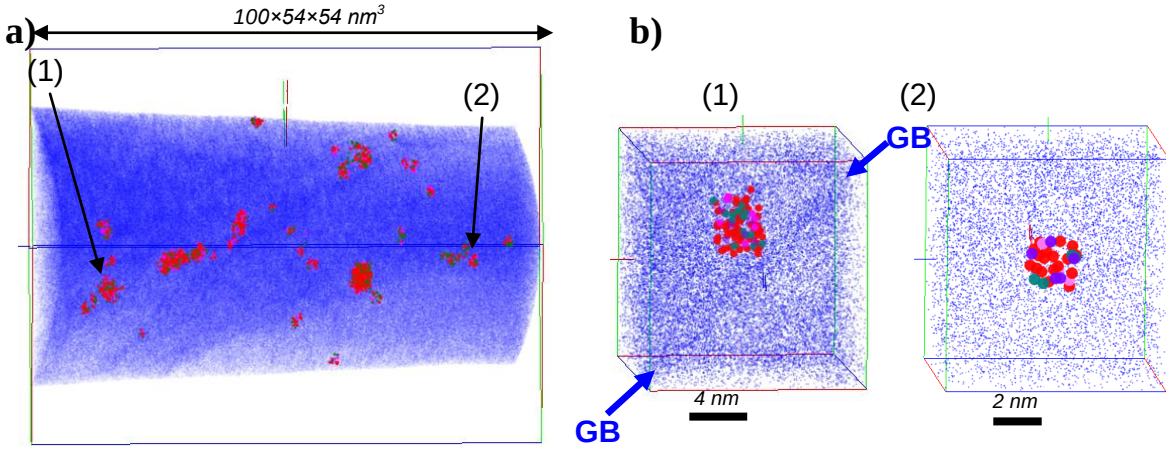

Figure 4.8. 3D reconstructions of MA NDS powder after annealing at 600°C/1h. (a) Nanoparticles that are isolated using detection algorithm are presented. Cr, Ti, TiN, N, TiO, Al, AlO and FeN, CrN species are shown. The analysed volume is 100×54×54nm³. (b) Zoom on indicated particles in (a) are presented: (1) located at grain boundary (GB), (2) located in the matrix (M).

No significant difference in size is observed between particles located along GB and into the matrix. Their Guinier radius varies from **0.9** to **2.7 nm** with a mean value equal to **1.6 nm**. A slightly higher number density (**(1.4±0.2)×10²³ m⁻³**) is observed in comparison to the previous case (powder annealed at 600°C/1h).

In the case of SANS results, two populations of nano-objects are observed. Radius and number density of the first population are 1.4 nm and 1.3×10^{24} m^{-3} respectively [2]. Concerning the size of this population there is a good agreement between both techniques. However, their number densities are very different. Several possibilities can be suggested to explain this discrepancy: a) it may be linked with local inhomogeneities in the material (information from APT is very local whereas SANS data are averaged over larger volumes); b) as it was shown by modelling (see Chapter II. section II.4 (d)), the field evaporation of high evaporation field nanoparticles results in a mixing of the particle atoms with surrounding matrix atoms. It is possible that this effect results in the "dissolution" of the smallest particles (<1nm) in the matrix. In this case, the number density of nanoparticles would be underestimated; c) SANS could see not only nanoparticles (observed by APT), but also another kind of nanofeatures that remains invisible by APT (e.g. nanovoids due to excess of vacancies introduced during MA).

As for second population of nanoparticles reported by SANS, their radius and number density are 3.6 nm and 1.3×10^{22} m^{-3} respectively. With such density, at least 4 nanoparticles should be intersected with APT volume of analyse. However, no nanoparticles with such sizes (R=3.6 nm) has been observed by APT.

Composition of each nanoparticle measured in the core as a function of their sizes is shown on *Figure 4.9*. The letter (M) indicates that particle is located in the matrix. Chemical compositions of both types of nanoparticles (located at GB and inside the matrix) are similar. The measured concentrations vary from 7 to 40 at.% for Ti, from 8 to 25 at.% for N and reach up to 6 at.% for O. The mean measured chemical composition is (at.%): **23.6**±2.3 **Ti**, **15.6**±2.0 **N**, **21.9**±2.3 **Cr, 30.4**±2.5 **Fe**, **5.4**±1.2 **O**, **1.5**±0.7 **Al**, **1.0**±0.5 **W**. Like in the previous case, these nanoparticles are mainly enriched in Ti, N, O and contain Fe. However, a slight enrichment in Cr as well as in Al is found in this case. As for O, the presence of Al is attributed to contamination during the elaboration process. Titanium over nitrogen ratio is **1.5** ±0.25.

It should be noticed that there is no clear dependence of the measured chemical composition with the nanoparticles size. However, the level of Fe (up to 40-50%) is higher than the upper limit given by SANS data, reporting that less than 20 at. % of Fe is present in Ti-N rich particles [1, 2]. A possible explanation could be following: during composition measurements (in small box placed inside core region) the limit between particle core

(containing true level of iron) and the mixed region (containing iron from cluster and from matrix) cannot be clearly identified. Thus, Fe coming from the matrix is also counted.

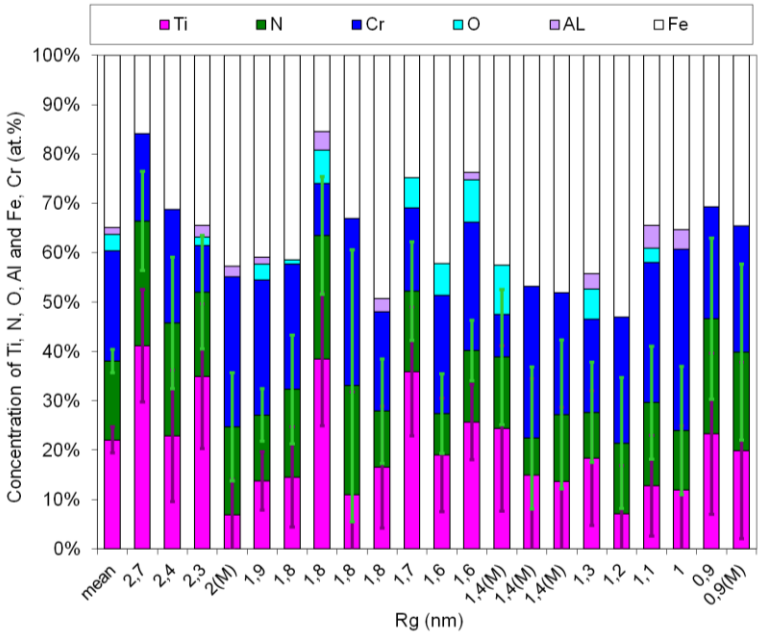

Figure 4.9. Chemical composition of particles in MA NDS steel after annealing at 600°C during 1h as a function of their size. Compositions are measured in the core of particles. Only Ti, N, Al, O and Fe, Cr (at.%) are shown. (M) indicates that the particle located in the matrix (otherwise it associated with grain boundary). For comparison mean chemical composition is shown.

To avoid this problem, concentration profile can be plotted through the biggest particles. A profile drawn across a Ti-N rich particle with R_g=2.7 nm is shown on *Figure 4.10*. As it can be seen from the profile, the Fe content inside core reaches 10-15 at.%. This result is consistent with SANS data. Another important observation also can be done from the profile. A Cr-rich region is observed next to Ti-N particles and matrix interface. Such behaviour of Cr, suggest existence of Cr-rich shell around Ti-N-rich particles. Such core-shell structures have been already observed in ODS [15].

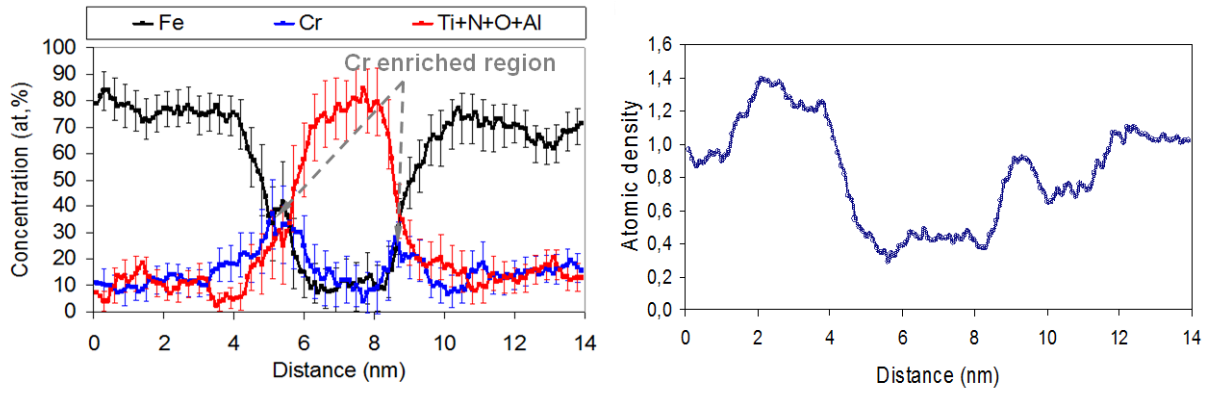

Figure 4.10. Concentration profile drawn through Ti-N rich particle in MA NDS powder (annealed at 600°C/1h). (a) Profile has been drawn along evaporation direction. Ti, N, O species are shown together, Cr and Fe elements are also presented. The Guinier radius of the particle is 2.7 nm. (b) Profile showing a reduction of the relative atomic density inside of particle. Sampling size is 1.5×1.5×1 nm^3.

c) Annealing at 700°C/1h

3D reconstruction of the microstructure observed in a MA NDS powder after annealing at 700°C during 1h is shown on *Figure 4.11* (a). As in previous cases, nanoparticles are observed. Like in powder annealed at 600°C during 1h, about 90% of them are located on GBs. Here again, these particles have a roughly spherical shape with a slight elongation in directions perpendicular to analysis axis. Examples of Ti-N rich particles located in the matrix and along the GB are depicted on *Figure 4.11* (b-1,2). The largest Ti-N rich particle located along GB is shown in *Figure 4.11* (b-3).

Concerning the sizes, it is worth noticing that no significant differences between Guinier radii of particles located along the grain boundaries and in the matrix are observed. They vary from **1.3** to **more than 5 nm** (the largest particle in analysed volume is cut by the edge of analysed volume, thus the precise size cannot be defined) with a mean value of **2.0 nm**. The number density, **(2.7±0.2)×10^{23} m^{-3}**, is significantly higher than in as-milled powder and powder annealed at 600°C. So, nucleation rate seems to be higher at 700°C than at 600°C.

As in the previous case (annealing at 600°C), the mean radius of particles estimated by APT (R_g=2.0 nm) is in reasonable agreement with the SANS measurement (R=1.7 nm) for the small size population of particles [2]. Also, there is slight discrepancy for number densities. A higher number density (8.8×10^{23} m^{-3}) is reported by SANS in comparison to APT (**(2.7±0.2)×10^{23} m^{-3}**). Such discrepancies were already discussed previously for annealed at 600°C powder. As for second population of nanoparticles reported by SANS,

their radius and number density are respectively: R=4.4 nm and 8.4 $\times 10^{21}$ m^{-3}. Considering the low number density of these nanoparticles and the volume analysed by APT, less than one such big particle is expected in APT volumes. Luckily, only one particle (the largest, Rg >5 nm) has been intercepted during APT experiments.

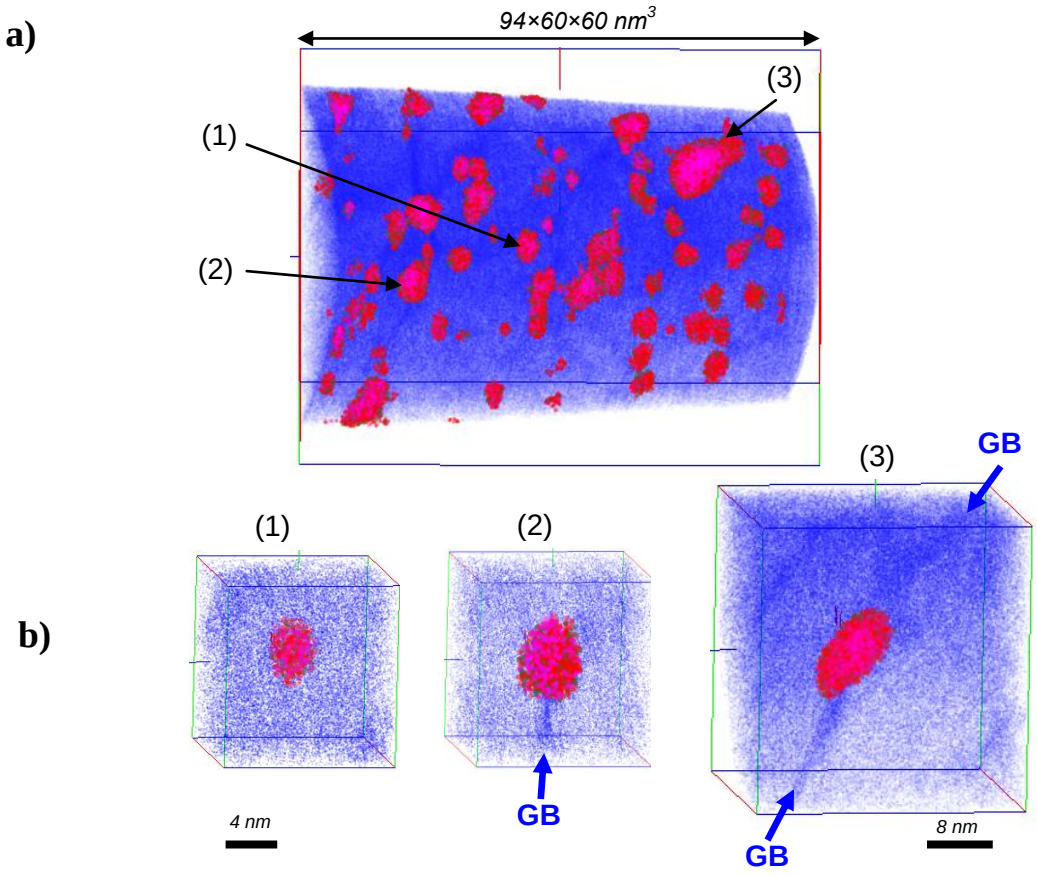

Figure 4.11. 3D reconstructions of MA NDS powder after annealing at 700°C during 1h. (a) Filtered image showing atoms and molecular ions (Ti, TiN, N, TiO, Al, AlO and FeN, CrN) belonging to particles identified by detection algorithm and Cr atoms representing matrix. The analysed volume is 94×60×60 nm^3. (b) Zoom on indicated particles in (a) are shown: (1) located in the matrix, (2) associated with grain boundary (GB) and (3) the largest detected Ti-N rich particle located along grain boundary.

The chemical composition of each analysed nanoparticle measured in the core as a function of their sizes is shown on *Figure 4.12*. There is no significant difference between particles located in the matrix and on the grain boundaries. The measured concentrations vary from 7 to 48 at.% for Ti, from 8 to 29 at.% for N and goes up to 9 at.% for O. The mean composition is: **24.2**±1.5 **Ti**, **15.9**±1.3 **N**, **24.4**±1.5 **Cr, 30.5**±1.5 **Fe**, **4.0**±0.7 **O**, **0.5**±0.3 **Al**, **0.41**±0.22 **W** at.%. The chemical composition is almost similar to the one measured in the powder annealed at 600°C. The titanium over nitrogen ratio is equal to **1.5**+/-0.2.

As in previous case, concentration profile drawn across a Ti-N rich particle with R_g=3.0 nm (*Figure 4.13)* revealed, that the Fe content inside core varies from 12 to 20 at.%. This result is consistent with SANS data. Also, like in previous case (powder annealed at 600ºC/1h), Cr enrichment is seen next to particle interface.

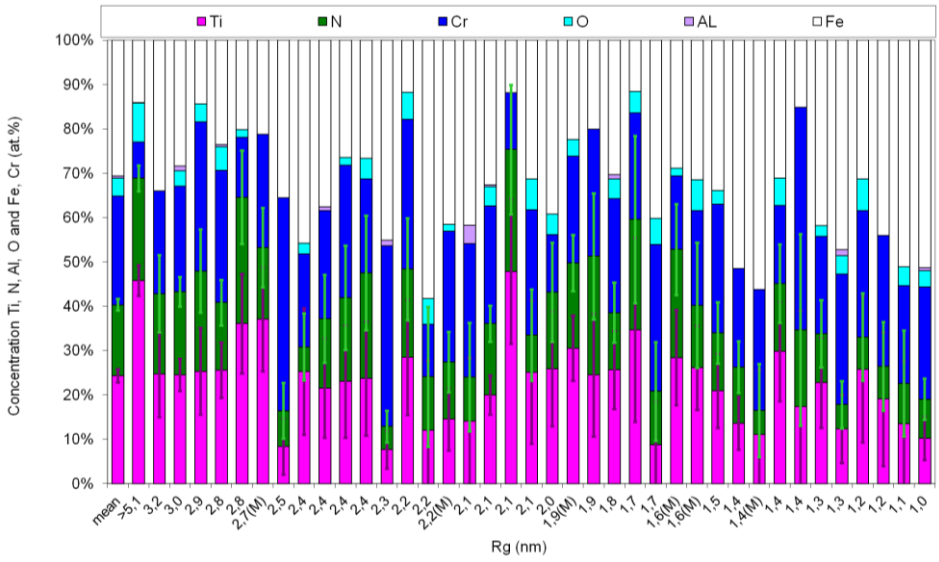

Figure 4.12. Composition of particles in MA NDS steel after annealing at 700°C during 1h as a function of their sizes. Compositions are measured in the core of particles. Only Ti, N, Al, O and Fe, Cr (at.%) are shown. Letter M indicates that the particle is located in the matrix (otherwise it is associated to grain boundary). For comparison the mean chemical composition is also shown.

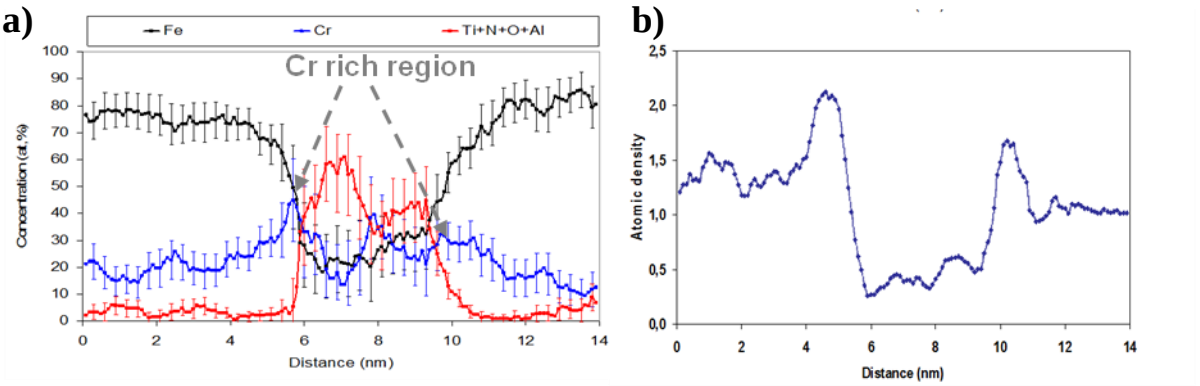

Figure 4.13. Concentration profile drawn through Ti-N rich particle in MA NDS powder (annealed at 600°C/1h). (a) Profile has been drawn along evaporation direction. Ti, N, O species are shown together, Cr and Fe elements are also presented. The Guinier radius of the particle is 3.0 nm. (b) Profile showing a reduction of the relative atomic density inside of particle. Sampling size is 1.5×1.5×1 nm^3.

d) Hot extruded condition (800°C)

As shown on *Figure 4.14* (a), here also Ti and N enriched nanoparticles are observed. As in powders, they are roughly spherical. All detected particles are located in the matrix. Their Guinier radius varies from **1** to **3.7 nm** with a mean value of **2.1 nm**. The number density is higher than the one measured in samples annealed at 700°C: **$(3.1\pm0.4)\times10^{23}$ m^{-3}**. These values are in good agreement with SANS results: a mean radius equal to 1.9 nm and a number density equal to 5.6×10^{23} m^{-3} [2] are reported. As for second population of these nanoparticles, they appear with sizes: R=4.1 nm and number densities 4.2 $\times10^{22}$ m^{-3}. Approximately 9 nanoparticles with such sizes should be intersected by APT volume, however no nanoparticles with sizes more than 3.7 nm has been detected by APT.

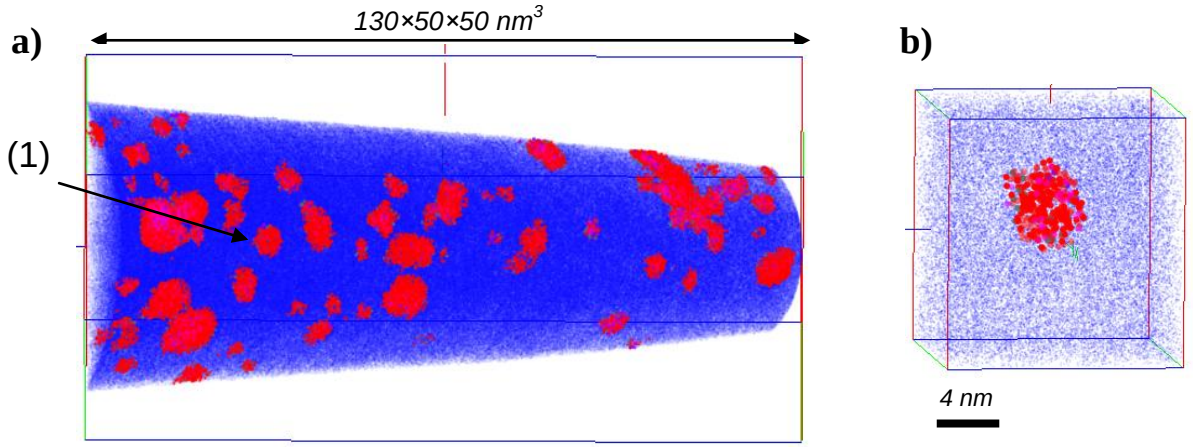

Figure 4.14. 3D reconstructions of MA NDS steel after hot extrusion (800°C). (a) Cr atoms and Ti, TiN, N, TiO, Al, AlO, FeN, CrN species belonging to the nanoparticles identified using detection algorithm are shown. The analysed volume is 130×50×50 nm^3. (b) Zoom on representative nanoparticle indicated in (a).

The chemical composition of each detected nanoparticle is shown on *Figure 4.15* as a function of size. These particles are enriched in Ti, N, Cr, O and Al. The mean measured chemical composition is: **22.1**±1.1 **Ti**, **16.7**±1.0 **N**, **23.8**±1.1 **Cr, 34.1**±1.2 **Fe**, **2.4**±0.4 **O**, **0.8**±0.3 **Al** at.%. It is comparable to the ones measured in nanoparticles in powders annealed at 600 and 700°C. The Ti/N ratio in that case of consolidated sample is equal to **1.3**+/-0.1.

A dependence of Ti and N concentrations as a function of nanoparticles size is visible on *Figure 4.15*: the smallest particles seem to contain more iron than the biggest ones. The reasons for that have been explained for MA NDS annealed at 600°C. Concentration profiles drawn through nanoparticles (R_g >2.5 nm) revealed that the Fe content varies between 10 and 20 at.%. These values are in agreement with SANS [2]. Also, Cr-rich region can be identified next to nanoparticle interface as in previous conditions (annealing at 600 and 700ºC/1).

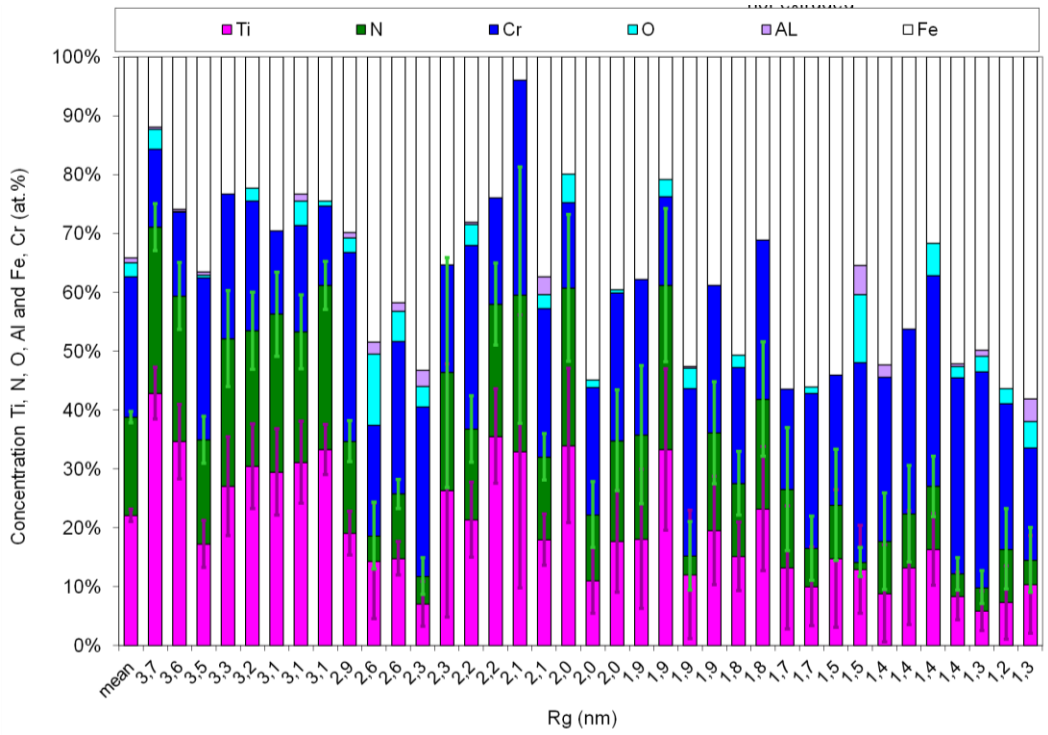

Figure 4.15. Composition of nanoparticles in MA NDS steel after hot extrusion (800°C) as a function of their sizes. Only Ti, N, Al, O and Fe, Cr (at.%) are shown. For comparison the mean chemical composition is reported.

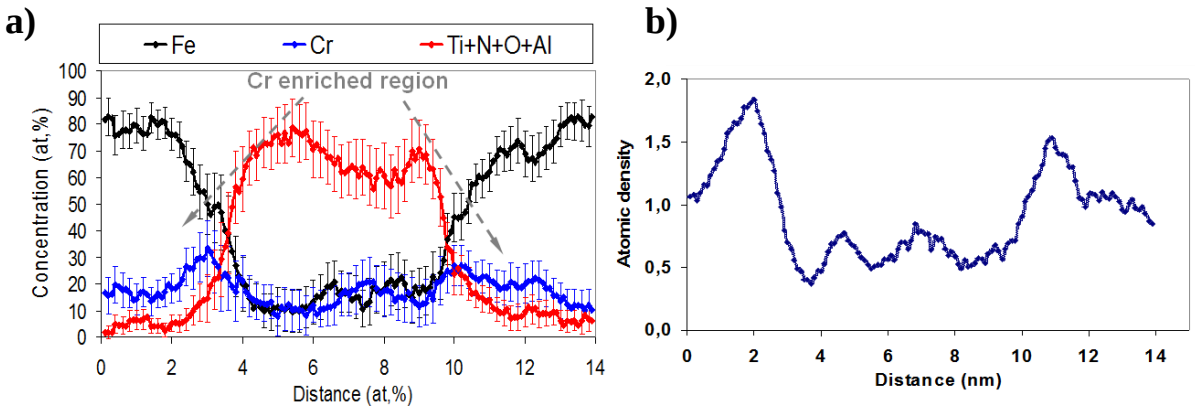

Figure 4.16. Concentration profile drawn through Ti-N rich particle in MA NDS powder (consolidated by hot extrusion). (a) Profile has been drawn along evaporation direction. Ti, N, O species are shown together, Cr and Fe elements are also presented. The Guinier radius of the particle is 3.7 nm. (b) Profile showing a reduction of the relative atomic density inside of particle. Sampling size is 1.5×1.5×1 nm^3.

e) Annealing at 850°C/1h

3D reconstruction of a small volume containing nanoparticles in powders annealed at 850°C during 1h is shown on *Figure 4.17* (a, b). Two distinct families of nanoparticles are observed in this analyse: Ti-N-rich and Ti-Al-O rich particles. It must be mentioned that

these two families of particles have been observed in only one experiment. No grain boundaries have been detected in all experiments (within this temperature condition) suggesting that no Cr segregation occurs at this temperature or that the grains became so large that the probability to be analysed during APT experiment tends to zero.

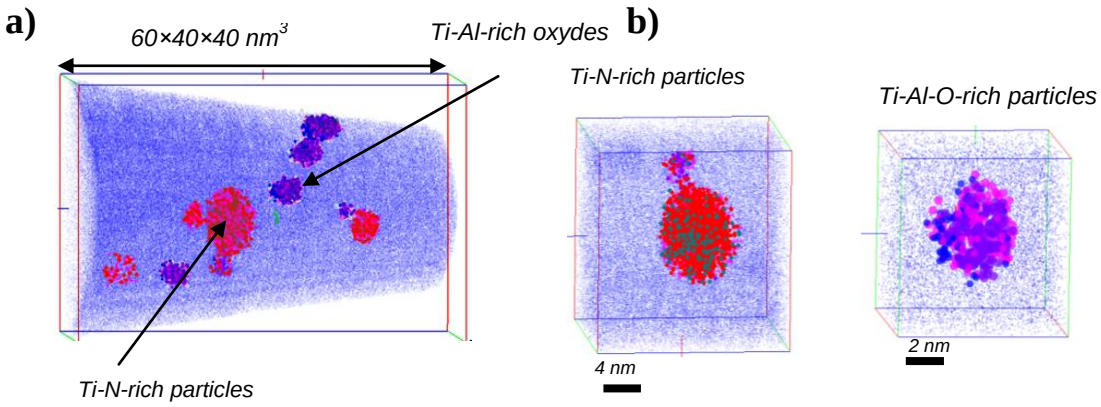

Figure 4.17. 3D reconstructions of MA NDS steel after annealing at 850°C during 1h. (a) Particles isolated using detection algorithm are presented. Cr, Ti, TiN, N, TiO, Al, AlO and FeN, CrN species are shown. Two families of nanoparticles (Ti-N- and Ti-Al-O-rich) can be distinguished. The analysed volume is 60×40×40 nm^3. (b) Zoom on indicated nanoparticles in (a): Ti-N-rich and Ti-Al-O-rich particles.

The shape of particles is roughly spherical but a) a slight elongation of Ti-N rich particles as well as b) slight compression of Ti-Al-O rich particles in the plane perpendicular to analysis direction is noticed. These effects can be explained by the local magnification effect during the field evaporation of respectively high-field (Ti-N) and low-field (Ti-Al-O) particles.

As for Ti-N-rich nanoparticles, their Guinier radius varies from **2** to **4.4 nm** with a mean value of **3.3 nm.** Their number density is equal to **(1.0±0.3)×10^{23} m^{-3}.** Concerning Ti-Al-rich oxides, their Guinier radii vary from **1.3** to **2.5 nm** with a mean value of **1.9 nm**. Their number density is equal to **(1.2±0.5)×10^{23} m^{-3}** and it is almost equal to the value obtained for Ti-N rich nanoparticles.

There is a good agreement between SANS and APT results for number densities of Ti-N-rich nanoparticles ~10^{23} m^{-3}. This is not the case for nanoparticles sizes. The mean radius estimated by SANS (R=2.0 nm) is slightly lower than the one measured by APT (R_g=3.3 nm). This could be attributed to the poor statistics, since a relatively small number of Ti-N rich particles were intersected during APT analyses. At the same time, 3DAP revealed the

presence a second population: Ti-Al-O-rich particles. SANS investigation do not report anything about this population of nanoparticles. Thus, probably the SANS signal have been mixed for both populations, influencing the value of mean radius.

The composition of each nanoparticle as a function of the size in the case of Ti-N-rich particles is depicted on *Figure 4.18* (a).

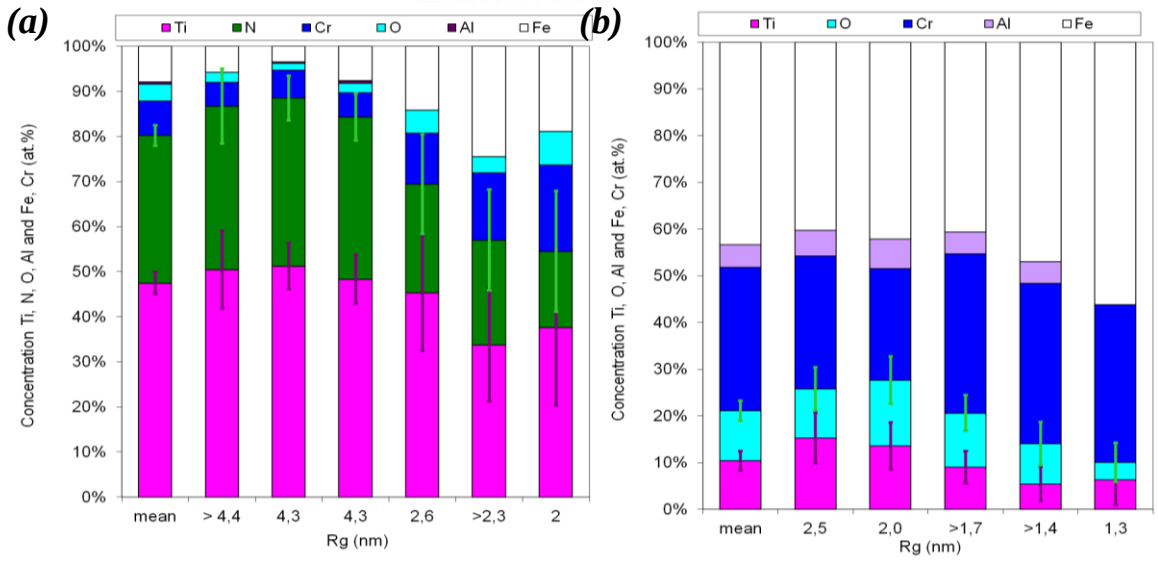

Figure 4.18. Composition of nanoparticles in MA NDS steel annealed at 850°C during 1h as a function of their size. (a) Only Ti, N, Al, O and Fe, Cr (at.%) are shown in case of Ti-N- rich particles and (b) only Ti, Al, O and Fe, Cr in shown in case of Ti-Al-O-rich particles. For comparison mean chemical compositions are also shown for both types of particles.

A slight dependence of the Fe level on particles size is noticed. The size of these nanoparticles is large (R_g > 2 nm) enough to measure core composition not affected by trajectory aberrations. Thus, at this temperature, real size dependence governed by thermodynamic is expected. The measured Ti, N and O concentrations vary from 38 to 48 at.%, from 17 to 37 at.% and from 1.5 to 5 at.% respectively. Traces of Al are observed in few nanoparticles. The mean core chemical composition is **48.6**±2.4 **Ti**, **34.5**±2.3 **N**, **7.0**±1.3 **Cr, 7.5**±1.3 **Fe, 2.3**±0.8 **O**. It is worth nothing that the concentration of Ti and N are significantly higher here, in comparison to all previous conditions. Annealing at higher temperature leads to enrichment of these phases in terms of Ti, N as well as significant depletion in Fe and Cr. This is confirmed by composition profiles showing about 5 at.% of Fe and Cr in the cluster core (*Figure 4.19* (a)). The level of oxygen is not significantly changed. The **Ti/N** ratio is **1.4**+/- 0.15. It should be pointed out, that this ratio does not

change in comparison to previous conditions. Here again, Cr-rich shell is clearly seen all around the particles (*Figure 4.19* (a, b)).

The composition of each Ti-Al-O rich particle as a function of their size is shown on *Figure 4.18* (b). Measured concentrations varies from 6 to 15 at.% for Ti, from 4 to 14 at.% for O and up to 6 at.% for Al. The mean measured composition is **10.2**±2.0 **Ti**, **1.4**±0.8 **N**, **30.3**±3.1 **Cr, 10.5**±2.1 **O**, **4.7**±1.4 **Al** and **42.7**±3.3 **Fe** at.%. The calculated **Ti/O** ratio is **1.0**+/-0.4.

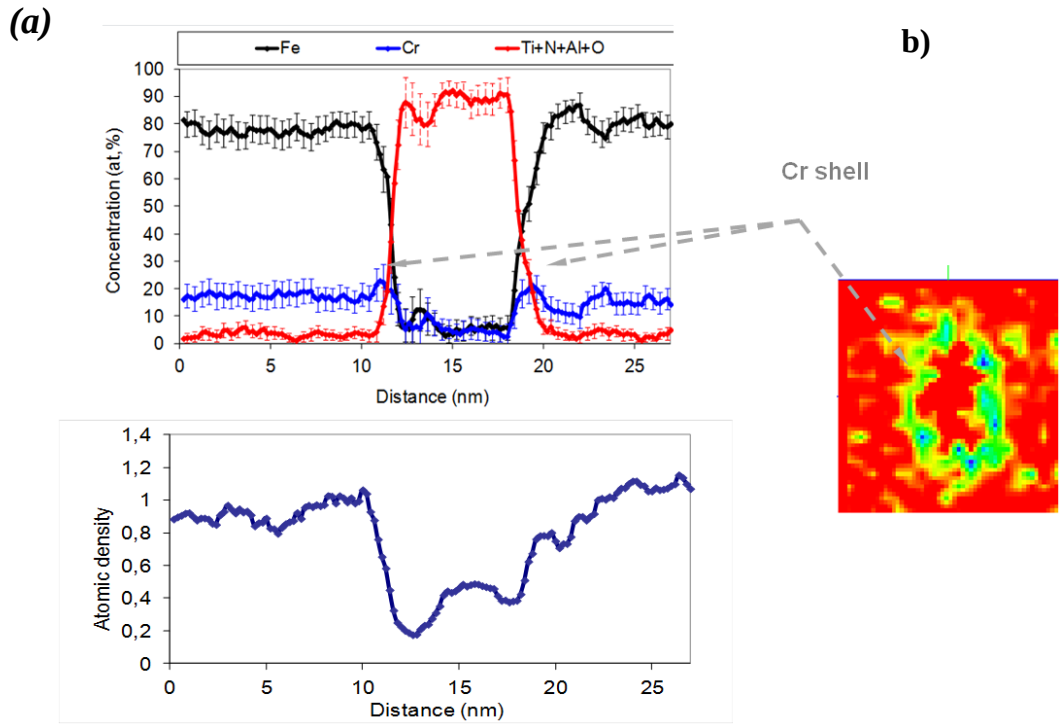

Figure 4.19. Concentration profiles drawn through Ti-N rich particle in MA NDS steel (annealing at 850°C/1h). (a) Profile has been drawn along evaporation direction. Ti, N, O, Al species are shown together, Cr and Fe elements are presented. Guinier radius is 4.4 nm. Cr rich area at the particle/matrix interface can be clearly seen. Sampling volume is 2.0-2.0-1.5 nm^3. (b) Isoconcentration profile for Cr. Cr rich region (green) between Cr depleted matrix and Ti-N rich core (red). (c) Profile showing a reduction of the relative atomic density inside of particle. Sampling size is 2.0×2.0×1.5 nm^3.

The driving force for precipitate formation is governed by the change in the Gibbs free energies, G° of the system. The *Table 4.3*, gives some examples (T=850°C) in the case of Al_2O_3, TiO_2 and TiN formation [16]. Hence, when sufficient amount of O is available, the nucleation of Ti-N phase is less favourable (the value of G° is less negative) in comparison to Al_2O_3 or TiO_2 phases. This suggests that to promote nucleation of TiN, the level of O should be strongly controlled.

Table 4.3 Change in the Gibbs free energies, G°, associated with Al_2O_3, TiO and TiN formation [16].

Nucleated phase	G° (J mol^{-1})	G°at T=850°C
$2Al + 3O_2 <=> 2Al_2O_3$	$G° = -16.9 \times 10^5 - 51.1\ T$	- 1 747 397 (J mol^{-1})
$Ti + O_2 <=> TiO_2$	$G° = -9.4 \times 10^5 - 50.2\ T$	- 996 374 (J mol^{-1})
Ti +N <=> TiN	$G° = -3.4 \times 10^5 - 30.1\ T$	- 373 802 (J mol^{-1})

f) Annealing at 1000°C/1h

A backscattered electrons SEM picture of an APT needle, prepared in a NDS powder annealed at 1000°C during 1h, is shown on *Figure 4.20* (a). Grains are clearly visible with sizes about 700 nm. Small dots that are visible correspond to nanoparticles. It is clearly seen, that the number density of these nanoparticles is very low. So the probability to intercept such particle during APT analyse is small. However, an isolated nanoparticle was luckily observed and is presented on *Figure 4.20* (b). Since only a part of the particle was intercepted, its size cannot be given. It is bigger than 10 nm. The estimated number density is about **4×10^{21} m^{-3}.**

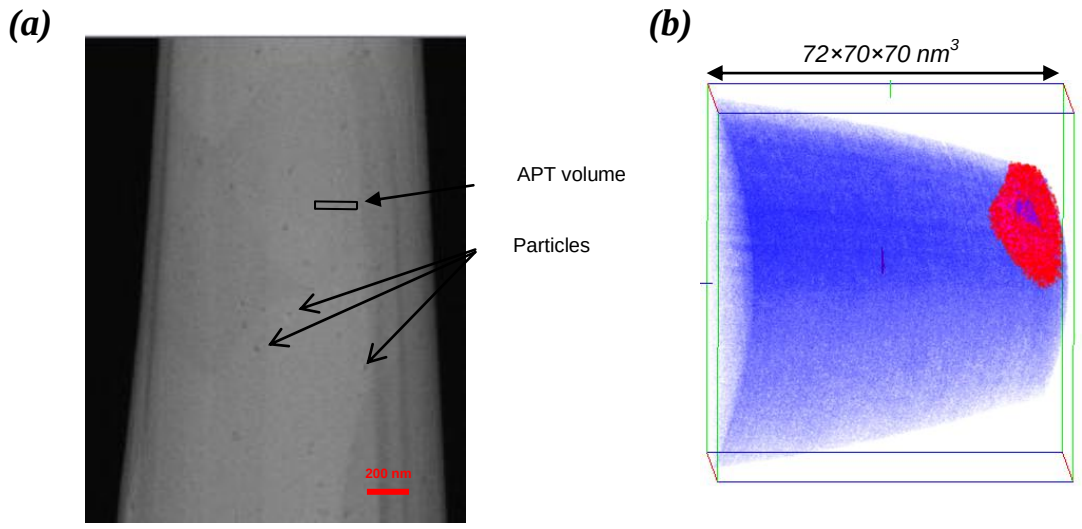

Figure 4.20. MA NDS steel annealed at 1000°C/1h. (a) SEM picture obtained during APT tip preparation; (b) isolated nanoparticle using detection algorithm. Cr, Ti, TiN, N, TiO, Al, AlO and FeN, CrN species are shown. The analysed volume is 72×70×70 nm^3.

The measured chemical composition of the particle is **52.5**±2.0 **Ti**, **36.3**±2.0 **N**, **4.4**±0.8 **Cr, 5.6**±1.0 **Fe**, **1.0**±0.4 **O** at.%. The composition is not significantly changed in comparison to the one measured in the samples annealed at 850°C. In comparison with previous cases, no

significant evolution is observed in terms **Ti/N** ratio: **1.45**+/-0.10. A concentration profile (*Figure 4.21* (a)) drawn across the Ti-N rich particle reveals 5 at.% of Fe as well as Cr inside the core of the particle. Cr rich region is not observed in this condition at nanoparticle/matrix interface. It is possible that the temperature is too high to promote formation of Cr-rich shell.

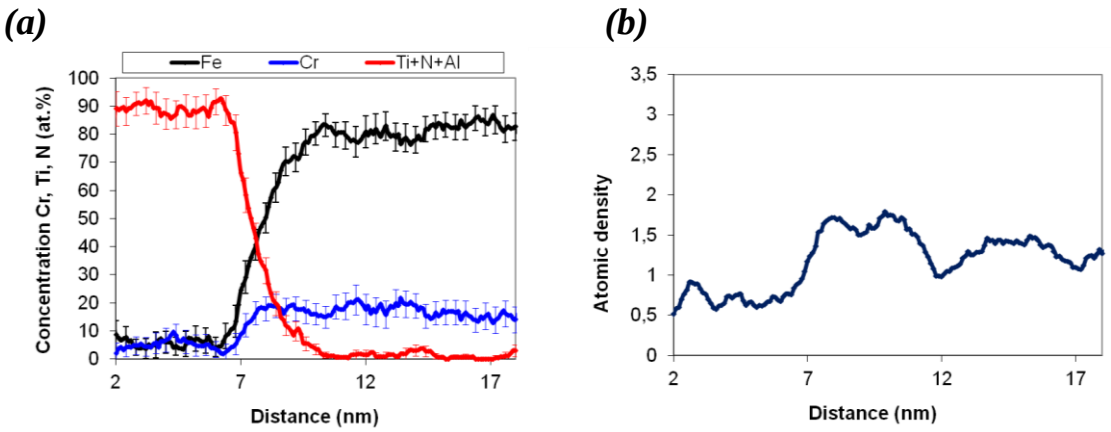

Figure 4.21. Concentration profile drawn through Ti-N rich particle in MA NDS steel (annealing at 1000°C/1h). (a) Profile has been drawn along evaporation direction. Ti, N, O, Al species are shown together, Cr and Fe elements are presented. (b) Profile showing a reduction of the relative atomic density inside of particle. Sampling size is 2.0×2.0×1 nm^3.

I.4. Discussion

An exhaustive investigation of NDS steel produced by mechanical alloying of pre-alloyed (Fe, Cr, W, N) powder with titanium hydride was performed. The different heat treatments favoured the formation of Ti and N-rich nanoparticles. In this part, a summary of the data is exposed, followed by a discussion on their formation mechanism and compared with MatCalc calculations.

a) Chemical composition of nanoparticles

Before, discussing about the formation mechanisms of Ti-N rich particles, it is necessary to have a clear idea of their nature. In particular, the evolution of the Ti over N ratio and the actual level of iron have to be discussed. The measured chemical composition of Ti-N-rich particles observed in MA NDS steel as a function of annealing temperature is depicted on *Figure 4.22 (a, b).* As it can be seen, the O concentration in particles remains almost constant in all experimental conditions. It does not exceed 5 at.%. Concerning Ti and N (*Figure 4.22 (a)*), the lowest concentrations are measured in the as-milled sample. Ti and N levels are quite constant in particles observed in powders annealed at 600 and 700°C as well as in hot

extruded material (800°C). Finally Ti and N concentrations are the highest in particles observed in powders annealed at 850 and 1000°C. It has to be noticed that whatever the "absolute" concentration of Ti and N into clusters, the Ti over N ratio is quite constant (~1.5). This value differs strongly from the expected chemistry of TiN (ratio equal to 1). It is known that preferential evaporation can result in selective loss of one element during APT analysis and so, modify the apparent chemical composition. However, in the case of titanium nitrides, in other research programs, APT analysis was performed on TiN layers elaborated by physical vapour deposition. It has been shown that the Ti over N ratio measured by APT is the right one [17,18]. Thus, it seems that the nitrides formed during MA and annealing have actually a different chemistry than the expected one. A possible explanation could be the presence of vacancies, introduced during milling, which allows gap in stoichiometry.

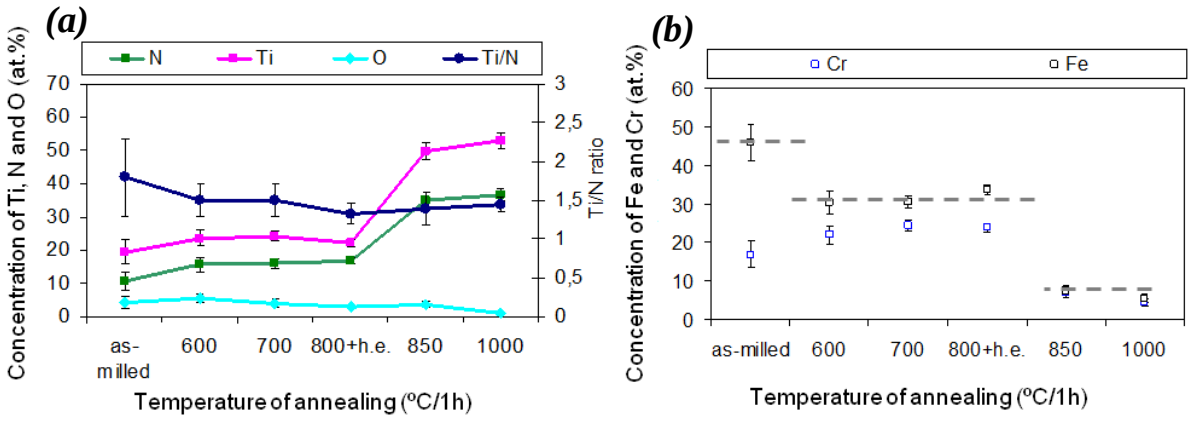

Figure 4.22. Mean chemical compositions of Ti-N rich particles measured in MA NDS steel as a function of annealing temperatures. (a) Ti, N, O as well as Ti/N ratio and (b) Fe and Cr levels in particles. Hot extruded condition (h.e.) is also taken into account.

In addition to their unusual chemistry, particles contain a significant amount of Cr and Fe. The Fe and Cr concentrations into the particles are discussed separately below.

- *Cr content*

As far as Cr is concerned (*Figure 4.22 (b)*), its concentration is slightly higher in nanoparticles observed in powders annealed at 600 and 700°C as well as in hot extruded state (~20-25 at.%), than in as milled powder (~18 at.%). The Cr level into particles is very low after annealing at 850 and 1000°C (5 at.%).

This temperature dependence could be explained by the presence of a Cr rich shell (low evaporation field in comparison to matrix) around Ti-N rich particles (high evaporation field

in comparison to matrix). The shell is clearly seen around all relatively large (more than 2.7 nm) rich Ti-N rich particles.

Now, as it is shown by the field evaporation model (section II.4 of the Chapter 2), atom from a low field shell can "fall" into a high field particle during evaporation process, at least for small particles (R < 1nm). According to [19], such overlap effects can affect areas of several nanometres from interfaces. Thus, it is possible that the model underestimates the size of particles for which the composition is biased. In this case, the Cr level into particles can be interpreted in such a way:

(i) The Cr content measured inside the core of the large (R_g=4.4 nm) particles is about 5at% (annealling at 850 and 1000°C). It can be reasonably assumed that this value is true, since the particle size (R_g=4.4 nm) exceeds zone affected by trajectory aberrations.

(ii) When size of particles is smaller (powder annealed at 600, 700°C and hot extruded samples), the volume defined as "core region", inside which compositions are measured, can be affected by trajectory overlaps. In this case, Cr from the shell is mixed with core atoms and a significant content of Cr is measured (*Figure 4.22* (b)). This appears on *Figure 4.23* (a, b), where Cr concentration in each particle of the different samples is represented as a function of particle size. Even for a given condition, the Cr level depends of the particle radius.

(iii) In as milled powder, the Cr level is lower certainly because Cr shell is not developed.

The presence of a complex core shell structure has been also observed in nanoparticles in different ODS steels [15, 19, 20] by APT. Several hypotheses are envisaged to explain the existence of the Cr rich shell around Ti-N rich particles. First, in the case of high nucleation barrier, the formation of the shell may act as an interfacial phase reducing the surface energy of the particles, favouring their nucleation [15,20]. Another possibility was suggested by Hsiung [22–24] in the case of nanoparticles in ODS steel. The solute rich shell could result from a complex formation mechanism:

(i) In a first step, amorphous particles containing Y, O and matrix metal are formed during the MA process. The crystallisation of these particles is not possible due to the associated increase of interfacial energy.

(ii) When these amorphous particles reach a critical size, the ratio surface over volume is low enough to allow crystallisation. During this step, matrix atoms are rejected from the

particle, forming the shell if solute depletion rate from the core is greater than solute diffusion rate from the oxide/matrix interface during the crystallization stage.

Such mechanism could also occurs during MA in NDS steel. This could explain why there is no evidence of Cr shell in as-milled samples.

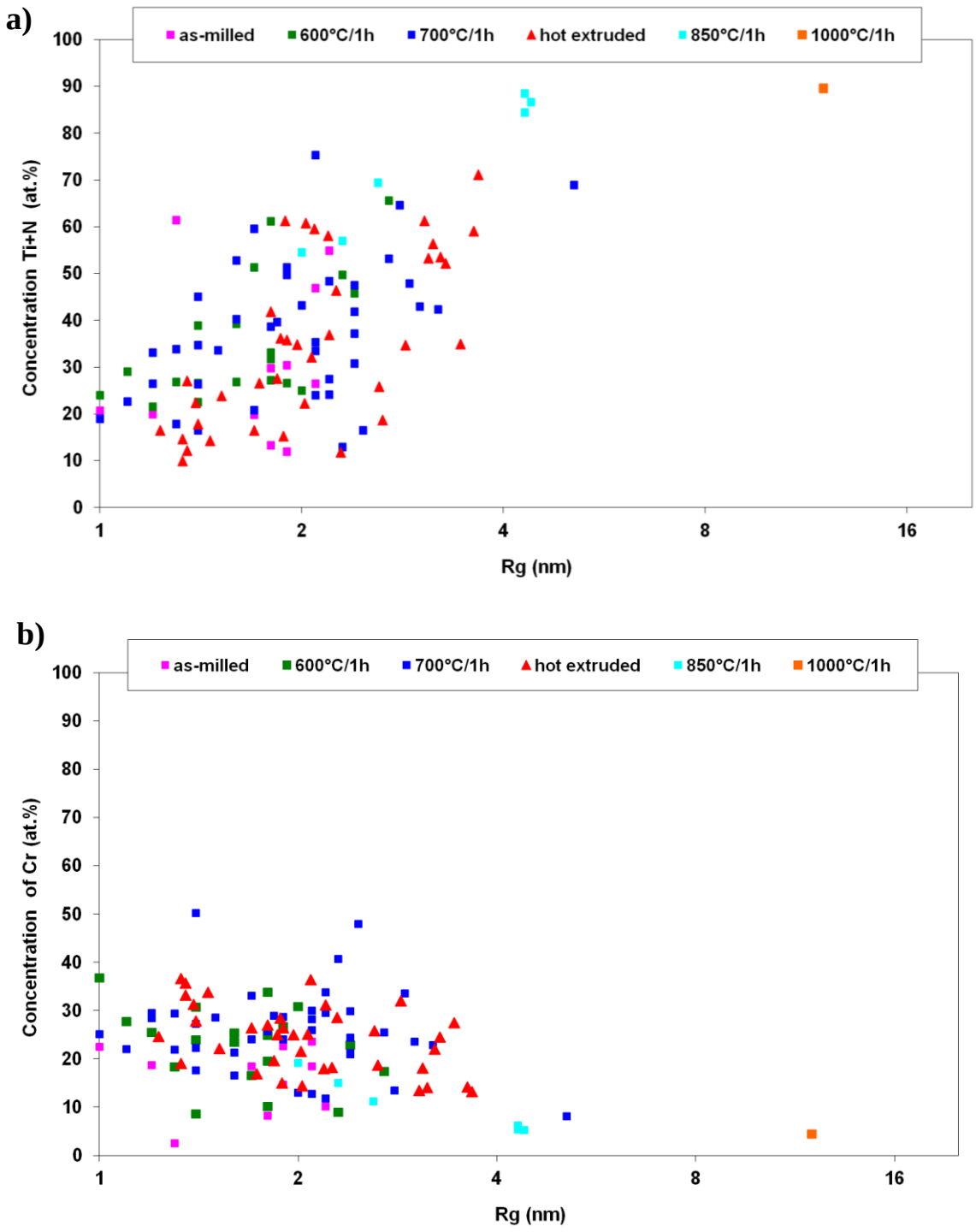

Figure 4.23. Evolution of concentration of (a) Ti+N (at.%) and (b) Cr measured in MA NDS steel as a function of Guinier radius (R_g). Hot extruded condition (h.e.) is also taken into account. Guinier Radius (x axis) is shown in logarithmic scale.

- *Fe content*

The concentration of Fe into the particles has the opposite behaviour than the concentration of Ti and N (*Figure 4.23 (a)*). The highest level is measured in as-milled samples (~45 at.%), the lowest in powders annealed at 850 and 1000°C (~5at.%), and an intermediate constant value (~30-35%) is measured in samples heat treated at 600, 700 and hot extruded state.

It is worth mentioning that, the fraction of Fe in Ti-N rich particles can be non-zero. As an example, it is suggested, that in the case of nanosized precipitates, thermodynamic barrier for nucleation may be lowered by increasing concentration of matrix atoms in the precipitates [19, 20]. However, this effect is less pronounced for particles reaching larger sizes (advanced growth stage and coarsening). This could explain that be biggest particles (observed in samples annealed at 850 and 1000°C) contain only few percents of iron. The presence of few percents of iron in nitrides is already reported elsewhere [17]. However, in all analyzed states, the measured Fe concentration is higher than the maximum value compatible with the interpretation of SANS data.

Local magnification effects [12,13] could be at the origin of this slight discrepancy (~30-35at.% of Fe according to APT and less than 20 at.% according to SANS). Modelling of field evaporation of high-field nanoparticles in MA NDS matrix (section II.4. (d) of the Chapter 2), shows that when radius of nanoparticle exceed 1 nm, the composition in the core is not affected by trajectory aberrations. However, as already said in the case of Cr atoms, even if the model reproduce qualitatively the experimental artefacts, it could underestimate their intensity and spatial extension because all the input parameters are not known (e.g. field evaporation of N and Ti inside a nitride) and because it is possible that some mechanisms are not considered (e.g. poor conductivity of nitrides). In addition, when measuring the composition, by introducing a small box inside particle, it is not possible to clearly define the limit between the area containing Fe actually present in the particle, and Fe introduced by overlap. In order to estimate the actual level of Fe, concentration profiles were drawn through Ti-N rich particles with $R_g > 2.5$ nm in all samples (except as-milled one, where nanoparticle with Rg=2.2 nm was studied). On the profiles, the level of Fe observed in the core of Ti-N rich particles is in the range 10 to 20 at % in case of particles annealed at 600 and 700°C as well as in hot extruded states. Smaller content of Fe (~5 at.%) is detected in particles after

annealing at 850 and 1000°C. The largest level of iron is observed on profile through as-milled nanoparticle (R_g=2.2 nm), which is 39 at.%.

Thus, it may be suggested that there is some true underlying Fe content in the Ti-N-rich particles. This Fe content is a function of temperature of annealing: the higher annealing temperature results in less iron in Ti-N rich particles. During APT analysis, this content may be artificially increased by trajectory overlaps for particles with radius smaller than about 2 nm (more than predicted by the model).

b) Precipitation and kinetics

Mechanical alloying is known as a process that leads the system toward non-equilibrium states [24, 25]. Here, it allows a Ti and N supersaturated solid solution to be obtained. In addition, as experimentally observed, Ti and N rich particles are present in this supersaturated solution. Since these two elements are coming from different powders, these particles cannot be remnant of initial powders. This means that nucleation occurs during ball milling, so that the atomic diffusion is sufficient to allow atoms to gather. Nitrogen is interstitial specie, it is a fast diffuser in bcc iron [14, 16]. In addition, very high dislocation densities [7, 26] as well as excess of vacancies [17] are introduced into material during MA. The presence of such defects may significantly change the behaviour of the system, accelerating solute diffusion and providing high diffusivity paths. Finally, during MA process, temperature rise due to ball collisions may occur [24, 27]. Therefore, all these events may significantly enhance the kinetic of the system, resulting in the formation of Ti-N-rich particles. Considering the discussion about Cr shell and Cr content in the particles, it seems that in as milled state, these particles are not well defined nitrides, but contain significant amount of matrix atoms.

The precipitation kinetics from a metastable solid solution can be divided into three stages: nucleation (N), growth (G) and coarsening (C) of the new phase (Ti-N rich particles in the present case). These three regimes can overlap. The comparison of particle characteristics, as well as the matrix composition after the different annealing treatments can give information about precipitation kinetics in the system.

- *Concentrations of Ti and N in the matrix*

Evolution of Ti and N concentration in the matrix as a function of annealing temperature is shown on *Figure 4.24*.

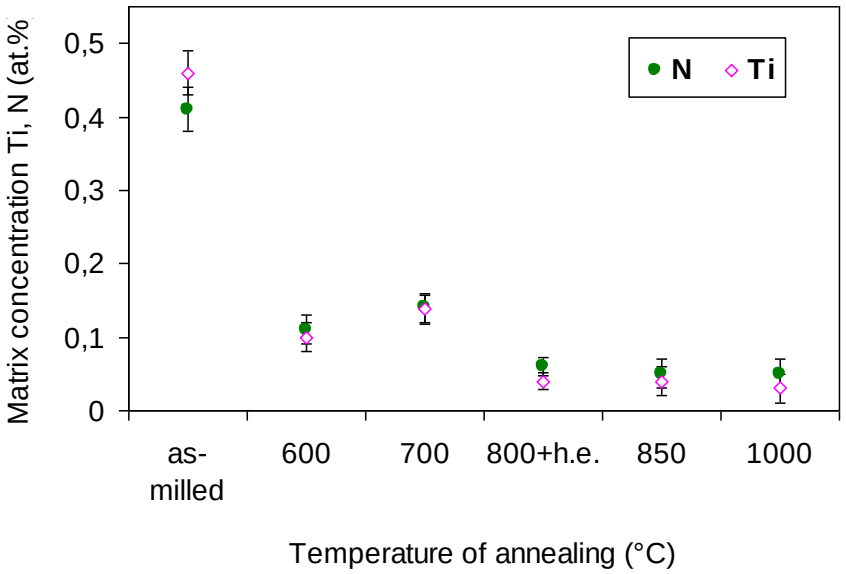

Figure 4.24. Evolution of Ti and N concentration in the matrix of MA NDS steel as a function of annealing temperature. Hot extruded condition (h.e.) is also taken into account.

Considerable levels of Ti (0.46±0.02 at.%) and N (0.41±0.02 at.%) are measured in the matrix of the as-milled powder. After annealing treatments, Ti and N concentrations in the matrix are much lower than in as the milled powder. This is a consequence of the nucleation and growth of nanoparticles. Indeed, during heat treatment, N and Ti are removed from matrix and are incorporated into particles. The Ti and N concentrations reach their minimum value in hot extruded samples (Ti 0.04±0.01 at.% and N 0.06±0.01 at.%). For annealing at higher temperature (850 and 1000°C), the concentrations of Ti and N in the matrix do not significantly change (e.g. for Ti, 0.04±0.01 and 0.03±0.01 at.% respectively) in comparison to hot extruded material. The solubility limit of titanium in ferritic matrix of a Fe-19%Cr-0.54%N-0.57%Ti-0.3%W alloy was estimated with the ThermoCalc software at 600, 700, 850 and 1000°C. It is suggested to be close to 0.029at.% in all cases. This value is in very good agreement with measurements done by APT. Thus, for heat treatments at 800°C and above during 1hour, it seems that the matrix is close to its equilibrium state.

- *Size and number density of Ti-N particles*

The number densities and mean sizes of Ti-N rich particles as function of annealing temperatures are depicted on *Figure 4.25*.

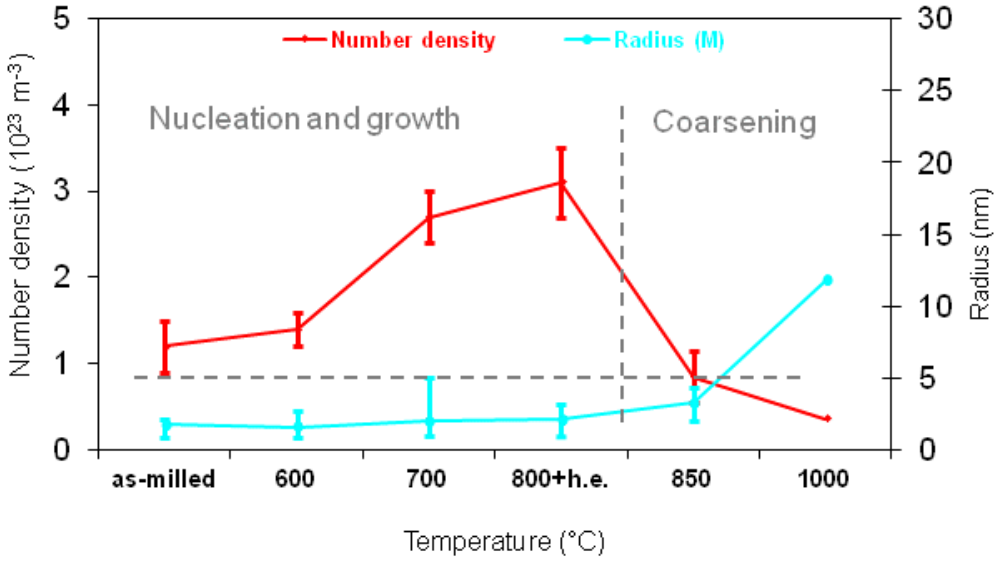

Figure 4.25. Evolution of number density and mean Guinier radii of nanoparticles observed in MA NDS steel as a function of annealing temperature. Hot extruded condition (h.e.) is also taken into account. Two stages can be evidenced owing to experimental results: i) nucleation and growth and ii) coarsening stage of Ti-N-rich particles.

The figure reveals that the number densities after heat treatment at 600, 700°C and 800°C (hot extrusion) increases with temperature. The highest value ($3.1\pm0.6\times10^{23}$m^{-3}) is observed in the hot extruded sample (800°C). At higher temperatures, the number density decreases with annealing temperature. An important point is that the number density in samples annealed at 850 and 1000°C is not only smaller than the one in samples annealed at lower temperatures (that could be explained by a lower nucleation rate at higher temperatures) but also lower than the initial number density in as-milled state (this demonstrates that a part of the particles is dissolved during annealing at high temperature). As far as sizes are concerned, there is no significant difference up to annealing at 850°C. At higher temperature, the size of particles increases.

These experimental results suggest that the precipitation kinetic of Ti-N rich particles can be divided into three stages:

(i) Nucleation of Ti and N enriched particles starts during mechanical alloying step. These particles could contain a high level of matrix atoms (Fe and Cr).

(ii) During annealing, nucleation is continuing and the matrix atoms are partly rejected from particles (evolution of their Fe and Cr contents), resulting in a Cr rich shell around particles. No significant growth is observed during this stage (600, 700 and 800°C). Maybe the shell limits the growth of particles.

(iii) When most of Ti and N are removed from matrix, coarsening of particle occurs. Considering 1 hour treatment, this step is only reached for annealing at 850°C or more. It cannot be excluded that the same behaviour could be observed at lower temperatures but for longer times. This could be a limitation for the use of NDS steels.

In order to get more information about this point, some kinetic calculations were performed with the MatCalc software. The input parameters as well as basic principles of MatCalc were described in Chapter 2. The script and results of simulation are given in the Appendix 5. As expected, MatCalc predicts the formation of stoichiometric TiN nitrides, which were not experimentally observed. Concerning the kinetic aspects, the *Figure 4.26*, shows an example of MatCalc results: the evolution of the size and number density of TiN nitrides as a function of time, during annealing at 700°C/1h.

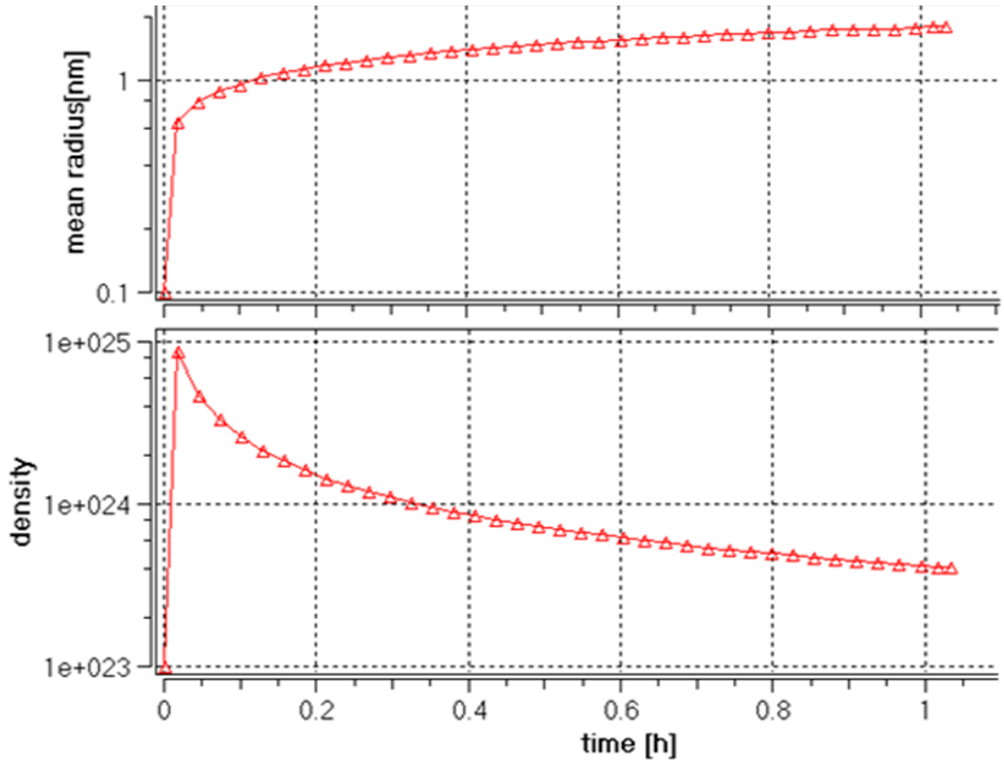

Figure 4.26. Evolution of number density and mean radius of nanoparticles as a function of time during annealing at 700°C (1 hour), as estimated by MatCalc.

According to this figure, nucleation of TiN particles occurs very quickly, and after few minutes, coarsening starts. This is not what is suggested by APT observations. Considering the radius and density after one hour, the comparison of APT and MatCalc data is depicted on Figure 4.27 *(a, b)*.

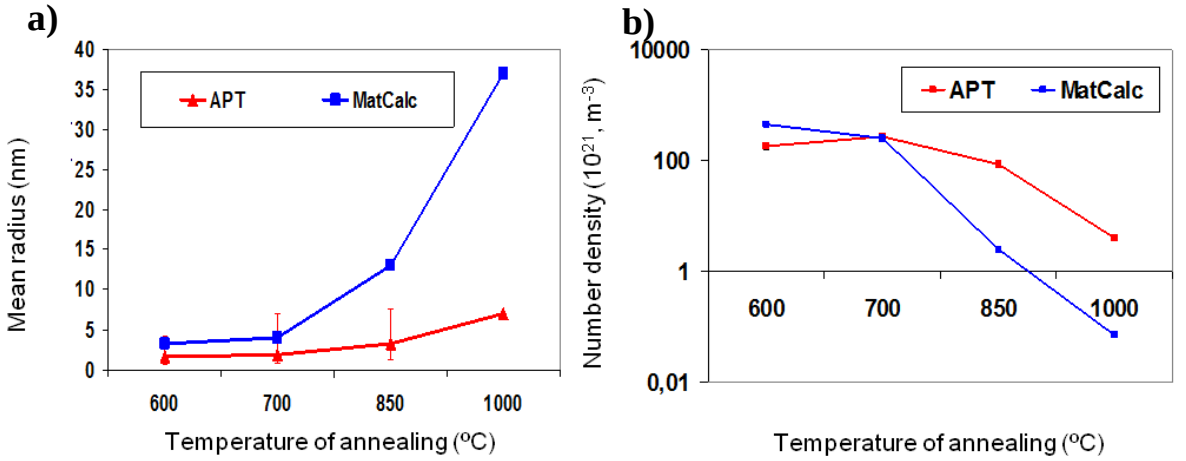

Figure 4.27. Comparison of APT results with MatCalc calculations: (a) size and (b) number densities.

As it can be seen, tendencies are similar (as expected): increase of the radius and decrease of the number density with annealing temperature. However, the mean radii given by MatCalc are higher than experimental ones and number densities smaller. So, in general only a qualitative agreement is found.

Several reasons can explain these differences. First, this can be linked with the fact that MatCalc is very sensitive to input data such as grain size, dislocation density, surface energy etc. Such data are rarely known for simple systems and especially in case of MA NDS where MA process is used. Second, particles are initially formed during mechanical alloying. Thus they originate from a non equilibrium process. This could have a strong influence on the evolution during annealing and is not taken into account in the software. Finally, the kinetic of the system can be slow down due to the presence of Cr rich shell which is not considered in the calculations. This could explain why, at a given temperature, the particles observed experimentally are smaller and more numerous than the MatCalc prediction.

c) Comparison between ODS and NDS

Up to now, two kinds of materials are described in the present work: ODS steel (described in Chapter 3) and NDS steel, both elaborated by MA. The difference between ODS and NDS is the nature of the nano-reinforcements introduced in the ferritic matrix. In the first case it is stable dispersion of oxides (Y-Ti-O rich nanoparticles) and in the second, nitrides (Ti-N-rich particles). A first attempt to clarify if NDS steels could be worthy alternative to ODS steel with at least comparable or even better properties is to compare the characteristic of the fine dispersion of nano-reinforcements in each case.

The microstructures of ODS and NDS steels in final states are shown on *Figure 4.28* (a,b), for the thermomechanical treatment giving the highest number density of particles in each case: (i) hot extrusion at 1100°C in the case of ODS (afterwards material is hot-rolled and finally annealed at 1050°C) and (ii) hot extrusion at 800°C without further treatment in the case of NDS.

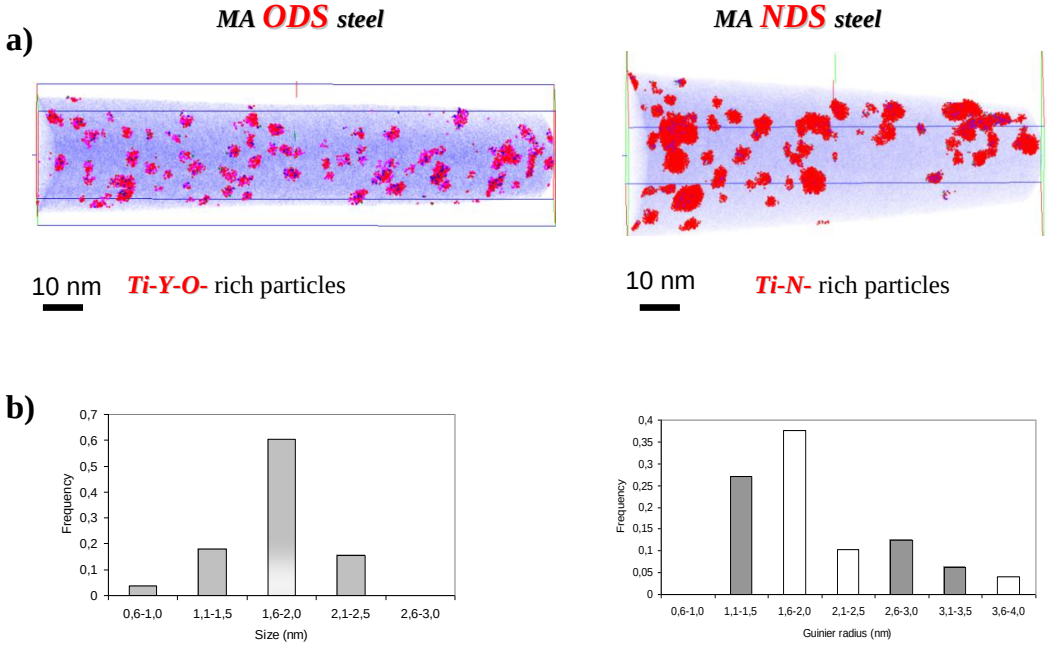

Figure 4.28. Comparison of ODS and NDS steels consolidated by hot extrusion. (a) Isolated Y-Ti-O rich (left) and Ti-N-rich (right) nanoparticles are shown. (b) Corresponding size distribution diagrams.

Consolidation of NDS powder at low temperature (800°C) allows keeping relatively high number density (4×10^{23} m^{-3}) of Ti-N particles. It is slightly lower than Ti-Y-O particles (7×10^{23} m^{-3}) in ODS steel. As for sizes, the mean Guinier radius of Ti-N-rich particles is slightly larger than Ti-Y-O nanoclusters: 2.1 and 1.8 nm for NDS and ODS steels respectively. In other words, the microstructures are comparable. It will be of interest to investigate the stability of both microstructures after long thermal ageing at operating temperatures of Gen IV reactors, in particular to investigate coarsening in the case of NDS steel (in general, lot of results can be found in the literature on ODS steels).

I.5. Partial conclusion

MA NDS steel, produced by mechanical alloying of Fe-18Cr-1W-0.14N pre-alloyed powder with 0.5 wt.% of TiH_2. The microstructure and especially nanoclusters are studied in as-milled, annealed (at 600, 700, 850, 1000°C during 1 hour) and hot extruded (800°C) states. In addition, grain boundaries study is also conducted since several GBs are revealed. Characterization by APT is compared to results reported by small angle neutron scattering (SANS). The main conclusions are :

- Ti-N-rich oxy-nitrides, sometime containing some trace of Al, are detected in all states. The level of iron in these particles depends of the heat treatment following MA (highest annealing temperature results in lower Fe content in particles). However, no significant evolution Ti/N ratio is observed.
- Nucleation of particles occurs since MA. During subsequent annealing treatments (600 and 700°C during 1h) nucleation preferentially occurs along grain boundaries.
- Evolution of particles number density and mean radius is estimated. The highest number density ($(3.1\pm0.4)\times10^{23}m^{-3}$) is observed in hot extruded sample. According to APT, the extrusion pre-heating during 1 hour must be performed at temperature lower than 850°C to avoid coarsening of particles.
- Annealing treatment results in Cr segregation to the grain boundaries (observed for all studied GBs). Segregation of Ti, N(Si), W, Mn species are also observed. More systematic study is needed to investigate these points in more details.

Since the number density and size of reinforcements are responsible of the mechanical properties of the material, these reinforcements should remain stable in the range of operating conditions. The behaviour of these Ti-N rich particles is not fully tested and other fundamental works are needed for further evaluation the potential capabilities of the MA NDS material. Nevertheless these first results are promising.

II. Study of nitrided NDS

Another way to elaborate NDS steel is to introduce nitrogen into ferritic matrix by nitriding. This second part is devoted to the samples elaborated in this way. Nitrided NDS powders were studied in their initial state, i.e. after nitriding treatment, as well as after annealing at 600 and 700°C during 1hour. Consolidated material is also investigated. As it is known, nitriding treatment may result in a non homogeneous distribution of nitrides through the microstructure. To achieve more uniform distribution of nitrogen, the powder before hot extrusion is subjected to homogenization treatment (for details see section II.4 of the Chapter 2). This is not the case for other powders.

For characterization of powders as well as consolidated material, the LAWATAP technique is preferably used, as it allows analyzing relatively large volumes. The summary of performed analyses performed on nitrided NDS powder is summarized in *Table 4.4*.

Table 4.4. APT experiments performed on nitrided NDS steel by APT.

Material	APT	Number of analyses	Number of atoms, LAWATAP
As-nitrided powder	LAWATAP	1	11.10^6at 13×10^6at
Annealed at 600°C/1h powder	LAWATAP	1	20×10^6at
Annealed 700°C/1h powder	LAWATAP	1	20×10^6at
Hot extruded sample	TAP	1	200 000at
	LAWATAP	2	22×10^6at 10×10^6at

The microstructures are described below. First, the information is provided on nitrided NDS powders. Afterwards, characterization of consolidated by hot extrusion material is discussed.

II.1. Characterization of powders

As it is described in Chapter II, Focused Ion Beam (FIB) annular milling is used to prepare APT thin needles from powder grains. However, in nitrided specimens, the content of nitrogen may vary from the surface to the centre of a powder grain [29]. So, the size of nitrided powder particles as well as the depth at which analyze is conducted should be defined to be able to make comparisons.

A SEM micrography of NDS powder in as-nitrided state is depicted in *Figure 4.29* (a). The powder particles have spherical morphology. The size distribution of powder grains is shown in *Figure 4.29* (b). According to this size distribution the peak size is in the range 30-60 μm and the mean value is 60 μm.

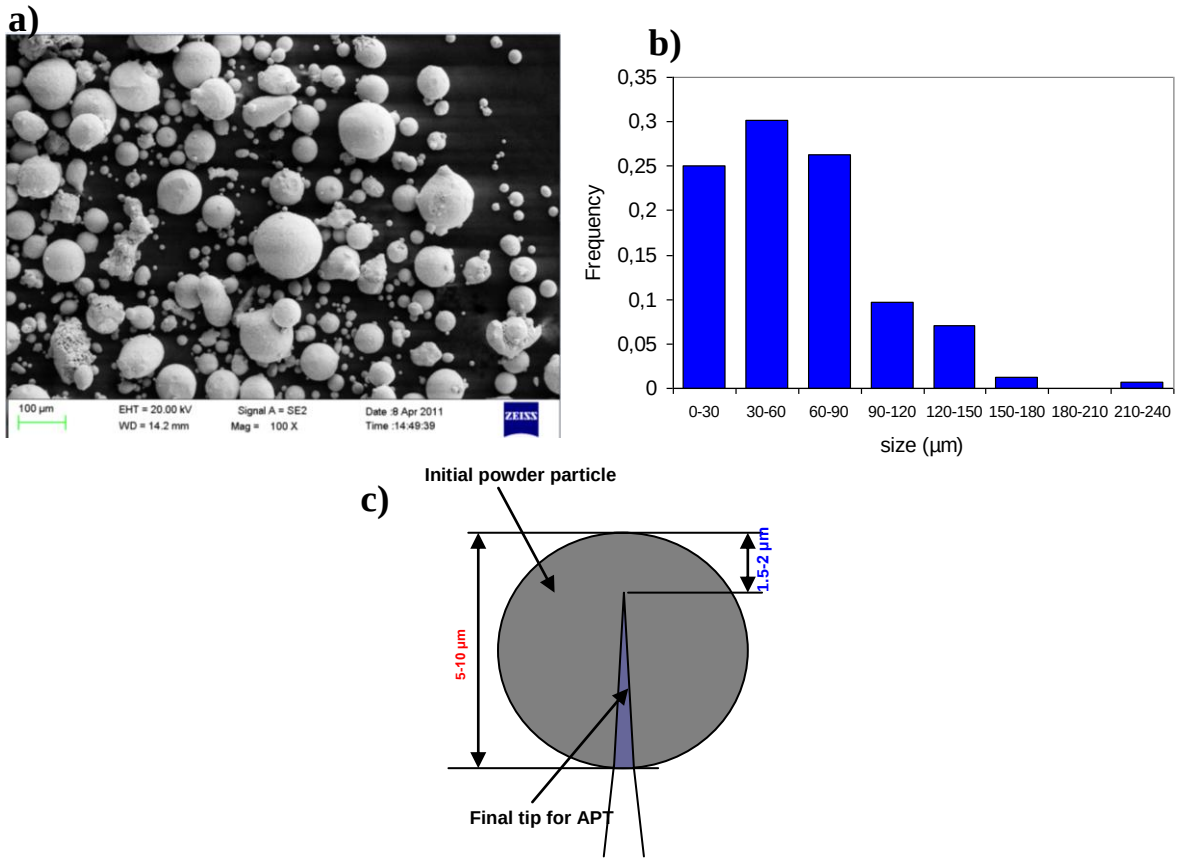

Figure 4.29. NDS powder in as-nitrided condition: (a) SEM micrography, (b) size distribution and (c) schematic representation of depth at which APT tips is prepared in comparison to initial powder.

As for powders, because of practical reasons, only the smallest ones (between 5 and 10µm) are characterized by APT. The final needles are prepared at the depth of about 1.5 to 2.0 µm from the surface of the powder grain, as shown on the sketch *Figure 4.29* (c).

a) Powder in as-nitrided state

In the present case, the mass resolution of the LAWATAP instrument was not high enough to give accurate global chemical composition, in particular for elements located just after Fe peaks on mass spectrum (e.g. Mn, Ni). Thus, only the concentrations of Ti, N, Cr, Si and W species are given here. It is noteworthy that the estimation of chemical composition takes into account CrN, FeN and TiN molecular ions detected on mass spectrum. Others elements are part of the "balance". Global chemical composition for nitrided NDS powder after nitriding is shown in *Table 4.5*.

Table 4.5. Global chemical composition of nitrided NDS powder in as-nitrided state by LAWATAP. Compositions are in at.%.

	Ti	N	Cr	Si	W
Expected	**0.86**	**0.67**	**19.1**	**-**	**0.30**
As-nitrided state	**0.40**	**10.3**	**15.7**	**0.60**	**0.24**

As it can be seen, in comparison to expected values, the measured content of W is slightly lower, Ti and Cr levels are significantly lower whereas significantly higher level of nitrogen is measured.

A 3D reconstruction is depicted on *Figure 4.30*.

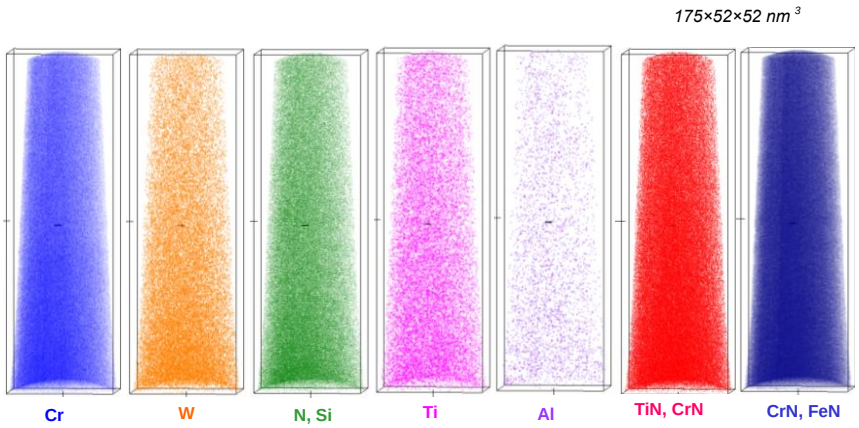

Figure 4.30. 3D reconstructions of NDS powder in as-nitrided condition. Analysed volume is 175× 52× 52 nm^3. No evidence of presence second phase is observed.

A visual analysis as well as the use of cluster search algorithm doesn't reveal any evidence of a second phase. Taking into account the analysed volume, if any second phase exists, its number density is lower than 2×10^{21} m^{-3}. This observation agrees well with SANS analysis which doesn't detect any second phase [2].

b) Powder annealing at 600°C/1h

Global chemical composition of nitrided NDS powder after annealing at 600°C during 1h is shown in *Table 4.6.*

Table 4.6. Global chemical composition of nitrided NDS powder after annealing at 600°C during 1h measured by LAWATAP. Concentrations are in at.%.

	Ti	N	Cr	Si	W
Expected	**0.86**	**0.67**	**19.1**	**-**	**0.30**
600°C/1h	**0.40**	**10.2**	**18.2**	**0.40**	**0.10**

As it can be seen, the measured content of Ti as well as W is lower than expected values. Contrary to what was observed in as nitrided powder, a good agreement is found with expected value for Cr concentration. Here again, a significantly higher content of N is measured in comparison to expected values. The measured contents of Ti and N are comparable to ones measured in as-nitrided condition.

3D atom maps are depicted on *Figure 4.31*.

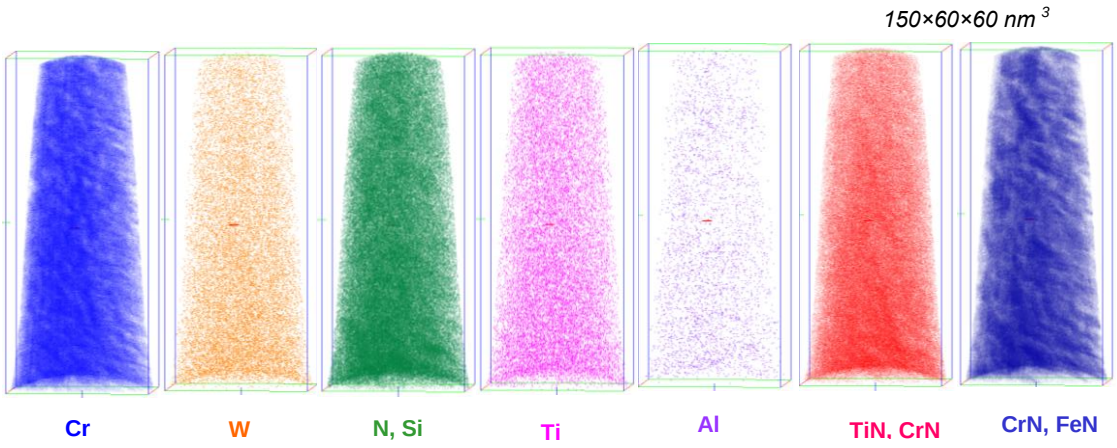

Figure 4.31. 3D reconstructions of nitrided NDS powder after annealing at 600°C/1h. Analysed volume is 150× 60× 60 nm^3. Distribution of Cr, N, Si and TiN, CrN, FeN molecular ions is not homogeneous.

The figure clearly reveals that distributions of Cr, N, CrN and FeN are not homogeneous. These elements are associated with nanoparticles. A rough estimation of the composition of these particles from a concentration profile drawn across the whole analyzed volume, allows to define a threshold value equal to 35 at% (Cr+N) in the cluster search algorithm.

The *Figure 4.32* is a filtered image showing Cr, N, CrN and FeN ions in regions where the concentration of Cr and N is higher than the threshold of 35%. Cr-N-rich particles are clearly highlighted. These particles are plate shaped and their spatial orientation is not random. Different habit planes, with specific angle relationships can be clearly distinguished.

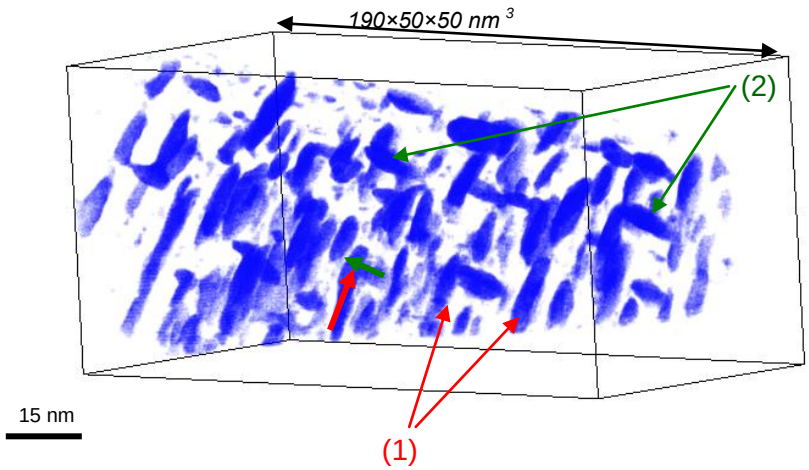

Figure 4.32. Isolated Cr-N rich particles observed in nitrided NDS powder after annealing at 600°C/1h. Particles (designated as (1) and (2)) with different habit planes are shown. Only Cr, N species and CrN, FeN molecular ions is shown.

As it is shown in the figure, two orientations, noted (1) and (2), are visible. The angles between the normal of these plates and the direction analyses are respectively 45 and 65° for (1) and (2) orientations. However, since neither crystallographic poles nor atomic planes are observed in reconstructed volume, the crystallographic orientation relationships between these particles and ferritic matrix cannot be determined. It worth to mentioned that usually, the particles in nitrided Fe-Cr and Fe-Ti alloys appear as a thin plates laying in {001} planes of ferrite to minimize the lattice strain. The most common relationship of these plates with the bcc iron is the Baker-Nutting orientation relationship (OR) [29–31]: $\{0\,0\,1\}_{\alpha\text{-Fe}}$ // $\{0\,0\,1\}_{\text{nitride}}$; $[1\,0\,0]_{\alpha\text{-Fe}}$ // $[1\,1\,0]_{\text{nitride}}$. So, this OR can be expected in the current case.

The number density of particles is about 2×10^{23} m^{-3}. Since the particles are found to be plate-shaped, their size has to be characterized in the three dimensions: thickness, width and

length. These values are measured manually. The width for both families (orientation) of particles varies from 3 to 13 nm, length from 5 to 28 nm and thickness from 1.6 to 5 nm. It is rather difficult to compare these values with the SANS data [2] since, in this latter case, the data are interpreted on the assumption that particles are spherical, which is not at all consistent with APT observations.

Concerning chemical composition, the nitride core composition as a function of thickness of the plates is given on *Figure 4.33*. Numbers (1) and (2) given next to values of thickness, correspond to the two orientations of particles (as indicated in *Figure 4.32*). No significant difference of chemical compositions as a function of the thickness or the orientation of the particles is observed, thus they are presented together for both orientations. Variations of measured chemical composition are observed. For instance, the Cr content varies from 29 to 51 at.% and N from 17 to 44 at.%. The mean chemical composition for both families of particles is: **46.4**±0.80 **Cr**, **32.3**±0.80 **N**, **20**±0.6 **Fe**, **0.74**±0.20 **Ti** and **0.13**±0.05 **Al** at.%. The chromium over nitrogen ratio (Cr/N) is 1.4±0.1.

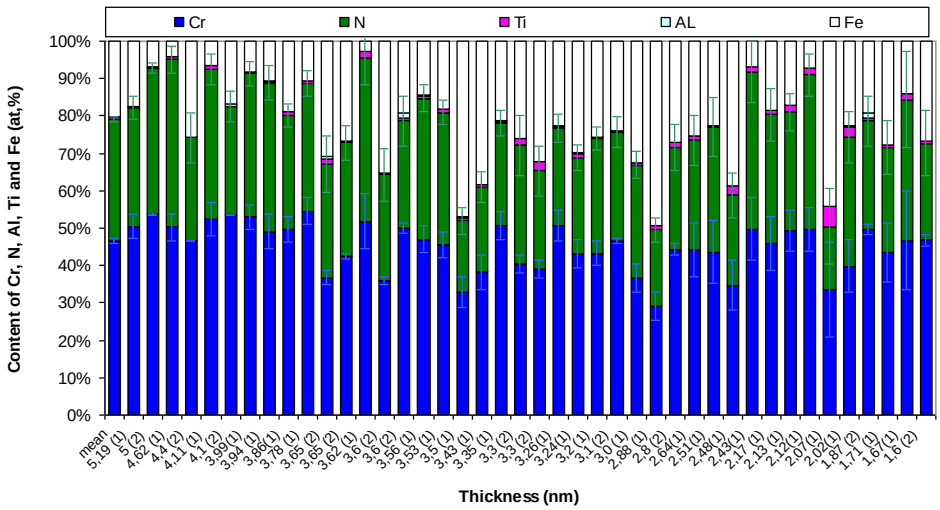

Figure 4.33. Composition of particles observed in nitrided NDS steel annealed at 600°C/1h as a function of their thickness. Composition is calculated for two families of particles (denoted as (1) and (2)) as indicated in Figure 4.32. Number (1) and (2) next to thickness indicate on family of particles. Only Cr, N, Ti, Al and Fe (at.%) are shown.

In APT, Cr-N rich particles have higher evaporation field than the ferritic matrix (similar observation is done in case of Fe-5Cr alloy in [29]). This leads to a local magnification effects [12, 13] and as a consequence, slight increase of particles dimensions in the lateral direction may occur. As for their chemical composition, it was shown in Ph.D. work of Jessner, that the nitrides can contain some iron [18]. However, trajectory overlaps can

artificially increase the level of iron measured inside thin plates, when their orientation is not perpendicular to analysis axis [18,32]. The content of Fe measured in these nanoparticles by APT (~20 at.%) is in good agreement with SANS data [2]. Thus it may be expected that composition is just slightly modified by trajectory aberrations.

c) Powder annealing at 700°C/1h

Global chemical composition of nitrided NDS steel after annealing at 700°C during 1h is shown in *Table 4.7*. As it can be seen, the measured contents of Ti as well as W are significantly lower than the expected ones. The Cr concentration is in good agreement with expected value. Here again, a significantly higher content of N is measured. The measured contents of Ti and N are comparable to values measured in previously reported powders (as-nitrided and annealed at 600°C during 1h).

Table 4.7. Global chemical composition of nitrided NDS steel after annealing at 700°C during 1h measured by LAWATAP. Compositions are in at.%.

	Ti	N	Cr	Si	W
Expected	**0.86**	**0.67**	**19.1**	**-**	**0.30**
700°C/1h	**0.36**	**9.7**	**19.0**	**0.40**	**0.10**

3D atom maps are depicted on *Figure 4.34*. Like in previous case, Cr, N, TiN, CrN and FeN are not homogeneously distributed. These ions are located in nanoparticles.

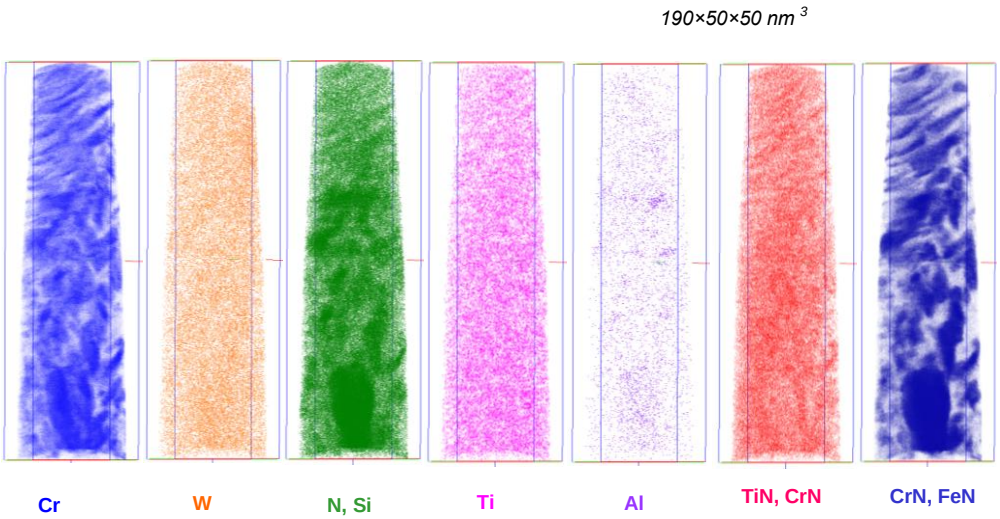

Figure 4.34. 3D reconstructions of nitrided NDS steel after annealing at 700°C during 1h. Analysed volume is 190× 50× 50 nm^3. Distribution of Cr, N, Si, Al and TiN, CrN, FeN molecular ions is not homogeneous.

A threshold of 32 at.% (Cr+N) is used for cluster search algorithm. The corresponding filtered atom map is represented on *Figure 4.35*. Particles having different habit planes can be clearly distinguished on 3D reconstruction. In the first part of the analysis, relatively thin plate-like particles are observed. The angle between the normal of these plates and the direction of analysis is about 30°. For further discussion, they are denoted as (1). In the second part of analysis, apparently thicker plate-like particles are visible. Their normal is perpendicular to the analysis axis. They are denoted as (2).

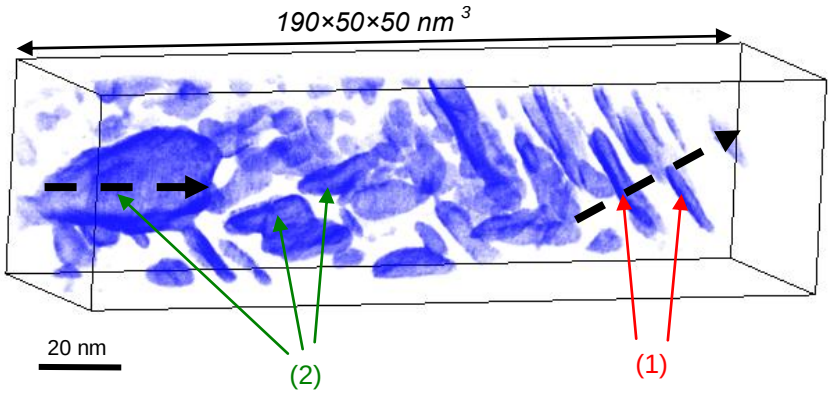

Figure 4.35. Isolated Cr-N rich phases observed in nitrided NDS steel after annealing at 700°C during 1h (only Cr, N species are shown). Two orientations of particles can be distinguished denoted as (1) (beginning of the analyse) and as (2) (second half of the analyse). Direction of composition profiles shown on Figure 4.36 and *Figure 4.38 are indicated by dashed black arrows. Analysed volume is 190× 50× 50 nm^3.*

A composition profile drawn perpendicularly to the particles (1) (as indicated by dashed black arrow on *Figure 4.35)* is shown in *Figure 4.36*. Enrichment of Cr and N as well as depletion of Fe corresponds to Cr-N rich particles. The contents of Cr and N inside these particles reaches 40 at.% and 26 at.% respectively. This approximately corresponds to the Cr_2N stoichiometry of hexagonal V_2N-type Cr nitride [33]. Here again, a slight part of the iron measured here certainly comes from the matrix [32].

As for particles denoted as (2), they are also plate-like, but appear thicker than the population (1). The thickness of these plates varies from 5 to 20 nm, width from 10 to 42 nm and their length from 17 to more than 44 nm. The length of the bigger particle (that is clearly seen in the end of analyze) cannot be evaluated from APT, since its size exceeds the analyzed volume (more than 44 nm). These particles are thick enough to have no or limited bias in core composition.

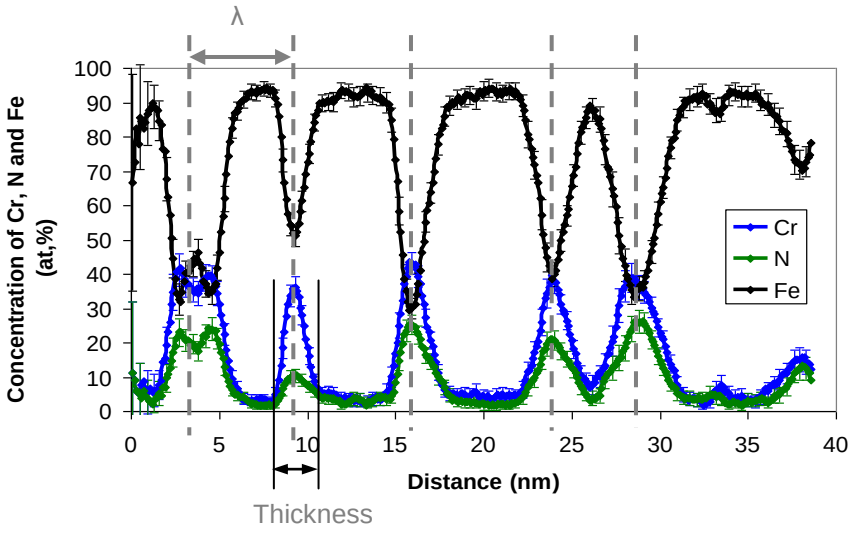

Figure 4.36. Composition profile through particles observed in nitrided NDS steel annealed at 700°C during 1h. Profile is drawn perpendicularly to particles denoted as (1) as indicated by black dashed line on Figure 4.35-(1). Sampling volume is 3×3×1 nm^3; λ is the characteristic distance between two Cr-N rich particles. Only Cr, N and Fe concentrations (at.%) are shown.

The compositions of particles denoted as (2) are shown on *Figure 4.37*. It can be seen, some Ti as well as traces of Al is detected. The measured Cr concentration in these particles varies from 45.7 to 55.5 at.% and it is quite constant. However, the variation of N concentration from 25 to 47 at.% is noted. Some of these particles appear more enriched in N. Thus, the mean chemical compositions are calculated separately for both types of nanoparticles (more and less enriched in N). The mean chemical composition for nanoparticles less enriched in N (denoted as (2)) is following: **52.4**±3.3 **Cr**, **28.1**±3.0 **N**, **18.4**±1.0 **Fe** and **0.73**±0.6 **Ti** at.%. The chromium over nitrogen ratio (Cr/N) is 1.9±0.2. Their stoichiometry is approximately corresponding to Cr_2N like in case of nanoparticles denoted as (1). The mean chemical composition for thicker particles more enriched in N (denoted as (2),) is the following: **50.9**±2.2 **Cr**, **42.9**±2.2 **N**, **5.0**±1.0 **Fe**, **0.6**±0.3 **Ti** and **0.41**±0.3 **Al** at.%. The chromium over nitrogen ratio (Cr/N) is 1.2±0.1and their stoichiometry is approximately corresponds to CrN. Thus, the APT data is consistent with existence of Cr_2N and CrN nanoparticles.

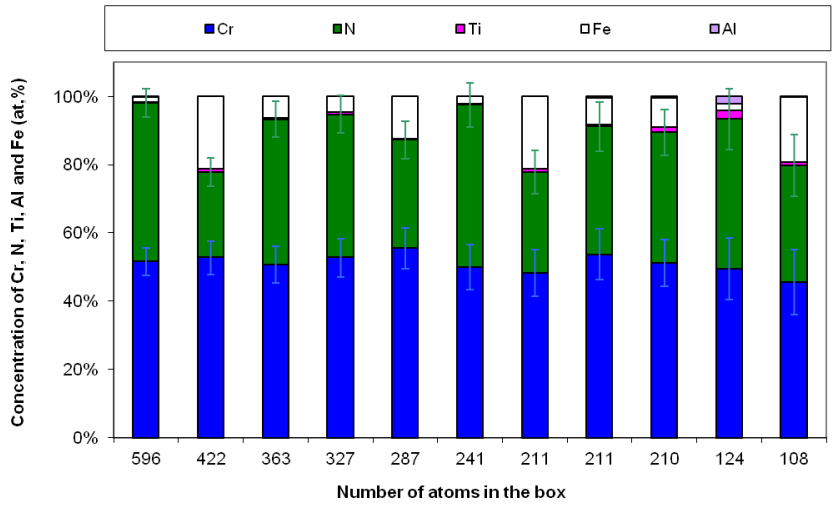

Figure 4.37. Composition of particles (denoted as (2)) observed in nitrided NDS steel annealed at 700°C during 1h. Only Cr, N, O, Al and Fe (at.%) is shown.

A composition profile plotted through the largest nanoparticle (as indicated by black dashed arrow *Figure 4.35*) is shown in *Figure 4.38*. From this profile, it can be seen that this particle is enriched in Cr and N and almost depleted in Fe. The content of Fe reaches 2.0 at.%.

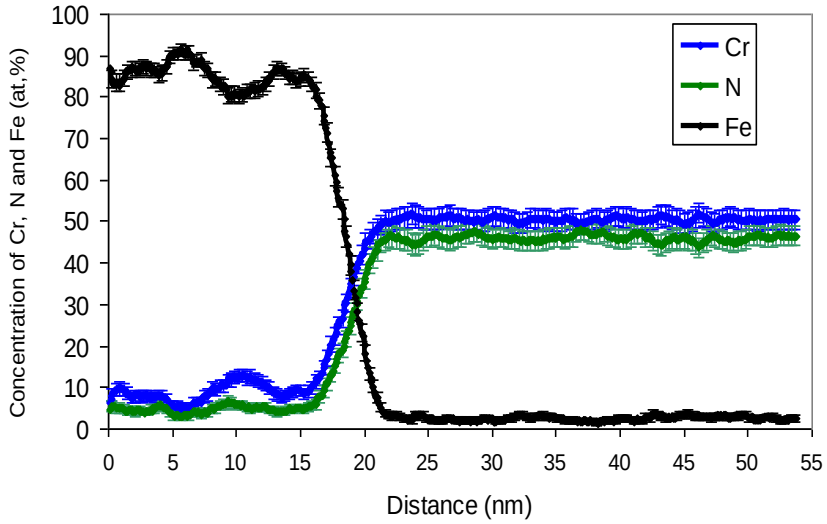

Figure 4.38. Composition profile for Cr-N-rich particle observed in nitrided NDS steel annealed at 700°C/1h. Profile drawn for large particle (which is clearly seen in the end of 3DAP analyse) in direction of analyse as indicated in Figure 4.35-(2). Sampling volume is 5×5×1 nm^3. Only Cr, N and Fe (at.%) are shown.

An estimation of the particle number density for this state is rather complicated, since particles are close to each other, partially interwoven and cross the analyzed volume.

However, volume fraction of both populations of particles can be estimated from mass balance[2]. It is about 25 to 30 %.

II.2. Characterization of consolidated material

One LATAP and two LAWATAP experiments are performed for nitrided NDS steel in hot extruded state. The performed experiments are described further one by one.

a) Experiment 1. LATAP

The spatial distributions of elements in nitrided NDS steel after hot extrusion are shown on *Figure 4.39*. As it can be seen the distribution of elements in that case is homogeneous, no evidence of second phase is observed. However, the volume analyzed here is quite small and if the second phase exists, its number density can be up to 1.5×10^{23} m^{-3}.

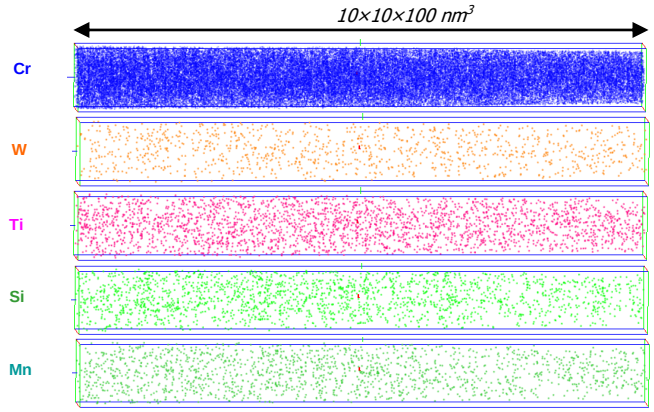

Figure 4.39. 3D reconstructions of a small volume ($10\times10\times100$ nm^3) of nitrided NDS steel after hot extrusion analysed by LATAP (experiment 1). Cr, W, Ti, Si and Mn species are shown.

The global chemical composition of this volume, which is also the matrix composition, is reported in the *Table 4.8*. As it can be seen, in comparison to expected chemical composition, there is relatively good agreement for Cr, Ti and W. However, a significant depletion of N is measured. This almost complete absence of nitrogen can be explained in 2 ways:

[2] *The volume fraction of nanoparticles, fv, can be estimated in accordance to the formula: $f_v=(C_0-C_m)/(C_p-C_m)$, where C_0, C_m and C_p are chemical compositions: global, matrix and nanoparticles respectively.*

i) Nitrogen may be involved in precipitation reaction, resulting in local depletion. However, one should keep in mind that almost all Cr and Ti (strong nitride forming elements) are present in solid solution.

ii) Nitriding and subsequent homogenization treatment could result in a non homogeneous distribution of nitrogen at larger scale.

To clarify this point, larger volumes of analyse are needed. The LAWATAP experiments are described below.

Table 4.8. Chemical composition of the volume of nitrided NDS steel after hot extrusion shown on Figure 4.39 (Experiment 1). Concentrations are in at.%. Balance is iron. Uncertainties are given by the standard deviation 2σ.

	Ti	**N**	**Cr**	**Mn**	**Si**	**W**
expected	**0.86**	**0.67**	**19.1**	**-**	**-**	**0.30**
Experiment 1	**0.75**±0.02	**0.02**±0.003	**18.8**±0.10	**0.30**±0.2	**0.47**±0.2	**0.24**±0.2

b) Experiment 2. LAWATAP

An estimation of the global chemical composition of nitrided NDS steel after consolidation is shown in *Table 4.9*.

Table 4.9. Global chemical composition in nitrided NDS steel after hot extrusion by LAWATAP (Experiment 2). Compositions are in at.%. Balance is iron

	Ti	**N**	**Cr**	**Mn**	**Si**	**W**
expected	**0.86**	**0.67**	**19.1**	**-**	**-**	**0.30**
Experiment 2	**0.63**	**0.63**	**17.6**	**-**	**0.37**	**0.24**

Contrary to the previous measurement, the concentration of nitrogen is very close to the expected one. It is worth to mention that it is significantly lower than the concentrations measured in as-nitrided and annealed (600 and 700°C) powders (~10 at.%).

The spatial distributions of solute atoms in this second volume are depicted on *Figure 4.40*. It clearly appears that N, Ti, CrN and TiN ions are associated with plate shaped particles. Carbon also contributes to these particles. Their larger dimensions of these particles are larger than the section of analyzed volume. The thickness can be defined for several particles. It varies from 3 to 14.5 nm. The number density of these particles is estimated to about $2 \times 10^{22} m^{-3}$.

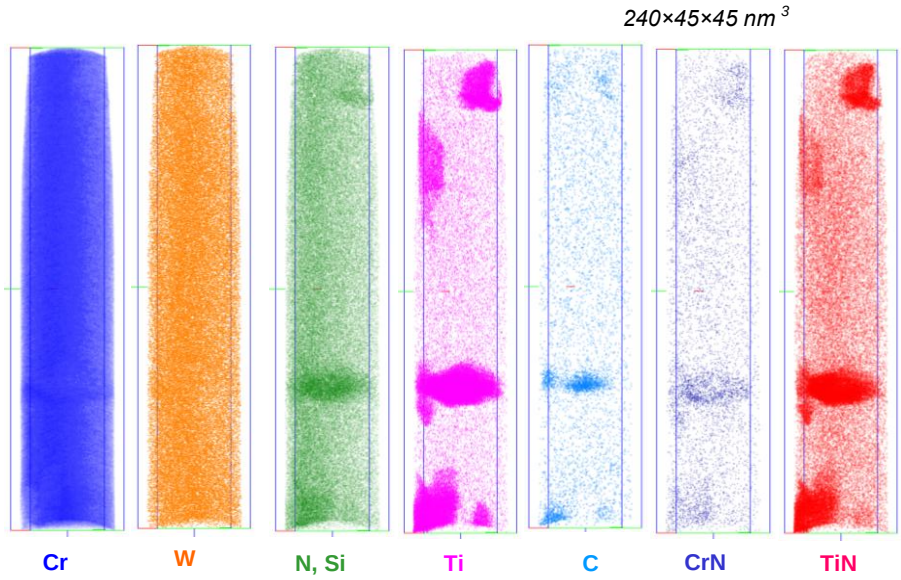

Figure 4.40. 3D reconstructions of nitrided NDS steel after hot extrusion. (Experiment 2) Analysed volume 240× 45× 45 nm^3. Distribution of N, Ti, C species and TiN, CrN molecular ions is not homogeneous.

As can be seen in *Figure 4.41*, specific orientations of the volume reveal angle relationship between these particles. They appear to be perpendicular. As it was discussed in the case of powder annealed at 600°C during 1h, it can be expected that there is Baker-Nutting orientation relationship, which is the most commonly observed in Fe-Cr and Fe-Ti alloys upon nitriding treatment [29–31,34].

The chemical composition of each particle as a function of its thickness is presented in *Figure 4.42*. These particles are mostly enriched in Ti and N. However, a small amount of C is also measured. The mean measured chemical composition is: **51.5**±1.0 **Ti**, **34.5**±1.0 **N**, **5.0**±0.4 **Fe**, **6.8**±0.50 **Cr, 0.17** ± 0.10 **O** and **1.9**±0.26 **Al** at.%. The Ti/(N+C) ratio is 1.40 ±0.10. It differs from expected TiN stoichiometry.

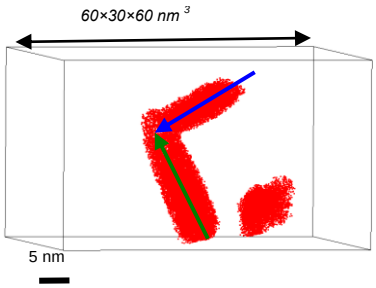

Figure 4.41. Isolated particles observed in nitrided NDS steel after hot extrusion (Experiment 2). Ti, N elements are shown. Particles with different habit planes are presented.

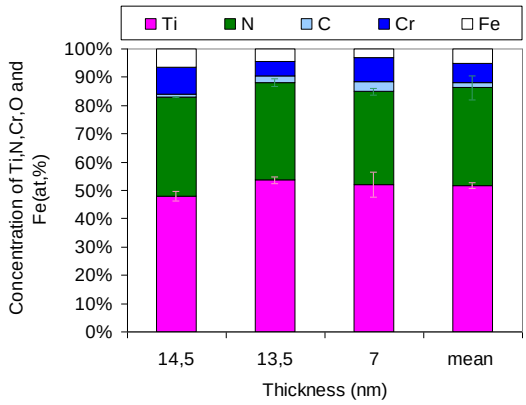

Figure 4.42. Composition of each particle observed in nitrided NDS steel after hot extrusion as a function of thickness. Ti, N, C, Cr and Fe are shown

The matrix composition measured in this volume is presented in *Table 4.10*. It can be compared to the one measured in experiment 1 (*Table 4.8*). Good agreement is found for Si and W. However, significantly lower content of Ti as well as higher level of N is observed in this case. Such difference can be indication that microstructure of the hot extruded state is heterogeneous.

Table 4.10. Chemical composition of the matrix in nitrided NDS steel after hot extrusion shown on Figure 4.40 (Experiment 2). Concentrations are in at.%. Balance is iron. Standard deviations are given by 2σ.

	Ti	**N**	**Cr**	**Mn**	**Si**	**W**
expected	**0.86**	**0.67**	**19.1**	**-**	**-**	**0.30**
Experiment 2	0.02	0.10	17.4	-	0.50	0.24

c) Experiment 3. LAWATAP

3D reconstruction of the volume is represented on *Figure 4.43*, for the different solute atoms. From the image, two different grains can be distinguished (they are denoted as 1 and 2). The chemical composition of each grain is reported in the *Table 4.11*. There is significant difference in Cr, N and Ti between both grains. The global composition is also shown for all volume in the *Table 4.11*. In comparison to expected chemical composition, the content of Cr is slightly lower, as well as Ti and W concentrations, which are less than half of expected values. On the contrary, a slightly higher concentration of N is measured.

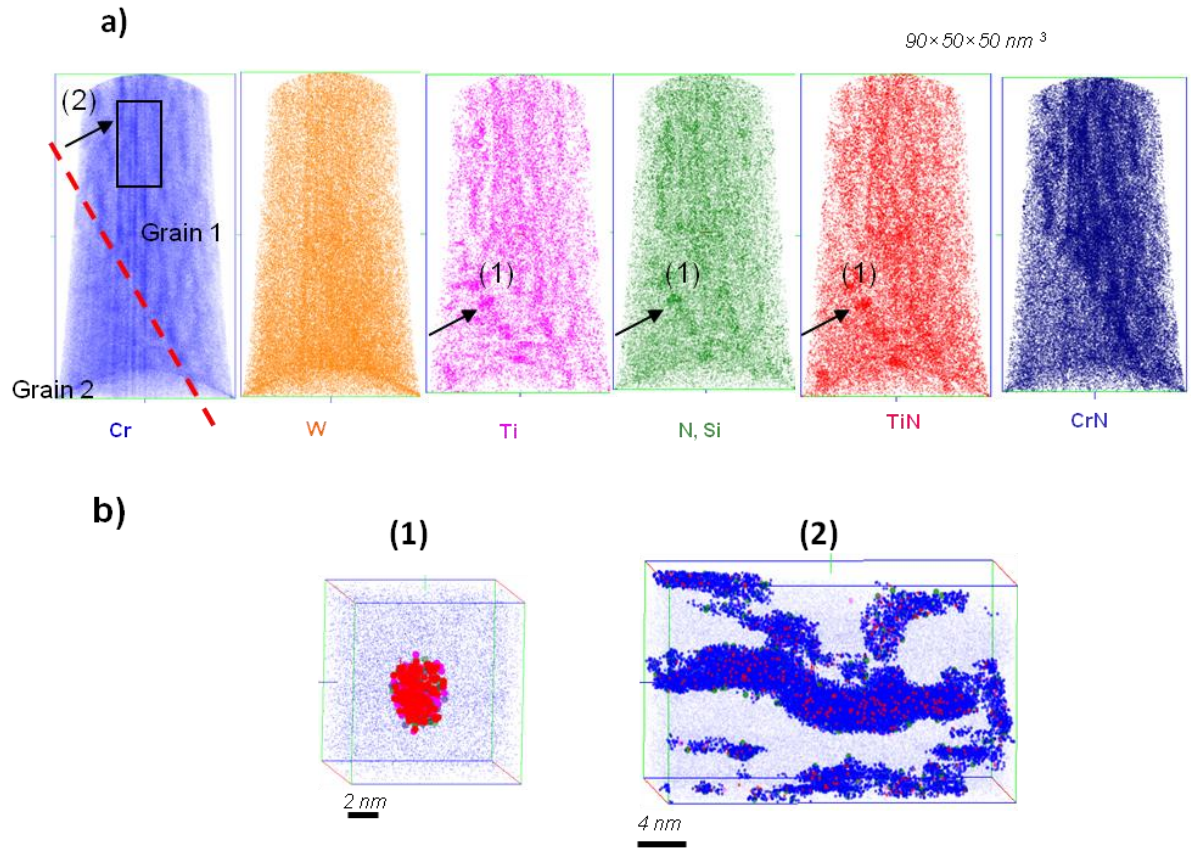

Figure 4.43. 3D reconstruction of the third analysed volume (90×50×50 nm^3) of nitrided NDS steel after hot extrusion. (a) Cr, W, Ti, N(Si) and TiN, FeN, CrN molecular ions are shown. (b) Zoom on indicated nanoparticles in (a): (1) spherical and (2) elongated particles.

Table 4.11. Global chemical composition in nitrided NDS steel after hot extrusion by LAWATAP (Experiment 3). Compositions are in at.%.

	Ti	N	Cr	Si	W
expected	**0.86**	**0.67**	**19.1**	**-**	**0.30**
Grain 1	**0.40**	**1.47**	**18.1**	**0.36**	**0.16**
Grain 2	**0.23**	**0.27**	**12.0**	**0.36**	**0.10**
Experiment 3 (mean)	**0.39**	**0.82**	**17.1**	**0.36**	**0.13**

As for microstructure, it strongly differs from the one observed in previous analysis (*Figure 4.43*). In this case, two families of particles with different morphologies and chemical compositions are distinguished. The first of them (denoted as (1) on the *Figure 4.43*) are spherical. It should be mentioned that they are located on the grain boundary. Their mean Guinier radius is **1.8** nm and their number density is **(3.6±1.4)**×**10^{22}**m^{-3}. The chemical composition of spherical particles as a function of their Guinier radii is presented in *Figure*

4.44 (a). These particles are mainly enriched in Ti, Cr and N. The measured concentration of Ti varies from 6 to 26 at.%, Cr from 23.3 to 25 at.% and N from 10 to 23 at.%. The mean measured core composition is **15.3**±2.5 **Ti**, **13.9** ±2.4 **N**, **29.9**±3.2 **Cr, 40.3**±3.4 **Fe** at.%. The titanium over nitrogen ratio is 1.1 ±0.3.

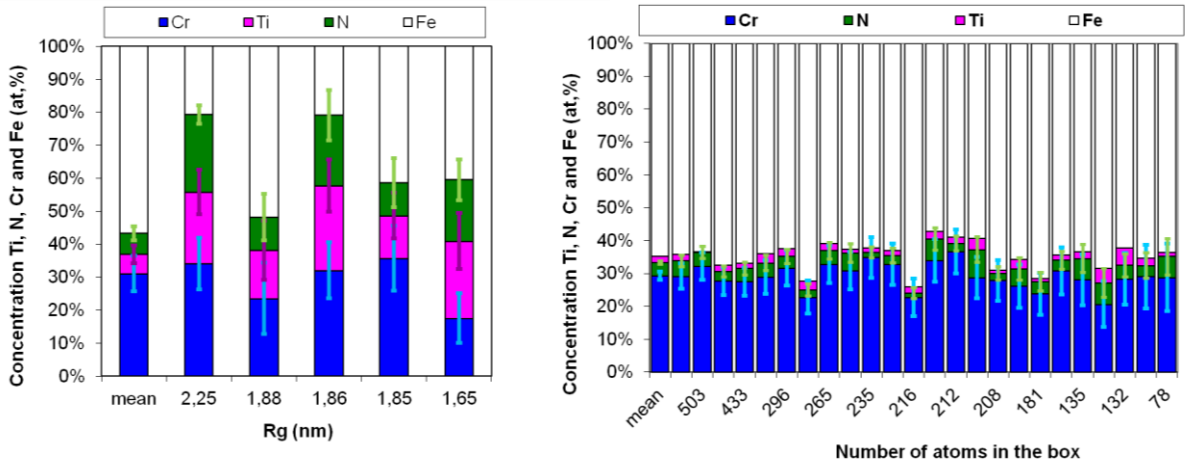

Figure 4.44. Composition of particles observed in nitrided NDS steel after hot extrusion. Composition is presented as a function of (a) mean radius in case of spherical nanoparticles and (b) number of atoms in the box in case of elongated particles. Only Cr, N, Ti and Fe (at.%) are shown.

The second family consists in the elongated particles (denoted as (2), *Figure 4.43*) located in the Grain 1. They appear as thin interwoven plates close to each other. So, it is difficult to estimate their number density as well as their dimensions. In addition, they are elongated in one direction which coincides with direction of analyze. It can be assumed, that this anisotropic structure is a consequence of hot extrusion. The chemical composition measured for elongated particles as a function of number of atoms in the box is shown on *Figure 4.44* (b). These particles are mainly enriched in Cr. However, small amount of Ti as well as N is also measured. The composition is quite constant for all analyzed particles. The mean measured composition is **29.3**±0.40 Cr, **1.95**±0.4 **Ti, 4.0**±0.5 **N, 64.6**±3.4 **Fe** at.%. The Cr/N ratio in that case is 7.2±0.15.

II.3. Discussion

In the present material, the nitrogen comes from plasma nitriding. Powders in as-nitrided state, as well as after annealing at 600 and 700°C during 1h are characterized. The final product, obtained after homogenization treatment of the nitrided powder (10 days at 400°C) followed by hot extrusion is also characterised.

As it has been shown, the level of nitrogen in small powder particles (5-10μm) is very high (about 10 at.%). Since the bigger powder grains were not analysed by APT, the representativeness of these analyses for the whole powder is not ensured. In addition, it is possible that N is heterogeneously distributed inside a same powder grain. Such heterogeneity could be at the origin of the formation of the large plate-shaped chromium nitrides during subsequent heating. This could be a real problem to get a fine distribution a nanometre size Ti nitrides.

The homogenisation treatment aims limiting this problem. In all experiments performed on consolidated material, significantly lower concentration of N (less than 1 at.%) is measured. This, suggest that homogenisation treatment of the powder is efficient to get a more uniform distribution of nitrogen. However, according to TEM investigations [3,35] on the same material, the microstructure observed in consolidated state remains heterogeneous at the micrometric scale. The grain size varies from several hundreds of nanometres to several tens of micrometres. Zones of large grains (> 1 μm) contain low density of nanoparticles. Thus, the possibility to analyse them by APT is also low. These large grains are surrounded by a "shell" of small grains (between 200 and 1 μm). In these small grains, high density of nanoparticles (<100 nm) and dislocations are observed (*Figure 4.45* (a-c)). These nanoparticles are enriched in Ti as well as depleted in Fe and Cr. As for light elements like N and O, TEM investigation does not allow to conclude. However, qualitative characterization of microstructure by Electron Probe Micro-Analysis (EPMA) showed that nitrogen is present everywhere in small powder grains.

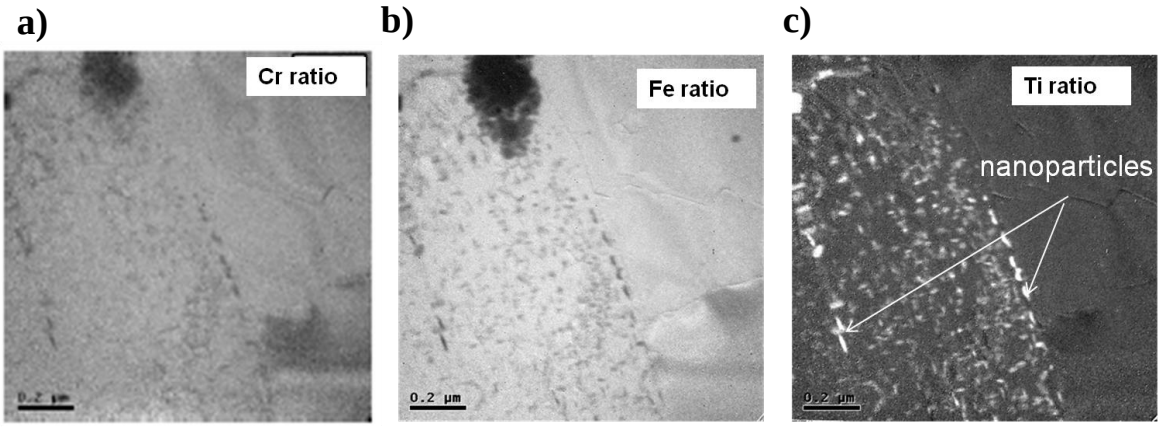

Figure 4.45. Energy filtered TEM image showing nanoparticles in small grains observed in nitrided NDS (consolidated material). These nanoparticles are enriched in Ti (appear in white) and depleted in Fe and Cr (appear in dark) [3,35].

APT reveals that different families of nanoparticles with different morphologies are present. As expected, nanometre scale platelet shape and spherical Ti-N rich particles are formed, but elongated Cr-rich particles are also found. These particles could be formed in areas containing high level of nitrogen, even after the homogenisation treatment (small powder grains). In these regions, Cr-N formation could occur during hot extrusion pre-heating. Their final morphology could be the results of extrusion induced deformation of plate-shape particles.

Thus, it seems that further optimisation of nitriding process is necessary to get an homogeneous microstructure. As a solution, it may be suggested to control homogeneity of nitrogen distribution before consolidation of the powder by using a smaller size distribution of powder grain for nitriding.

II.4. Partial conclusions

Nitrided NDS steel produced by plasma nitriding of Fe-18Cr-1W-0.75 Ti powder in Bodycote-Nitruvid Company. The microstructure is studied in as-nitrided, annealed at 600 and 700°C during 1hour and after hot extrusion (800°C). The main conclusions of the work are:

- Significant amount of nitrogen (~10at.%) is measured in all studied powders (5-10μm). Measurements are done at 2 μm depth from the surface.
- No nanoparticles are observed in as-nitrided state whereas platelike Cr-N-rich particles are observed in powder subjected to annealing treatment at 600 and 700°C during 1hour.
- Smaller amount of nitrogen (less than 1at.%) is measured in all analyses performed on consolidated material. Homogenization treatment of the powder before extrusion seems to result in a more uniform distribution of nitrogen.
- However, the microstructure after consolidation remains heterogeneous. Different types of particles are observed in each experiment: Ti-N rich, Cr-rich.

Further optimisation of nitriding process is necessary. As a possible solution, it is proposed to use more homogeneous population of powder particles (smaller ones).

III. Bibliography of Chapter 4

[1] M. Ratti, Développement De Nouvelles Nuances D'acier Ferritiques/martensitiques Pour Le Gainage D'élément Combustible Des Réacteurs à Neutrons Rapides Au Sodium. Thèse, Institut Polytechnique de Grenoble, 2009.

[2] M.H. Mathon, Bilan Des Caractérisation Des Alliages NDS Par Diffusion De Neutrons Aux Petits Angles. Présentation. ANR AXTREM Réunion, Saclay, 27 Septembre, 2011.

[3] F. Delabrouille, Rapport H-T27-2010-00646-FR. Caractérisation Au Microscope Electronique En Transmission D'alliages NDS Et ODS (ANR AXTREM), 2010.

[4] P. Lejcek, Grain Boundary Segregation in Metals, Springer, 2010.

[5] J.D. Rittner, D.N. Seidman, Acta Materialia 45 (1997) 3191–3202.

[6] S.-I. Baik, M.J. Olszta, S.M. Bruemmer, D.N. Seidman, Scripta Materialia 66 (2012) 809–812.

[7] M.J. Alinger, G.R. Odette, D.T. Hoelzer, Acta Materialia 57 (2009) 392–406.

[8] M.K. Miller, D.T. Hoelzer, E.A. Kenik, K.F. Russell, Intermetallics 13 (2005) 387–392.

[9] E.A. Marquis, S. Lozano-Perez, V. de Castro, Journal of Nuclear Materials 417 (2011) 257–261.

[10] R.G. Faulkner, Acta Metallurgica 35 (1987) 2905–2914.

[11] D. McLean, Grain Boundaries in Metals, Clarendon Press, 1957.

[12] D. Blavette, F. Vurpillot, P. Pareige, A. Menand, Ultramicroscopy 89 (2001) 145–153.

[13] F. Vurpillot, A. Bostel, D. Blavette, Appl. Phys. Lett. 76 (2000) 3127.

[14] Porter D.A., K.E. Easterling, M.Y. Sherif, Phase Transformation in Metals and Alloys, 3rd ed., Taylor and Francis Group, United Kindom, 2009.

[15] E.A. Marquis, Applied Physics Letters 93 (2008) 181904.

[16] T.C. Totemeier, C.J. Smithells, Smithells Metals Reference Book, Butterworth-Heinemann, 2004.

[17] F. Danoix, Personal Communication, 2011.

[18] P. Jessner, Ph.D. Université De Rouen, 2009, to be Published.

[19] G. Sha, A. Cerezo, Ultramicroscopy 102 (2005) 151–159.

[20] C.A. Williams, E.A. Marquis, A. Cerezo, G.D.W. Smith, Journal of Nuclear Materials 400 (2010) 37–45.

[21] M. Klimenkov, R. Lindau, A. Möslang, Journal of Nuclear Materials 386-388 (2009) 553–556.

[22] L.L. Hsiung, M.J. Fluss, A. Kimura, Materials Letters 64 (2010) 1782–1785.

[23] L.L. Hsiung, M.J. Fluss, S.J. Tumey, B.W. Choi, Y. Serruys, F. Willaime, A. Kimura, Phys. Rev. B 82 (2010) 184103.

[24] L. Hsiung, M. Fluss, S. Tumey, J. Kuntz, B. El-Dasher, M. Wall, B. Choi, A. Kimura, F. Willaime, Y. Serruys, Journal of Nuclear Materials 409 (2011) 72–79.

[25] R.B. Schwarz, MSF 269-272 (1998) 665–674.

[26] M.S. El-Eskandarany, Mechanical Alloying for Fabrication of Advanced Engineering Materials, William Andrew, 2001.

[27] H. Kishimoto, M.. Alinger, G.. Odette, T. Yamamoto, Journal of Nuclear Materials 329-333, Part A (2004) 369–371.

[28] M. Ruhle, T. Steffens, Zeitschrift Für Metallkunde 83 (1992) 436–440.

[29] P. Jessner, R. Danoix, B. Hannoyer, F. Danoix, Ultramicroscopy 109 (2009) 530–534.

[30] Mortimer, B., Grieveson, P., Jack, K.H., 1, (1972) 203–209.

[31] K.S. Jung, R.E. Schacherl, E. Bischoff, E.J. Mittemeijer, Surface and Coatings Technology 204 (2010) 1942–1946.

[32] D. Blavette, L. Letellier, P. Duval, M. Guttmann, Materials Science Forum 207-209 (1996) 76–92.

[33] P. Franke, D. Neuschütz, Scientific Group Thermodata Europe (SGTE), in:, P. Franke, D. Neuschütz (Eds.), Binary Systems. Part 2: Elements and Binary Systems from B – C to Cr – Zr, Springer-Verlag, Berlin/Heidelberg, 2004, pp. 1–2.

[34] D.H. Jack, Acta Metallurgica 24 (1976) 137–146.

[35] F. Delabrouille, Présentation. ANR AXTREM Réunion, Saclay, 27 Septembre, 2011.

General conclusions and perspectives

The research work was realized in the framework of the ANR aXTREM project (Aciers ferritiques/martensitiques renforcés par nano-particules pour application à haute température en conditions extrêmes - Ferritic/Martensitic steels reinforced with nanoparticles for high temperature application in extreme conditions). In the program, two types of materials have been investigated: *Oxide-Dispersion-Strengthened* (ODS) steel and model alloy and *Nitride-Dispersion-Strengthened* (NDS) steels. Today, ODS form the basis of materials which are envisaged for application in nuclear fuel cladding for the next generation of nuclear reactors (GEN IV). Thus, ferritic industrial Fe-18CrTiW ODS steel has been designed by CEA [1]. The study was also performed on Fe-9CrWTi ODS model alloy.

Based on ODS principle, new steels reinforced by nitrides (NDS steels), were developed owing to different elaboration ways. In first case, Fe-18Cr-W-N pre-alloyed powder was mechanically alloyed with titanium hydrate (TiH_2) and hot extruded (MA NDS). In second case, Fe-18Cr-W-Ti powder was nitrided in Bodycote-Nitruvid Company (nitrided NDS).

In this context, the main objective of the present work was to provide a wide range of microstructural information and to improve, or to give for the first time, an understanding of the basic mechanisms on the origin of the formation of nano-reinforcements in these ODS and NDS steels. As the size of the particles formed in the materials is in the range of nanometres, the *Tomographic Atom Probe* (APT) technique has been used for the investigations. The results were compared to other data obtained with complementary techniques when available.

As reported in the first chapter, it is, up to now, widely accepted that the dissolution of Y_2O_3 occurs during ball milling whereas nucleation of complex oxides occurs after subsequent heat treatments. It must be pointed out, that this widely accepted mechanism relies on a relatively small amount of works where the “initial” microstructures of as-milled powders were studied [2–4]. Most of these conclusions are drawn from investigations of material in the “final” state (i.e. after consolidation and heat treatments) [5–7]. In this work, a specific attention has been paid to follow the Y_2O_3 dissolution during the Mechanical Alloying (MA) process for an ODS model alloy containing a large amount of Y, Ti and O. The APT technique revealed that its microstructure after MA is a two phase structure, that includes: i) a Fe-Cr-rich phase with a composition close to the nominal composition of the initial pre-alloyed powder and ii) Y-Ti-O rich phase, where the ratio of Y over O is close to the one in the initial Y_2O_3 powder. So, this work shows that during mechanical alloying, the

complete dissolution of Y and O is not achieved. However, there is no more Y_2O_3 remaining, but an Y, Ti and O rich phase. Considering neutron diffraction results [8,9], it can be assumed that this phase is amorphous.

Considering these results, further works could be envisaged.

- ✓ Specific TEM studies are required in order to conclude about the possible amorphization of Y-Ti-O-rich regions after MA. This hypothesis is not in contradiction with the present results but needs some more experimental results.
- ✓ 3DAP investigation of the same model alloy after mechanical alloying of FeCrW pre-alloyed powder with TiH_2 can provide information about the Ti "initial" location (is it fully dissolved in the FeCrW matrix or does some Ti-rich inhomogeneities exist? What are the proportions of both in this latter case?) as well as a general picture of the microstructure of the material at this step.
- ✓ 3DAP investigation of the same model alloy after heat treatment can give important information about precipitating phases. X-ray study have been already performed [8] in this state and $YTiO_3$, Y_2O_3 and TiO phases were identified. The comparison of the results from both techniques could provide the information on the accuracy of chemical composition measured by APT.

Concerning industrial ferritic ODS steel, the samples were characterized in the as-milled condition as well as after: i) annealing treatment (850C°/1h) and ii) consolidation by hot extrusion. APT experiments revealed nanometre scale particles in the three states. Diluted Y-O-rich clusters are present just after MA, whereas spherical Y-Ti-O-rich nanoparticles were found after high temperature treatments. In all cases, the number density of particles is rather high (10^{23}-10^{24} m^{-3}) and is comparable to the number density of nanoparticles reported in other Ti-containing ODS steels [3,10]. The study of the interface of the nanoparticles suggests the existence of a core-shell structure (Cr-rich shell around Y-Ti-O-rich core) as recently reported [11]. The comparison of APT results with TEM and SANS ones coming from other laboratories involved in this project showed reasonable agreement for annealed and hot extruded samples.

From these observed microstructures a scenario describing the evolution of nanoparticles can be given: 1) two simultaneous mechanisms occur during MA, i) dissolution of initial Y_2O_3 powder inducing Y and O supersaturation of the matrix and ii) formation of Y-O-rich clusters due to precipitation and/or resulting from an incomplete initial dissolution of Y_2O_3

powder. The origin of the latter one is not clear at the moment, as suggested above. 2) During subsequent annealing and consolidation, Y-O-rich clusters act as nuclei for formation of Y-Ti-O-rich nanoparticles.

On that part, perspectives works are numerous and further questions should be answered:

- ✓ Origin and the nature of these core-shell structures of nanoparticles are not clear at the moment. Moreover, influence of ageing times on the stability of these core-shell structures need to be studied. For instance, presence of shell has been observed after prolonged annealing during 4, 24 and 48 h at 750º in Fe-12Cr ODS alloy [12].
- ✓ An important question remains concerning the real compositions of oxide particles. As an example, the Fe content measured by APT varies in a wide range [5, 10, 13] and should be deeply studied. In order to answer this question, a specific study (PhD, CPR ODISEE) started in the *Groupe de Physique des Matériaux (GPM), University of Rouen*. In this study, combination of APT and TEM characterisations, coupled with modelling of field evaporation during APT experiments should give some information on the accuracy of chemical composition obtained from the analyses of nanooxides particles embedded in a ferritic matrix.

As for MA NDS steel, studies of the microstructure evolution have been carried out directly after MA as well as after annealing treatments up 1000°C. The APT technique revealed presence of nanoparticles in all states. They are mainly enriched in Ti and N whereas their stoichiometry differs from the equilibrium stoichiometry TiN. This can results from the "non-equilibrium" MA process. A small amount of O (1-5 at.%) is also measured, indicating that these phases can be designated as oxy-nitrides [14]. Moreover, a second family of particles has been observed: Ti-Al-O-rich. Al and O are considered as impurities coming from the elaboration process. This indicates that the control of the TiN particles size distribution is also controlled by the purity of the alloy and process itself (introduction of impurities).

The precipitation kinetics of Ti-N-rich particles can be described as a three stages process, according to the experimental observations: i) nanoparticles are formed during the MA process and therefore can contain considerable amounts of matrix Fe and Cr atoms. ii) subsequent annealing results in a partial rejection of Fe and Cr atoms from the nanoparticles leading to the formation of a Cr-rich shell (annealing at 600, 700°C/1h and hot extruded state); iii) coarsening of nanoparticles starts when all N and Ti is removed (down to solubility limits) from the matrix.

Concerning the kinetic and the structural parameters, only qualitative agreement is found between APT results and MatCalc simulations. The reasons could be the following: a) MatCalc is very sensitive to input data which are rarely known (especially when non-equilibrium process as MA is used), b) particles are initially formed during mechanical alloying, that can have a strong effect (initial structure) and is not taken into account by MatCalc and iii) the existence of a Cr-rich shell cannot be considered in the calculations.

Finally, as observed by APT, microstructures of MA NDS and industrial ODS steels in the consolidated state are comparable. This is encouraging for the NDS elaboration process.

However, this work is a first step and more systematic investigations are needed. The following researches should include:

- ✓ Investigation of an alternative way to introduce nitrogen during MA. For exsample, Fe_xN can be used as a «nitrogen donor » [8]. X-ray study has been already performed and APT can provide an important information at atomic level.
- ✓ Microstructural evolution and behaviour (long term stability) of these nitrides under high temperatures and irradiation still need to be tested. The combination of TEM, SANS and APT can give complementary information about microstructure evolutions.
- ✓ Segregation to GB may significantly change material properties. Some studies have been initiated in the present work but specific studies by APT and TEM must be undertaken to clarify: 1) the equilibrium segregation behaviour, 2) the effect of temperature (longer ageing times) and alloying elements on the Cr segregation; 3) segregation behaviour under irradiation. These questions are also important for ODS systems as reported in literature [3, 13, 15].

As far as nitrided NDS powders produced by plasma nitriding are concerned, the microstructure has been studied in as-nitrided state, after annealing treatments at different temperatures and in consolidated state. No chemical composition heterogeneity has been observed in the as-nitrided samples, at the scale of an APT volume. However, the very high content of N found in these samples suggests heterogeneities at larger scale.

Precipitation occurs after heat treatments. The decomposition of the system leads to the formation of Cr-N-rich particles having a plate-like shape after annealing at 600 and 700°C during 1h. In the consolidated state, different populations of nanoparticles are observed, Cr-rich and Ti-N-rich particles. The microstructure is very different from one analysed volume to another. These observations agree well with TEM results indicating that the microstructure of

the consolidated material is highly heterogeneous. So the nature of the particles may depend on the location. This could be a consequence of the initial heterogeneities of N distribution in nitride powder grains.

An optimization of the elaboration process is necessary in this case. A solution could be to use powder particles with a more uniform size distribution for nitriding. This could allow avoiding smaller powder grains and improving homogeneity of nitrogen distribution before consolidation of the powder.

To conclude the present work, the need of experimental data at very fine scale for the development of new materials for next generation of nuclear reactors pushes experimental techniques to their limits. As it was demonstrated in this Ph.D, Atom Probe Tomography (APT) is an efficient technique providing important information about microstructural evolution in case of nano-reinforced materials. Quantification of chemical composition, number density and dimensions of nanoparticles, as well as information about local segregations (e.g. on dislocations or at grain boundaries) can be obtained. However, like all experimental techniques APT has its own limitations, such as bias in measurements due to the physics of field evaporation. To overcome this, combination of complementary techniques such as Transmission Electron Microscopy (TEM), Small Angle Neutron Scattering (SANS) as well as atomistic modelling should be used to get full and reliable description of materials behaviour under heat, stress, irradiation...

Bibliography of General Conclusions and Perspectives:

[1] Y. de Carlan, J.-L. Bechade, P. Dubuisson, J.-L. Seran, P. Billot, A. Bougault, T. Cozzika, S. Doriot, D. Hamon, J. Henry, M. Ratti, N. Lochet, D. Nunes, P. Olier, T. Leblond, M.H. Mathon, Journal of Nuclear Materials 386-388 (2009) 430–432.

[2] T. Okuda, M. Fujiwara, J Mater Sci Lett 14 (1995) 1600–1603.

[3] M.J. Alinger, G.R. Odette, D.T. Hoelzer, Acta Materialia 57 (2009) 392–406.

[4] M.K. Miller, C.L. Fu, M. Krcmar, D.T. Hoelzer, C.T. Liu, Front. Mater. Sci. China 3 (2008) 9–14.

[5] D. Larson, P. Maziasz, I. Kim, K. Miyahara, Scripta Materialia 44 (2001) 359–364.

[6] S. Yamashita, S. Ohtsuka, N. Akasaka, S. Ukai, S. Ohnuki, Philosophical Magazine Letters 84 (2004) 525.

[7] M.K. Miller, K.F. Russell, D.T. Hoelzer, Journal of Nuclear Materials 351 (2006) 261–268.

[8] M. Ratti, Développement De Nouvelles Nuances D'acier Ferritiques/martensitiques Pour Le Gainage D'élément Combustible Des Réacteurs à Neutrons Rapides Au Sodium. Thèse, Institut Polytechnique de Grenoble, 2009.

[9] L. Toualbi, M. Ratti, G. André, F. Onimus, Y. de Carlan, Journal of Nuclear Materials 417 (2011) 225–228.

[10] M.K. Miller, E.A. Kenik, K.F. Russell, L. Heatherly, D.T. Hoelzer, P.J. Maziasz, Materials Science and Engineering A 353 (2003) 140–145.

[11] E.A. Marquis, Applied Physics Letters 93 (2008) 181904.

[12] V. de Castro, E.A. Marquis, S. Lozano-Perez, R. Pareja, M.L. Jenkins, Acta Materialia In Press (2011).

[13] M.K. Miller, D.T. Hoelzer, E.A. Kenik, K.F. Russell, Intermetallics 13 (2005) 387–392.

[14] D.H. Jack, K.H. Jack, Materials Science and Engineering 11 (1973) 1–27.

[15] E.A. Marquis, S. Lozano-Perez, V. de Castro, Journal of Nuclear Materials 417 (2011) 257–261.

Table of content

Appendix 1. ANR AXTREM program 193
Appendix 2. 3DAP sample preparation methods 195
a)"Double layer" method 195
b) "Micro-loop" method 196
c) Preparation of APT tips from powders 196
d) Specimen preparation for neutron diffraction experiments 198
Appendix 3. 3DAP data treatment methods 200
a) Statistical tests 200
b) Method of "iso position" 201
c) "Erosion" method 203
Appendix 4. Field evaporation model 205
Appendix 5. MatCalc script 207
Bibliography of Appendixes 211

Appendix 1. ANR AXTREM program

The AXTREM ANR program has been discussed briefly in the introduction. Here, more detailed information about the partners participated in the program are given. All groups (industrial and research) are shown on the *Figure 1* and detailed below.

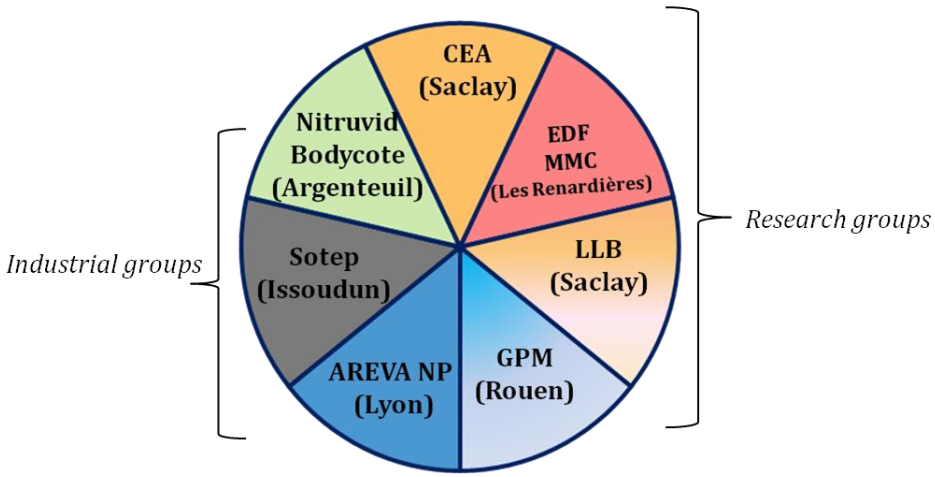

Figure 1. Industrial and research groups participated in ANR aXTREM program. Collaboration of all these groups gives complete cycle that includes: i) material elaboration (CEA, Nitruvid), ii) microstructure investigation (EDF&MMC, LLB, GPM), iii) testing and application of final cladding tube (SOTEP, AREVA NP).

The project is leaded *by Commissariat à l'Energie Atomique (CEA) in Saclay*. This organization conducts fundamental and applied research into many areas, including the design of nuclear reactors. In the AXTREM project, CEA designed the materials (ODS/NDS), conducted mechanical alloying and consolidation steps as well as mechanical testing and Electron Probe Micro Analysis (EPMA) characterization.

Nitruvid Bodycote (Argenteuil) is a leading provider of thermal processing services (heat treatments, metal joining and coatings services) worldwide. In the program, this industrial team performed nitriding treatments in case of NDS materials. Nitriding conditions were selected and equipment was optimized to apply this process to powders as well as to consolidated material. In addition, the possibility to performed nitriding on final cladding tubes was also evaluated.

Sociéte Technique d'etirage de précision (Sotep) in Issoudun is a precision tube drawing out company. In the program, the aim was to conduct final step of cladding elaboration from ODS/NDS - final tube with a geometry representative of the cladding for future SFR. During program this aim was successfully achieved.

AREVA NP (Lyon) is a company that designs and build nuclear power plants all over the world. The task of this participant within the program was to evaluate the applicability of ODS and NDS materials for cladding tubes of new generation of reactors. It was concluded that ODS industrial steel in non irradiated state show promising characteristics (thermal creep, tensile strength) at operating conditions of SFR. First results available for NDS materials also approach for SFR objectives (encouraging result!). But still some testing and optimization of elaboration process is required.

Électricité de France, Département Matériaux et Mécanique des Composants (EDF-MMC), Les Renardières is research group that performed Transmission Electron Microscopy (TEM), Optical Microscopy (OM), Scanning Electron Microscopy (SEM) investigation of microstructure of ODS/NDS steels.

Laboratoire Léon Brillouin (LLB), Saclay performed characterisation of microstructure by means of Small-Angle Neutron Scattering (SANS). This instrument gives information about precipitating phases (size, density, volume fractions). Characterization of the microstructure by means of Neutron and X-ray diffraction (ODS model alloy) also has been provided.

Centre National de la Recherche Scientifique - Groupe de Physique des matériaux (CNRS-GPM), Rouen performed characterisation of microstructure near atomic level by Atom Probe Tomography. This technique gives important information especially in case nano-reinforced steels (dimensions, density, composition, distribution of nanoparticles). It may also provide some quantitative information about local segregations on grain boundaries (or dislocations) for example.

In current Ph.D. work APT was chosen as main tool for characterization of ODS and NDS materials. The results obtained by APT are compared to those of SANS and TEM whenever possible through the Ph.D. The combination of TEM, SANS and APT provides complete information about microstructure from the micrometric (TEM, SEM) up to nanometric scale (APT).

Appendix 2. 3DAP sample preparation methods

For APT analyses, samples need to be prepared in the shape of thin needles with circular cross section and an end radius smaller than 50 nm.

In the case of bulk/massive materials, matches-shaped samples are cut with a cross-section of approximately 300×300 μm^2 and submitted to two main electro-chemical polishing techniques: the "double layer" and "micro-loop" polishing methods [1].

In the case of powder grains the use of a dual beam scanning electron microscope / focused ion beam (SEM–FIB) instrument provides an alternative method for the fabrication of APT samples [2]. All listed methods are discussed below.

a)"Double layer" method

The principle of preparation of the tip by this method is shown in *Figure 2*. The anode (sample) is plugged to a positive potential (~10…18 volts) and placed into an electrolyte composed of 25% perchloric and 75% acetic acids floating on an inert solution (Galden). The sample should be moved up and down in order to avoid preferential etching in the area of "electrolyte-air" interface. After some period of time, a "neck" starts to form in the active part of the liquid (stage 1).

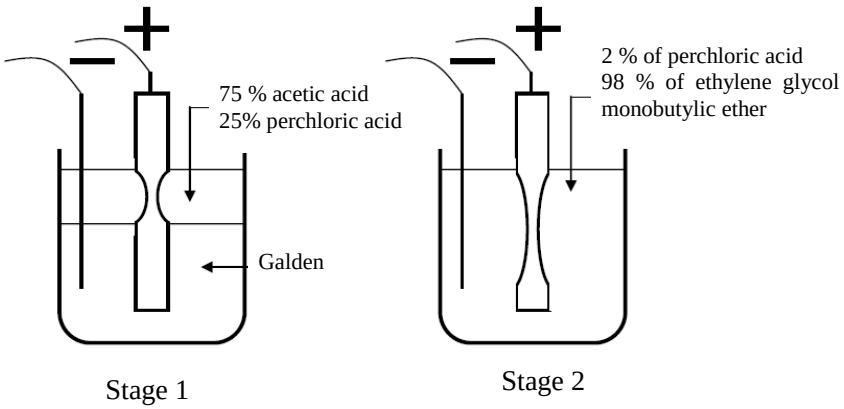

Figure 2. 3DAP tip preparation by the "double layer" method (from [3]).

When the "neck" is thin and long enough, the sample is placed in a second electrolyte composed of 2% of perchloric acid and 98% ethyleneglycol monobutyl ether. A lower tension of 4…7 volts is then applied, until the neck breaks and the lower part of the match fall down (2 stage). If the lower part of the match is long enough, it can be used to prepare a second tip using the "micro-loop" method (see below).

The tip (upper part of the match) is then cleaned in alcohol and the radius at apex is checked in TEM. Samples are kept in vacuum until APT experiment starts.

b) "Micro-loop" method

The micro-loop method is mainly used to re-sharpen tips that have been already analysed by 3DAP. It is also used to make tips from the broken match of the previous method and when it is not longer possible to use double layer technique. The method is schematically represented on *Figure 3*.

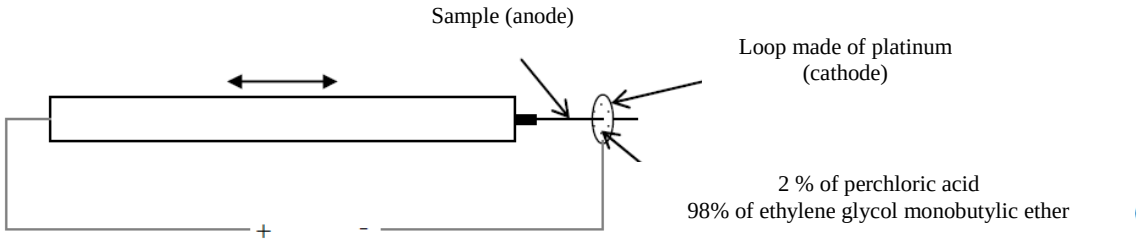

Figure 3. 3DAP tip preparation using the "micro-loop" method (from [4]).

The electrolyte that is used is a mixing of 2 % of perchloric acid and 98 % of ethylene glycol monobutylic ether. A loop made of platinum is filled with the above electrolyte and a constant voltage is applied between the loop and the specimen. The specimen moves frequently through the loop (back and forth) and is polished. To control the polishing process, the loop is observed under an optical microscope. Like in the "double layer" process, after some period of time a neck forms. At the final stage of the polishing, when the neck is thin enough to break down, the voltage is applied only when the neck comes out the electrolyte in the direction of sample free end. This procedure is repeated until the break of the neck is observed.

Like in the case of the "double layer" method, the final sample is cleaned and its dimensions are checked in TEM.

c) Preparation of APT tips from powders

The preparation of a needle-shaped tip, starting from a powder grain, consists of several stages: i) preparation of pre-tip, ii) fixing the powder particle on the pre-tip and iii) milling the powder in the form of a tip (with an end radius R~50 nm) by means of the focused ion beam (FIB). These stages are detailed below.

Preparation of the pre-tip. The pre-tip is special tip on which a powder grain is maintained (see *Figure 4* (a)). Pre-tips are usually made of tungsten. The electropolishing is performed in 90% H_2O and 10% of NaOH electrolyte. In the present case, the "micro-loop" method was used. Afterwards, in order to facilitate and insure a better fixation of the powder grain on the pre-tip, a "flat area" at the apex of pre-tip is done using the focused ion beam (FIB). The diameter of the flat area is about 3 to 6 μm.

Fixation of the powder grain on the pre-tip. This is realized by means of micromanipulators (under optical microscope, see *Figure 4* (b)). The powder grain is fixed on the pre-tip using special silver glue (see *Figure 4* (a)). It should be mentioned that the size of a powder grain that will be processed by FIB must not exceed 10 to 13 μm in diameter. Above these sizes, the milling time is too long.

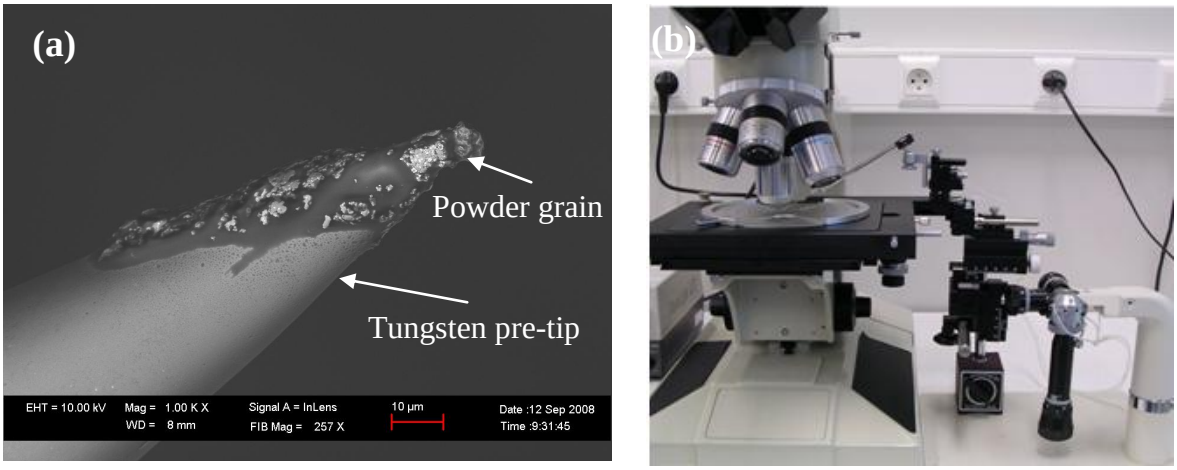

Figure 4. (a) Tungsten pre-tip with a powder grain at the end (b) SEM image of a micromanipulator used to fix a powder grain on the pre-tip.

Milling the final shape by FIB. The powder is transformed into sharp needle-like tip by annular milling FIB. For this final preparation LEO 1530 and NVISION 40 SEM microscopes of the GPM laboratory were used under the supervision of **F. Cuvilly**.

The basic idea of the ion milling using the FIB technique is the following: the sample (pre-tip) is aligned parallel to and centred on the column of the ion beam. The ion beam scan the end of the specimen in a circular annular pattern [1]. A general scheme is shown on *Figure 5* (a). The milling is generally performed in a series of stages with successively smaller inner and outer diameters of the mask and decreasing the ion current. Finally, the connection between the tungsten pre-tip and the powder particle (silver glue) is additionally reinforced by the deposition of a layer of platinum, *Figure 5* (b).

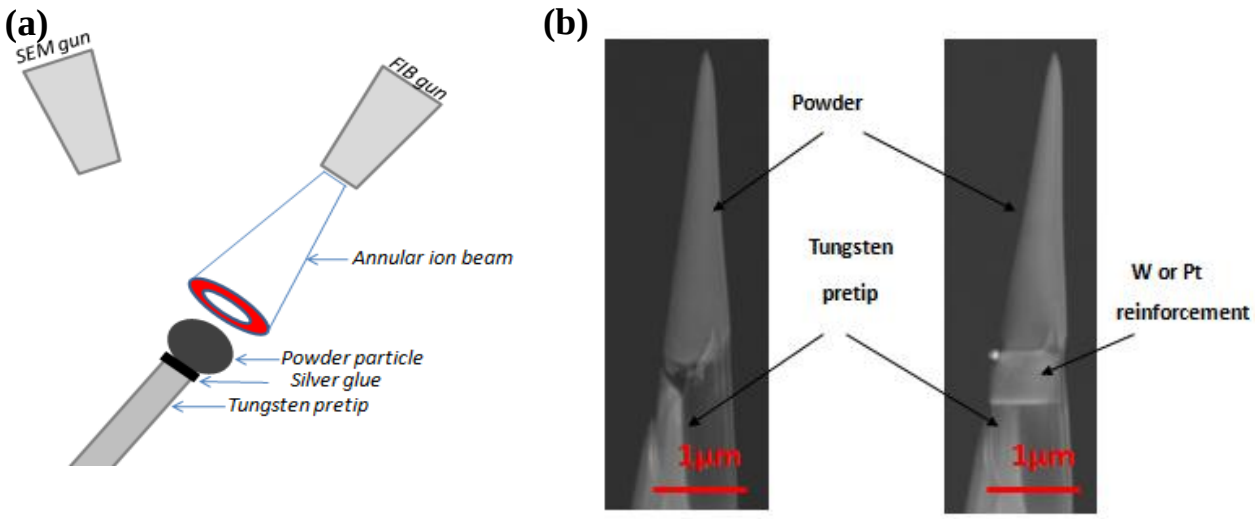

Figure 5. (a) FIB principle; (b) SEM image of a powder at the final stage of annular milling without and after Pt (W) reinforcement (done by F. Cuvilly).

d) Specimen preparation for neutron diffraction experiments

In order to perform X-ray diffraction experiments on a single powder particle of an ODS model alloy, specific specimens were prepared at GPM. The preparation includes several stages. They are schematically represented in *Figure 6*.

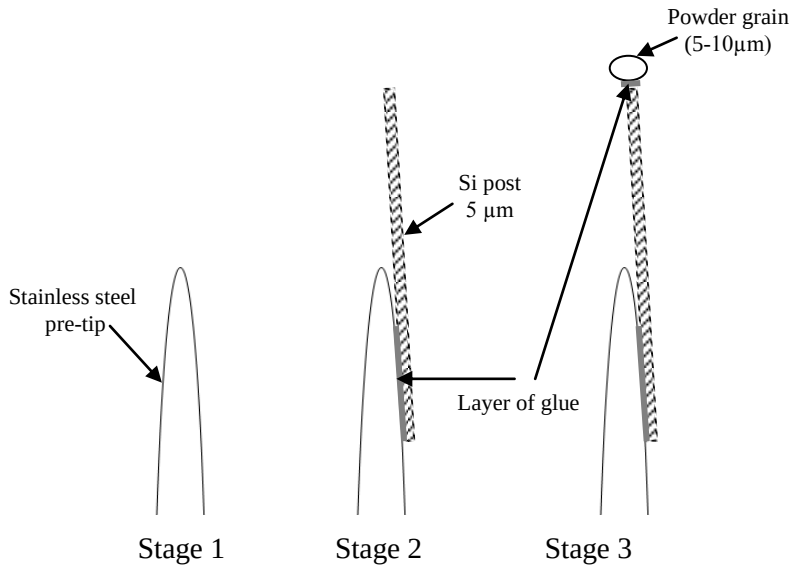

Figure 6. Schematic representation of necessary stages for the preparation of a powder grain for X-ray diffraction study.

First, a stainless steel pre-tip with an end radius of few micrometers is prepared by electropolishing. The "double layer" method is used.

Second, a Si post with a diameter of 5 µm is stuck by silver glue on the pre-tip using the micromanipulator.

Finally, the ODS powder particle is maintained on the flat surface of the Si post using micromanipulator. The final sample is represented in *Figure 7*.

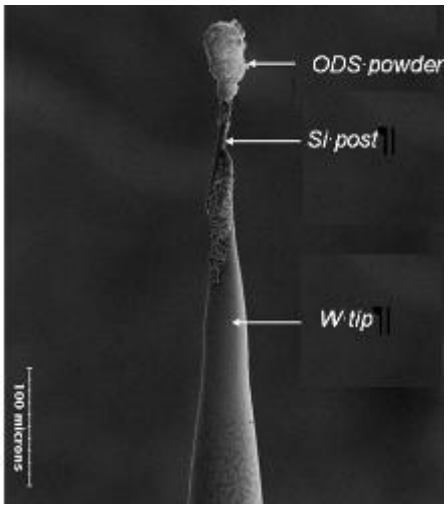

Figure 7. Specimen prepared from ODS model alloy for X-ray diffraction study.

Appendix 3. 3DAP data treatment methods

The procedure for the data treatment is similar for all materials and consists of several steps. The assumption of a random distribution of solute atoms is tested by methods discussed below.

a) Statistical tests

3DAP technique is used to check fine scale variations of composition in materials. If there are slight variations of chemical compositions, the so called frequency distribution (FD) may reveal microstructural features that are not visible (by eyes) on 3D pictures.

When atoms are randomly distributed a binomial distribution (BD) of the local concentrations is expected. If precipitation, clustering or segregation occurs in the material, the FD becomes broader than the BD or even shows well separated peaks corresponding to different phases.

In order to construct the FD, the APT data are divided into blocks, usually containing equal number of atoms (N_{box}), called the sampling block size (typically 50…500 atoms). However, the shape of the FD may vary with the chosen block size. For those cases, data should be analysed in a more careful way.

A convenient and straightforward test is suggested by Thuvander et al [5]. It is usually used when small variations of composition or ordering are of interest. The random or non random distribution of solute atoms is tested by comparing the value of the standard error (s) calculated from experimental data and standard deviation (σ) of the binomial distribution calculated from the experimental data set.

The mean concentration, c_0, of element A is calculated using the experimental data. Then the standard error, *s*, is calculated for every block size in a range, typically 100-500 atoms, using the expression:

$$s^2 = \frac{1}{n_b - 1} \sum_{i=1}^{n_b} (c_i - c_0)^2 \qquad (1)$$

where n_b is the total number of blocks and c_i is the concentration of element *A* in block *i*. With increasing of block size, *s* generally decreases. The experimentally obtained *s* is compared with the standard deviation, σ, of the BD:

$$\sigma^2 = c_0(1-c_0)/N_b \qquad (2)$$

where N_b is the block size. Then both *s* and σ are plotted as functions of N_b, see *Figure 8* (a,b). The use of series of block sizes will reveal characteristic information of the width of the FD. For a randomly distributed element the experimental s-curve will fluctuate around the binomial σ-curve. If the composition varies in the material, for example, due to phase separation or segregation, the s-curve will be above the σ –curve.

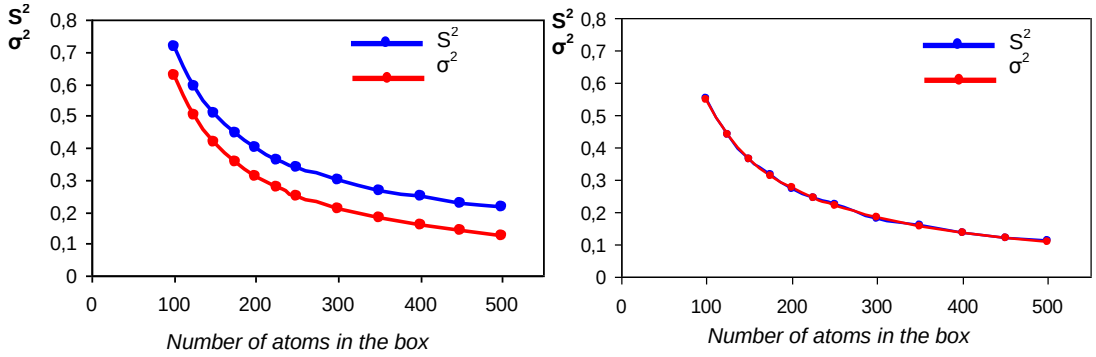

Figure 8. Comparison of the standard error (s) of the experimental frequency distribution with the standard deviation (σ) of the binomial distribution in the as-milled ODS steel. (a) Experimental distribution does not coincide with the binomial one. Y, YO, O, FeO and CrO species are not homogeneously distributed. (b) Experimental distribution almost coincides with the binomial one. Ti, TiO atoms are homogeneously distributed.

b) Method of "iso position"

Different algorithms could be used for the detection of nanoparticles in APT data sets [1,6]. In the present work, nanoparticles are isolated from the matrix using the "iso position" method. The principle of this method is the following. The analysed volume is divided into small sub-volumes where concentration of A atoms is determined. In the centre of each sub-volume the concentration in A atoms is estimated as, C^i_A. Then, for each atom with coordinates *x, y, z* neighbouring the sub-volume, the concentration C_A^{xyz} is estimated due to linear interpolation. For clarity a schematic drawing is represented in *Figure 9*.

If the concentration C_A^{xyz} exceeds the fixed concentration C_A^0 then atom located in (x, y, z) is selected. On the opposite, if C_A^{xyz} is less than C_A^0 then atom is not taken into account. As a result, a selected region where concentration of A is more than C_A^0 is obtained. The identification of clusters is also dependent on a parameter linked to the distance between A

atoms. If two selected atoms are separated by a proposed distance R_{min} then they belong to the same cluster. If not, they may belong to different clusters. If the number of atoms in the considered cluster is less than a minimum number of ions, N_{min}, then the atoms are considered belonging to the matrix.

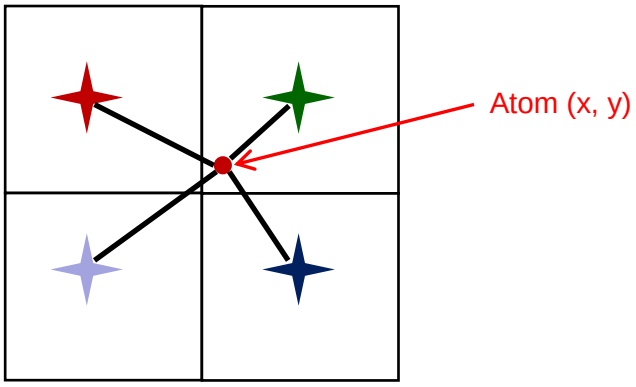

Figure 9. Schematic representation of iso position principle [4,7].

The advantage of this method is its high speed for data treatment. It is preferably used for isolated nanoparticles.

Some choices of parameters are obviously important for the results and is usually not a straightforward task. The choice of elements and their thresholds C_{min}, will influence not only the size, but also the composition of the clusters. As a point of interest in this work, different oxide and nitride particles, chemical species that are associated to them may be selected. Several thresholds, for each, have been tried with the iso position method in order to find the best one. Chosen parameters for the cluster detection in ODS and NDS materials are summarized in *Table 1*.

Table 1. Chosen elements and corresponding thresholds for ODS and NDS materials used as a criterion for defining the nanoparticles from general APT volume.

Materials	**ODS steel**	**MA NDS**	**Nitrided NDS**
Elements used to define nanoparticles	Y, Ti, O and YO, TiO, CrO, FeO molecular ions	Ti, N, Al and TiN, CrN, AlO and TiO molecular ions	Cr, N and CrN molecular ions
Threshold, $C_{min,}$ (at.%)	2.5/3.0	4.0	32-35

Finally, after the nanoparticles are isolated from the matrix using detection algorithms, a shell of matrix atoms close to the interface of the nanoparticle may be still associated with nanoparticles. As a result, the size and composition of these nanoparticles would be overestimated and biased respectively. In order to define the best location of cluster's interface

and to avoid the shell of matrix atoms next to particle/matrix interface, another method, known as "erosion method" is used.

c) "Erosion" method

The principle of the erosion method is the following. The distance between each atom of the defined nanoparticle and each atom in the matrix are calculated. Distances for atoms of nanoparticles are considered as negative while for matrix atoms they are positive, *Figure 10.*

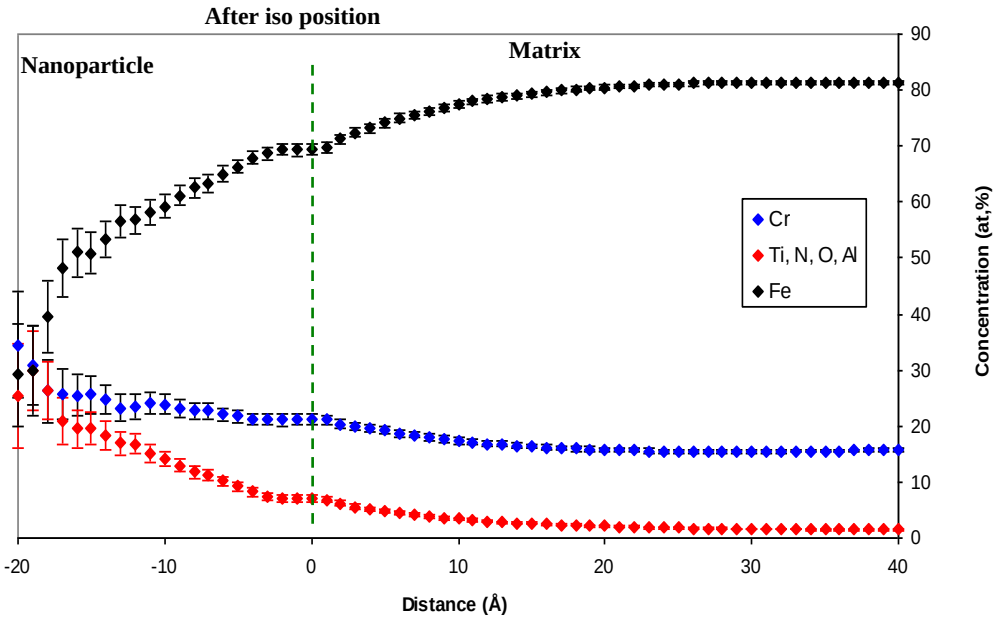

Figure 10. Erosion profile through the nanoparticle. Negative distance corresponds to the ions located in the nanoparticle. The zero distance corresponds to the location of nanoparticle/matrix interface when only detection algorithm is used.

The zero distance corresponds to the interface between nanoparticle and matrix just after detection algorithm (iso position), *Figure 11* (a). In the majority of cases it does not correspond to the real interface between the nanoparticle and the matrix. In this case, the nanoparticle includes a shell of matrix atoms. By erosion, it is possible to displace this interface closer to the real interface of the nano-particle. As a consequence, a layer of matrix atoms next to particle interface are removed.

The Guinier radius of the nanoparticle is calculated such as:

(a) each nanoparticle, defined by iso position, is extracted from the general volume in a smaller volume (typically $10\times10\times10$ nm^3) (*Figure 11* (a));

(b) in this smaller volume, the detection algorithm (iso position) is used a second time (*Figure 11* (b)). In this case, parameters (threshold value, C_{min},

sphere radius, R_{max}) are carefully chosen. The choice of parameters in this case may differ from one particle to another;

(c) in order to get the best location of the nanoparticle interface, erosion is used. It is considered that the real interface of the nanoparticle is reached, when the difference between sizes of nanoparticle containing Fe (*Figure 11* (*c*)) and without Fe (*Figure 11* (*d*)) is less than 0.2 nm.

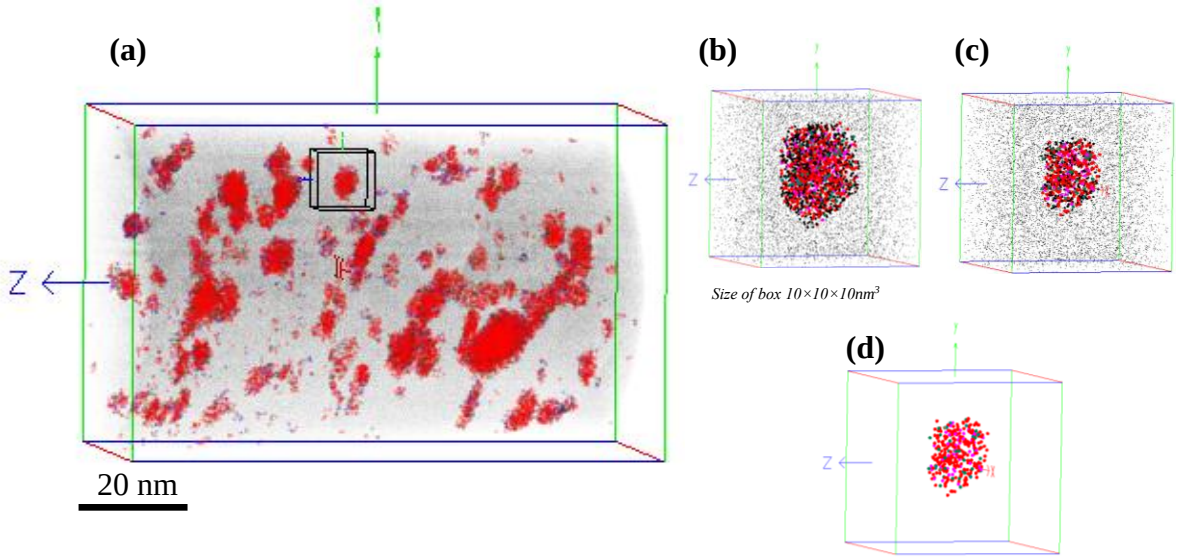

Figure 11. 3DAP reconstructions of nanoparticle observed in MA NDS steel annealed at 700°C/1h. a) Isolated nanoparticles after iso position in the general volume, (b) extracted nanoparticle with R_g=3.2 nm, (c) nanoparticle after erosion, R_g=2.2 nm (d) same nanoparticle composed only of Ti, N, Al and molecular ions TiO, TiN, CrN, AlO R_g=2.1 nm. The real interface of nanoparticle is reached since $0<R_g^{(Fe)}-R_g^{(no\ Fe)}<0.2$ nm.

Appendix 4. Field evaporation model

A model, which simulates the field evaporation of atoms and their trajectories from the tip apex to a detector was developed in the laboratory GPM [8–10]. The field emitter is represented as a stack of atoms in the form of a cylinder terminated by a hemispherical cap of radius R. The shape of the atomic volume is defined by the Wigner–Seitz cell of the chosen crystalline structure [11].

This tip is submitted to an electric potential, V_0. Far from the tip, the potential is fixed at 0. Between the sample and null voltage electrode the partial distribution of potential can be calculated by solving numerically the Laplace equation:

$$\Delta V=0 \qquad (1)$$

The space between the tip and the electrode is divided into a regular cubic grid of discrete points. Each site is represented by three coordinates i, j, k. The potential in each site is noted $V_{i,j,k}$ (*Figure 12*). In each site, local Laplace equation (1) can be applied. By this way, the value of potential V in each point of the volume can be estimated. This numerical solution can be simplified to local mean value in each point. Thus, the value in each point is determined by the six first neighbours of this point:

$$V_{ijk} = \frac{1}{6}\left[V_{i+1,j,k} + V_{i-1,j,k} + V_{i,j+1,k} + V_{i,j-1,k} + V_{i,j,k+1} + V_{i,j,k-1}\right] \qquad (2)$$

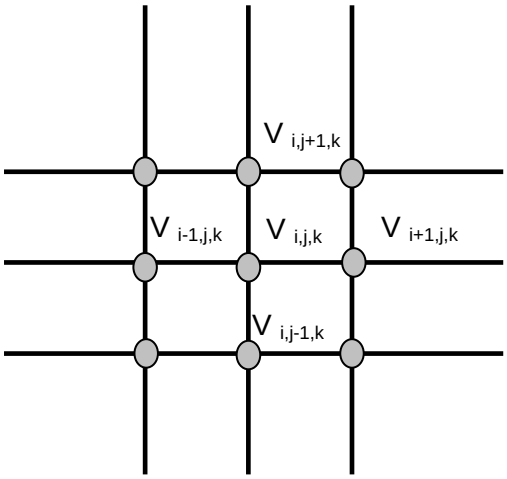

Figure 12. Each cell is given by its coordinates i,j,k [12].

This condition has to be satisfied in each point of the tip. Just the limits of the volume are not affected by the potential resolution.

In order to represent a thermally activated process of evaporation, the choice of evaporation atoms is determined by Monte Carlo algorithm [8]. The choice of the evaporated atom is obtained by calculating the relative rate of evaporation, k_i^r, for every atom:

$$k_i^r = \frac{K_i}{\sum_{S=1}^{N} K_s} \tag{3}$$

To these rates, an angular section of $2\Pi\, k_i^r$ is attributed. The total probability being, 1, the segments fill the circular diagram in *Figure 13.* Several segments are big enough to be visible, but most atoms have a probability too small to be distinguished. Then a given angle is chosen randomly, that will lie in one of the before defined sections. The corresponding atom is then chosen for evaporation. In this way the probability to have an atom with the highest rate k_i to be chosen is very high, but non systematic. In addition this process takes into account both the distribution of the EF at the tip surface and the stochastic nature of field evaporation as thermal process.

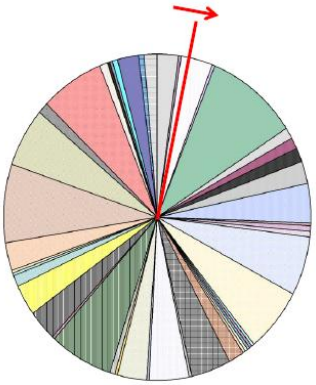

Figure 13. Circular diagram showing relative rates of evaporation of surface atoms.

The trajectories of ions at the close vicinity of the tip are calculated using the Newton equation of motion, ($F = eE = md^2r/dt^2$). Ion impacts on a detector placed in front of the tip are deduced from these trajectories. More details about the model can be found in ref [8–10].

Appendix 5. MatCalc script

The script used for MatCalc simulation of precipitation kinetic in Fe-18Cr-1W-0.14 N NDS steel is shown below:

MatCalc script: annealing 850

```
select-elements Cr Ti N Fe
select-phase bcc_a2 fcc_a1
set-reference-element fe
read-thermodyn-database
change-phase-status fcc_a1#01 f s s
enter-composition wp Cr=18 N=0.14 Ti=0.5
$*****************************************************************
$  DEFINED VARIABLES : Temperatures... Times...
$*****************************************************************
set-variable-value x_scale 0.0
set-variable-value ipdcf 1e-2                $ inner particle diffusion coefficient
set-variable-value npc 100                   $ number of particle classes
set-variable-value ssprl 100                 $ store every
set-variable-value irf 5                   $ inactive radius factor
$  TIMES in s.
set-variable-value t_heating 60
set-variable-value t_tempering 3600
set-variable-value t_cool 60
$ TEMPERATURES in °C
set-variable-value Temp_RT 25                $ Température ambiante
set-variable-value Temp_tempering 850
$ read diffusion data and physical constants
read-mobility-database IWS_Steel
read-physical-database PhysData.pdb
set-temperature-celsius 1200
set-automatic-startvalues
calc-equilibrium
$*****************************************************************
$ PRECIPITATES DOMAINS
$*****************************************************************
create-precipitate-domain Ferrite
set-precipitation-parameter Ferrite x bcc_a2
set-precipitation-parameter Ferrite d 1e14 $ densité de dislocations dans la ferrite [ref. Hoelzer Ph.D]
set-precipitation-parameter Ferrite g 9e-7          $ taille de "grains" de la martensite correspond au bloc de lattes
set-precipitation-parameter Ferrite l 1          $ facteur de forme
set-precipitation-parameter Ferrite o 1          $ facteur de forme
$*****************************************************************
$    PRECIPITATES
$*****************************************************************
```

```
$ New ppt. phase MX (fcc_a1#01)
create-new-phase fcc_a1#01 p
set-precipitation-parameter fcc_a1#01_p0 c npc
set-precipitation-parameter fcc_a1#01_p0 d Ferrite      $"Ca précipite dans l'austénite"
set-precipitation-parameter fcc_a1#01_p0 i 0
set-precipitation-parameter fcc_a1#01_p0 l 1e100
set-precipitation-parameter fcc_a1#01_p0 n s g d      $nucleation site = joints de grains, dislocations
set-precipitation-parameter fcc_a1#01_p0 n n t
set-precipitation-parameter fcc_a1#01_p0 n c o
set-precipitation-parameter fcc_a1#01_p0 n i y
set-precipitation-parameter fcc_a1#01_p0 n r irf
set-precipitation-parameter fcc_a1#01_p0 n a m
set-precipitation-parameter fcc_a1#01_p0 n m i
set-precipitation-parameter fcc_a1#01_p0 n t 1.0
set-precipitation-parameter fcc_a1#01_p0 n u 1.0

set-precipitation-parameter fcc_a1#01_p0 s d r ipdcf
$_____
create-global-table tabl1
$ tempering
add-table-entry tabl1 0 Temp_RT
add-table-entry tabl1 t_heating Temp_tempering
add-table-entry tabl1 t_heating+t_tempering Temp_tempering
add-table-entry tabl1 t_heating+t_tempering+t_cool Temp_RT

set-sim-parameter e t_heating+t_tempering+t_cool
set-sim-parameter t t tabl1 10
set-sim-parameter s r
set-sim-parameter c w y
set-sim-parameter c o y
set-sim-parameter c d 0
set-sim-parameter u 100
set-sim-parameter r l ssprl
start-precipitate-simulation
$*****************************************************************
$    script with Definition GUI windows, plots...
$*****************************************************************
new-gui-window p1
set-gui-window-property . m y
set-gui-window-property . X stepvalue/3600  $ pour diviser les abcisses par 3600 (s->h)
set-plot-option . s n b t$c                    $ add series: Temperature
set-plot-option . s m -1 t$c T                 $ pour nommer la série
set-plot-option . a x 1 t temps[h]             $ change x-axis title
set-plot-option . a x 1 y lin                  $ échelle des abcisses: linéaire
set-plot-option . a x 1 s 0..1                 $ échelle des abcisses: valeurs 0..1
set-plot-option . a y 1 t T[°C]            $ change y-axis title
set-plot-option . l r                      $ define legend: right
set-gui-window-property . m n                  $ Disable the GUI window manual update.
update-gui-window .                        $ Update the GUI window
```

```
$ Phase fractions
new-gui-window p1
set-gui-window-property . m y
set-gui-window-property . X stepvalue/3600  $ pour diviser les abcisses par 3600 (s->h)
set-plot-option . s n b f$fcc_a1#01_p0              $ add series: MX
set-plot-option . s m -1 f$fcc_a1#01_p0 TiN $ pour nommer la série
set-plot-option . a x 1 t time [h]              $ change x-axis title
set-plot-option . a x 1 y lin                   $ échelle des abcisses linéaire
set-plot-option . a x 1 s 0..1                      $ échelle des abcisses: valeurs 0..1
set-plot-option . a y 1 f 100                   $ pour multiplier les y par 100
set-plot-option . a y 1 t weight%               $ change y-axis title
set-plot-option . l r                           $ define legend: right
set-gui-window-property . m n                   $ Disable the GUI window manual update.
update-gui-window .                                 $ Update the GUI window
new-gui-window p1
set-gui-window-property . m y
set-gui-window-property . X stepvalue/3600        $ pour diviser les abcisses par 3600 (s->h)
                                                        $ Number of Particles
set-plot-option . s n b num_part$fcc_a1#01_p0           $ add series: MX
set-plot-option . s m -1 num_part$fcc_a1#01_p0 MX       $ pour nommer la série
set-plot-option . a x 1 t time [h]                  $ change x-axis title
set-plot-option . a x 1 y lin                       $ échelle des abcisses linéaire
set-plot-option . a x 1 s 0..1                      $ échelle des abcisses: valeurs 0..1
set-plot-option . a y 1 t density               $ change y-axis title
set-plot-option . a y 1 y log                   $ échelle des ordonnées: log
set-plot-option . a y 1 s 1e24..1e25            $ éscale of y axis
set-plot-option . l r                           $ define legend: right
set-gui-window-property . m n                   $ Disable the GUI window manual update.
update-gui-window .                                 $ Update the GUI window

$ Mean radius
new-gui-window p1
set-gui-window-property . m y
set-gui-window-property . X stepvalue/3600 $ pour diviser les abcisses par 3600 (s->h)
set-plot-option . s n b r_mean$fcc_a1#01_p0         $ add series: MX
set-plot-option . s m -1 r_mean$fcc_a1#01_p0 MX  $ pour nommer la série
set-plot-option . a x 1 t time [h]              $ change x-axis title
set-plot-option . a x 1 y lin                   $ échelle des abcisses linéaire
set-plot-option . a x 1 s 0..1                  $ échelle des abcisses: valeurs 0..1
set-plot-option . a y 1 f 1e9                   $ pour multiplier les y par 1e9
set-plot-option . a y 1 t mean radius[nm]       $ change y-axis title
set-plot-option . a y 1 y log                   $ échelle des ordonnées: log
set-plot-option . a y 1 s 0.1..2                $ scale of y axis
set-plot-option . l r                           $ define legend: right
set-gui-window-property . m n                   $ Disable the GUI window manual update.
update-gui-window .                                 $ Update the GUI window
```

Results of simulation are reported below. Number density and mean radius are represented for each temperature condition below:

600°C : mean radius = 1.7 nm ; mean density = 4.5×10^{23} m^{-3}
700°C : mean radius = 2.1 nm ; mean density = 2.5×10^{23} m^{-3}
850°C : mean radius =9.8 nm ; mean density = 2.5×10^{21} m^{-3}
1000°C : mean radius = >30 nm ; mean density = 6.5×10^{19} m^{-3}

Bibliography of Appendixes

[1] M. K. Miller, Atom-probe Tomography: Analysis at the Atomic Level, Kluwer Academic/Plenum, New York, 2000.

[2] L.A. Giannuzzi, F.A. Stevie, Introduction to Focused Ion Beams: Instrumentation, Theory, Techniques, and Practice, 2005.

[3] S. Novy, Mécanismes De Vieillissement à Très Longue Échéance Des Aciers Inoxydables Austénoferritiques. Thèse, Université de Rouen, 2009.

[4] A. Etienne, Etude Des Effets D'irradiations Et De La Nanostructuration Dans Des Aciers Austénitiques Inoxydables. Thèse, Université de Rouen, 2009.

[5] M. Thuvander, H.-O. Andrén, K. Stiller, Q.-H. Hu, Ultramicroscopy 73 (1998) 279–285.

[6] D. Vaumousse, A. Cerezo, P.J. Warren, Ultramicroscopy 95 (2003) 215–221.

[7] G. Da Costa, 3D Data Processing for Atom Probe. Atom Probe Tomography School, GPM - Rouen, (2008).

[8] M. Gruber, F. Vurpillot, A. Bostel, B. Deconihout, Surface Science 605 (2011) 2025–2031.

[9] F. Vurpillot, M. Gruber, G. Da Costa, I. Martin, L. Renaud, A. Bostel, Ultramicroscopy 111 (2011) 1286–1294.

[10] M. Gruber, Ph.D. Université De Rouen. In Progress.

[11] E. Wigner, F. Seitz, Phys. Rev. 43 (1933) 804–810.

[12] F. Vurpillot. Thèse, Université de Rouen, 2001.

Study of the formation of nano-particles in ODS and NDS steels by Atom Probe Tomography

FeCr ferritic or martensitic matrix reinforced by a thin and dense oxide dispersion (ODS steels) exhibit good radiation resistance and mechanical properties at high temperature. Thus, ODS steels are considered as candidate materials for core elements of future nuclear reactors. Based on this positive experience, a new type of material, inside which the oxide dispersion is replaced by a nitride dispersion (NDS steels) was elaborated at CEA Saclay. Two distinct ways of elaboration were used: mechanical alloying (MA) and nitriding. In this work, ODS and NDS steels were investigated at different steps of elaboration process (as-milled/as-nitrided, annealed up to 1000ºC and consolidated states) by Atom Probe Tomography and others complementary techniques. In ODS steels, it was shown that two simultaneous mechanisms occur during MA: dissolution of initial yttria powder and formation of Y-O-rich clusters due to precipitation and/or resulting from an incomplete dissolution. During subsequent annealing and consolidation, Y-O-rich clusters act as nuclei for formation of Y-Ti-O-rich nanoparticles. As far as NDS steels are concerned, it was shown that MA is an effective elaboration process. The microstructure contains significant amount of nanometer scale nitrides. An important feature is that their nucleation starts during MA process. As for the consolidated material, nanometer sizes and high number densities of nitrides are comparable to the values measured in different ODS steels. Concerning nitriding process, different types of nitrides (CrN, TiN) were observed in the NDS steels. However, the investigations showed that the microstructure is largely heterogeneous in this case and further optimization of the process are required for further application.

Étude par Sonde Atomique Tomographique de la formation de nano-particules dans les aciers ODS et NDS

Les aciers ferritiques-martensitiques (FeCr) renforcés par une dispersion fine et dense d'oxydes (acier ODS - Oxide Dispersion Strengthened) possèdent une bonne résistance à l'irradiation et des propriétés mécaniques élevées à haute température. Les aciers ODS sont ainsi de bons candidats comme matériaux des structures de cœur des réacteurs de Génération IV. Il est envisageable de renforcer ces aciers par des nitrures nanométriques plutôt que par des oxydes (aciers NDS - Nitride Dispersion Strengthened). Dans cette thèse, des aciers ODS et NDS élaborés au CEA Saclay par 2 procédés distincts (mécanosynthèse et nitruration) sont étudiés par sonde atomique tomographique et d'autres techniques complémentaires, à différentes étapes du procédé d'élaboration (brut de broyage/nitruration, après recuit, après consolidation). Dans les aciers ODS, il apparait que deux mécanismes se produisent pendant la mécanosynthèse : la dissolution de la poudre d'oxyde d'yttrium initiale et la formation d'amas riches en Y et O. Il n'a pas été possible de déterminer si ces amas résultent d'un phénomène de précipitation ou d'une dissolution incomplète de l'oxyde initial. Pendant les recuits et la consolidation, ces amas servent de germes à la formation de particules riches en Y, Ti et O. En ce qui concerne les aciers NDS, que la mécanosynthèse est un procédé efficace pour obtenir une fine et dense dispersion de nitrures. Ces nitrures germent pendant l'étape de broyage mécanique. La taille et la densité numérique de ces nano-renforts dans le matériau consolidé sont similaires à ce qui est généralement observé dans les aciers ODS. Concernant le procédé de nitruration, différents nitrures sont observés (CrN, TiN). Il apparait que la microstructure obtenue est très hétérogène et que le procédé doit être optimisé.